Titre: Title:	A Non-Linear Frequency Domain Potential Flow Model for Compressible, Transonic and Viscous Aeroelastic Analyses
Auteur: Author:	Matthieu Parenteau
Date:	2021
Type:	Mémoire ou thèse / Dissertation or Thesis
Référence: Citation:	Parenteau, M. (2021). A Non-Linear Frequency Domain Potential Flow Model for Compressible, Transonic and Viscous Aeroelastic Analyses [Thèse de doctorat, Polytechnique Montréal]. PolyPublie. https://publications.polymtl.ca/6629/

POLYTECHNIQUE MONTRÉAL
affiliée à l'Université de Montréal

A Non-Linear Frequency Domain Potential flow Model for Compressible, Transonic and Viscous Aeroelastic Analyses

MATTHIEU PARENTEAU
Département de Génie Mécanique

Thèse présentée en vue de l'obtention du diplôme de *Philosophiæ Doctor*
Génie mécanique

Mai 2021

POLYTECHNIQUE MONTRÉAL
affiliée à l'Université de Montréal

Cette thèse intitulée :

A Non-Linear Frequency Domain Potential flow Model for Compressible, Transonic and Viscous Aeroelastic Analyses

présentée par **Matthieu PARENTEAU**
en vue de l'obtention du diplôme de *Philosophiæ Doctor*
a été dûment acceptée par le jury d'examen constitué de :

Aouni A. LAKIS, président
Éric LAURENDEAU, membre et directeur de recherche
Afzal SULEMAN, membre
Marco CARINI, membre externe

DEDICATION

À tous mes collègues du NS-LAB et mention spéciale aux co-créateurs de CHAMPS, je n'oublierai jamais les débuts dans le sous-sol de Simon...

ACKNOWLEDGEMENTS

J'aimerais tout d'abord remercier mon directeur de recherche Éric Laurendeau de m'avoir donné la chance d'effectuer ce projet de recherche. Il a toujours été présent pour m'offrir du support et il a toujours su rester optimiste par rapport au projet, ce qui fut d'une très grande aide.

Je voudrais également remercier particulièrement Simon et Frédéric. Nous sommes ensemble dans le laboratoire depuis la maitrise et je vous remercie pour votre aide et pour toutes nos conversations "pertinentes" de pause café.

Je remercie également mes parents, Nicole et René, pour m'avoir supporté et encouragé de poursuivre mes études au doctorat. Finalement, j'aimerais remercier ma conjointe Audrey pour tout le support qu'elle m'a offert. Le doctorat aura été beaucoup plus agréable grâce à elle.

RÉSUMÉ

La prochaine génération d'avions civils vise des réductions ambitieuses des émissions de carbone. Un objectif de réduction de 50% des émissions de CO2 a été fixé par l'Organisation de l'Aviation Civile Internationale (OACI). Pour atteindre cet objectif, les avionneurs doivent envisager des configurations non conventionnelles, amenant ainsi de nouveaux problèmes de conception.

Une préoccupation majeure est l'instabilité aéroélastique, telle que le flottement qui peut provoquer une défaillance structurelle quasi-instantanée dans des conditions de vol spécifiques. En effet, il s'agit d'un phénomène aéroélastique critique pour les aéronefs impactant directement l'enveloppe de vol. Malheureusement, la prochaine génération d'avions est plus sensible à cette instabilité en raison de l'utilisation de matériaux plus légers et plus flexibles et d'ailes de plus en plus effilées. Par conséquent, l'aéroélasticité est en voie de devenir un des principal moteur de conception.

De ce fait, le travail présenté dans cette thèse aborde le problème de la mise oeuvre d'outils numériques rapides et précis pour l'analyse aéroélastique qui conviennent à la conception conceptuelle et préliminaire. Le défi principal concerne la mise en oeuvre du modèle aérodynamique. La réponse aéroélastique non linéaire de l'aéronef est principalement attribuée au fluide, ce qui nécessite des modèles précis pour représenter le phénomène. Cependant, les modèles de fluides haute fidélité ont tendance à avoir un coût de calcul très élevé, nécessitant des ressources de calcul qui ne sont pas nécessairement disponibles ou qui ne sont pas applicables dans les premières étapes de conception. C'est pourquoi seuls les outils de basse fidélité conviennent aux premières phases de conception.

L'objectif principal de cette thèse est de développer un ensemble logiciel pour la simulation aéroélastique avec une fidélité suffisante pour représenter les instabilités aéroélastiques critiques, tout en maintenant un faible coût de calcul. Les outils développés doivent ainsi convenir à la conception préliminaire d'aéronefs. La solution proposée est basée sur la méthode Unsteady Vortex Lattice, qui est une méthode d'écoulement potentiel linéarisé. Des modifications au modèle sont proposées pour ainsi augmenter sa fidélité et améliorer son efficacité en matière d'analyse aéroélastique.

Une formulation linéaire dans le domaine fréquentiel est proposée pour le UVLM afin de réduire le temps de calcul pour la solution de problèmes périodiques. Par la suite, le système linéaire est reformulé dans le problème aéroélastique classique pour obtenir une formulation compatible avec les normes de l'industrie pour l'analyse de stabilité concernant le flottement

(méthode p-k). Les résultats montrent que la formulation est équivalente au Doublet Lattice Method (DLM), un standard de l'industrie, mais sans les hypothèses de dynamique hors plan. Par conséquent, l'approche est générale et est appliquée à un problème de flottement plus compliqué impliquant une dynamique dans le plan, soit la configuration empennage en T.

La formulation fréquentielle linéaire est applicable uniquement aux problèmes aéroélastiques linéaires, par conséquent une formulation non linéaire est nécessaire pour l'analyse des oscillations de cycle limite (LCO). Les LCO sont un autre type de condition aéroélastique instable étroitement liée au flottement et peuvent causer une fatigue structurelle importante. Une extension non linéaire fréquentielle est donc développée en utilisant l'approche *harmonic balance*. La solution proposée peut résoudre des problèmes dynamiques non linéaires avec la même précision que le UVLM standard dans le domaine temporel. Cependant, plus d'un ordre de grandeur est gagné en termes de coût de calcul. Le *harmonic balance* VLM montre ainsi un grand potentiel pour l'analyse aéroélastique dynamique linéaire et non linéaire. La méthode est, cependant, toujours basée sur la théorie de l'écoulement potentiel linéaire, qui est rarement applicable à des conditions réelles.

Afin d'améliorer la fidélité du modèle aérodynamique, une méthodologie de corrections est proposée pour introduire des effets d'épaisseur, visqueux et compressibles. Le schéma de couplage est basé sur une méthode de correction de l'angle d'attaque bien établie pour la méthode VLM stationnaire. Les corrections sont calculées de manière itérative avec des données bi-dimensionnelles (2D) aérodynamiques, comme la portance, la traînée et le moment de tangage. Les données aérodynamiques sont cependant calculées avec un modèle de fluide haute fidélité qui intègre l'épaisseur, la compressibilité, les effets transsoniques et les effets visqueux. Dans ce travail, un solveur Euler/RANS est utilisé pour fournir les données. De plus, les effets d'écoulement transversal dus à l'angle de flèche de l'aile sont introduits à travers des conditions d'aile en flèche infinie, ce qui améliore les capacités de modélisation. Étant donné que les données haute fidélité restent 2D et stables, le coût de calcul reste relativement faible, car elles sont calculées une fois et peuvent être stockées. Néanmoins, les données haute fidélité restent stationnaires, donc une extension quasi stationnaire est proposée pour les simulations instationnaires dans le domaine fréquentiel avec le VLM. Par contre, l'effet de compressibilité instationnaire n'est pas modélisé par le UVLM et il ne peut pas être introduit par l'algorithme de couplage puisque les données de section sont stationnaires. Donc, une approximation du temps retardé est proposée et mise en oeuvre dans la formulation *harmonic balance* du VLM. Par la suite, l'approche est vérifiée à l'aide de solutions Euler/RANS haute fidélité instationnaires pour des profils aérodynamiques oscillants. Le résultat montre que le temps retardé améliore considérablement la précision des solutions

des écoulements compressibles instationnaires, tandis que l'algorithme de couplage introduit avec succès l'effet de l'épaisseur et de la viscosité. Le *harmonic balance* VLM avec corrections montre des capacités de modélisation suffisantes pour l'analyse aéroélastique dynamique non linéaire.

La dernière partie de la thèse se concentre sur l'application du *harmonic balance* VLM à des problèmes aéroélastiques dynamiques. En premier lieu, les problèmes 2D sont considérés en utilisant un système aéroélastique classique à deux degrés de liberté. La limite de flottement est calculée sur la configuration Isogai et la solution est comparée à des solveurs haute fidélité. Les branches inférieure et supérieure de la limite de flottement sont calculées avec succès. Par la suite, les branches LCO sont calculées sur une configuration légèrement différente jusqu'à un nombre de Mach de 0.84. Les branches faibles instables et fortes stables sont bien représentées avec des résultats comparables à ceux des solutions Euler haute fidélité. Par la suite, la méthode est appliquée à deux cas 3D, à savoir l'aile supercritique BSCW et l'aile Agard. Pour l'aile BSCW, la pression dynamique de flottement obtenue est à moins de 1% de celle des données expérimentales. Pour l'aile Agard, la limite de flottement est également bien calculée jusqu'à un nombre de Mach de 0.678. Malheureusement, le creux de flottement à un nombre de Mach de 0.96 est sous-estimé. Finalement, le comportement LCO de l'aile Agard est étudié dans des conditions visqueuses et les résultats sont cohérents avec la littérature.

L'ensemble logiciel développé dans cette thèse montre un grand potentiel d'application industrielle pour la conception d'avions. La formulation fréquentielle linéaire est efficace et inclut naturellement une dynamique dans le plan. Par conséquent, il offre de meilleures capacités de modélisation par rapport à son homologue le DLM, qui est encore largement utilisé aujourd'hui pour la certification des aéronefs. D'autre part, la formulation du domaine de fréquence non linéaire montre des capacités de modélisation non linéaire impressionnantes et l'ajout de corrections sectionnelles et compressibles permet de simuler divers problèmes aéroélastiques dynamiques non linéaires. En effet, pour des nombres de Mach modérés, la précision est comparable à celle des solveurs haute fidélité. Cependant, lorsque les effets de compressibilité deviennent important, le *harmonic balance* VLM est malheureusement moins fiable. Ces limites sont conformes à l'hypothèse quasi stationnaire faite pour les corrections de section. La correction du moment de tangage est également limitée aux corrections stationnaires. Par conséquent, le VLM introduit des erreurs supplémentaires pour la composante instationnaire puisque l'effet de l'épaisseur n'est pas modélisé. Enfin, la correction de compressibilité instable introduite comme un temps retardé n'est qu'une approximation. Par conséquent, un travail supplémentaire pourrait être fait sur son intégration afin d'améliorer les résultats à des nombres de Mach plus élevés. Néanmoins, ces travaux apportent des con-

tributions majeures au domaine de l'aérodynamique numérique instationnaire, ainsi qu'au domaine de l'aéroélasticité dynamique.

ABSTRACT

The next generation of civil aircraft is aiming at ambitious reductions of carbon emissions. A goal of 50% reduction in CO2 emissions has been set by IATA. In order to achieve this goal, aircraft manufacturers will have to consider unconventional configurations, which bring new design problems.

One major concern is aeroelastic instability, such as flutter which can cause structural failure in normal flight conditions. Indeed, it is the most critical aeroelastic phenomenon for aircraft impacting directly the flight envelope. Unfortunately, the next generation of aircraft is more susceptible to this instability due to the use of lighter, more flexible materials and higher aspect ratio wings. As a result, aeroelasticity is becoming the main design driver.

The field of aeroelasticity studies the interaction of inertial, elastic and aerodynamic forces. Aeroelastic analysis is therefore complex, due to the interaction between the structure of the aircraft and the airflow. Consequently, implementing numerical tools capable of carrying these simulations with a relatively low computational cost represents a significant challenge. However, critical design problems can be avoided if these analyses are included as soon as possible in the design process.

Therefore, the work presented in this thesis tackles the problem of implementing fast and accurate numerical tools for aeroelastic analysis that are suitable for conceptual and preliminary design. The main challenge behind this problem concerns the aerodynamic model. The non-linear aeroelastic response of the aircraft is mainly attributed to the fluid, thus requiring accurate models to capture the essential phenomenon. However, accurate fluid models tend to have a high computational cost, thus requiring computing resources that are not often available or not practical in the early design stages. As a result, only low-fidelity tools are suitable for conceptual design.

The main goal of this thesis is to develop an efficient aeroelastic framework with sufficient fidelity to capture critical aeroelastic instabilities, while maintaining a low computational cost to be used early on in the design process. The proposed solution is based on the Unsteady Vortex Lattice Method, which is a linearized potential flow method. Modifications to the model are proposed to increase its fidelity and to improve its efficiency in regards of aeroelastic analysis.

A linear formulation in the frequency domain is proposed for the UVLM to reduce the computational time for periodic problems. Thereafter, the linear system is recast into the

classical aeroelastic problem to provide a formulation compatible with the industry standards for stability analysis to compute the flutter onset using the p-k method. The result shows that the linear frequency domain formulation is equivalent to the DLM, but without the assumptions of out-of-plane dynamics. Consequently, the approach is general and is applied to a more complicated flutter problem involving in-plane dynamics, the T-tail configuration.

The linear frequency formulation is applicable to linear aeroelastic problems only, therefore a non-linear formulation is required for the analysis of Limit Cyle Oscillations. LCOs are another type of unstable aeroelastic condition closely related to flutter and it can cause serious structural fatigue. A non-linear frequency domain formulation is therefore developed using the harmonic balance approach. The proposed solution can solve non-linear dynamic problems with the same accuracy than the standard time-domain UVLM. However, more than one order of magnitude is gained in terms of computational cost. As a result, this harmonic balance VLM shows great potential for linear and non-linear dynamic aeroelastic analysis. The approach is, however, still based on linear potential flow theory, which is rarely applicable to any real aircraft flow conditions.

In order to improve the fidelity of the aerodynamic model, a correction scheme is proposed to introduce thickness, viscous and compressible effects. The coupling scheme is based on a well-established angle of attack correction method for the steady Vortex Lattice Method. The corrections are computed iteratively with aerodynamic sectional data, namely the lift, drag and pitching moment. The aerodynamic data is, however, computed with a two-dimensional high-fidelity fluid model that incorporates thickness, compressibility and viscous effects. In this work, a RANS flow solver is used to provide the data. Moreover, cross-flow effects due to a geometric sweep in the wing are introduced through an infinite swept wing conditions, which improves the modeling capabilities for swept wings. Since the high-fidelity data remains 2D and steady, the computational cost remains relatively low since they are computed once and they can be stored to be used whenever necessary. Nevertheless, the high-fidelity data remains steady, thus a quasi-steady extension is proposed for the unsteady simulations with the frequency domain VLM. Furthermore, the effect of unsteady compressibility is not modeled by the UVLM and it cannot be introduced through the coupling algorithm since the sectional data is steady. As a result, an approximation of the retarded time is proposed and implemented within the harmonic balance VLM. Thereafter, the approach is verified against unsteady high-fidelity Euler/RANS solutions for pitching/heaving airfoils and a pitching wing. The result shows that the retarded time improves significantly the solution of unsteady compressible flows, while the coupling algorithm with sectional data introduces successfully the effect of thickness and viscosity. The harmonic balance VLM with corrections shows sufficient modeling capabilities for dynamic aeroelastic analysis.

The final part of the thesis focuses on the application of the harmonic balance VLM to dynamic aeroelastic problems. First, 2D problems are considered using a classical two degree of freedom aeroelastic system. The complete flutter boundary is computed on the Isogai configuration with comparison against high-fidelity solution. The lower and upper branches of the flutter boundary are successfully captured by the harmonic balance. Thereafter, LCO branches are computed on a slightly different configuration up to a Mach number of 0.84. The weak unstable and strong stable branches are well captured with comparable results to high-fidelity Euler solutions. Afterward, the framework is applied to two 3D cases, namely the supercritical BSCW wing and the Agard wing. For the BSCW wing, the flutter dynamic pressure is well captured within 1% of the experimental data. For the Agard wing, the flutter boundary is also well captured up to a Mach number of 0.678. Unfortunately, the flutter dip at a Mach number of 0.96 is underestimated. The LCO behavior of the Agard wing is also investigated in viscous conditions and the results are consistent with the literature.

The framework developed in this thesis shows great potential for industrial application for the design of aircraft. The linearized frequency formulation is efficient and includes naturally in-plane dynamics. Consequently, it offers better modeling capabilities when compared to its counterpart the DLM, which is still widely used today for aircraft certification. On the other hand, the non-linear frequency domain formulation shows impressive non-linear modeling capabilities and with the addition of sectional and compressible corrections, the approach can compute various non-linear dynamic aeroelastic problems with sufficient accuracy. Indeed, for moderate Mach numbers the accuracy is comparable to high-fidelity solvers. However, when compressibility effects become strong along with the unsteadiness of the flow, the harmonic balance VLM is struggling. These limitations are in line with the quasi-steady assumption made for the sectional corrections. The pitching moment correction is also limited to steady corrections, thus the VLM introduces additional errors for the unsteady component since the effect of thickness is not modeled. Finally, the unsteady compressibility correction introduced as a retarded time is only an approximation. Therefore, additional work could be done on the implementation to hopefully improve the results at higher Mach numbers. Nonetheless, this work provides main contributions to the field of unsteady aerodynamics and aeroelasticity.

TABLE OF CONTENTS

LIST OF TABLES

LIST OF FIGURES

LIST OF SYMBOLS AND ACRONYMS

IATA	International Air Transport Association
MDO	Multi-disciplinary Design Optimization
CFD	Computational Fluid Dynamic
CSD	Computational Structural Dynamic
RANS	Reynolds-Averaged Navier-Stokes
URANS	Unsteady Reynolds-Averaged Navier-Stokes
TSD	Transonic Small-Disturbance
BEM	Boundary Element Method
DOF	Degree-Of-Freedom
SDOF	Single Degree-Of-Freedom
AoA	Angle-Of-Attack
EC	Elastic Center
LCO	Limit-Cycle Oscillation
GAF	Generalized Aerodynamic Force
VLM	Vortex Lattice Method
DLM	Doublet Lattice Method
NL-VLM	Non-Linear Vortex Lattice Method
UVLM	Unsteady Vortex Lattice Method
NLFD	Non-Linear Frequency Domain
HB	Harmonic Balance
TS	Time Spectral
FFT	Fast Fourier Transform
DFT	Discrete Fourier Transform
CRM	Commmon Research Model
FEM	Finite Element Model
GFEM	Global Finite Element Model
HB VLM	Harmonic Balance Vortex Lattice Method
NL-HB VLM	Non-Linear Harmonic Balance Vortex Lattice Method
RBF	Radial Basis Function
TPS	Thin Plate Spline
TE	Trailing Edge
LHS	Left-Hand Side
RHS	Right-Hand Side

CPU	Central Processing Unit
PG	Prandtl-Glauert
SA	Spalart-Allmaras
AePW2	Aeroelastic Prediction Workshop 2

LIST OF APPENDICES

CHAPTER 1 INTRODUCTION

Commercial aviation is responsible for about 2-3% of global carbon emissions[1]. As a result, the following ambitious targets have been set by the International Air Transport Association (IATA):

- An average improvement in fuel efficiency of 1.5% per year from 2009 to 2020
- A cap on net aviation CO2 emissions from 2020 (carbon-neutral growth)
- A reduction in net aviation CO2 emissions of 50% by 2050, relative to 2005 levels

Achieving these ambitious goals requires improvement in many facets of commercial aviation and one solution is to improve the global efficiency of civil aircraft.

In the past few years, commercial flights have seen the arrival of new aircraft with improved fuel consumption, such as the Boeing 787, the Airbus A-350 and the Airbus A-220, formerly the Bombardier Cseries. All these aircraft make use of lighter composite materials and higher aspect ratio wing that leads to more flexible structures. The use of high aspect ratio wing reduces the induced drag, which in turn translates into a reduction of fuel consumption since less power is required from the engine to overcome the drag force. Consequently, next-generation aircraft, such as the truss-braced wing from the Subsonic Ultra Green Aircraft Research (SUGAR) program[2, 3], are aiming at very high aspect ratio wings to achieve maximum efficiency. Another example is the AlbatrossOne aircraft concept from Airbus, which is designed with semi-aeroelastic hinged wing-tips. These wing-tips can flap freely with wind gusts, thereby reducing the aerodynamic loads on the structure, while improving the aircraft overall efficiency. The truss-braced wing and the AlbatrossOne are shown in Figure 1.1.

However, the combination of light materials with flexible structures for high aspect ratio wings generally leads to aeroelastic instabilities, such as flutter, which is regarded as one of the most dangerous phenomena, since it can lead to catastrophic structural failure. A famous example, outside the field of aerospace, is the Tacoma Bridge in 1941. The bridge entered a flutter condition due to the interaction of high winds and the bridge's natural modes of vibration. The structure finally collapsed after exhibiting large amplifying oscillations. It is a dangerous phenomena affecting aircraft, but careful design and adequate tools ensure these instabilities are well outside the normal flight conditions. The first ever recorded structural failure due to aeroelasticity can be traced back to the very beginning of man-powered flight

(a) Airbus AlbatrosOne prototype[4]

(b) Boeing transonic truss-braced wing[5]

Figure 1.1 Examples of new aircraft concepts from Boeing and Airbus.

in 1903[6]. Nine days before the historic flight of the Wright brothers, Samuel Langley encountered for the first time torsional divergence on its monoplane, which inevitably caused the airplane to crash. Aeroelasticity has always been a crucial part of aircraft design and its importance is now even more critical for the design of the next generation of aircraft.

1.1 Motivation and problem statement

The field of aeroelasticity is becoming an important driver[3, 7] behind the design of new aircraft. Consequently, it is essential that aeroelasticity analyses are included throughout the design process.

The design of an aircraft is usually divided into three distinct phases[8, 9]: conceptual, preliminary and detailed. The fidelity of the design tools varies accordingly with the design phases, where low-fidelity methods are favored during the conceptual phase and high-fidelity tools are involved later during the preliminary and detailed design stages.

Low-fidelity approach tends to be simpler and fast as opposed to high-fidelity methods that often require intensive computations and a significant overhead time in preparing the computation, such as mesh generation. Therefore during conceptual design, where hundreds of different configurations are evaluated, tools with fast turnaround time are mandatory. However, due to their simplicity, these fast turnaround tools are often inadequate to fully model the problem at hand. Nonetheless, the early design phase has a significant impact over the final product, thus fidelity is also required. Indeed, up to 80% of the life cycle cost is induced by choices made during the conceptual phase[9], as shown graphically in Figure 1.2. Additionally, mistakes made at this phase may require a redesign much later in the design process, which can create financial problems for the aircraft program. Therefore, the tools

used to evaluate the aeroelastic characteristics of the aircraft at both the conceptual and preliminary phases should have sufficient fidelity while maintaining a fast turnaround time. Combining fidelity and computational cost represents a significant challenge, especially for the evaluation aerodynamic forces.

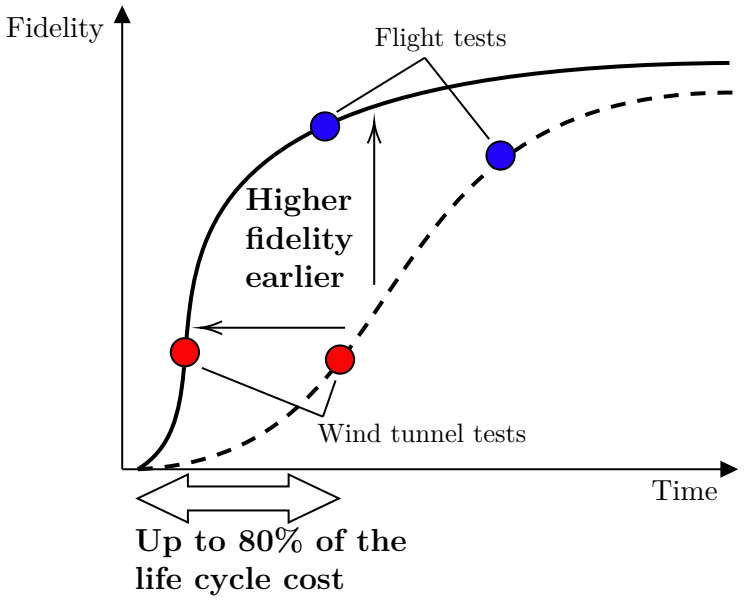

Figure 1.2 Impact of fidelity for the life cycle cost of the aircraft. (reproduced [9])

Consequently, the work presented in this thesis tackles the following problem statement:

> *The design of efficient civil aircraft requires an adequate framework for the analysis of various aeroelastic phenomena, with sufficient fidelity to provide accurate prediction for the entire flight envelope while maintaining a low-computational cost to enable quick estimation of various configurations during the early design phases, which would also enable Multi-Disciplinary Design Optimization (MDO) with aeroelastic constraints.*

A review of the aeroelastic solution procedure is presented next to discuss basic concepts and existing approaches in regards of aeroelastic analysis.

1.2 Overview of numerical aeroelastic solution procedure[1]

Aeroelasticity is a field that studies the interaction between the aerodynamic forces, the inertia forces and the elastic forces. These complex interactions with their associated phenomena are well represented by Collar's triangle of forces[6] in Figure 1.3. The main disciplines of aeroelasticity require the interaction of aerodynamic forces with at least one additional force, while dynamic aeroelasticy requires interaction of all three.

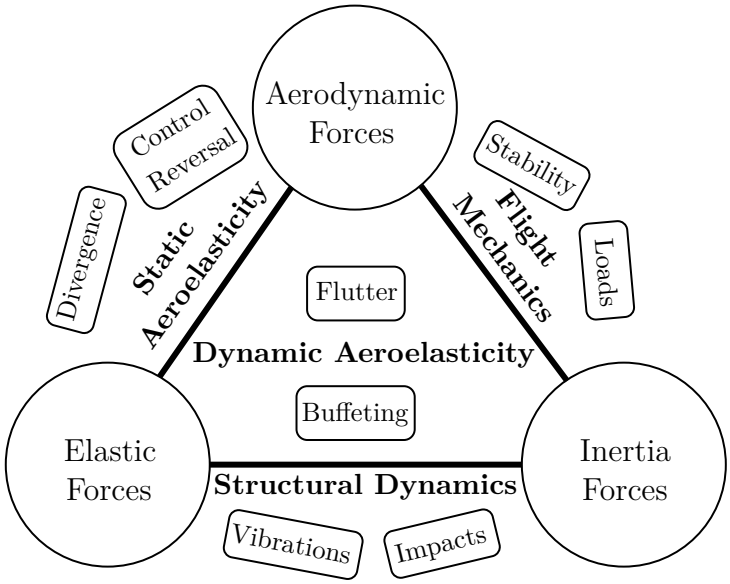

Figure 1.3 Aeroelasticity Collar's triangle of forces.

1.2.1 Static aeroelasticity

Static aeroelastic phenomenon involves the interaction of steady aerodynamics and elastic forces. As the aircraft flies, the wings generate a lift force distributed along the surface of the wing. The aerodynamic force increases exponentially with the speed of the aircraft, which causes static deflections of the wing. However, since the aerodynamic forces are directly dependent of the shape of the wing, its distribution along the wing surface changes accordingly. As a result, a typical aircraft can encounter two main static aeroelastic problems[10, 11, 12]: divergence and control reversal. The overall wing efficiency is also impacted by these static deflections causing a possible increase in total drag, thus reducing the total aircraft efficiency.

[1]This section contains material published in Journal of Fluids and Structures titled "*A general modal frequency-domain vortex lattice method for aeroelastic analyses*"(2020) and also in AIAA Journal titled "*Nonlinear Frequency-Domain Solver for Vortex Lattice Method*" (2018). The dissertation author is the main author and contributor for both papers and copyrights are held by M. Parenteau and E. Laurendeau.

However, if taken into account during the design process, these deflections can lead to more efficient configurations.

Divergence

Wing divergence is observed when the aerodynamic moment overcomes the restoring moments from structural stiffness, which leads eventually to structural failure of the wing. This critical phenomena is illustrated in Figure 1.4 with a simple Single Degree-Of-Freedom (SDOF) airfoil, where the airfoil is submitted to a free stream velocity V_∞ at an Angle Of Attack (AoA) α. The airfoil generates an aerodynamic moment around the Elastic Center (EC) that is balanced by the airfoil internal moment stiffness, which in turn induces a torsional deflection α_T. As the free stream velocity increases, the aerodynamic moment increases along with α_T and a critical velocity is reached when the internal moment stiffness can no longer balance the external aerodynamic moment. At this point, the resulting torsional deflection is divergent and causes structural failure. In other words, divergence is an unstable condition of the aeroelastic system.

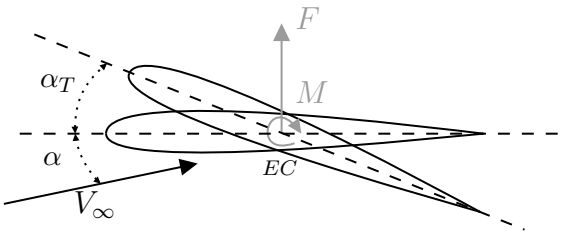

Figure 1.4 Illustration of divergence for a SDOF airfoil section.

Control reversal

As opposed to divergence, control reversal is not an instability, but it affects the overall aircraft maneuverability. The aircraft response to a control surface is affected by the resulting structural deflection. For example, when the aileron is deflected to create a rolling moment of the aircraft, a negative moment is induced from the pressure distribution over the deflected control surface. As a result, the wing undergoes a torsional deflection that reduces the effectiveness of the aileron, as illustrated in Figure 1.5, where δ is the aileron deflection angle. As the speed of the aircraft increases, the loads over the control surface increases and the torsional deflection becomes more important, thus reducing the aileron effectiveness with the speed. Aileron reversal is observed when its deflection creates an opposite response, thus inducing a rolling moment in the opposite of the intended direction.

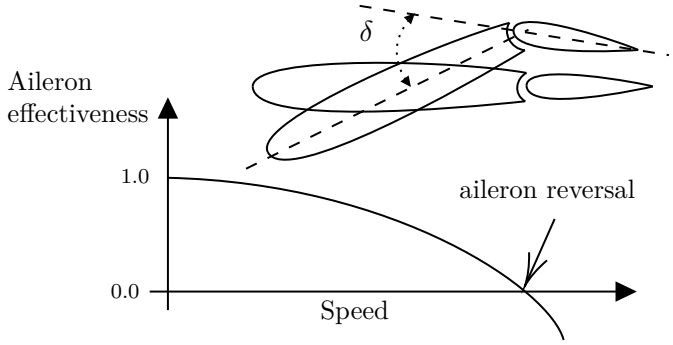

Figure 1.5 Illustration of aileron reversal.

1.2.2 Dynamic aeroelasticity

As shown in Collar's triangle of forces in Figure 1.3, dynamic aeroelasticity requires the interaction of unsteady aerodynamic forces, elastic forces and inertia forces. The most important dynamic aeroelastic phenomenon are[10]:

- Flutter
- Buffeting
- Aeroelastic response to dynamic load
- Dynamic stability and maneuverability of deformable aircraft
- Aero-servoelasticity

Aircraft manufacturers are mainly concerned about flutter, which is one of the most important aeroelastic phenomena[11].

Flutter

Flutter is an unstable self-excited vibration where the structure extracts energy from the airstream. At the critical flutter speed, the extracted energy from the airstream equals the dissipated energy by the internal damping. Consequently, the system is neutrally stable and maintains a periodic motion that becomes unstable at higher speeds with amplification of the periodic motion. Below the flutter speed, these oscillations are damped. This phenomenon leads rapidly to structural failure and for this reason it remains one of the most important aeroelastic phenomena.

There are different types of flutter often described as either classical or nonclassical flutter. Classical flutter involves coupling of two or more modes of motion. An example of this type of flutter is the coupling of the wing-bending and wing-torsion modes. Normally, these motions alone are stable, but a phase shift occurs at the flutter condition causing a coupling of both modes to extract energy together from the air stream. This simple example is shown in Figure 1.6, where a phase shift of 90 degrees between the bending mode and the torsion mode causes the resulting lift force due to each mode to be in phase.

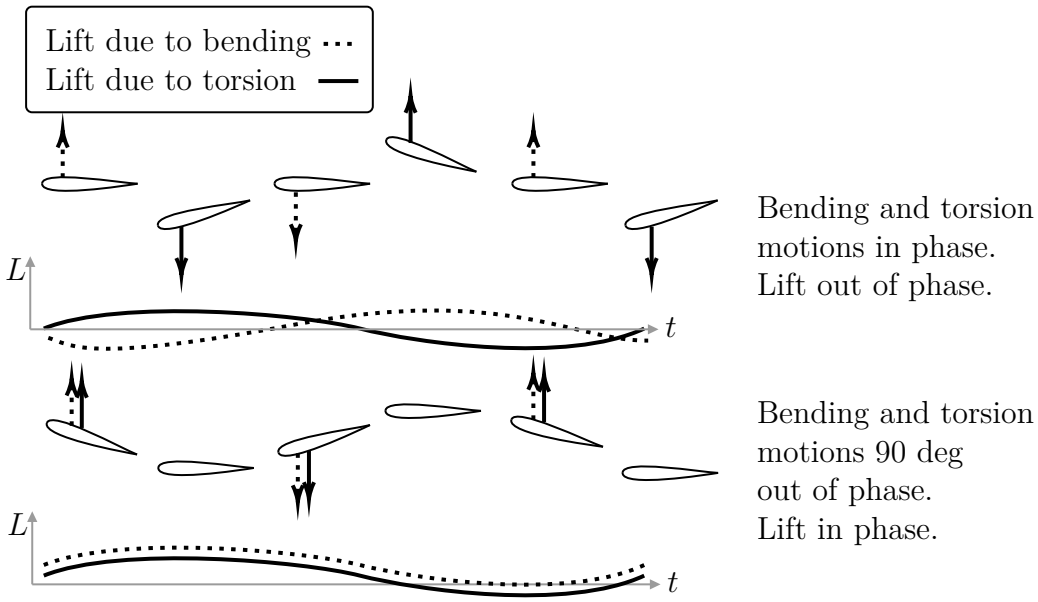

Figure 1.6 Classical flutter for a binary system of bending and torsion mode.(reproduced [11])

Non-classical flutter often involves a single type of motion, such as stall flutter which is encountered at higher angles of attack where flow separation occurs. Aileron buzz is another type of non-classical flutter, that is mainly caused by shock induced separation. The aileron starts oscillating along with the shock wave, causing the aileron to vibrate. The main driver behind these types of flutter is nonlinear perturbation from the flow. Since classical flutter can occur in normal flow conditions (i.e. low incidence angle and fully attached), it is considered more dangerous.

The flutter onset is well predicted by linear theory and the motion amplitude is expected to grow exponentially until structural failure. However, this is not always observed, where the amplitude of oscillations might grow until a Limit Cycle Oscillation (LCO) is reached.

Limit cycle oscillation

LCO is closely related to the flutter onset and generally occurs past the flutter boundary when the sustained oscillations have reached a stable amplitude. Typical LCO branches are depicted in Figure 1.7. An LCO is considered strong when nonlinearity is important or when the amplitude in terms of reduced velocity bends strongly on either side. Furthermore, when the amplitude increases along with the reduced velocity, it is considered stable, since the amplitude increases gradually with the reduced velocity. The LCO is described as unstable when an increase in amplitude is observed for velocities below the flutter point. In these conditions, the LCO can occur below the flutter speed, but a small perturbation can cause a significant jump in amplitude toward the stable branch at higher amplitudes. Consequently, predicting LCOs is also very important since it can induce serious vibration, which in turn causes fatigue, thus reducing the useful life of the structure[10, 11, 13]. However, the prediction of LCO is more complex since it requires a dynamically nonlinear aerodynamic model.

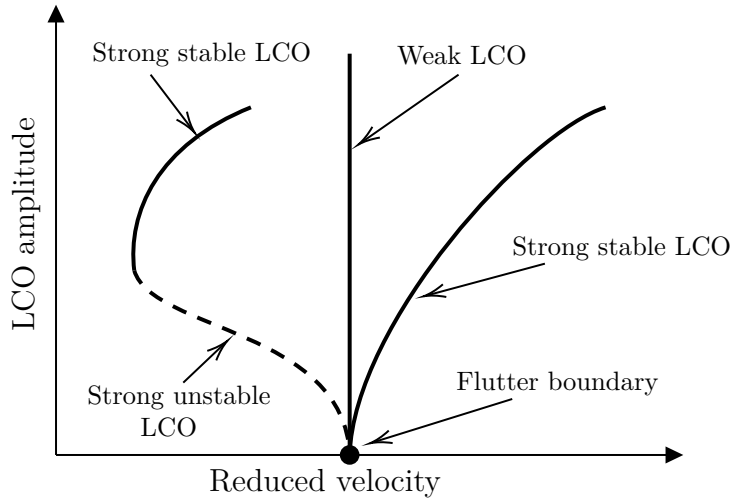

Figure 1.7 Illustration of LCO behavior.(reproduced[14])

1.2.3 Numerical evaluation of flutter and LCO

The numerical analysis of flutter and LCO usually involves the integration of a Computational Structural Dynamic (CSD) model with a Computational Fluid Dynamic (CFD) model to solve the aeroelastic system.

An aeroelastic problem can be defined as either a response problem or a stability problem[15]. When treated as a response problem, both the CSD and CFD models are integrated in time at

various free stream conditions until the amplitude of oscillation due to an initial perturbation is maintained or when the aeroelastic system has zero damping[16, 17], see Figure 1.8.

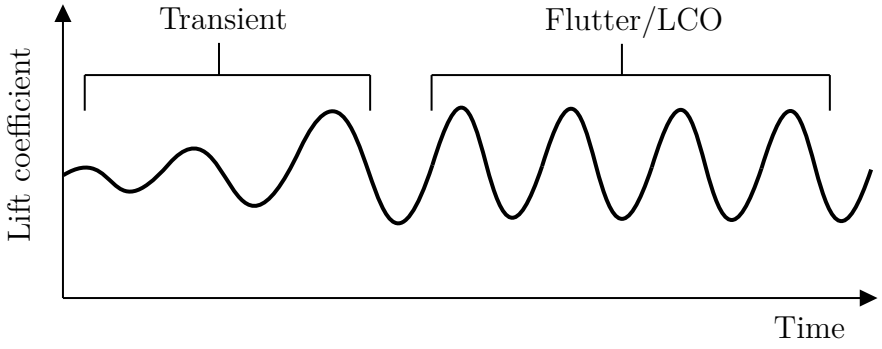

Figure 1.8 Time domain evaluation of a flutter point.

This approach can model nonlinear dynamics and is applicable to many aeroelastic problems such as flutter, LCO and buffeting[15]. However, the time domain approach requires several simulations to find a single flutter point. Additionally, in the case of flutter or LCO analysis, only the converged periodic solution is of interest, thus the transient must be fully resolved. Consequently, the response approach is of high-fidelity, but not efficient.

If the aeroelastic system is treated as a stability problem, an eigenvalue approach is usually taken to determine when the system is unstable or, in other words, when a flutter condition is reached. For dynamic stability problems, the system is generally treated in the frequency domain; thus the converged periodic solution is solved directly, thereby increasing the overall efficiency of the solution process to find the flutter boundary. Additionally, the system can be treated linearly for flutter analysis and an estimation of the true damping value of the aeroelastic system can be computed to determine the flutter point. The *p-k*[18] method provides such estimation of damping. The flutter point is found when the damping reaches zero through the use of a *V-g* plot as illustrated in Figure 1.9. Due to its simplicity, this approach is still widely used today in the industry. However, the Generalized Aerodynamic Force (GAF) matrix must be computed as a function of the various modes of vibration of the structure and for different frequency as well. Therefore, depending on the size of the problem and the aerodynamic model, evaluating the GAF matrix can incur a high computational cost. Furthermore, the *p-k* method is not applicable to LCO.

In order to solve LCOs, recent development has been made using a nonlinear frequency domain approach[14, 19, 20, 21, 22, 23] to solve directly the amplitude and frequency of the sustained oscillations. Additionally, since LCOs and flutter are closely related, these methods are also applicable to determine the flutter point[20, 23]. These approaches are interesting,

since they can model nonlinear dynamic systems assuming a periodic solution. Therefore, they are much more efficient than time domain methods. The aerodynamic models are further discussed in the next section.

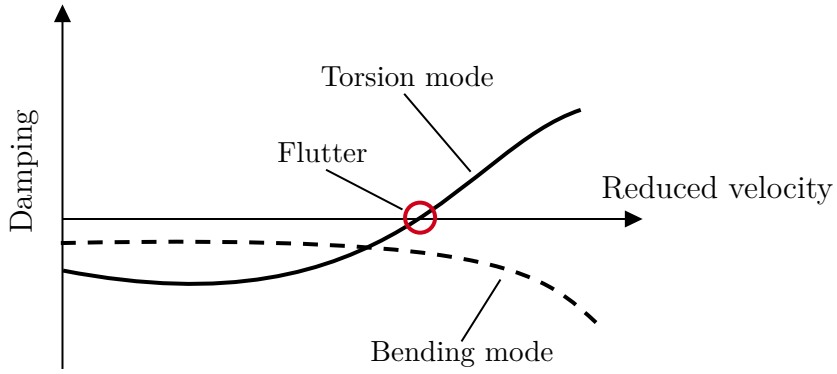

Figure 1.9 Example of damping as a function of reduced velocity.

1.2.4 Aerodynamic models

The fidelity and computational cost of an aeroelastic simulation is mostly dependent on the aerodynamic model. Consequently, great care must be taken to ensure that the model is mathematically capable of modeling the physical phenomena behind the aeroelastic instability we wish to evaluate. Unfortunately, higher fidelity incurs higher computational cost, thus only low to medium fidelity tools are applicable for conceptual design. The main hierarchy of fluid models is presented in Figure 1.10.

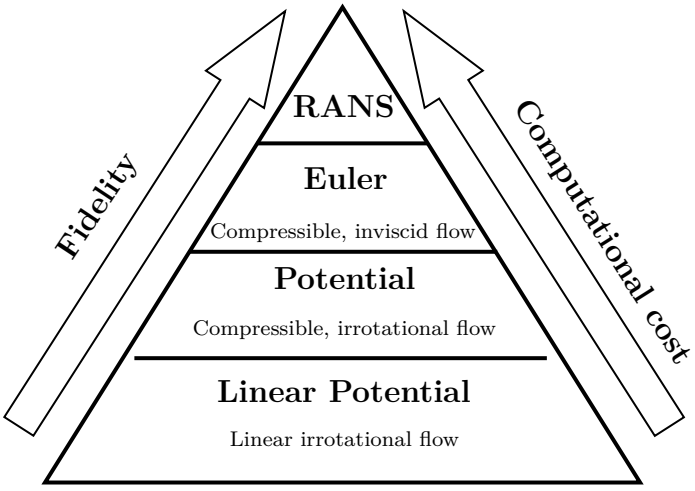

Figure 1.10 Hierarchy of fluid models. (adapted [24])

For aircraft design, the highest fidelity used in industry is usually the Reynolds Average Navier-Stokes (RANS) model[25], where the turbulence is modeled rather than solved numerically. 3D RANS flow solvers can model complex unsteady flows, along with flow separation and flow instabilities, such as buffet[26]. However, they require extensive computational resources along with significant overhead time. Indeed, a volume mesh is necessary and for complex configurations, such as high-lift configurations, the mesh generation process is complex and difficult to automate.

If viscous effects are omitted, the volume mesh requires much less elements, since there is no boundary layer to capture around the surface of the aircraft. The Euler equations can model both transonic and compressible effects. Consequently, an Euler flow solver can be used for transonic flutter and transonic LCOs problems[23, 27, 28, 29].

The model is further simplified by removing the flow rotationality. As a result, the fluid can be modeled as a potential, thus only one variable must be solved, as opposed to the Euler equation that requires five variables in 3D. However, an irrotational flow does not produce any lift, thus a wake behind the wing trailing edge must be model to enforce a Kutta condition[30] to ensure the flow leaves smoothly the trailing edge, see Figure 1.11. The Kutta condition is based on a real physical phenomenon and it can be seen as a viscous model.

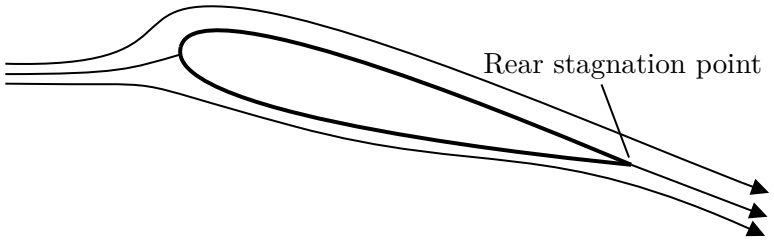

Figure 1.11 Illustration of the Kutta condition.(adapted[30])

If small perturbation is assumed, the full potential equations are further simplified into what is known as Transonic Small-Disturbance (TSD)[31, 32, 33]. Solution of the TSD equation still requires a volume mesh, but the lifting body is modeled without thickness, thus reducing considerably the mesh size. The TSD model is capable of modeling high Mach number flow conditions with weak shocks, thus providing fairly accurate prediction of transonic flutter boundaries for thin wings[34, 35, 36].

Finally, if nonlinear terms are removed, the model can now be solved with a Boundary Element Method (BEM), thus removing the requirement for a volume mesh. Only a surface mesh is necessary, thus reducing not only the computational cost but the overhead time as well. These fluid models are described by Laplace's equation, which models incompressible,

irrotational and attached flows. The well-known lifting line theory[37], Vortex Lattice Method (VLM)[25] and the Panel Method[38, 39] are examples of linear potential flow methods. Table 1.1 summarizes the distinction between these various models.

Table 1.1 Comparison of fluid models.

	RANS	**Euler**	**Potential**	**Linear Potential**
Viscosity	yes	no	no	no
Compressibility	yes	yes	yes	yes (PG)
Transonic	yes	yes	yes (weak shock)	no
Volume mesh	yes	yes	yes	no
Mesh size	1 - 100M	100K - 1M	100K - 1M	100 - 10K
CPU time	$>$ 1 hr.	$\sim$ 1 hr.	5 min. - 1 hr.	5 sec. - 5 min.

Frequency domain approach

Time marching schemes for the Euler and URANS equations require significant computational efforts. However, many unsteady flow problems are periodic in time, thus allowing the use of frequency domain solvers. The periodic flow is reformulated as a steady problem, thus reducing considerably its computational cost. If small amplitude oscillations are assumed, the problem can be linearized around the steady-state solution and the unsteady perturbation is solved separately for the first harmonic, referred to as linear frequency domain (LFD). In recent years, many efforts have been put into the development of Nonlinear Frequency Domain solutions (NLFD)[40, 41, 42] of the Euler/URANS equations, also known as Time Spectral (TS) or Harmonic Balance (HB). In these methods, the flow solution is assumed periodic and is described by a Fourier series using multiple time instances, thus allowing full nonlinearities to be captured without the restriction of small unsteady perturbations. The flow is calculated at each time instance in the time domain so that calculation of fluxes remains simple without complex arithmetic. In the Harmonic Balance approach[40] or equivalent Time Spectral[41], the solutions at the various time instances are coupled together with a truncated Fourier series. The solutions are updated in the time domain until the Euler/RANS equations are satisfied. This approach is also known as High Dimensional Harmonic Balance. As opposed to the HB and TS, the NLFD approach developed by McMullen et al.[42] updates the solution directly in the frequency domain with the Fourier

coefficients. The NLFD approach requires direct and inverse Fast Fourier Transform (FFT) at each iteration to calculate the fluxes in the time domain and update the solution in the frequency domain. It was demonstrated by Hall et al.[43] that the NLFD, TS and HB are equivalent. A similar approach to the NLFD is the Alternating Frequency/Time method[44] that is used for nonlinear dynamic systems. In this approach, nonlinear terms are evaluated in the time domain to avoid complex arithmetic. Like the NLFD method, back and forth FFT are performed to update the solution in the frequency domain from the time domain evaluations. The nonlinear frequency domain approach has recently become a center of interest for applications in aeroelastic analysis[19, 20, 22, 23, 45, 46, 47]. Limit-cycle oscillations (LCO) and flutter can be analyzed efficiently through the use of these nonlinear frequency domain methods[19, 20].

Although linear frequency domain formulations for potential flow methods exist[48, 49, 50, 51], to the best of the author's knowledge, no development has been made toward nonlinear frequency methods, such as the ones developed for the Euler/RANS equations.

1.2.5 Linear potential methods

When considering computational cost, linear potential methods are interesting. They require a surface mesh only, thus most computations can be done with a simple desktop computer. Additionally, the use of such models is robust and requires almost no manual intervention, making them well suited for conceptual MDO[52]. However, the model is hardly applicable to any real conditions encountered by an aircraft, as highlighted in Table 1.1, but compressible, transonic and viscous corrections have been developed and are discussed in this section.

There are two well-established linear potential flow methods for lifting surfaces, the Vortex Lattice Method (VLM)[30] and the Doublet Lattice Method (DLM)[53, 54, 55, 56]. Both methods model lifting bodies as thin surfaces using superposition of singularity elements. Thus, the aerodynamic effect of wing thickness is not modeled. The VLM uses vortices while the DLM employs acceleration doublet potential derived from acoustic theory. The DLM is formulated in the linearized frequency domain and is particularly suited for aeroelastic stability analyses[57].

The Unsteady Vortex Lattice Method (UVLM)[30, 58, 59], which is simply the standard VLM with a time stepping procedure, has drawn attention in many research areas with its interesting modeling capabilities. The force-free wake allows the approach to model complex motions while capturing nonlinear effects from the wake. As a result, the method is widely used in various applications such as aeroelastic analyses of flexible low-speed aircraft[60] and wind turbines[61]. It was also successfully applied to flapping wings[62] and rotary wings[63]

with complex wing-wake interactions. The UVLM is therefore a very flexible tool with many possible applications, but its time-domain formulation is not particularly suited for stability analyses, such as the one performed in industry for the prediction of aeroelastic instabilities like divergence and flutter. However, a linearization over a frozen geometry can be carried out to obtain a state-space formulation in discrete time that is suitable for stability analyses[64]. Since the UVLM naturally includes arbitrary loads and motions, it is well suited for more complex flutter simulations, such as the T-tail configuration[65]. The DLM, on the other hand, requires external corrections[66] to obtain accurate results in the presence of static loading over the horizontal stabilizer and to include in-plane dynamics[65]. More recently, a modal frequency-domain generalized force matrix for the VLM has been developed[49] to provide an approach that is compatible with industry techniques for flutter analyses such as the p-k method[18]. In their work[49], the VLM generalized aerodynamic force matrix is derived and verified against the DLM over a flat plate flutter analysis in low-speed conditions. However, their implementation is assuming out-of-plane motion and out-of-plane forces only, thus limiting its applications like the standard DLM.

The UVLM is therefore more interesting for nonlinear dynamics, but the DLM has superior modeling capabilities for unsteady compressible flow, since its mathematical development is derived from acoustic theory. The DLM's influence kernel includes the effect of retarded time[56, 67], where a perturbation is felt only after a certain time delay. This lag becomes important as the Mach number increases and cannot be ignored. The UVLM does not include this effect, thus limiting its applicability to low-speed unsteady flows.

Steady viscous and compressible corrections

Since linear potential flow methods lack viscosity, thickness and compressibility, corrections have been developed to increase their fidelity.

Many techniques have been developed for the DLM[57, 68, 69, 70, 71], which has become common practice in industry. With these corrections, the DLM can provide fairly accurate results for complex geometries[68]. For this reason, the DLM remains a critical tool in aeroelastic aircraft certification. These correction techniques usually involves the use of external high-fidelity solutions, such as 3D RANS. These high-fidelity solutions are then mapped onto the DLM using stripwise sections and a correction matrix is computed using a least square approach so that the spanwise load distribution of the DLM matches the one from the high-fidelity solution. Afterward, the correction matrix is applied to the GAF matrix in the aeroelastic system to provide higher accuracy. This approach allows the DLM to incorporate nonlinear effects from viscosity, transonic shock wave and thickness. However,

3D high-fidelity solutions are still required, thus 3D grid generation is not avoided. The overall process demands important resources that are not always available in the early design phases.

For the VLM, there are also different correction techniques based on stripwise corrections. However, these corrections techniques are iteratively coupled[72, 73, 74, 75] with the VLM. Consequently, 2D, instead of 3D, high-fidelity solutions can be used, thus reducing considerably the overall process when compared to the DLM's correction techniques. In the iterative coupling process, a solution is first computed from which the effective angle of attack distribution along the span is retrieved. Afterward, using the effective angle of attack, a correction for each stripwise section is computed using a 2D high-fidelity solution and the process is repeated until convergence. The coupling techniques for the VLM fall into two categories: Γ method and α method.

For the Γ method[37, 72], corrections are applied to the circulation Γ of each spanwise section so that the stripwise lift coefficient corresponds to a 2D high-fidelity solution at the corresponding effective angle of attack. Γ methods have poor convergence properties[76] and require a low relaxation factor. More over, the approach fails at stall[77], but artificial dissipation[72] can be added to stabilize the solution.

In the α approach[73, 75, 78, 79, 80], corrections are applied to the local angle of attack. These angle of attack corrections are computed iteratively for each individual stripwise section. This methodology provides fairly accurate results for high-lift systems, even though corrections are applied from two-dimensional external data[75, 81]. However, for swept wings, the cross-flow can introduce nonlinear effects that impact the flow separation and the transonic shock as well. Indeed, at high Mach numbers compressibility is deeply affected by the geometric sweep angle.

A solution has been proposed to include cross-flow effects using an infinite swept flow solver[82, 83, 84, 85] to generate the two-dimensional high-fidelity data. The infinite swept flow solver, or 2.5D, improves significantly the solution with comparable fidelity to 3D RANS. Figure 1.12 shows the 3D reconstructed surface solution from a VLM solution coupled with 2D and 2.5D sectional data, where the solution using 2.5D sectional data compares well with 3D RANS. The lift curve slope for the same configuration is presented in Figure 1.13. The solution using the quarter-chord sweep line captures well the maximum lift coefficient. The same trend is observed in transonic conditions over swept wings, where the use of 2.5D sectional data improves significantly the fidelity of the VLM[83, 86]. This approach was also successfully applied to nonlinear static aeroelasticity[87], capable of providing accurate prediction of wing deflection in transonic conditions for the Common Research Model (CRM).

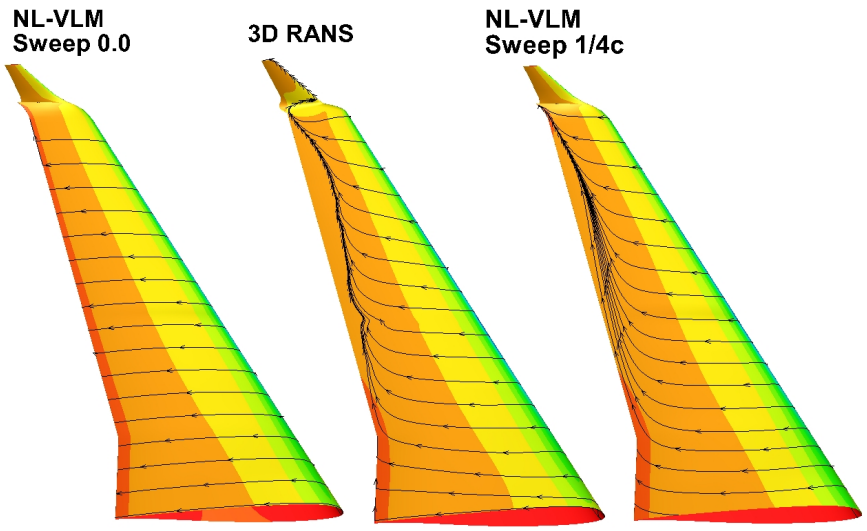

Figure 1.12 3D reconstructed surface solution from a VLM coupled with 2D and 2.5D sectional data at a lift coefficient of 1.4 at Mach = 0.2.[85]

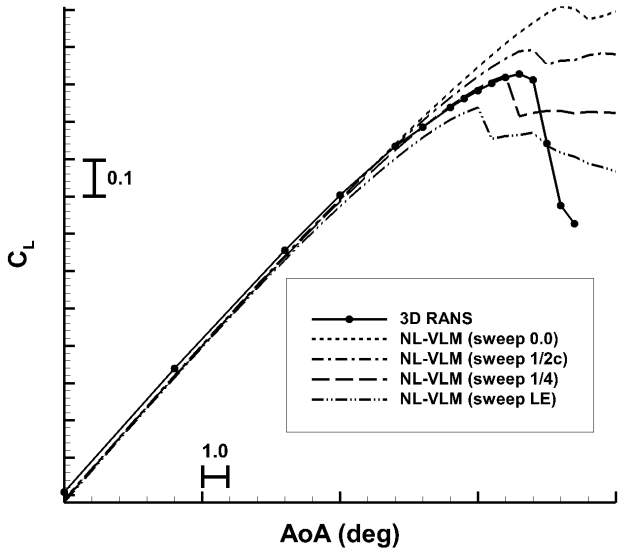

Figure 1.13 Lift curve slope computed with different sweep line for the 2.5D sectional data at Mach = 0.2.[85]

This concludes the overview of aerodynamic models. The general practices in regards of the structural model are discussed next, in a high-level manner as they are not the focus of the thesis.

1.2.6 Structural model

In aircraft aeroelasticity, the wing can be considered as an elastic continuum. A popular approach for modeling continuous systems is the Finite Element Method[88], where the distributed mass and stiffness are discretized spatially. Since the structure of the aircraft is often very complex, it can yield a very detailed computational grid with many degrees of freedom, leading to a complicated model that might not be appropriate for aeroelastic simulation. A lower-order model of the complete aircraft is often used instead, called the Global Finite Element Model (GFEM)[89].

However, even the GFEM can have more than 100,000 degrees of freedom[90]. This level of detail is not always necessary to represent accurately the vibrational characteristics of the aircraft, which is the key element for dynamic aeroelastic analysis. Therefore, the wing's structural model is often reduced to a simpler form to yield a more computationally efficient model, while ensuring that the vibrational characteristics of the wing are still accurately represented. An example of the various models and computational grids involved in the aeroelastic analysis within the aircraft design process is presented in Figure 1.14.

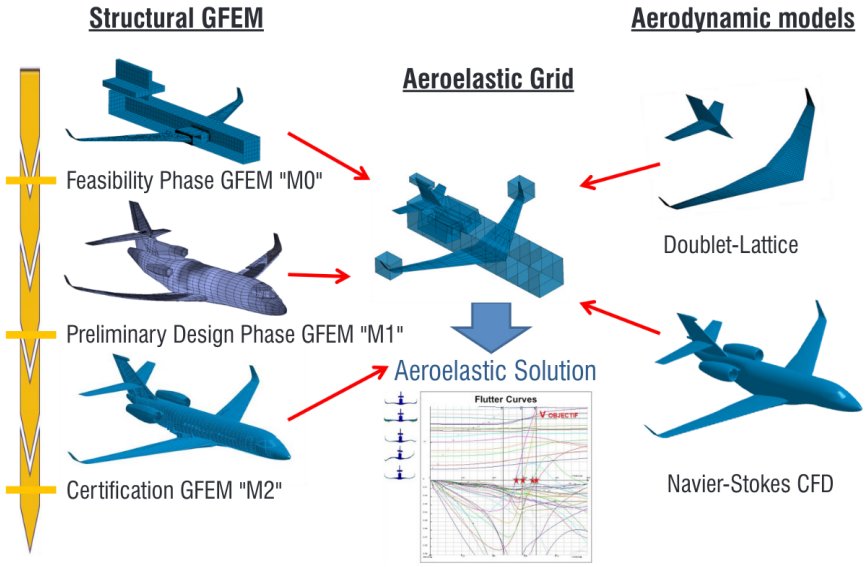

Figure 1.14 The computational grids behind the aeroelastic process.[90]

Consequently, reduced order models are created from the GFEM and a standard practice in industry is to use a stick representation of the aircraft. The global structure of the aircraft is simply represented by beam elements that are placed along the axis of the main components of the aircraft. An example for the wing is shown in Figure 1.15. The complexity of the stick model resides in the definition of the beam properties, since they must represent the

vibrational characteristics of the wing. Different techniques exist[91, 92] to compute the sectional properties of the beam elements with sufficient fidelity. Finally, the number of degrees of freedom can be further reduced using the modal approach using the Rayleigh-Ritz assumed shapes method. In this approach, the wing's dynamic behavior is represented by linear superposition of a set number of assumed shapes. These assumed shapes are typically the normal modes of vibration of the structure. As a result, the FEM model is transposed into modal form, which reduces the number of degrees of freedom below 100 for a typical aircraft. In this form, the structural model is easily coupled with the aerodynamic model resulting in an efficient aeroelastic simulation suitable for aircraft design.

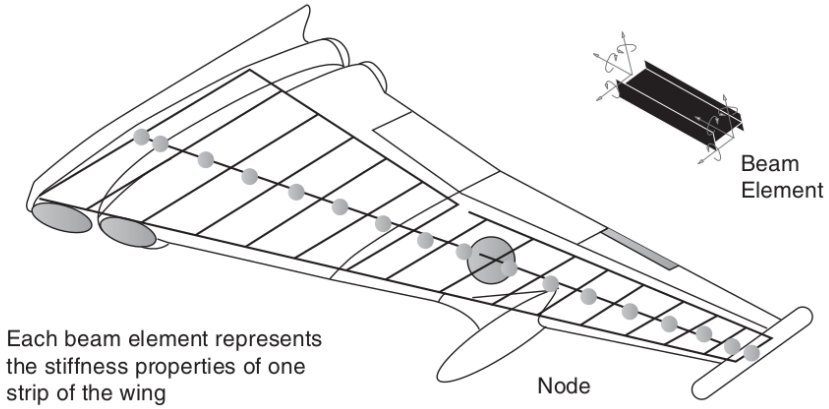

Figure 1.15 Wing model using a beam-like representation.[13]

1.2.7 Summary

The design of more efficient aircraft will require aircraft manufacturers to reinvent some of their well-established design tools[90], since unconventional design must be considered. High aspect ratio wings are necessary to minimize drag and combined with lighter materials, the wing is more susceptible to aeroelastic instabilities.

An important aeroelastic phenomenon is flutter, since it can lead rapidly to structural failure. The behavior of limit cycle oscillations is also critical, since they can cause premature structural fatigue, thus reducing the life of the aircraft. Consequently, these phenomena impose strict constraints that impact the overall performance and safety of the aircraft. Consequently, these instabilities must be evaluated as soon as possible in the design process to avoid a costly redesign later and ensure the aircraft airworthiness.

The numerical solution of flutter and LCO for a typical transport aircraft is not straight forward. It requires integration of a CSD model along with a CFD model. Since the flight

envelope covers low-speed conditions to transonic conditions in cruise configuration, the fluid model must be able to model viscous, transonic and nonlinear dynamic conditions. Additionally, the model must maintain a relatively low computational cost for conceptual and preliminary design phases, where hundreds of configurations can be explored with many design variables.

If the aeroelastic system is treated in the frequency domain, the stability problem can be treated much more efficiently, thus providing a valuable approach to evaluate the flutter boundary. For LCO, a significant gain is also made if treated in the frequency domain. However, due to their nonlinear dynamic behavior with potentially large amplitude, nonlinear frequency domain approach is necessary for the fluid model.

In regards of the fluid model, the Doublet Lattice Method remains the main approach for aeroelastic analyses in industry. However, it has many restrictions since the method assumes out-of-plane motion only and cannot account for non-zero lifting surface. A strong contender as a replacement for the DLM is the Unsteady Vortex Lattice Method. The UVLM naturally models nonlinear dynamics and has been widely used for low-speed nonlinear aeroelasticity. It is a time-domain approach, but some efforts have been made into extending the method to the linearized frequency domain, to provide a formulation similar to the DLM. However, the UVLM, unlike the DLM, does not incorporate the effects of retarded time for unsteady compressible flows.

The VLM has a long history of iterative corrections using sectional high-fidelity data. In steady analyses, it provides fidelity comparable to 3D RANS, even in transonic conditions[83]. The use of infinite swept wing solution allows the VLM to solve nonlinear conditions with sufficient fidelity to enable its use in MDO for the entire flight envelope of the aircraft. The development of a nonlinear frequency domain UVLM, coupled with 2.5D sectional corrections, would be of interest for aircraft manufacturers, as it would allow the analysis of LCO and flutter early in the design process with sufficient fidelity.

Finally, the structural model of the aircraft can be reduced in terms of complexity and degrees of freedom without a significant loss in terms of vibrational representation of the original model. Consequently, the main components of the aircraft are often simplified using beam elements, where the material properties are carefully chosen to conserve the vibrational characteristics. Furthermore, the dynamic response can be represented as a linear superposition of the structure's normal modes of vibration, which in turn reduces considerably the number of degrees of freedom. As a result, an efficient and compact structural model is obtained for aeroelastic analysis.

1.3 Research Objectives

Following the problem statement and the literature review of numerical solutions for aeroelastic problems, the overarching goal of the current work is defined as follows:

> *Develop an aeroelastic framework, based on the Unsteady Vortex Lattice Method in the frequency domain that is compatible with industry standard stability analysis and capable of capturing flutter and Limit Cycle Oscillations for the entire flight envelope of a typical transport aircraft.*

In order to achieve this goal, the following specific objectives are defined

1. Explore a frequency domain extension to the UVLM, that can be compatible with stability analysis for flutter.
2. Seek a correction for both viscous and transonic effects that can model more specifically unsteady compressibility.
3. Apply the framework based on the UVLM to various dynamic aeroelastic problems involving flutter and LCOs.

and the following methodology is proposed

1. Extend the UVLM time domain to a modal generalized frequency domain that includes arbitrary kinematics.
   (a) The approach should be compatible with the p-k method for flutter analyses.
   (b) It should be equivalent to the DLM for a simple flat plate configuration
   (c) The method needs to capture T-tail flutter naturally.
   (d) The effect of non-zero lifting surface should be captured as well.
2. Extend the UVLM time domain to the nonlinear frequency domain using the harmonic balance.
   (a) With a sufficient number of harmonics, the harmonic balance formulation should provide the same accuracy than the time domain UVLM.
3. Extend the steady *alpha* viscous coupling algorithm to the harmonic balance UVLM to include quasi-steady viscous and compressible effects.

   (a) The coupling algorithm should be compatible with infinite swept wing (2.5D) sectional data.

   (b) For reduced frequencies under 0.1, the approach should provide accurate lift values for harmonically pitching airfoils when compared to high-fidelity Euler/RANS solutions.

4. Develop an approximation of the retarded time for UVLM kernel to account for unsteady compressibility.

5. Compute flutter boundaries and LCOs at high Mach numbers using the harmonic balance UVLM with sectional corrections.

   (a) Strong nonlinear LCO branch should be captured.

   (b) The flutter boundary of the Agard wing should be captured and within the range of other numerical results from the literature.

1.4 Thesis outline

Since the proposed solution and framework is based on the Unsteady Vortex Lattice Method, the mathematical background and numerical implementation of the time domain UVLM are first presented in Chapter 2. The chosen structural model is then discussed along with the fluid-structure interpolation scheme in Chapter 3.

After the underlying aerodynamic and structural model have been described, the complete mathematical development for a modal generalized aerodynamic matrix for the UVLM is presented in Chapter 4. The approach is verified against the DLM for a simple configuration, the flat plate. The approach is general and includes in-plane dynamics and it is verified on a flutter case for a T-tail configuration.

The harmonic balance approach is then derived for the UVLM in Chapter 5. The model is verified against theoretical 2D unsteady solutions. Its capability to model complex dynamic motions is also demonstrated.

Following the development of the harmonic balance UVLM, Chapter 6 applies the steady viscous coupling algorithm to include compressible, viscous, transonic and thickness effect. More over, infinite swept wing data is used to include cross-flow effects, which has a significant impact over swept wings. The retarded time is also approximated and included in the UVLM kernel to include the effect of unsteady compressibility.

Finally, the framework based on the harmonic balance with sectional correction is applied to flutter and LCO analyses in Chapter 7 for both 2D and 3D cases. The thesis concludes on the limitations of the proposed solution and with suggestions for future research and development.

1.5 Softwares

For verification and validation purposes, steady and unsteady Euler/RANS high-fidelity solutions are required. Additionally, two-dimensional high-fidelity solutions are also required to provide the aerodynamic data for the sectional correction scheme. In this work, the high-fidelity data is computed using an in-house 3D unstructured Euler/RANS flow solver named CHAMPS[93] and the computational volume grids are generated with the commercial software Pointwise. The UVLM time domain and frequency domain framework presented in this thesis is also developed within CHAMPS using the Chapel programing language[94]. The mode shapes, the modal mass matrix and the modal stiffness matrix are obtained with the commercial software NASTRAN.

CHAPTER 2 UNSTEADY VORTEX LATTICE METHOD[1]

The proposed aerodynamic model in this thesis is based on linear potential flow theory for its simplicity, but more importantly for its efficiency. A frequency domain approach of the unsteady vortex lattice method is sought, but the standard time domain UVLM formulation is first presented in this chapter. The linear system is presented followed by a discussion on the wake treatment. Finally, the computation of aerodynamic forces is described along with a sensitivity study on the mesh discretization for both the wing and the wake.

2.1 UVLM kernel

Inviscid, irrotational and incompressible flows are governed by Laplace's equation that is derived from the continuity equation

$$\nabla^2 \boldsymbol{\phi} = 0 \tag{2.1}$$

where $\boldsymbol{\phi}$ is the velocity potential. By means of Green's theory, the solution can be solved by the boundary element method, thus avoiding discretization of the flow field. Since Laplace's equation is linear, elementary solutions can be superposed to solve the flow around complex geometries. The VLM uses vortex ring elements placed along the camber line to model lifting bodies, where the vortex rings are composed of 4 vortex segments. The induced velocity from a vortex segment, as shown in Figure 2.1 is obtained with the equation of Biot-Savart

$$\boldsymbol{q}_{1,2} = \frac{\Gamma}{4\pi} \frac{\boldsymbol{r_1} \times \boldsymbol{r_2}}{|\boldsymbol{r_1} \times \boldsymbol{r_2}|^2} \boldsymbol{r_0} \cdot \left(\frac{\boldsymbol{r_1}}{r_1} - \frac{\boldsymbol{r_2}}{r_2} \right) \tag{2.2}$$

where $\boldsymbol{q}_{1,2}$ represents the induced velocity from a vortex segment and Γ the circulation. $\boldsymbol{r_1}$ and $\boldsymbol{r_2}$ are geometrical vectors for the distance between the vortex segments endpoints and the point in space where the induced velocity is computed, see Figure 2.1. $\boldsymbol{r}_0$ is the vortex segment itself.

The Laplace equation is time-independent, but unsteady simulations can still be performed through application of the boundary condition[30]. Figure 2.2 illustrates the vortex ring placement in regards of the wing, where the bound vortices are placed on the wing panel's 1/4 chord.

The Neumann boundary condition of no penetration (flow tangency) is enforced at the col-

[1]This chapter contains material published in AIAA Journal titled "*Nonlinear Frequency-Domain Solver for Vortex Lattice Method*" (2018). The dissertation author is the main author and contributor of the paper and copyrights are held by M. Parenteau and E. Laurendeau.

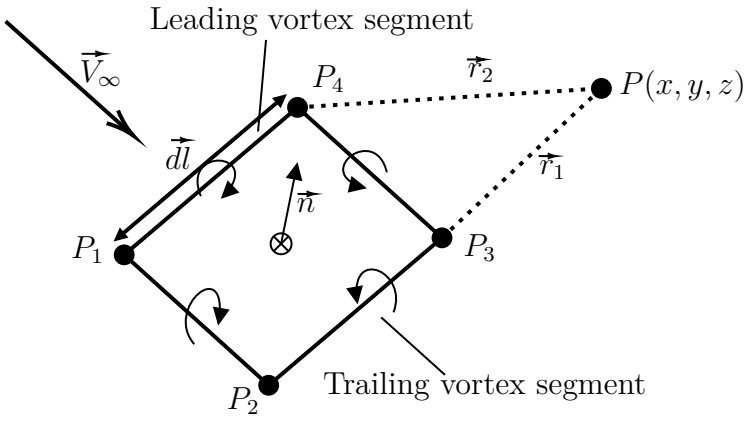

Figure 2.1 Topology of a vortex ring.

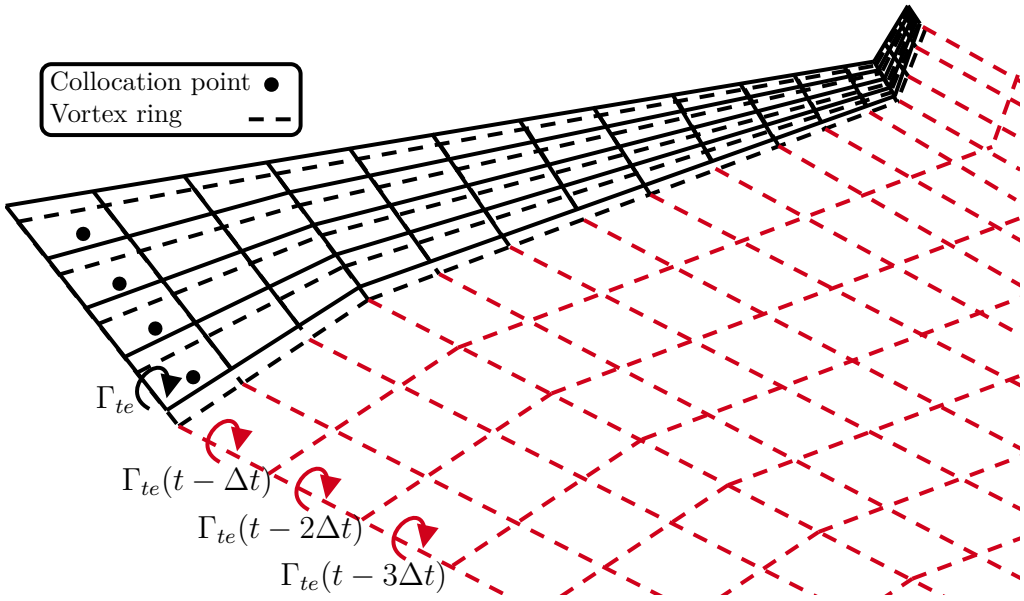

Figure 2.2 Illustration of the time marching UVLM.

location point located at the 3/4 chord of the wing panels as shown in Figure 2.3. This is referred to as the "1/4-3/4" rule and is a fundamental concept for Vortex Lattice Methods derived by Pistolesi[95] who found that by placing the vortex point at the 1/4 chord and the boundary condition at the 3/4 chord for a single panel element, the section lift curve slope corresponds exactly that of thin airfoil theory (2π).

To perform unsteady simulations, a time marching scheme is applied where every time step a new row of vortex rings is released into the wake with the same circulation as the trailing edge panel from which it was shed at the previous time step as shown in Figure 2.4. The circulation Γ of the newly shed wake panel stays unchanged for the remaining of the simulation as

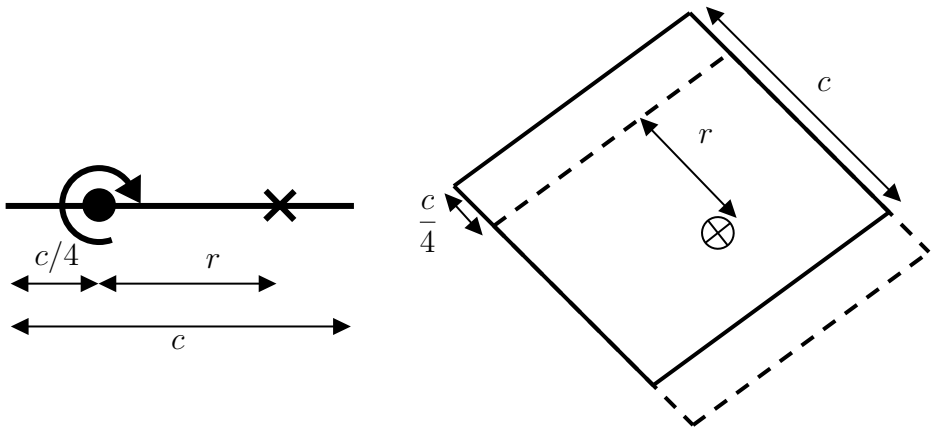

Figure 2.3 Position of the collocation point.

dictated by Helmholtz's theorem. The wing releases a force-free wake (no aerodynamic loads) that convects with the local velocity, which allows the method to capture wake-rollup.

The UVLM linear system is represented by Equation 2.3. It contains the geometry influence on itself ($\boldsymbol{A}$) and the wake influence ($\boldsymbol{B}$),

$$\begin{pmatrix} A_{1,1} & A_{1,2} & \cdots & A_{1,m} \\ A_{2,1} & A_{2,2} & \cdots & A_{2,m} \\ \vdots & \vdots & \ddots & \vdots \\ A_{m,1} & A_{m,2} & \cdots & A_{m,m} \end{pmatrix} \begin{pmatrix} \Gamma_1 \\ \Gamma_2 \\ \vdots \\ \Gamma_m \end{pmatrix} + \begin{pmatrix} B_{1,1} & B_{1,2} & \cdots & B_{1,w} \\ B_{2,1} & B_{2,2} & \cdots & B_{2,w} \\ \vdots & \vdots & \ddots & \vdots \\ B_{m,1} & B_{m,2} & \cdots & B_{m,w} \end{pmatrix} \begin{pmatrix} \Gamma_{W_1} \\ \Gamma_{W_2} \\ \vdots \\ \Gamma_{W_w} \end{pmatrix} + \boldsymbol{V} \cdot \boldsymbol{n} = 0 \tag{2.3}$$

where $A_{i,j}$ is the influence of panel j on panel i. The matrix $\boldsymbol{A}$ is of size $n \times n$ and $\boldsymbol{B}$ of size $n \times n_w$, where n is the number on panels on the wing and n_w is the number of panels in the wake. The onset flow with the velocity induced by the motion of the wing ($\vec{V}$) for panel i is defined as

$$\boldsymbol{V_i} \cdot \boldsymbol{n_i} = (U_\infty + u(t), V_\infty + v(t), W_\infty + w(t))_i \cdot \boldsymbol{n}_i \tag{2.4}$$

Since the wake circulation Γ_W is known every time step, the system is solved for the unknowns Γ_i of the wing and the wake influence is then computed directly in the right-hand side. In this work, the linear system is solved using the krylov subspace iterative solver Bi-CGSTAB[96].

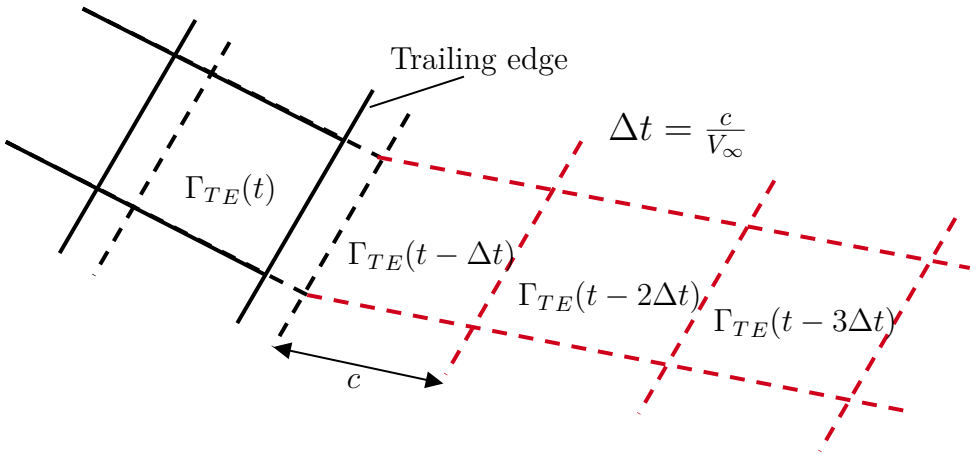

Figure 2.4 Wake circulation relation to the trailing edge circulation.

2.2 Wake rollup

The wake in the UVLM model plays an important role in unsteady simulations and in the development of frequency formulation. Two different types of wake treatment are discussed in this section: rigid and free with rollup.

The wake rollup enables the UVLM to model non-linear effects due to deformations induced by the local velocity on the wake. During the time marching process, after the linear system is solved for the current time step, the induced velocity from both the wing and the wake is computed at every point of the wake. Afterward, the wake points are simply moved with the local velocity by an Euler explicit step approach. However, predictor-corrector techniques can also be used, such as the fourth order Adams–Bashforth–Moulton method[97] to obtain a more accurate and robust procedure. The wake rollup is particularly important in wake-interaction problems such as in helicopter rotor problems where the aerodynamic response is strongly influenced by the wake.

Figure 2.5 illustrates the difference between a rigid wake and a wake with rollup for a simple heave motion. A symmetry plane is applied at the wing root at $y = 0$ and the amplitude for the wake with rollup is increased to show more clearly the effects of rollup. At the far right, the starting vortex can be seen, along with the different vortices of opposite sign released by the wing, thus showing that the wake rollup can model real physical phenomena. However, when the rollup becomes too strong the wake becomes unstable and nonphysical velocities are induced causing unrealistic deformation. This is mainly caused by the singularity at $r = 0$ in the Biot-Savart kernel. The singularity can be overcome with the use of vortex-core models[98, 99].

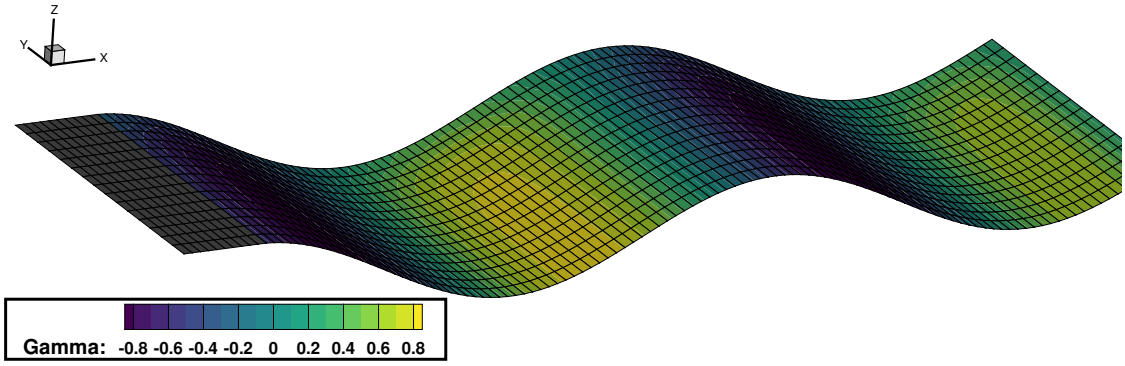

(a) Heave motion with a rigid wake

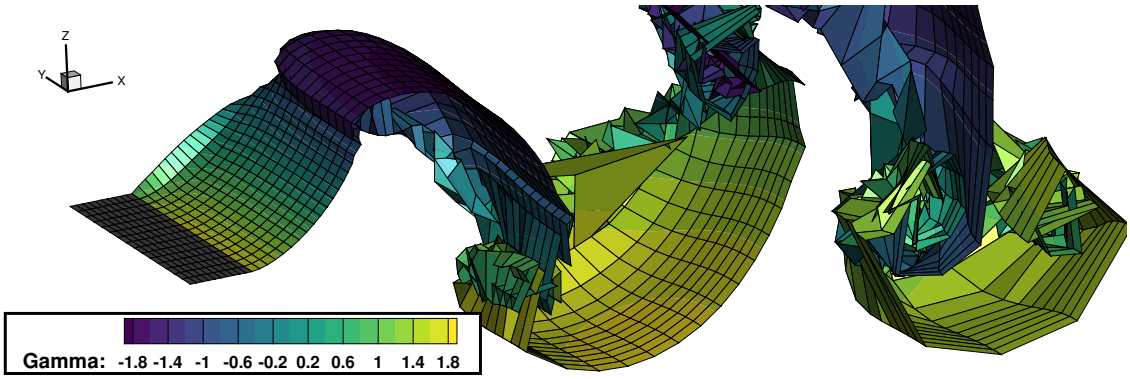

(b) Heave motion with a force-free wake with rollup

Figure 2.5 Illustration of a rigid wake and a force-free wake with rollup.

On the other hand, the rigid wake is simply released from the trailing edge and convected with the freestream, following the time history of the wing trailing edge in space. Consequently, a rigid wake is more efficient in terms of computational cost, since it does not involve a computation of complexity $\mathcal{O}(n^2)$, with n being the number of wake panels to evaluate the rollup. Depending on the simulation type and the wing discretization, the number of wake panels can become significant, thereby introducing serious computational cost. As a remedy, the fast multipole method can be used[100] to reduce the problem from $\mathcal{O}(n^2)$ to $\mathcal{O}(n \log n)$. However, for the rigid wake model, if the wing motion is prescribed, then the wake can also be prescribed and its influence on the wing is computed once.

For a typical transport aircraft in cruise condition at low reduced frequencies, the wake is quickly convected downstream thus reducing the impact of its shape on the wing. Consequently, the wake can remain rigid in those conditions with a negligible difference over the aerodynamic solution. A verification is performed for a simple rectangular wing of 8 aspect

ratio undergoing a heave motion. The results are presented in Figure 2.6, where h/c is the nondimensional heave amplitude and k the reduced frequency. A difference higher than 2% is encountered only for the case with a large amplitude of 1.0 and for a large reduced frequency of 0.5. Otherwise, the overall difference remains under 1%, thus confirming that the shape of the wake has minimal effect over the aerodynamic solution for typical wing configurations. Furthermore, for linear aeroelastic analysis, such as flutter, the amplitude is considered infinitely small, while the flutter reduced frequencies for the various cases considered in this thesis is varying between 0.05 and 0.3. Consequently, the wake is treated as rigid in this thesis with negligible effects over the aerodynamic solution.

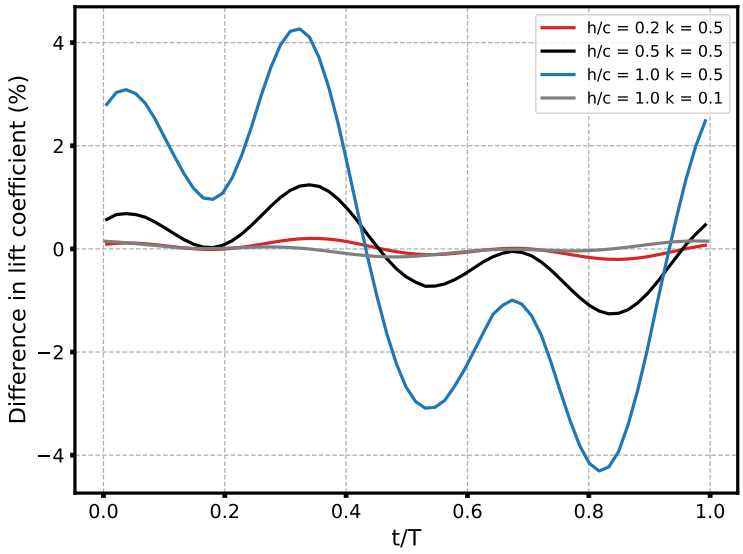

Figure 2.6 Relative difference in the aerodynamic forces for a rectangular wing undergoing a heave motion with and without wake rollup. The solution with wake rollup is taken as the reference.

2.3 Aerodynamic force calculation

The literature is poor in regards of the evaluation unsteady aerodynamic forces for the UVLM. Two methods are proposed. The first approach suggested by Katz and Plotkin[30] uses the unsteady Bernoulli equation

$$\Delta \boldsymbol{F}_{i,j} = \rho \Big\{ [U(t)+u_w, V(t)+v_w, W(t)+w_w]_{ij} \cdot \boldsymbol{\tau_i} \frac{\Gamma_{i,j} - \Gamma_{i-1,j}}{\Delta c_{ij}} + [U(t)+u_w, V(t)+v_w, W(t)+w_w]_{ij} \cdot \boldsymbol{\tau_j} \frac{\Gamma_{i,j} - \Gamma_{i,j-1}}{\Delta b_{ij}} + \frac{\partial}{\partial t} \Gamma_{ij} \Big\} \Delta A_{ij} \boldsymbol{n}_{ij} \tag{2.5}$$

where the induced velocities (u_w, v_w, w_w) from the vortex rings are evaluated at the collocation point. $\boldsymbol{\tau}_i$ and $\boldsymbol{\tau}_j$ are the tangential unit vectors in the chordwise direction and spanwise direction respectively, while ΔA_{ij} represents the panel's surface area. A second approach, the Joukowski method, is proposed by Simpson et al.[101] where the force on every vortex ring is obtained by summing the steady contribution with the unsteady contribution

$$\Delta \boldsymbol{F}_{i,j} = \Delta \boldsymbol{F}_{steady_{i,j}} + \Delta \boldsymbol{F}_{unsteady_{i,j}} \tag{2.6}$$

where

$$\Delta \boldsymbol{F}_{steady_{i,j}} = \rho \Gamma_{i,j} (\boldsymbol{V} \times \boldsymbol{dl}) \tag{2.7}$$

and

$$\Delta \boldsymbol{F}_{unsteady_{i,j}} = \rho \frac{\partial \Gamma_{i,j}}{\partial t} \Delta A_{i,j} \boldsymbol{n}_{i,j} \tag{2.8}$$

where $\boldsymbol{dl}$ is the vortex segment and $\boldsymbol{n}$ the panel normal vector. Equation 2.7 is the Kutta-Joukowski theorem and Equation 5.2.3 originates from the unsteady part of Bernoulli's equation. The induced velocity is evaluated at the vortex segment's midpoint, thus avoiding the discretization error of the Katz and Plotkin approach where the induced velocity in evaluated at the collocation point only. Furthermore, the unsteady force contribution is oriented along the normal of the panel and both methods provide the same level of accuracy for the lift calculation. For unsteady induced drag calculations, Simpson et al.[101] demonstrated that the Joukowski method can provide the same level of accuracy than the Katz and Plotkin method, but with coarser mesh discretizations. Consequently, the Joukowski method is used in this work. A validation of the UVLM is presented in Appendix A. The UVLM is verified against unsteady thin airfoil theory from Theodorsen[102] and from Wagner[103].

2.4 Wing and wake discretization

There are three important discretization parameters affecting the solution of the unsteady vortex lattice method: the wake discretization, the wing's chordwise discretization and the wake length. In order to characterize the sensitivity of the UVLM in regards of those parameters, a verification is performed against the well-known Theodorsen formulation[102] of unsteady lift. The Theodorsen formulation of lift assumes a flat wake with small oscillations and is defined as

$$L_{Theodorsen} = \rho b^2 \Big(U_\infty \pi \dot{\alpha} + \pi \ddot{h} - \pi b a \ddot{\alpha} \Big) + 2\pi \rho U_\infty b C(k) \Big(U_\infty \alpha + \dot{h} + b(\frac{1}{2} - a)\dot{\alpha} \Big) \tag{2.9}$$

where $C(k)$ is the complex Theodorsen function. Since the VLM and the Theodorsen formulation are both derived from thin airfoil theory, they should provide the same results for simple heave and pitch harmonic motions. However, small differences are expected since the wake is rigid and not flat for the UVLM, which is not the case for the Theodorsen formulation. In order to obtain 2D results with the UVLM, an aspect ratio of 1000 is used with 5 panels along the span.

In the time-domain UVLM methodology, the circulation Γ of a wake panel is equal to the trailing edge panel from which it was shed. Therefore, the time step must be chosen carefully to ensure that the wake panel length is similar to the wing trailing edge panel length in order to preserve the total circulation[64, 101]. Consequently, if the wing is discretized uniformly along the chord, the time step Δt should be defined as

$$\Delta t = \frac{c}{n_i V_\infty} \tag{2.10}$$

where c is the wing's chord length and n_i the number of chordwise panels. Figure 2.7 compares different values of Δt with the theoretical solution of Theodorsen. The solution with wake panels having the same length as the wing panel compares well with Theodorsen, while if larger or smaller time steps are used for the wake, errors in the total circulation arise yielding an incorrect solution for the lift coefficient. Therefore, when choosing a chordwise discretization, the size of the time step must be adjusted in order for the wake discretization to be consistent with the wing's trailing edge panel.

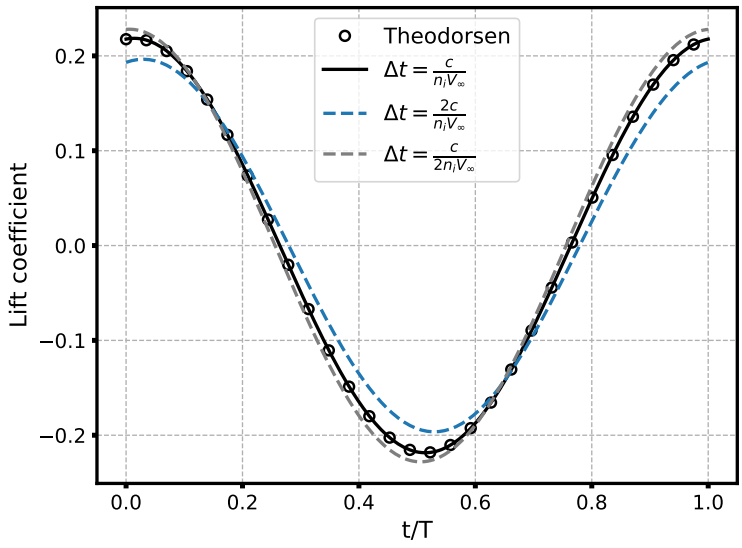

Figure 2.7 Harmonic heave motion; $h = 0.1\sin(\omega t)$; $k = 0.25$; $n_i = 10$.

In the next numerical verification, the chordwise discretization is analyzed. The error between the UVLM and Theodorsen is presented in Figure 2.8 for a heave motion at three different reduced frequencies and for different discretization of panels along the chord. The error is computed with 200 points over one period as follows

$$Error = \frac{RMS(C_L - C_{L_{Theodorsen}})}{\max |C_{L_{Theodorsen}}|} \tag{2.11}$$

The error increases with the reduced frequency, which is expected since the shape of the prescribed wake has more influence at higher reduced frequencies, thus creating more differences in comparison to Theodorsen, but the error remains under 0.5%. Moreover, Figure 2.8 shows that 10 panels are sufficient to obtain a minimal error for a heave motion.

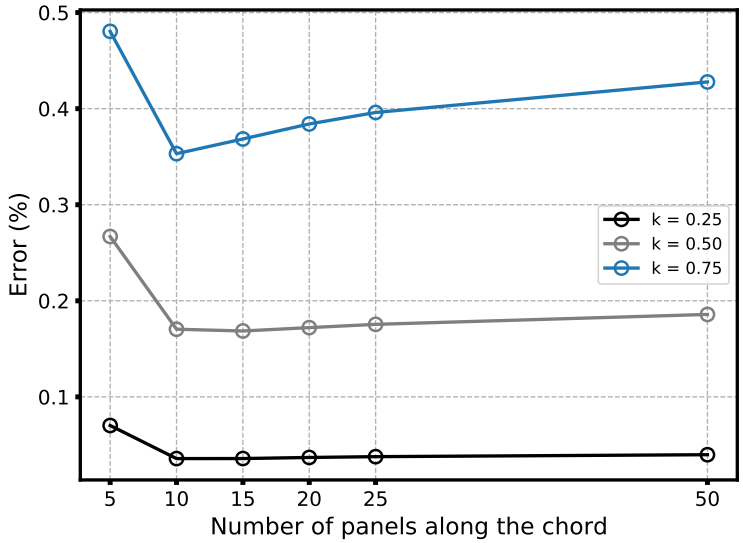

Figure 2.8 Error between the UVLM and Theodorsen for a harmonic heave motion for different numbers of chordwise panels; $h = 0.1\sin(\omega t)$

The same analysis is performed, but for a harmonic pitch motion, see Figure 2.9. For a pitching motion, the lift solution seems more sensitive to the chordwise discretization and the error remains under 0.8% for both reduced frequencies with 10 panels along the chord. A relative error of 0.2% is achieved for both frequencies with 50 panels. Considering these two results, a distribution of 15 panels along the chord is sufficient to maintain the relative error under 0.5 %.

The last parameter to consider is the wakelength. Results for a pitching motion show that a 50-chord length wake is enough to obtain a converged solution, see Figure 2.10.

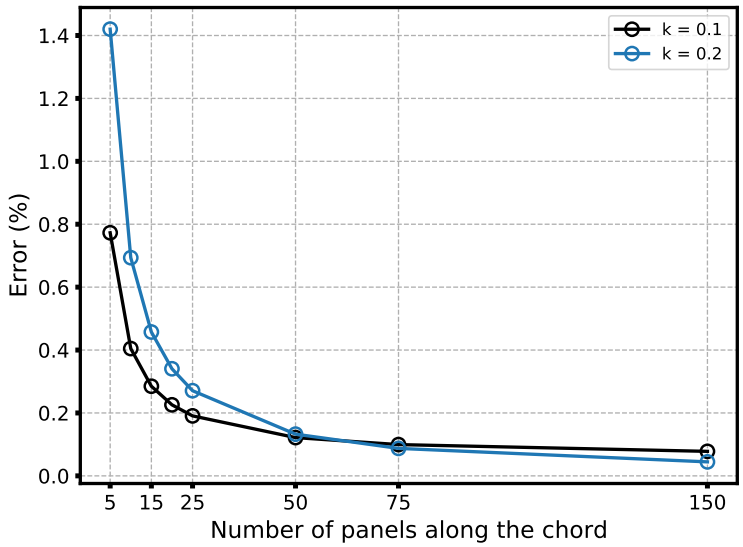

Figure 2.9 Error between the UVLM and Theodorsen models for a harmonic pitch motion; $\alpha = 2.0\sin(\omega t)$

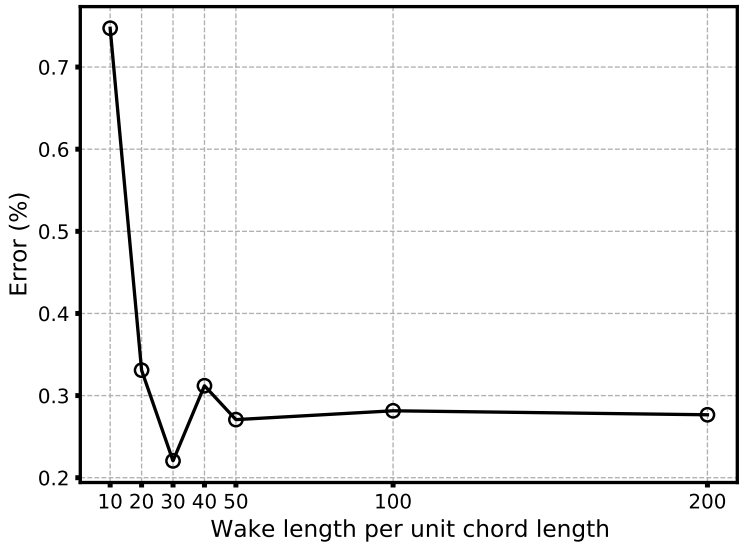

Figure 2.10 Wake length convergence, harmonic pitch motion; $\alpha = 2.0\sin(\omega t)$; $n_i = 25$

2.5 Summary

The UVLM time domain formulation is revisited with emphasis on the wake treatment, since it represents a key element in the frequency domain formulation presented next. Indeed, the aerodynamic lag is caused by the time history of the wake, which will be derived in the frequency domain in Chapter 4. Furthermore, since typical aircraft wing configurations

are considered in this work, a rigid wake is applied, since the wake rollup does not provide significant differences for these configurations in normal conditions. Furthermore, the use of a rigid wake reduces considerably the computational cost.

The numerical verification of the wing and wake discretization presented in Figure 2.7 shows that the time step must be consistent with the wing's discretization in order for the total circulation to be preserved. In other words, the streamwise length of the wake panels needs to be consistent with the wing's trailing edge panels. Finally, a discretization of at least 15 panels is sufficient to maintain the relative error under 0.5% for both pitching and heaving motions. Consequently, the chordwise discretization for the various cases presented in this thesis will use at least 15 panels along the chord, since it is a good tradeoff between efficiency and accuracy. Indeed, a smaller discretization of the wing induces a smaller discretization for the wake as well and since the UVLM is of complexity $\mathcal{O}(n^2)$, the computational cost increases rapidly.

CHAPTER 3 FLUID-STRUCTURE INTERFACE[1]

In this chapter, the structural governing set of equations are derived followed by the fluid-structure interpolation scheme necessary to transfer the aerodynamic loads to the structural grid in a conservative manner. The goal of this chapter is to provide the necessary tools and the general 3D aeroelastic system of equation to be solved for the 3D dynamic problems of Chapter 7.

3.1 Structural governing equation

The most efficient approach to derive the equations of motion for complex dynamic systems is to use the Lagrange's equations and the Rayleigh-Ritz assumed shapes method[11, 13]. The Lagrange's equation of motion without damping is given by

$$\frac{d}{dt}\frac{\partial L}{\partial \dot{x}_i} - \frac{\partial L}{\partial x_i} = Q_i(x,t) \tag{3.1}$$

where

$$L = T - U \tag{3.2}$$

and T is the kinetic energy, U the potential energy, x_i the generalized coordinates and Q_i the generalized forces. If considering the single degree of freedom of Figure 3.1, the kinetic energy and potential energy are given as

$$T = \frac{1}{2}m\dot{x}^2 \tag{3.3}$$

and

$$U = \frac{1}{2}kx^2 \tag{3.4}$$

where m is the mass and k the spring stiffness. Substituting Equations 3.3 and 3.4 in Equation 3.1 yields

$$m\ddot{x} + kx = Q(t) \tag{3.5}$$

[1]This chapter contains material published in Journal of Fluids and Structures titled "*A general modal frequency-domain vortex lattice method for aeroelastic analyses*"(2020). The dissertation author is the main author and contributor of the paper and copyrights are held by M. Parenteau and E. Laurendeau.

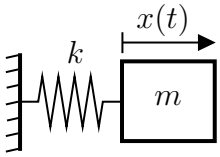

Figure 3.1 Illustration of a single degree of freedom system.

Equation 3.5 can be generalized to multiple degree of freedom systems to obtain the classical aeroelastic system of equations in matrix form as

$$\boldsymbol{M}\ddot{\boldsymbol{x}} + \boldsymbol{K}\boldsymbol{x} = \boldsymbol{F} \tag{3.6}$$

where $\boldsymbol{M}$ is the mass matrix, $\boldsymbol{K}$ the stiffness matrix and $\boldsymbol{F}$ the aerodynamic forces. Typically, $\boldsymbol{M}$ and $\boldsymbol{K}$ are assembled from a finite element model. The aeroelastic system of equation can be further simplified by reducing the number of structural degrees of freedom. The reduction is done using linear modal expansion, where the structural node displacements are expressed as a linear combination of the mode shapes and generalized modal coordinates

$$\boldsymbol{x}(t) = q_1(t)\boldsymbol{\eta}_1 + q_2(t)\boldsymbol{\eta}_2 + q_3(t)\boldsymbol{\eta}_3 + ... \tag{3.7}$$

where $\boldsymbol{\eta}_i$ is the i-th mode shape and q_i the modal generalized coordinate for the i-th mode. Equation 3.6 is then rearranged as

$$\boldsymbol{M}\boldsymbol{\eta}\ddot{\boldsymbol{q}} + \boldsymbol{K}\boldsymbol{\eta}\boldsymbol{q} = \boldsymbol{F} \tag{3.8}$$

where $\boldsymbol{\eta}$ is the mode shape matrix where each column corresponds to a mode shape vector

$$\boldsymbol{\eta} = [\boldsymbol{\eta}_1\ \boldsymbol{\eta}_2\ \boldsymbol{\eta}_3\ ...] \tag{3.9}$$

and $\boldsymbol{q}$ the vector of modal generalized coordinates. If Equation 3.8 is premultiply by $\boldsymbol{\eta}^\mathsf{T}$ then the following equation is obtained

$$\bar{\boldsymbol{M}}\ddot{\boldsymbol{q}} + \bar{\boldsymbol{K}}\boldsymbol{q} = \bar{\boldsymbol{F}} \tag{3.10}$$

where the modal mass matrix ($\bar{\boldsymbol{M}}$), modal stiffness matrix ($\bar{\boldsymbol{K}}$) and generalized modal Forces ($\bar{\boldsymbol{F}}$) are defined as

$$\bar{\boldsymbol{M}} = \boldsymbol{\eta}^\mathsf{T}\boldsymbol{M}\boldsymbol{\eta} \tag{3.11}$$

$$\bar{\boldsymbol{K}} = \boldsymbol{\eta}^\mathsf{T}\boldsymbol{K}\boldsymbol{\eta} \tag{3.12}$$

$$\bar{\boldsymbol{F}} = \boldsymbol{\eta}^{\mathsf{T}} \boldsymbol{F} \tag{3.13}$$

The modal mass matrix and modal stiffness matrix are diagonal matrices of size *number of modes* $\times$ *number of modes*. As a result, the system is now decoupled and the problem size is considerably reduced when compared to the original problem. Furthermore, if $\bar{\boldsymbol{W}}$ is the diagonal matrix composed of the structure's natural frequencies $\tilde{\omega}_n^2$

$$\bar{\boldsymbol{W}} = \begin{bmatrix} \tilde{\omega}_1^2 & & \\ & \ddots & \\ & & \tilde{\omega}_n^2 \end{bmatrix} \tag{3.14}$$

and if the system of equation is expressed in the frequency domain, Equation 3.10 is rearranged as

$$-\omega^2 \bar{\boldsymbol{M}} \hat{\boldsymbol{q}} + \bar{\boldsymbol{M}} \bar{\boldsymbol{W}} \hat{\boldsymbol{q}} = \hat{\boldsymbol{F}} \tag{3.15}$$

where ω is the frequency and $\hat{\boldsymbol{q}}$ and $\hat{\boldsymbol{F}}$ are the modal complex amplitude for the generalized coordinates and the modal aerodynamic forces respectively. Equation 3.15 is dimensional, but it is more convenient to work in nondimensional form, especially for fluid-structure interaction problems. Therefore, if the definition of flutter reduced velocity $\tilde{V}$ and mass ratio μ are introduced

$$\tilde{V} = \frac{V_\infty 2}{\sqrt{\mu}\omega_\alpha c} \tag{3.16}$$

$$\mu = \frac{m}{\rho_\infty \nu} \tag{3.17}$$

the following nondimensional form of Equation 3.15 is obtained

$$\frac{1}{\tilde{V}^2 \mu \omega_\alpha} \cdot \tilde{\boldsymbol{M}} [\bar{\boldsymbol{W}} - \boldsymbol{I} \cdot k^2] \tilde{\boldsymbol{q}} = \tilde{\boldsymbol{F}} \cdot \frac{c^3}{8\mu\nu} \tag{3.18}$$

where ω_α is the natural frequency for the first torsion mode, k the reduced frequency ($k = \frac{2\omega}{cV_\infty}$), m the wing mass, c the wing reference chord and ν the volume of conical frustrum[1] enclosing the wing.

Furthermore, $\tilde{\boldsymbol{M}}$, $\tilde{\boldsymbol{q}}$ and $\tilde{\boldsymbol{F}}$ are defined as

$$\tilde{\boldsymbol{M}} = \frac{\bar{\boldsymbol{M}}}{m} \; ; \; \tilde{\boldsymbol{q}} = \frac{\hat{\boldsymbol{q}}}{c} \; ; \; \tilde{\boldsymbol{F}} = \frac{\hat{\boldsymbol{F}}}{1/2 \rho_\infty V_\infty^2 c^2} \tag{3.19}$$

[1] A conical frustum is a frustum created by slicing the top off a cone. In this case, it is a truncated cone that encloses the wing.

3.2 Fluid-structure interpolation

The structure and the fluid both have specific requirements in regards to computational grids, which varies with the chosen model. Consequently, it is very unlikely that the structure and fluid grids will coincide exactly. As a result, displacements from the structural grid must be interpolated to the fluid grid and the resulting aerodynamic forces must be interpolated back to the structural grid. Since the flutter phenomena is a process involving energy extraction, it is important that the energy is conserved in the interpolation process[104]. Moreover, the interpolation scheme should conserve the total forces and moments, along with exact recovery of translation and rotation. In order to ensure energy conservation, the loads interpolation matrix is defined to ensure the equivalence of virtual work $\delta \boldsymbol{W}$ between the aerodynamic (a) and structural (s) systems as

$$\delta \boldsymbol{W} = \delta \boldsymbol{u}_a^\mathsf{T} \boldsymbol{F}_a = \delta \boldsymbol{u}_s^\mathsf{T} \boldsymbol{F}_s \tag{3.20}$$

where $\delta \boldsymbol{u}$ denotes the virtual displacements and $\boldsymbol{F}$ the force vector. If the interpolation matrix $\boldsymbol{H}$ relates the virtual displacements of the aerodynamic grid points to the structural grid points then

$$\delta \boldsymbol{u}_a = \boldsymbol{H} \delta \boldsymbol{u}_s \tag{3.21}$$

and Equation 3.20 yields

$$\delta \boldsymbol{u}_s^\mathsf{T} \boldsymbol{H}^\mathsf{T} \boldsymbol{F}_a = \delta \boldsymbol{u}_s^\mathsf{T} \boldsymbol{F}_s \tag{3.22}$$

from which the relation between the aerodynamic and structural forces is obtained

$$\boldsymbol{F}_s = \boldsymbol{H}^\mathsf{T} \boldsymbol{F}_a \tag{3.23}$$

The loads transfer matrix is then only defined by the displacements interpolation matrix $\boldsymbol{H}$. In this work, radial basis functions[105] are used to derive $\boldsymbol{H}$. The RBF strategy is chosen, because unlike other available solutions in the literature[106], it does not require some form of connectivity. The RBF based interpolation works only on a set of points without any connectivity information needed. Consequently, the approach can be general for any fluid-structure models, it does not require additional information from the user depending on the chosen aerodynamic or structural model. Furthermore, the approach has shown success in the field of aeroelasticity[107, 108, 109, 110, 111, 112, 113]. However, for the special case where the structure is represented by a stick model, the interpolation matrix is derived using a simple linear interpolation. Note that the RBF scheme could also be used with a stick model by simply adding additional nodes rigidly linked to the stick model without mass. Translations and rotations are transferred to these additional nodes, which then forms the

cloud-based points for the RBF system.

3.2.1 RBF based interpolation

The basic interpolant is defined as a linear combination of basis functions (ϕ) where the interpolated value s is given by

$$s(x) = \sum_{i=1}^{N} w_i \phi(||\boldsymbol{x} - \boldsymbol{x}_i||) + \sum_{j=1}^{m} \lambda_j p_j(\boldsymbol{x}) \tag{3.24}$$

where w and λ are the weights for the RBFs and for the polynomials respectively. The polynomial p of degree $m-1$ is added for higher accuracy.

There are several types of radial basis functions available and the Thin Plate Spline (TPS) is used in this work. The TPS has demonstrated robust and accurate results in CFD applications[112, 114]. An important characteristic of the TPS is that not only rotation and translation are exactly recovered, forces and moments are also conserved[115] which leads to a conservative and accurate interpolation scheme for fluid-structure interaction problems. Note that this is true only if the polynomial term is added. In this work, a first-order polynomial term is used. The TPS function is given by

$$\phi(r) = r^2 \log r \tag{3.25}$$

where r is the Euclidean norm. They are many other basis functions that can be used, such as Wendland's compact basis function[116], which is especially interesting for large systems. Thereafter, the following linear system is formed using the structural grid points

$$\boldsymbol{C}_{ss} \begin{bmatrix} \boldsymbol{w} \\ \boldsymbol{\lambda} \end{bmatrix} = \begin{bmatrix} \boldsymbol{f} \\ \boldsymbol{0} \end{bmatrix} \tag{3.26}$$

where $\boldsymbol{f}$ represents the values to interpolate. $\boldsymbol{C}_{ss}$ is defined as

$$\boldsymbol{C}_{ss} = \begin{bmatrix} \boldsymbol{\Phi} & \boldsymbol{P} \\ \boldsymbol{P}^{\mathsf{T}} & \boldsymbol{0} \end{bmatrix} \tag{3.27}$$

where $\mathbf{\Phi}$ is written as

$$\mathbf{\Phi} = \begin{bmatrix} \phi_{s1s1} & \phi_{s1s2} & \dots & \phi_{s1sN} \\ \phi_{s2s1} & \phi_{s2s2} & \dots & \phi_{s2sN} \\ \vdots & \vdots & \ddots & \vdots \\ \phi_{sNs1} & \phi_{sNs2} & \dots & \phi_{sNsN} \end{bmatrix} \tag{3.28}$$

with ϕ_{s1s3} representing the RBF evaluation with the first and third structural node

$$\phi_{s1s3} = \phi(||\boldsymbol{x}_1 - \boldsymbol{x}_3||) \tag{3.29}$$

For a first-order polynomial, $\boldsymbol{P}$ is written as

$$\boldsymbol{P} = \begin{bmatrix} 1 & x_{s1} & y_{s1} & z_{s1} \\ 1 & x_{s2} & y_{s2} & z_{s2} \\ \vdots & \vdots & \vdots & \vdots \\ 1 & x_{sN} & y_{sN} & z_{sN} \end{bmatrix} \tag{3.30}$$

The interpolation matrix $\boldsymbol{H}$ is finally retrieved as

$$\boldsymbol{H} = \boldsymbol{C}_{as}\boldsymbol{C}_{ss}^{-1} \tag{3.31}$$

where $\boldsymbol{C}_{as}$ contains the aerodynamic grid points relative location to the structural grid points evaluated with the RBFs and the polynomial term. $\boldsymbol{C}_{as}$ is written similarly to $\boldsymbol{C}_{ss}$ as

$$\boldsymbol{C}_{as} = \begin{bmatrix} \phi_{a1s1} & \phi_{a1s2} & \dots & \phi_{a1sN} & 1 & x_{a1} & y_{a1} & z_{a1} \\ \phi_{a2s1} & \phi_{a2s2} & \dots & \phi_{a2sN} & 1 & x_{a2} & y_{a2} & z_{a2} \\ \vdots & \vdots & \ddots & \vdots & \vdots & \vdots & \vdots & \vdots \\ \phi_{aMs1} & \phi_{aMs2} & \dots & \phi_{aMsN} & 1 & x_{aM} & y_{aM} & z_{aM} \end{bmatrix} \tag{3.32}$$

3.2.2 Linear interpolation

In this work, if the wing's structure is reduced to a stick model a simple linear interpolation is performed. The aerodynamic points are rigidly attached to the stick model to transfer the structural displacements and rotations. An example is presented in Figure 3.2, showing rigid attachments for the VLM collocation points and for the force acting points at the midpoint of the vortex segment. The resulting interpolation matrix $\boldsymbol{H}$ is a sparse matrix with a maximum number of two non-zero values per row, since a linear interpolation is performed.

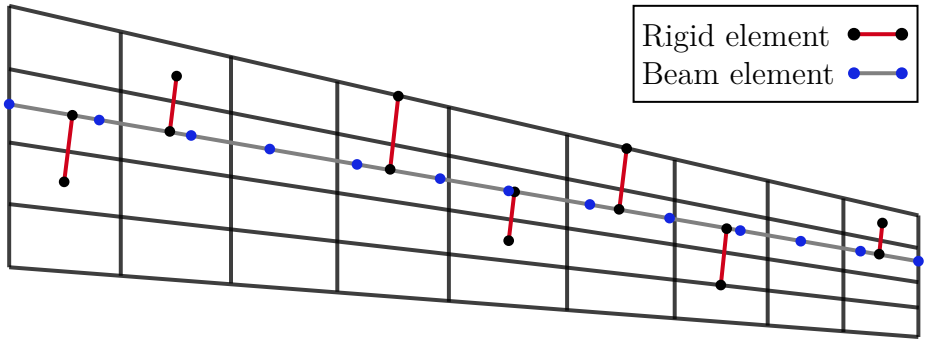

Figure 3.2 Linear interpolation between the aerodynamic grid points and the structural grid points for a stick model.

CHAPTER 4 GENERALIZED MODAL FREQUENCY DOMAIN VORTEX LATTICE METHOD[1]

The Unsteady Vortex Lattice Method is a flexible tool with many possible applications, but its time-domain formulation is not particularly suited for stability analyses. However, since the UVLM naturally includes arbitrary loads and motions, it is well suited for more complex flutter simulations, such as the T-tail configuration. Consequently, the goal of this chapter is to derive a general modal frequency domain VLM that can provide a Generalized Aerodynamic Force (GAF) matrix compatible with the industry standard practices for aeroelastic analyses using the *p-k* method. The GAF matrix should include nonzero lift effects, as well as in-plane dynamics, which are two limitations of the DLM. This is accomplished first by deriving a linear frequency formulation of the UVLM. Thereafter, the complete and general modal frequency aerodynamic force matrix is derived in detail. Afterward, the GAF matrix is compared directly to its counterpart DLM for verification purposes and validation is performed on two distinct flutter cases, a simple flat plate with variable sweep[49] and a canonical T-tail configuration[65].

4.1 Linear frequency domain UVLM

In order to obtain a linearized frequency domain formulation, a periodic solution is assumed with small amplitudes at a given angular frequency (ω) such that the circulation $\mathbf{\Gamma}$ can be expressed by a complex harmonic given by

$$\mathbf{\Gamma} = \hat{\mathbf{\Gamma}} e^{i\omega t} \tag{4.1}$$

where $\hat{\mathbf{\Gamma}}$ is the complex amplitude of circulation. Since the wake circulation can be expressed as a function of the wing's trailing edge circulation, a time lag can be introduced to describe the evolution of the wake circulation as

$$\hat{\Gamma}_w e^{i\omega t} = \hat{\Gamma}_{te} e^{i\omega(t - n\cdot\Delta t)} = \hat{\Gamma}_{te} e^{i\omega t} e^{-i\omega n\cdot\Delta t} \tag{4.2}$$

[1]This chapter contains material published in Journal of Fluids and Structures titled "*A general modal frequency-domain vortex lattice method for aeroelastic analyses*"(2020). The dissertation author is the main author and contributor of the paper and copyrights are held by M. Parenteau and E. Laurendeau.

where $e^{-i\omega n\cdot\Delta t}$ is referred to as the lag term

$$e^{-i\omega n\cdot\Delta t} = \cos(\omega n\cdot\Delta t) - i\sin(\omega n\cdot\Delta t) \tag{4.3}$$

and with Δt imposed from the chord size c of the wake panel

$$\Delta t = \frac{c}{V_\infty} \tag{4.4}$$

As mentioned in Chapter 2, Δt is determined by the discretization of the wake and the size of the wake panel must be similar to the wing's TE panel to avoid numerical errors[85]. Now that the wake's circulation is expressed as a function of the wing's complex amplitude ($\hat{\boldsymbol{\Gamma}}$), the shape of the wake must be prescribed and frozen to include its influence in the wing's influence matrix $\boldsymbol{A}$. However, it does not mean that its shape must remain flat. If a periodic motion is assumed, the wake shape can be prescribed such that it reflects the motion history of the wing trailing edge, referred to as rigid. The effect of the prescribed shape of the wake was discussed in Chapter 2, where the aerodynamic impact is only significant for high amplitudes and/or high reduced frequencies. The final complex linear system is defined as

$$\boldsymbol{A}(\omega)\hat{\boldsymbol{\Gamma}}e^{i\omega t} = -\boldsymbol{V}\boldsymbol{n} \tag{4.5}$$

where $\boldsymbol{A}$ is now frequency dependent because of the added lag term from the wake. $\boldsymbol{V}$ is the sum of the freestream velocity ($\boldsymbol{V}_\infty$) with the local unsteady perturbation ($\hat{\boldsymbol{V}}e^{i\omega t}$).

$$\boldsymbol{V} = \boldsymbol{V}_\infty + \hat{\boldsymbol{V}}e^{i\omega t} \tag{4.6}$$

As a result, two systems are solved independently: a steady ($\boldsymbol{\Gamma}_0$) and a complex unsteady solution ($\hat{\boldsymbol{\Gamma}}$). The complex unsteady forces are then computed using the Joukowki formulation presented in Chapter 2. Thereafter, the complex formulation of aerodynamic forces must be expressed as a function of the aeroelastic system and the modal coordinates to obtain the GAF matrix.

4.2 Generalized Aerodynamic Force Matrix

The classical aeroelastic equations of motion can be written in the following form without damping

$$\bar{\boldsymbol{M}}\ddot{\boldsymbol{q}} + \bar{\boldsymbol{K}}\boldsymbol{q} - \frac{1}{2}\rho v^2\boldsymbol{Q}(k,M)\boldsymbol{q} = 0 \tag{4.7}$$

where $\bar{\boldsymbol{M}}$ is the generalized mass matrix, $\bar{\boldsymbol{K}}$ the generalized stiffness matrix and $\boldsymbol{Q}$ the Generalized Aerodynamic Force (GAF) matrix, which depends on the reduced frequency k and Mach number M. The term $\frac{1}{2}\rho v^2$ represents the dynamic pressure and $\boldsymbol{q}$ the vector of generalized coordinates. To obtain the GAF matrix, the aerodynamic forces computed with the solution of Equation 4.5 must be expressed as a function of the generalized coordinates $\boldsymbol{q}$. To do so, the rotations and velocities from structural deflection must first be included in the right-hand side of the UVLM linear system given by Equation 4.5.

Using linear modal expansion, the structural node displacements are expressed as a linear combination of the mode shapes and generalized coordinates

$$\boldsymbol{x}(t) = q_1(t)\boldsymbol{\eta}_1 + q_2(t)\boldsymbol{\eta}_2 + q_3(t)\boldsymbol{\eta}_3 + ... \tag{4.8}$$

where $\boldsymbol{\eta}_i$ is the i-th mode shape. If a periodic solution is assumed and represented by a single harmonic, the displacement or rotation for every structural node is expressed as

$$\boldsymbol{x}(t) = \boldsymbol{\eta}\boldsymbol{q}e^{i\omega t} \tag{4.9}$$

and the velocity as

$$\dot{\boldsymbol{x}}(t) = i\omega\boldsymbol{\eta}\boldsymbol{q}e^{i\omega t} \tag{4.10}$$

where $\boldsymbol{\eta}$ is the mode shape matrix where each column corresponds to a mode shape vector.

$$\boldsymbol{\eta} = [\boldsymbol{\eta}_1\ \boldsymbol{\eta}_2\ \boldsymbol{\eta}_3\ ...] \tag{4.11}$$

Note that for simplicity, the term $e^{i\omega t}$ will be omitted for the remainder of the chapter. The geometry changes are accounted for by the rotations induced from structural deformation and they are applied to the normal vector $\boldsymbol{n}$ in the RHS of Equation 4.5. With the assumption of small angles and ignoring higher-order terms, these rotations become a simple cross-product

$$\boldsymbol{n} = \boldsymbol{n} + \delta\boldsymbol{n} \tag{4.12}$$

with

$$\delta n = \begin{bmatrix} -n_y R_z + n_z R_y \\ n_x R_z - n_z R_x \\ -n_x R_y + n_y R_x \end{bmatrix} \tag{4.13}$$

where R_x, R_y and R_z are the rotations around the x, y and z -axis respectively. These

rotations are then defined in terms of the generalized coordinates as follows

$$\boldsymbol{R}_x = \boldsymbol{H}\boldsymbol{\eta}\boldsymbol{q} \tag{4.14}$$

where $\boldsymbol{H}$ is the transfer matrix from the structural model to the aerodynamic model, which was defined in the previous chapter. These rotations are then added to the RHS ($\boldsymbol{B}$) in a more compact form given by

$$\delta\boldsymbol{n} = \boldsymbol{R}\boldsymbol{q} \tag{4.15}$$

$$\boldsymbol{B} = -\boldsymbol{V}(\boldsymbol{n} + \boldsymbol{R}\boldsymbol{q}) \tag{4.16}$$

where $\boldsymbol{R}$ represents the matrix of cross-products to obtain $\delta\boldsymbol{n}$ for every panel. With the induced velocities from structural deflections, the RHS is finally defined as

$$\boldsymbol{B} = -\boldsymbol{V}_\infty\boldsymbol{n} - \boldsymbol{V}_\infty\boldsymbol{R}\boldsymbol{q} - i\omega\boldsymbol{H}\boldsymbol{\eta}\boldsymbol{q}\boldsymbol{n} - i\omega\boldsymbol{H}\boldsymbol{\eta}\boldsymbol{R}\boldsymbol{q}^{\boldsymbol{2}} \tag{4.17}$$

The last term in Equation 4.17 represents the induced velocities from structural deflection on the rotation of the panel's normal vector. Since small amplitudes are assumed, this last term is very small compared to the other terms and it is therefore negligible. The RHS is further divided into a steady ($\boldsymbol{B}_0$) and unsteady contribution ($\hat{\boldsymbol{B}}$)

$$\boldsymbol{B} = \boldsymbol{B}_0 + \hat{\boldsymbol{B}}\boldsymbol{q} \tag{4.18}$$

where

$$\boldsymbol{B}_0 = -\boldsymbol{V}_{\boldsymbol{\infty}}\boldsymbol{n} \tag{4.19}$$

and

$$\hat{\boldsymbol{B}} = [-\boldsymbol{V}_\infty\boldsymbol{R} - i\omega\boldsymbol{H}\boldsymbol{\eta}\boldsymbol{n}] \tag{4.20}$$

The three translations (x,y,z) and the three rotations (Rx, Ry, Rz) are included in the RHS, thus incorporating naturally out-of-plane and in-plane dynamics. In the unsteady component, the first term represents the contribution of the steady flow on the static deflections and the second term represents the motion induced velocity from the deflections. Recall that the total circulation is composed of a steady and unsteady contribution as

$$\boldsymbol{\Gamma} = \boldsymbol{\Gamma}_0 + \hat{\boldsymbol{\Gamma}}\boldsymbol{q} \tag{4.21}$$

where the steady part is defined as

$$\boldsymbol{\Gamma}_0 = \boldsymbol{A}^{-1}_{(\omega=0)}\boldsymbol{B}_0 \tag{4.22}$$

with zero frequency and the unsteady contribution as

$$\hat{\boldsymbol{\Gamma}} = \boldsymbol{A}^{-1}_{(\omega \neq 0)} \hat{\boldsymbol{B}} \tag{4.23}$$

Thereafter, the aerodynamic forces are computed using the unsteady Joukowski method as presented in Chapter 2, where the quasi-steady contribution of every vortex segment is added to the unsteady component from each panel.

$$\boldsymbol{F} = \boldsymbol{F}_{st} + \boldsymbol{F}_{unst} \tag{4.24}$$

The quasi-steady contribution acts at the mid-point of the vortex segment, while the unsteady component acts at the mid-point of the panel leading segment[117]. The local velocity $\boldsymbol{V}$ is the sum of the steady freestream flow and the motion induced velocities defined as

$$\boldsymbol{V} = \boldsymbol{V}_\infty + \boldsymbol{V}_d \boldsymbol{q} \tag{4.25}$$

where $\boldsymbol{V}_d = -i\omega \boldsymbol{H} \boldsymbol{\eta}$ and includes induced velocities in the x, y and z directions. After including Equation 4.21 and removing nonlinear terms, the definition of the aerodynamic forces becomes

$$\boldsymbol{F} = \rho_\infty (\boldsymbol{V}_\infty \times \boldsymbol{dl}) \boldsymbol{\Gamma_0} + \Big[\Big(\rho_\infty (\boldsymbol{V}_\infty \times \boldsymbol{dl}) + i\omega \rho_\infty S \boldsymbol{n} \Big) \hat{\boldsymbol{\Gamma}} + \rho_\infty (\boldsymbol{V}_d \times \boldsymbol{dl}) \boldsymbol{\Gamma}_0 \Big] \boldsymbol{q} \tag{4.26}$$

where the first term is the steady contribution and the second term the unsteady contribution expressed as a function of the generalized coordinates

$$\boldsymbol{F} = \boldsymbol{F}_0 + \hat{\boldsymbol{F}} \boldsymbol{q} \tag{4.27}$$

The last term in the unsteady component, $\rho_\infty (\boldsymbol{V}_d \times \delta \boldsymbol{l}) \boldsymbol{\Gamma}_0$, is critical for T-tail flutter as it includes the steady solution $\boldsymbol{\Gamma}_0$. For a T-tail configuration, this would be for example the steady trim load of the horizontal stabilizer which has a significant impact over the flutter onset velocity[65]. The importance of this term is further discussed in Section 4.4.2. Finally, $\hat{\boldsymbol{F}}$ is transferred to the structural model and into modal forces to obtain the GAF matrix

$$\boldsymbol{Q} = \boldsymbol{\eta}^\top \boldsymbol{H}^\top \hat{\boldsymbol{F}} \cdot \frac{1}{\frac{1}{2} \rho_\infty V_\infty^2} \tag{4.28}$$

The contribution of every degree of freedom is added together to obtain the final GAF, which incorporates general 3D kinematics with the assumption of small amplitude deflections.

4.3 GAF Verification

The VLM GAF is verified against the DLM from NASTRAN for a simple flat plate case for which the VLM should provide similar results. The verification is performed using the flat plate of Dimitriadis *et al.*[49], where the structural model consists of quad elements. It is a flat plate with variable sweep and variable aspect ratio with a root and tip chord of 0.2 m. The configuration with an aspect ratio of 4 is used. The same discretization is applied for the aerodynamic model and the structural model with 30 panels chordwise and 60 panels spanwise.

The same structural model is used for both the DLM and the VLM with the same discretization as well. The GAF is also computed at a zero Mach number to remove any compressibility corrections. The real and imaginary parts of the GAF are presented in Figure 4.1 for both the VLM and the DLM with a zero degree sweep. The results are very similar and the only noticeable difference appears at a reduced frequency higher than 1.5 for the third mode $\boldsymbol{Q}_{3,3}$. Some differences are expected as the reduced frequency increases since the aerodynamic models are not exactly equivalent, but globally the VLM provides the same GAF matrix than the DLM for this simple case, where in-plane dynamics are not significant.

4.4 Flutter Results

Two flutter cases are presented in this section: the flat plate configuration used in Dimitriadis *et al.*[49] and a canonical T-tail configuration from Murua *et al.*[65]. For the prediction of flutter, the p-k method[18] is used to provide damping approximation for both the VLM and the DLM.

4.4.1 Variable Sweep Flat Plate

This is the same configuration used in Section 4.3 for the GAF verification using the configuration of Dimitriadis *et al.*[49]. The flat plate has an aspect ratio of 4 with a variable sweep ranging from 0 to 45 degrees and with experimental flutter results[49]. The same discretization is applied for the aerodynamic model and the structural model with 30 panels chordwise and 60 panels spanwise.

Since the computed GAF matrix is similar between the DLM and the VLM, the p-k method should provide similar results as well. The $V-g$ plot and $V-\omega$ plot are presented in Figure 4.2 for the first three modes with a sweep of 45 degrees. The damping and frequency values computed with the VLM follow closely the DLM solution from NASTRAN as expected.

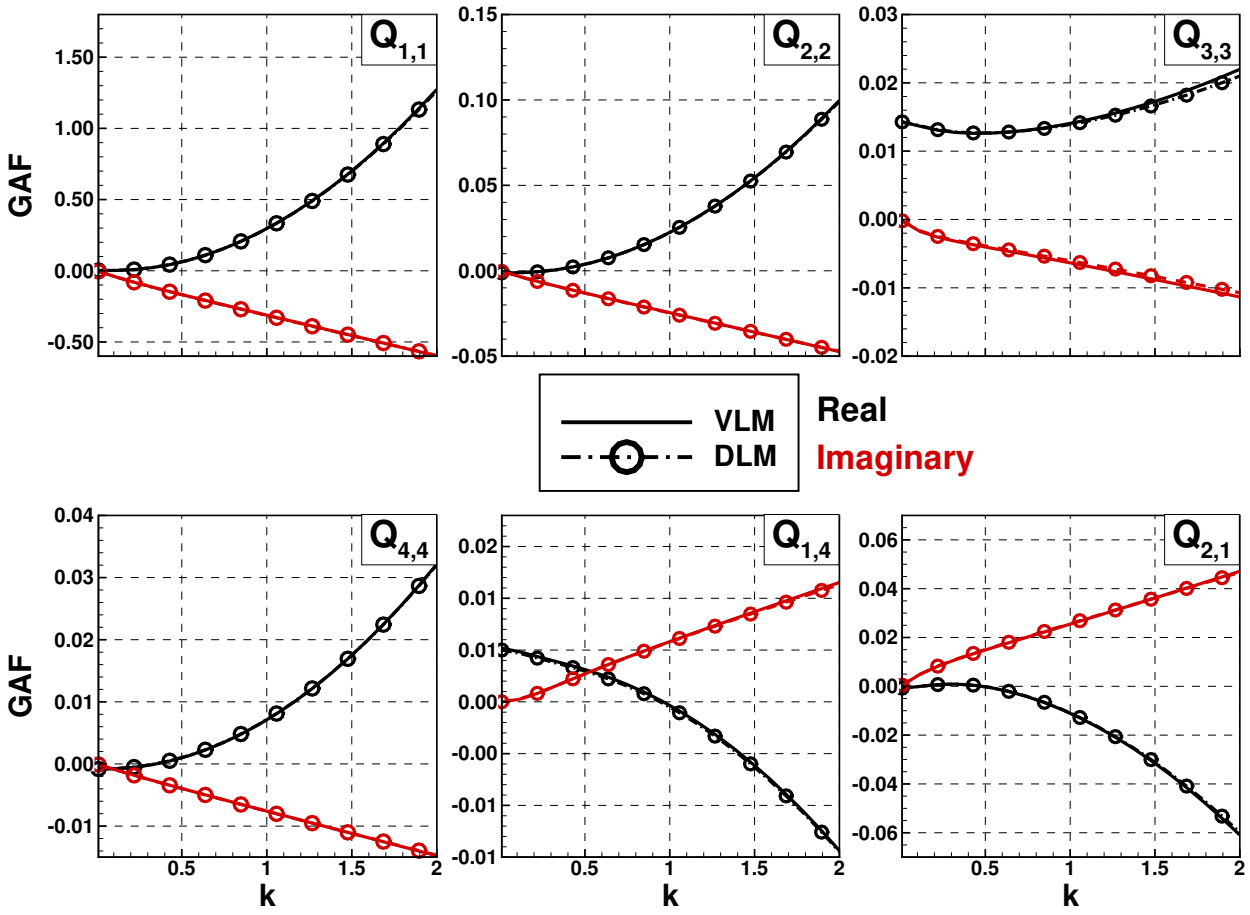

Figure 4.1 Generalized aerodynamic force as a function of reduced frequency, real part in black and imaginary part in red.

Results for the flutter speed and flutter frequency as a function of sweep are presented in Figure 4.3 and Figure 4.4 respectively. As expected, the DLM runs with NASTRAN provide similar results to the VLM. The flutter boundary is under-predicted when compared to the experimental results, but the overall trend as a function of sweep is captured. These results confirm that for a simple configuration without in-plane dynamics, the VLM GAF formulation is equivalent to the DLM.

4.4.2 T-Tail

The final test case of this chapter is a simple isolated T-tail configuration[65] to demonstrate that the derived GAF matrix with the VLM naturally includes in-plane motion and in-plane forces along with steady loading, unlike the DLM. Including steady loads over the horizontal

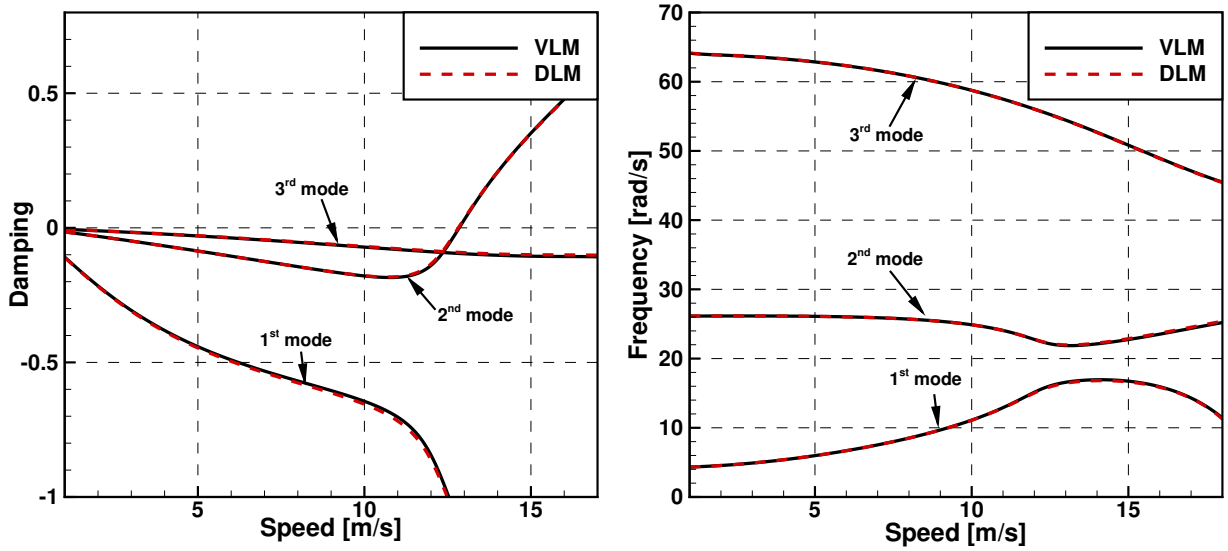

(a) V-g plot (b) V-ω plot

Figure 4.2 V-g and V-ω plot for the flat plate with a sweep of 45 degrees.

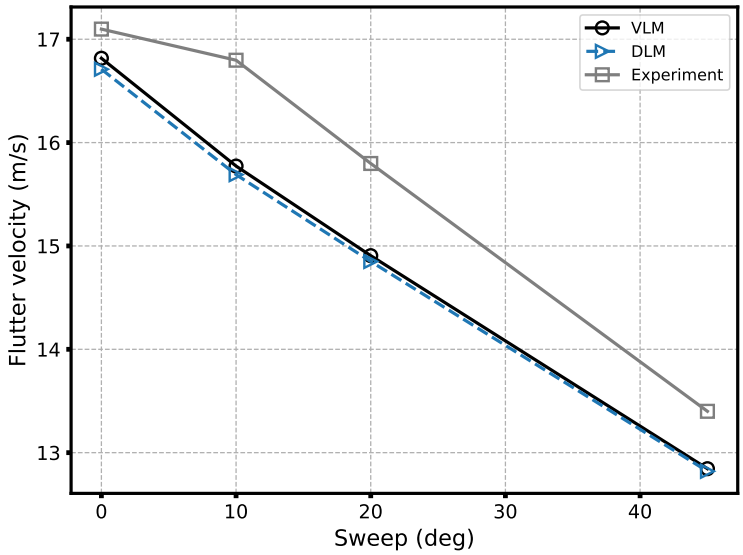

Figure 4.3 Flutter speed

stabilizer is essential for accurate predictions of T-tail flutter[65].

The structural model is represented by beam elements and the T-tail properties are listed in Table 4.1. Since the stiffness of the horizontal stabilizer is infinite, the non-zero steady solution has no effects on the geometry. However, on a more flexible configuration, the non-zero reference state can have an influence over the geometry and should be included through

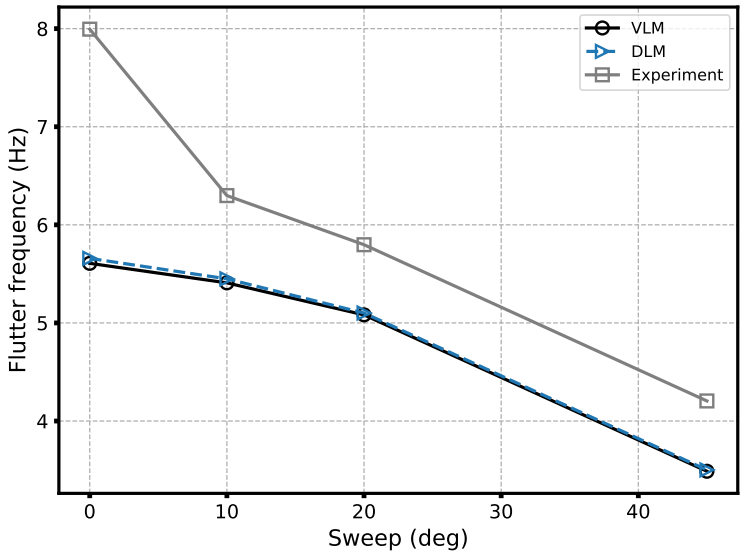

Figure 4.4 Flutter frequency

linearization of the Biot-Savart law or by applying the steady deflections to the reference state before computing the GAF matrix. In this work, the beam elements are modeled with NASTRAN using CBEAM elements, while Murua *et al.* are using an in-house software (SHARP) with geometrically nonlinear composite beams. The same structural model is used for the DLM and the VLM.

Property	**Vertical stab.**	**Horizontal stab.**
Chord	2 m	2 m
Span	6 m	8 m
Elastic axis	25%	25%
Centre of gravity	35%	35%
Mass per unit length	35 kg/m	35 kg/m
Torsional stiffness	$10^7 Nm^2$	∞
Out-of-plane bending stiffness	$10^7 Nm^2$	∞
Inplane bending stiffness	∞	∞

Table 4.1 T-tail properties

The aerodynamic and structural meshes are presented in Figure 4.5. With these properties, the natural frequencies for the T-tail first bending mode and first torsion mode are 2.82 Hz and 5.27 Hz respectively as shown in Figure 4.6. The standard DLM cannot model steady loads, but data computed externally can be added to the DLM to account for these effects[66]. For this test case, the flutter speed is therefore evaluated for different values of AoA and H-tail dihedral angles to demonstrate that the VLM GAF matrix includes naturally these effects.

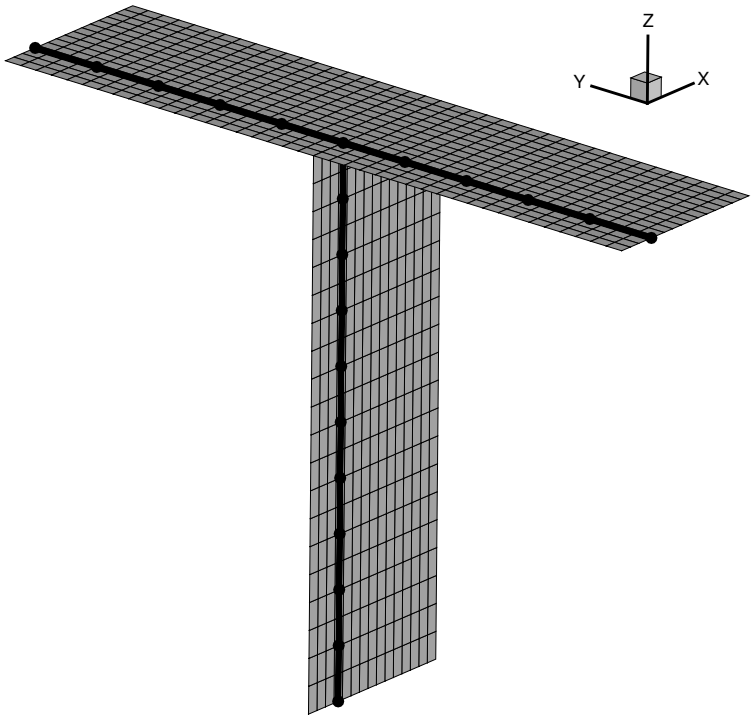

Figure 4.5 T-tail aerodynamic and structural mesh

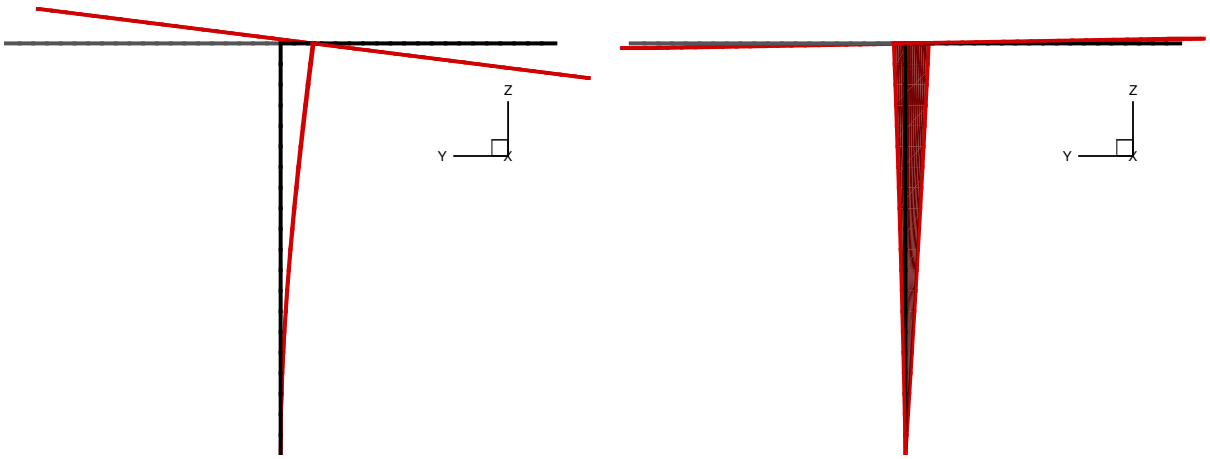

(a) First bending (2.81 Hz)

(b) First torsion (5.27 Hz)

Figure 4.6 First bending and torsion modes for the T-tail

The flutter speed and frequency are presented in Figure 4.7 and 4.8 respectively. The solution for the standard DLM is at zero dihedral angle. The flutter speed and frequency computed by the VLM at 0 AoA and 0 dihedral angle are fairly similar with the DLM since there are no steady loads. However, with an increasing AoA, the flutter velocity is considerably reduced

by around 100 m/s from 0 degree AoA to 8 degrees AoA. This result clearly indicates that including the effects of steady loads over the H-tail is essential for accurate predictions. As mentioned in Section 4.2, the term associated with $\mathbf{\Gamma}_0$ in Equation 4.26 is critical to include these effects. This is highlighted in Figure 4.9 where the solution without $\mathbf{\Gamma}_0$ does not fully capture the effect of AoA.

Finally, as observed by Murua *et al.*[65], a positive dihedral angle has a destabilizing effect over the flutter boundary. However, the dihedral angle does not have a significant effect on the flutter frequency.

The differences in flutter prediction between Murua and the modal frequency domain VLM can be attributed to the employed structural model. For this simple configuration at zero AoA, the results should be similar with the DLM. However, there are significant differences between the solutions of Murua *et al.* and the DLM, thus suggesting that the structural model used in this work with NASTRAN is not equivalent to Murua's geometrically nonlinear composite beam model. The results with zero dihedral angle are very close to the DLM for both flutter speed and flutter frequency, since the same structural model is used. Nonetheless, both models should behave similarly with respect to dihedral angle and AoA. The results in Figure 4.7 and 4.8 show that the same trends are observed.

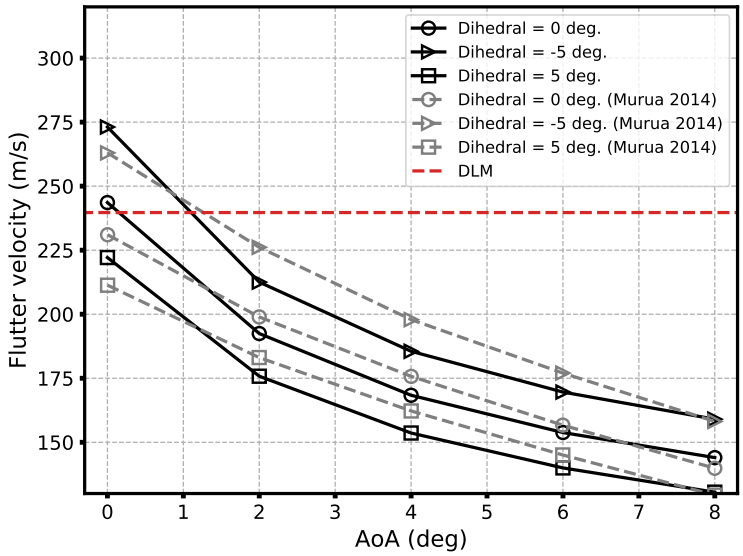

Figure 4.7 Effect of angle of attack and dihedral angle over the flutter. onset velocity

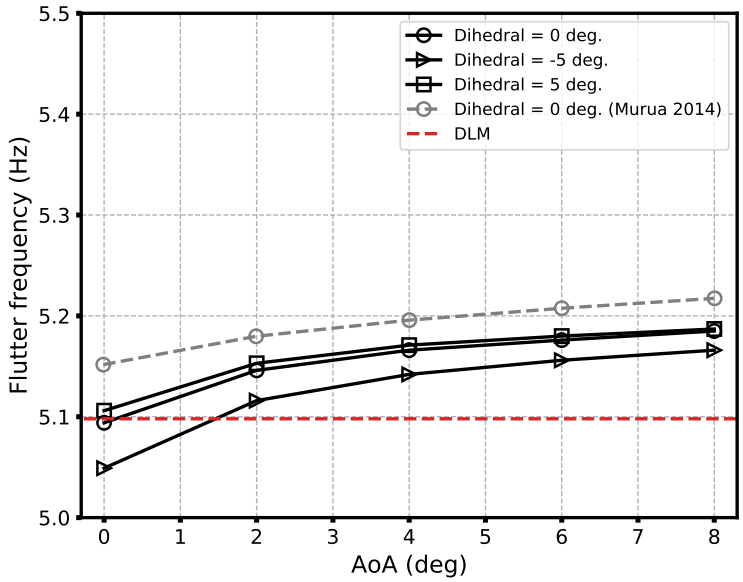

Figure 4.8 Effect of angle of attack and dihedral angle over the flutter. frequency

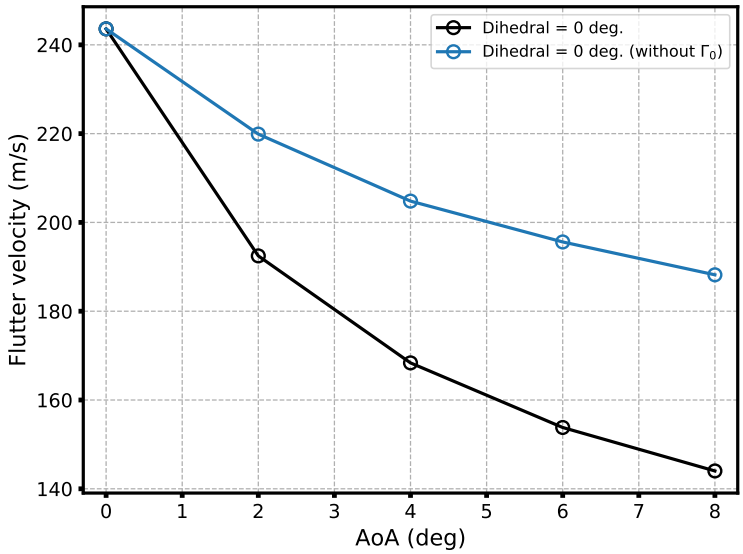

Figure 4.9 Impact of the steady term ($\mathbf{\Gamma}_0$) in the GAF matrix on the flutter solution.

4.5 Summary

A linearized frequency domain formulation for the UVLM was derived with the assumption of small amplitude oscillation, from which the generalized aerodynamic force matrix is obtained without the assumption of out-of-plane dynamics. As a result, the GAFs naturally include in-plane dynamics, along with the ability to model complex configurations without

external corrections. Thus, the effects of camber, twist and AoA are all intrinsically modeled. Furthermore, the VLM GAF matrix is compatible with the industry-standard techniques for stability analysis allowing efficient flutter analyses. This is verified with the flat plate case of Dimitriadis *et al.* and compared against the DLM. For this simple test case, the VLM provides similar results to the DLM. However, the VLM includes naturally in-plane dynamics and steady loading, thus providing more accurate results for T-tail configurations. This was demonstrated with a canonical T-tail configuration with a varying dihedral angle and AoA. The VLM modal frequency domain formulation is therefore a viable replacement to the DLM, with similar computational efficiency, but with superior modeling capabilities. However, the approach is applicable to incompressible and inviscid flows only, but the standard external correction techniques developed for the DLM using 3D RANS are also applicable to this VLM formulation. Consequently, accurate linear aeroelastic analyses can be performed with this VLM formulation, but for non-linear aeroelastic analyses, a non-linear frequency domain approach is required.

CHAPTER 5 NON-LINEAR FREQUENCY DOMAIN SOLVER[1]

In this chapter, a non-linear frequency domain formulation for the UVLM is developed using the harmonic balance approach. Two different methodology are proposed to solve the non-linear frequency domain problem, a direct and an iterative approach. The harmonic balance VLM is verified against the standard time-domain UVLM for three distinct non-linear dynamic problems with increasing difficulty. Thereafter, the chapter concludes with a comparison of computational cost between the UVLM and the proposed non-linear frequency domain solver.

5.1 Harmonic balance formulation

The same assumption as in Chapter 4 is made here where the solution is assumed periodic. In the previous chapter, the UVLM was linearized around a frozen geometry with the assumption of small unsteady perturbations leading to a decomposed problem, where the steady solution is solved independently from the unsteady complex solution. For the NLFD formulation, the problem is no longer linearized around a frozen geometry and there is no assumption of small amplitude. Consequently, instead of using a single harmonic to represent the periodic solution, a Fourier series is applied as follows

$$\Gamma = \sum_{k=-N}^{N} \hat{\Gamma}_k \cdot e^{j\omega k t} \tag{5.1}$$

where ω is the dominant frequency. If Equation 5.1 is introduced in the UVLM linear system (Equation 2.3), the following equation is obtained

$$\boldsymbol{A} \sum_{k=-N}^{N} \hat{\Gamma}_k \cdot e^{j\omega k t} + \boldsymbol{B} \sum_{k=-N}^{N} \hat{\Gamma}_{Wk} \cdot e^{j\omega k t} + \sum_{k=-N}^{N} \hat{V}_k \cdot e^{j\omega k t} = 0 \tag{5.2}$$

where $\hat{\boldsymbol{V}}$ are the Fourier coefficients for the onset flow and the velocity induced by the harmonic motion. As mentioned in Chapter 2, the circulation of the wake is shed from the trailing edge and remains unchanged, hence the circulation Γ_W at a position downstream i

[1]This chapter contains material published in AIAA Journal titled "*Nonlinear Frequency-Domain Solver for Vortex Lattice Method*" (2018). The dissertation author is the main author and contributor of the paper and copyrights are held by M. Parenteau and E. Laurendeau.

is equal to the circulation forward at the previous time step.

$$\Gamma_{W_i}(t) = \Gamma_{W_{i-1}}(t - \Delta t) \tag{5.3}$$

As a result, the circulation of the wake is expressed only in terms of the trailing edge circulation

$$\Gamma_{W_i}(t) = \Gamma_{TE}(t - (i+1) \cdot \Delta t) \tag{5.4}$$

and the linear system in terms of the unknown Fourier coefficients of the wing circulation $\hat{\Gamma}$ is given by

$$\boldsymbol{A} \sum_{k=-N}^{N} \hat{\Gamma}_k \cdot e^{j\omega k t} + \boldsymbol{B} \sum_{k=-N}^{N} \hat{\Gamma}_k \cdot e^{j\omega k (t-(i+1)\Delta t)} + \sum_{k=-N}^{N} \hat{V} \cdot e^{j\omega k t} = 0 \tag{5.5}$$

Moreover, since the circulation Γ are real values

$$\Gamma_{-k} = \overline{\Gamma}_k \tag{5.6}$$

where $\overline{\Gamma}_k$ is the complex conjugate, only non-negative terms of k are retained for the Fourier coefficients. If N harmonics are retained to describe the solution of Γ, $2N + 1$ Fourier coefficients are necessary

$$\Gamma = a_0 + \sum_{k=1}^{N} \Big(a_k \cos(\omega k t) + b_k \sin(\omega k t) \Big) \tag{5.7}$$

with the Fourier coefficients $\hat{\boldsymbol{\Gamma}}$ of the circulation defined as

$$\hat{\boldsymbol{\Gamma}} = \begin{pmatrix} a_0 & a_1 & b_1 & \cdots & a_k & b_k \end{pmatrix} \tag{5.8}$$

The use of a Fourier series to model the periodic solution creates $2N+1$ times more unknowns in the linear system. Therefore, $2N+1$ systems are evaluated at equally spaced time instances t_n along the period T

$$t_n = \frac{n}{2N+1} \mathsf{T} \tag{5.9}$$

to allow a well-posed problem. Since a periodic motion is assumed, the positions of the wing and the wake are known at each time instances t_n, thus $2N+1$ meshes are generated for the wing and for the prescribed wake, as illustrated in Figure 5.1. The wing and wake influence matrices are computed at all time instances t_n, thus forming an augmented system. The prescribed wake is generated from the motion history of the trailing edge and calculations are

performed at different time instance in the time domain, such that the computation remains similar to that of the UVLM formulation. As a result, the implementation is straightforward from a time-domain UVLM since the kernel remains unchanged.

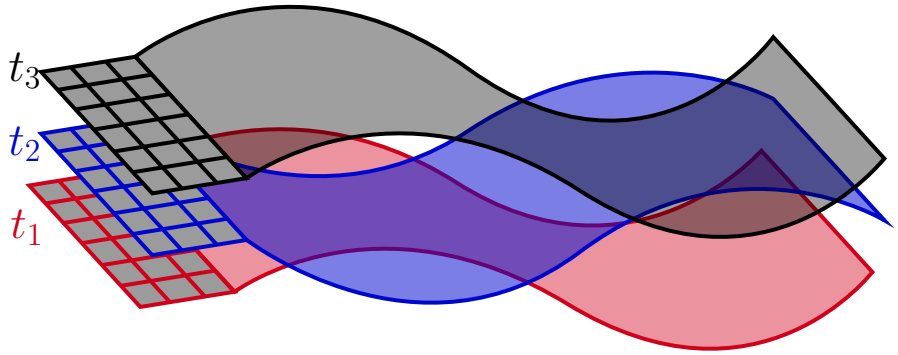

Figure 5.1 Illustration of the 3 time instances for a single harmonic heave motion.

5.2 Non-linear frequency domain solver

In this section, two different approaches are presented for solving the non-linear frequency domain formulation of the UVLM (Equation 5.5). In the first approach, Equation 5.5 is solved directly in the frequency domain for the Fourier coefficients of each vortex ring. The second approach solves the $2N+1$ linear system independently in the time domain and in an iterative fashion for $\mathbf{\Gamma}$. The frequency domain solution of $\mathbf{\Gamma}$ is obtained afterward with a discrete Fourier transform.

5.2.1 Direct frequency domain solver

For the direct approach, the induced velocity is expressed in terms of the Fourier coefficients

$$A_{p,q} \cdot \Gamma_q = A_{p,q} \cdot \left[a_0 + \sum_{k=1}^{N} \Big(a_k \cos(\omega k t) + b_k \sin(\omega k t) \Big) \right]_q = A_{p,q} \cdot \widetilde{\boldsymbol{P}} \cdot \hat{\mathbf{\Gamma}}_q \tag{5.10}$$

where $A_{p,q}$ is the influence coefficient from panel q on panel p calculated with Biot-Savart's equation. $\hat{\mathbf{\Gamma}}_q$ are the unknown Fourier coefficients of panel q where $\widetilde{\boldsymbol{P}}$ is defined as

$$\widetilde{\boldsymbol{P}} = \begin{pmatrix} 1 & \cos(\omega t) & \sin(\omega t) & \cdots & \cos(\omega k t) & \sin(\omega k t) \end{pmatrix} \tag{5.11}$$

The influence coefficient $A_{p,q}$ is computed in the same manner than for the UVLM and the influence matrix is augmented by the length of $\widetilde{\boldsymbol{P}}$ which depends on the chosen number of harmonics. $\widetilde{\boldsymbol{P}}$ is also computed with the current time of the instance t_n defined by Equation 5.9. The same is done for the wake influence where $\widetilde{\boldsymbol{P}}$ is computed with the time at which the wake panel was shed from the trailing edge defined by Equation 5.4. Both the wake and the wing influence coefficients are combined together in the left-hand side to obtain

$$(\widetilde{\boldsymbol{A}} + \widetilde{\boldsymbol{B}}) \cdot \hat{\boldsymbol{\Gamma}} + \widetilde{\boldsymbol{V}} \cdot \tilde{\boldsymbol{n}} = 0 \tag{5.12}$$

where

$$\widetilde{\boldsymbol{A}} = \begin{pmatrix} \boldsymbol{A}_{t_1} \\ \boldsymbol{A}_{t_2} \\ \vdots \\ \boldsymbol{A}_{t_n} \end{pmatrix} \tag{5.13}$$

and

$$\boldsymbol{A}_t = \begin{pmatrix} A_{1,1}(t) \cdot \widetilde{\boldsymbol{P}}(t) & A_{1,2}(t) \cdot \widetilde{\boldsymbol{P}}(t) & \cdots & A_{1,m}(t) \cdot \widetilde{\boldsymbol{P}}(t) \\ A_{2,1}(t) \cdot \widetilde{\boldsymbol{P}}(t) & A_{2,2}(t) \cdot \widetilde{\boldsymbol{P}}(t) & \cdots & A_{2,m}(t) \cdot \widetilde{\boldsymbol{P}}(t) \\ \vdots & \vdots & \ddots & \vdots \\ A_{m,1}(t) \cdot \widetilde{\boldsymbol{P}}(t) & A_{m,2}(t) \cdot \widetilde{\boldsymbol{P}}(t) & \cdots & A_{m,m}(t) \cdot \widetilde{\boldsymbol{P}}(t) \end{pmatrix} \tag{5.14}$$

The augmented matrices $\widetilde{\boldsymbol{A}}$ and $\widetilde{\boldsymbol{B}}$ are of size $[m \cdot (2N+1)] \times [m \cdot (2N+1)]$, where m is the number of panels on the wing and N the number of harmonics.

Similarly, $\widetilde{\boldsymbol{V}}$ and $\tilde{\boldsymbol{n}}$ are augmented vectors for every time instances defined as

$$\widetilde{\boldsymbol{V}} = \begin{pmatrix} \boldsymbol{V}_{t_1} \\ \boldsymbol{V}_{t_2} \\ \vdots \\ \boldsymbol{V}_{t_n} \end{pmatrix} \quad ; \quad \tilde{\boldsymbol{n}} = \begin{pmatrix} \boldsymbol{n}_{t_1} \\ \boldsymbol{n}_{t_2} \\ \vdots \\ \boldsymbol{n}_{t_n} \end{pmatrix} \tag{5.15}$$

$\boldsymbol{V}_{t_1}$ is therefore the vector of total induced velocities for every element on the wing at the time instance t_1 and $\boldsymbol{n}_{t_1}$ is the vector of normal vectors for every element at time instance t_1. For rigid rotation and/or flexible deformation, $\boldsymbol{n}_{t_n}$ will be different between the various time instances, since the geometry will differ. This linear system can be solved directly for the Fourier coefficients $\hat{\boldsymbol{\Gamma}}$ using any linear solver. In this work, the iterative Krylov subspace bi-conjugate gradient stabilized method is used.

5.2.2 Iterative solver

The iterative approach requires minimal modification from a standard time-domain UVLM solver. Each system at the $2N+1$ time instances are solved independently in the time domain, as it would be solved in a UVLM algorithm for a single step. Once computed, the circulation $\mathbf{\Gamma}$ at the $2N+1$ time instances are coupled together through a discrete Fourier transform (DFT) to obtain $\hat{\Gamma}$. For example, the Fourier coefficients of circulation for the element j are given by

$$DFT \cdot \hat{\mathbf{\Gamma}}_j = \begin{pmatrix} \Gamma_1^j \\ \Gamma_2^j \\ \vdots \\ \Gamma_n^j \end{pmatrix} \tag{5.16}$$

where the DFT is defined as a function of the time instances by

$$DFT = \begin{pmatrix} 1 & \cos(\omega t_1) & \sin(\omega t_1) & \cdots & \cos(\omega k t_1) & \sin(\omega k t_1) \\ 1 & \cos(\omega t_2) & \sin(\omega t_2) & \cdots & \cos(\omega k t_2) & \sin(\omega k t_2) \\ \vdots & \vdots & \vdots & \ddots & \vdots & \vdots \\ 1 & \cos(\omega t_n) & \sin(\omega t_n) & \cdots & \cos(\omega k t_n) & \sin(\omega k t_n) \end{pmatrix} \tag{5.17}$$

Since a periodic solution is assumed, the wake circulation is exactly equal to the trailing edge circulation at a previous time step. Therefore, the Fourier coefficients of the trailing edge panels are used to compute the circulation of all the wake panels that are shed by the corresponding trailing edge panel with the appropriate time step using Equation 5.4

$$\Gamma_{W_i} = a_{0_{TE}} + \sum_{k=1}^{N} \Big(a_{k_{TE}} \cos(\omega k (t_n - (i+1) \cdot \Delta t)) + b_{k_{TE}} \sin(\omega k (t_n - (i+1) \cdot \Delta t)) \Big) \tag{5.18}$$

Since the Fourier coefficients must be known in order to evaluate the wake circulation, the coupled system has to be solved iteratively. The iterative scheme is summarized as follows

1. Initialize the grids for every time instances
2. Apply the corresponding induced velocity for the $2N+1$ linear systems
3. Assume a wake circulation (i.e. 0 wake circulation)
4. Solve all $2N+1$ linear systems to obtain $\mathbf{\Gamma}$
5. Compute the Fourier coefficients $\hat{\mathbf{\Gamma}}$ with a DFT

6. Update the wake circulation $\boldsymbol{\Gamma}_W$ for every wake panels using Equation 5.18

7. Compute the residual $\boldsymbol{R}$ of the linear systems with the updated wake circulation ($\boldsymbol{\Gamma}_{W_{new}}$)

$$\boldsymbol{R} = \boldsymbol{A} \cdot \boldsymbol{\Gamma} + \boldsymbol{B} \cdot \boldsymbol{\Gamma}_{W_{new}} + \boldsymbol{V} \cdot \boldsymbol{n} \tag{5.19}$$

8. Repeat steps 4-7 until $||\boldsymbol{R}||_2 < \epsilon$

The iterative approach can be viewed as $2N+1$ independent UVLM systems that are coupled together through a Fourier series.

5.2.3 Aerodynamic force calculation

The aerodynamic forces are computed for every time instances using the unsteady Joukowski method described in Chapter 2 given by

$$\Delta \boldsymbol{F}_{i,j} = \Delta \boldsymbol{F}_{steady_{i,j}} + \Delta \boldsymbol{F}_{unsteady_{i,j}}$$

where

$$\Delta \boldsymbol{F}_{steady_{i,j}} = \rho \Gamma_{i,j} (\boldsymbol{V} \times \boldsymbol{dl})$$

and

$$\Delta \boldsymbol{F}_{unsteady_{i,j}} = \rho \frac{\partial \Gamma_{i,j}}{\partial t} \Delta A_{i,j} \boldsymbol{n}_{i,j}$$

Unlike Chapter 2, where $\frac{\partial}{\partial t}\Gamma_{ij}$ was computed in the time domain with a second order backward difference, the unsteady term is now evaluated from the analytical derivative of the Fourier series and the Fourier coefficients $\hat{\boldsymbol{F}}$ are obtained through a discrete Fourier transform

$$\hat{\boldsymbol{F}} = DFT^{-1} \begin{pmatrix} \boldsymbol{F}_1 \\ \boldsymbol{F}_2 \\ \vdots \\ \boldsymbol{F}_n \end{pmatrix} \tag{5.20}$$

Real and complex components of aerodynamic forces are then obtained through the equivalent form of the Fourier series:

$$F(t) = a_0 + \sum_{k=1}^{N} \Big(a_k \cos(\omega k t) + b_k \sin(\omega k t) \Big) = \sum_{k=-N}^{N} c_n \cdot e^{j\omega k t} \tag{5.21}$$

where

$$c_n = \begin{cases} \frac{1}{2}(a_k - jb_k) & \text{for } k > 0 \\ \frac{1}{2}a_0 & \text{for } k = 0 \\ c^*_{|k|} & \text{for } k < 0 \end{cases} \tag{5.22}$$

The asterisk denotes the complex conjugate.

For the remainder of the thesis, the NLFD formulation of the time-domain UVLM will be referred to as Harmonic Balance VLM (HB VLM). A numerical verification for the HB VLM is presented in Appendix B for both the direct and the iterative approach against Theodorsen. In the next section, the HB VLM is applied to non-linear dynamic problems and compared against the time-domain UVLM.

5.3 Non-linear dynamic problems

In this section, the goal is to verify the solver capabilities to model non-linear dynamic problems, where a single harmonic is not sufficient. All cases are performed on a rectangular wing with an aspect ratio of eight. The same mesh is used for the HB VLM and the UVLM, where the Δt is chosen carefully to ensure that the discretization of the wake mesh is consistent with the wing.

5.3.1 Double pitch motion

The first test case is a pitching motion defined with two reduced frequencies[118], where the second reduced frequency is seven times higher than the first. The angle of attack is described by the following equation

$$\alpha = 2.0\sin(\omega t) + 2.0\sin(7 \times \omega t) \tag{5.23}$$

where the reduced frequency is set to 0.05. Theoretically, the HB VLM should require at least seven harmonics in order to solve accurately the unsteady lift coefficient. Solutions with different numbers of harmonics are presented in Figure 5.2 and compared against the UVLM. The solution with seven harmonics matches the time-domain UVLM results as expected.

5.3.2 Non-linear pitching motion

A simple pitching motion was involved in the previous test case. To verify the spectral accuracy and convergence, a more complicated pitching motion proposed by Gopinath and

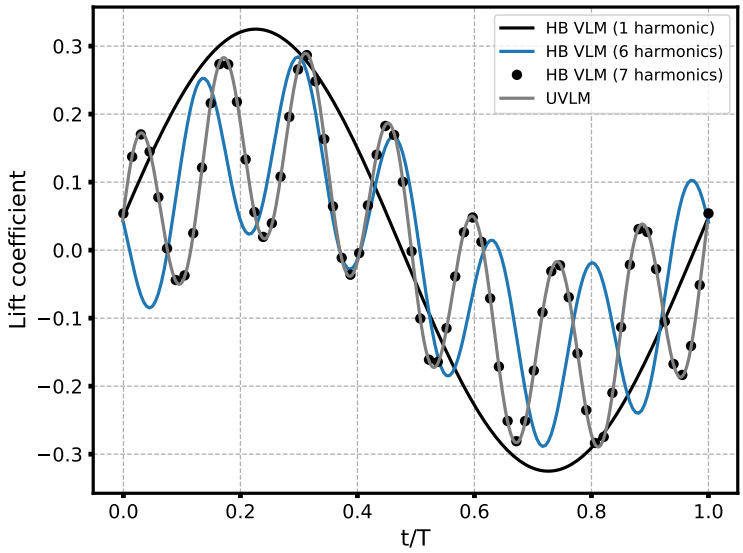

Figure 5.2 Lift coefficient comparison between UVLM and HB VLM for a double pitch motion

Jameson [41] is applied and described by

$$\alpha = \frac{3.0}{5.0 - 4.0 \cdot \cos(t)} \tag{5.24}$$

Figure 5.3 shows the angle of attack variation for one period. Solutions for the HB VLM are computed using 1, 5, 10 and 15 harmonics for the Fourier series and compared to the UVLM in Figure 5.4. As the number of harmonics is increased, the lift coefficient computed with the HB VLM gradually converges toward the solution computed using the UVLM. Around 15 harmonics are necessary to obtain a solution that is in good agreement with the UVLM. These results are in line with the spectral convergence presented by Gopinath and Jameson [41] for a time spectral method applied to the Euler equations.

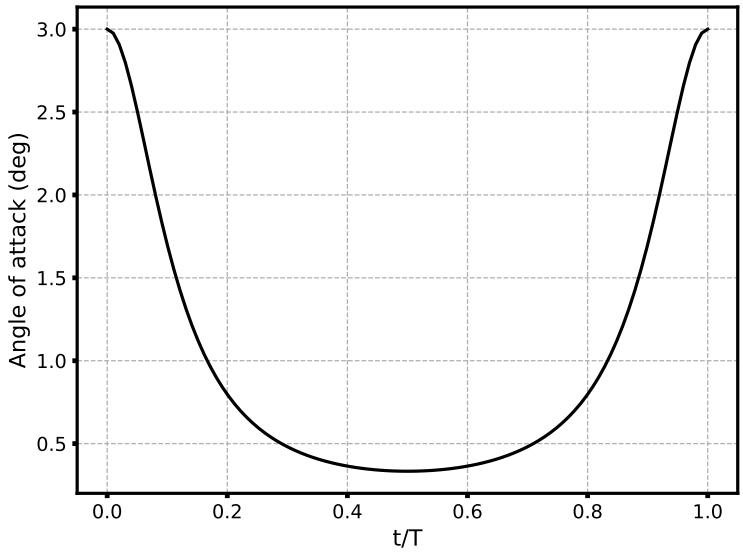

Figure 5.3 Pitching motion for one period. $\alpha = \frac{3.0}{5.0-4.0\cdot\cos(t)}$

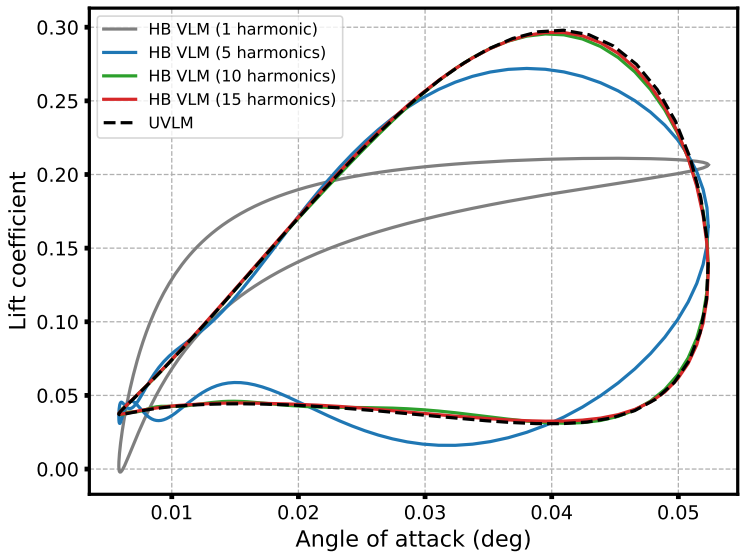

Figure 5.4 Lift coefficient as a function of angle of attack. $\alpha = \frac{3.0}{5.0-4.0\cdot\cos(t)}$

5.3.3 Wake intersection

For the last test case, the motion remains linear, but a non-linear aerodynamic effect is introduced through the wake. The problem involves a heaving motion of two wings with one wing placed four chords in front of the other as shown in Figure 5.5. Both wings undergo a heaving motion at 0.1 reduced frequency with an amplitude of $h = 0.8/c$. As a result, the second wing periodically intersects the wake of the first wing at $t/T = 0.23$ and $t/T = 0.74$,

thus influencing the lift coefficient of the second wing. The wake intersection cannot be accurately modeled without a force-free wake with roll-up, but some effects are still captured with a prescribed wake. The goal of this case is to verify that the HB VLM can perform complicated cases involving wake-intersection effects with the same accuracy than the UVLM.

To avoid the singularity issue when the wing intersects the wake, the two wings are generated with the same discretization, thus the wake vortex rings are perfectly aligned with the second wing. Since the influence calculation is performed in the time domain with Biot-Savart, vortex core models could also be implemented with the HB VLM to avoid these singularities. Both wings are modeled with 5 panels chordwise and 20 panels spanwise. The solution of the lift coefficient is presented in Figure 5.6 over 1 period for both wings using the UVLM and the HB VLM. The lift coefficient of the first wing is captured with only 1 harmonic while 15 harmonics are necessary to capture the influence from the wake on the lift coefficient of the second wing. The difference in the lift coefficient for the second wing between the HB VLM and the UVLM is presented in Figure 5.7. Since the intersection appears at a specific time, it would require a significant number of harmonics to match perfectly the UVLM. However, a good approximation under 0.5% error is obtained with 15 harmonics. The error is evaluated as follows

$$Error = \frac{RMS(C_L - C_{L_{UVLM}})}{max|C_{L_{UVLM}}|} \tag{5.25}$$

and using the UVLM as the reference with 300 points along the period.

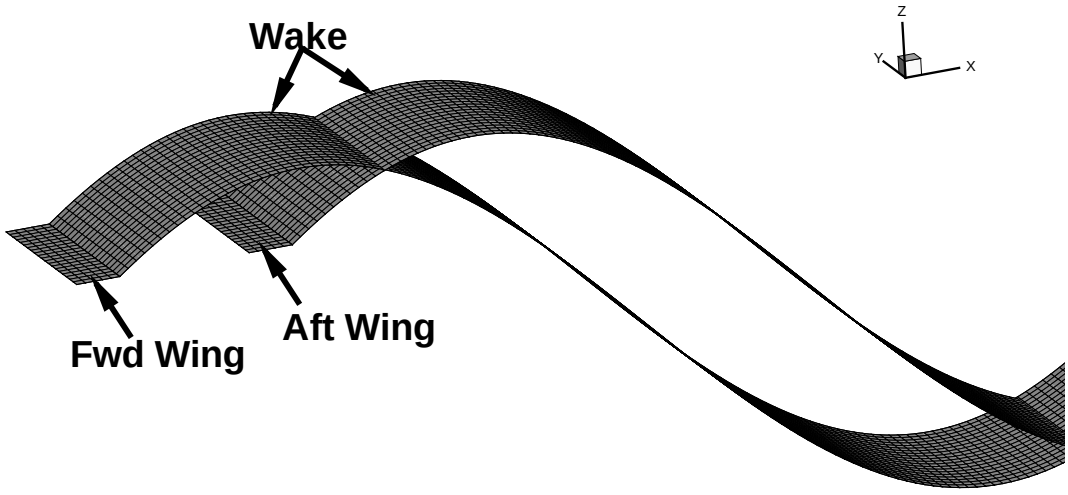

Figure 5.5 Heave motion of two wings with wake intersection

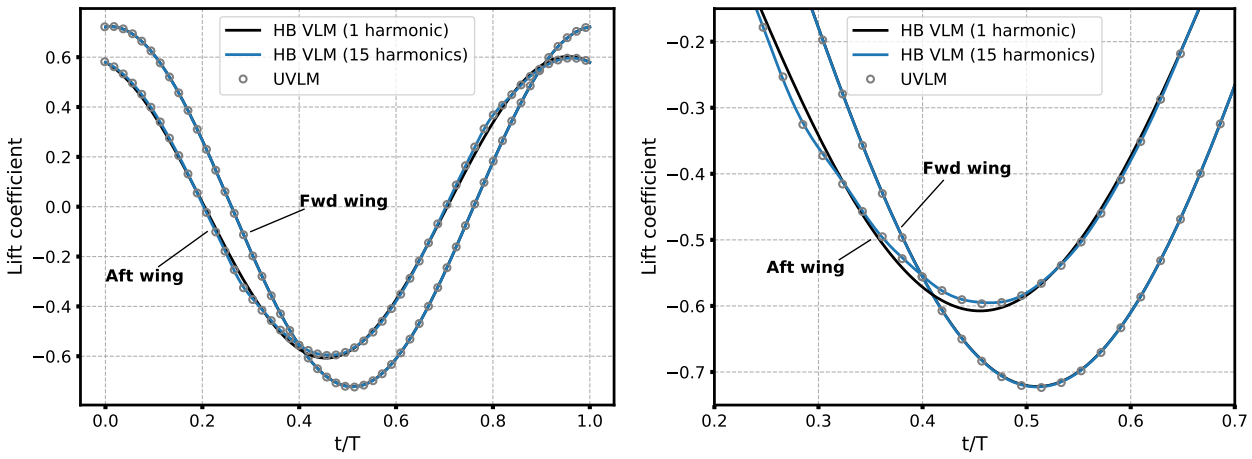

(a) Lift coefficient

(b) Zoom over the wake intersection effect

Figure 5.6 Lift coefficient comparison between UVLM and HB VLM.

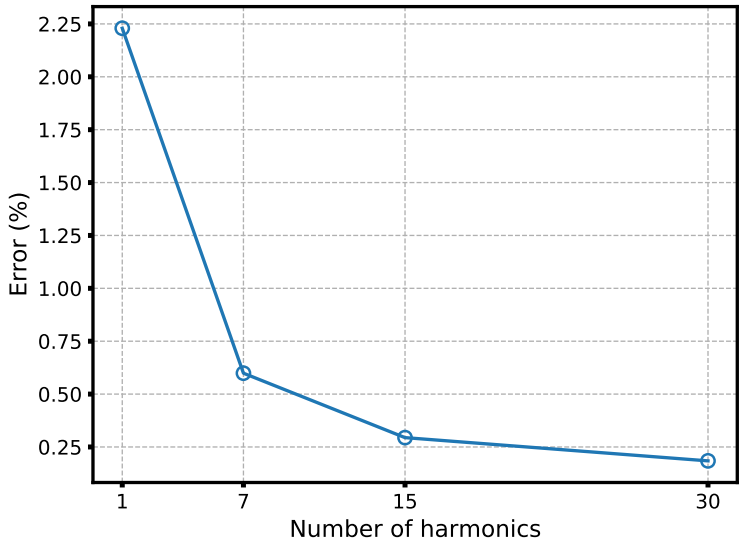

Figure 5.7 Error of lift coefficient using the UVLM as reference for different numbers of harmonics.

5.4 CPU time and memory

The HB VLM can reduce significantly the overall compute time for periodic problems when compared to the UVLM. In this section, the CPU time is evaluated for the wake-intersection problem. Figure 5.8 compares the CPU time with different numbers of spanwise elements and different numbers of harmonics retained for the Fourier series. The UVLM was computed for four periods to obtain a converged periodic solution and the wake influence was calculated

up to a distance of 50 chord length to match the HB VLM conditions. With 15 harmonics the HB VLM is approximately four times faster with 20 panels spanwise and 100 times faster with a single harmonic. For most applications, 15 harmonics should be sufficient, hence the HB VLM is at least one order of magnitude faster than the UVLM.

Furthermore, the CPU time in Figure 5.8 are with the direct solver for the HB VLM, which has a larger linear system to solve than the iterative approach. In Figure 5.9, the direct approach is compared with the iterative approach for the same wake-interaction case. For a higher number of harmonics, the iterative approach requires less CPU time than the direct approach, which is explained by the linear system being solved. The direct method solves one system of size $[m \cdot (2N+1)] \times [m \cdot (2N+1)]$, where m is the number of panels on the wing. The problem size increases exponentially with the number of harmonics, while the iterative method solves $2N + 1$ systems of size $m \times m$. Consequently, the iterative approach scales linearly with the number of harmonics. For a high number of time instances, the iterative solver is therefore faster and requires less memory as well. Table 5.1 presents a comparison of the memory usage for the iterative and the direct solvers for the LHS. It shows clearly that the direct solver requires a significant amount of memory when the number of harmonics increases.

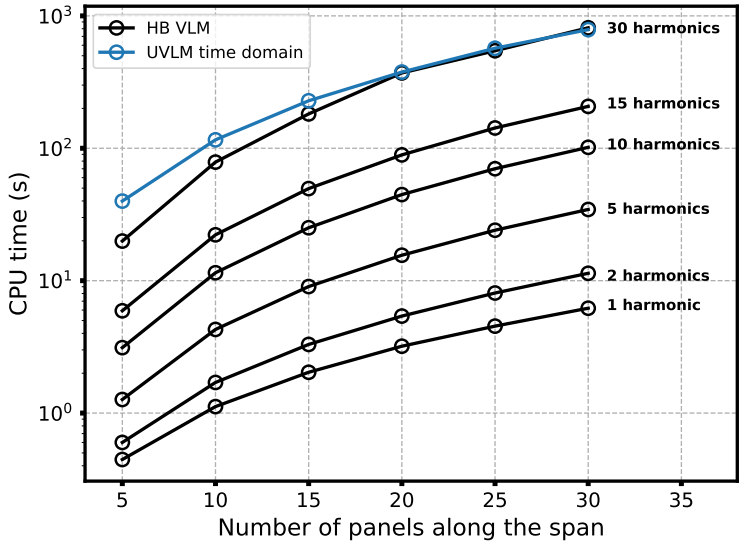

Figure 5.8 CPU time comparison between UVLM and strongly coupled time spectral for different number of panels spanwise

Table 5.1 Comparison of memory usage in gigabyte for the LHS between the iterative and direct solvers for a wing with 5000 elements in double precision.

Num. harmonics	Iterative solver	Direct solver
1	0.56 GB	1.68 GB
2	0.93 GB	4.67 GB
5	2.06 GB	22.62 GB
10	3.93 GB	82.43 GB

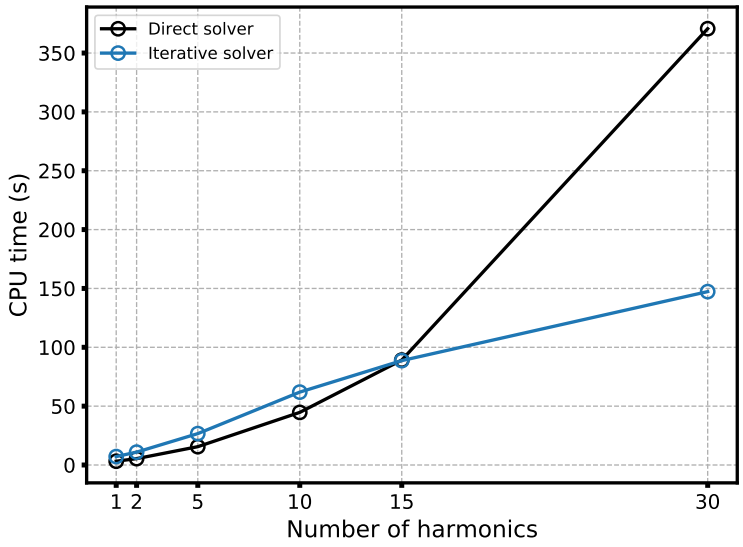

Figure 5.9 HB VLM CPU time comparison between iterative and direct approach

5.5 Summary

A non-linear frequency domain solver was developed for the unsteady vortex lattice method by representing the solution Γ in time with a Fourier series. Multiple time instances are used to solve the UVLM in the frequency domain and two formulations are proposed. The first approach solves directly the Fourier coefficients with an augmented influence matrix containing all the time instances. The second approach solves independently each time instance in the time domain and the Fourier coefficients are computed through a discrete Fourier transform. The procedure is repeated until the solution of each time instance converges. The Spectral convergence and accuracy were demonstrated over three different non-linear dynamic problems with increasing difficulty. It was shown for each test case that the HB VLM converges to the UVLM time domain solution, thus providing the same level of accuracy, but with a significant reduction in computational cost.

The HB VLM shows great potential for aeroelastic simulations with capabilities of mod-

eling large deflection with non-linear effects. Since the system is still solved in the time domain using the same kernels, a viscous coupling method using high-fidelity data could be implemented with minimal changes to the original algorithm. These viscous corrections could provide additional modeling capabilities to include transonic effects and boundary layer separation. A methodology to include these corrections into the HB VLM is presented next.

CHAPTER 6 VISCOUS AND COMPRESSIBLE CORRECTIONS

The UVLM has been extended to the non-linear frequency domain using the harmonic balance approach, which is now referred to as HB VLM. The HB VLM can model nonlinear dynamics much more efficiently, but it is still limited to incompressible and irrotational attached flows. Corrections are needed to include viscous and compressible effects. This chapter first presents a coupling algorithm that has been widely used with the VLM to improve its modeling capabilities by using high-fidelity sectional data. Afterward, an extension of the algorithm for unsteady solutions is proposed, along with a numerical verification performed for heaving and pitching airfoils/wings with comparison against high-fidelity unsteady Euler/RANS solutions.

6.1 Coupling algorithm

In this section, the steady coupling algorithm using high-fidelity data is described. The methodology is based on a correction of the local angle of attack to match the local lift coefficient between the VLM and the computed database using a high-fidelity flow solver. It is an iterative process that can be summarized as follows

1. Solve the linear system to obtain $\mathbf{\Gamma}$ and compute $C_{l_{inviscid}}$ for every section
2. For every spanwise section, compute the effective angle of attack α_e

$$\alpha_e = \frac{C_{l_{inviscid}}}{2\pi} - \alpha_{local} + \alpha_{3D} \tag{6.1}$$

3. Interpolate the corresponding C_l in the associated database with α_e
4. Update the local angle of attack

$$\alpha_{local} = \alpha_{local} + \frac{C_l - C_{l_{inviscid}}}{2\pi} \tag{6.2}$$

5. Update the local angle of attack in the RHS and repeat until the lift coefficient is converged for a given tolerance value ϵ

$$||C_{l_{inviscid}} - C_{l_{viscous}}||_2 < \epsilon \tag{6.3}$$

The iterative process is also illustrated in Figure 6.1. In Equation 6.1 and 6.30, α_{local} is the sum of the local correction $\Delta\alpha$ and the freestream angle of attack α_{3D}.

$$\alpha_{local} = \alpha_{3D} + \Delta\alpha \tag{6.4}$$

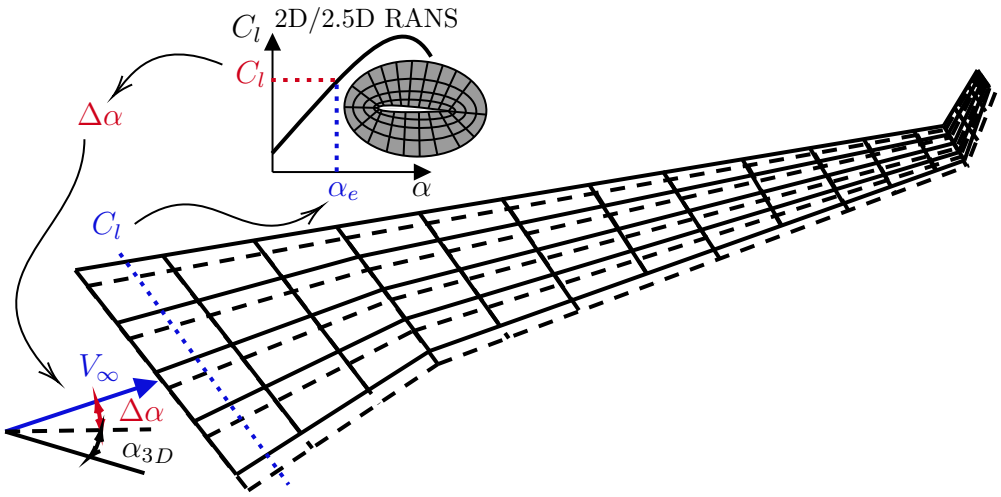

Figure 6.1 Coupling algorithm between a stripwise section of the wing with a database.

The coupling algorithm is defined such that for a local correction in the angle of attack $\Delta\alpha$, the inviscid lift coefficient is equal to a given lift coefficient computed with a higher fidelity solver. Hence, using thin-airfoil theory, the lift coefficient for the section is defined as

$$C_{l_{inviscid}} = C_{l_{visc}} = 2\pi(\alpha - \alpha_i + \Delta\alpha) \tag{6.5}$$

where $C_{l_{inviscid}}$ is the computed lift from the VLM and $C_{l_{visc}}$ is the computed lift using higher fidelity tools. Equation 6.5 is represented graphically in Figure 6.2. Additionally, using the definition of effective angle of attack

$$\alpha_e = \alpha - \alpha_i \tag{6.6}$$

Equation 6.5 is redefined as

$$\alpha_e = \frac{C_{l_{inv}}}{2\pi} - \Delta\alpha \tag{6.7}$$

which corresponds to Equation 6.1 in the coupling algorithm. The effective angle of attack is therefore computed iteratively until $C_{l_{inv}} = C_{l_{visc}}$ for a given tolerance. This formulation is efficient, since the induced angle of attack does not need to be computed explicitly.

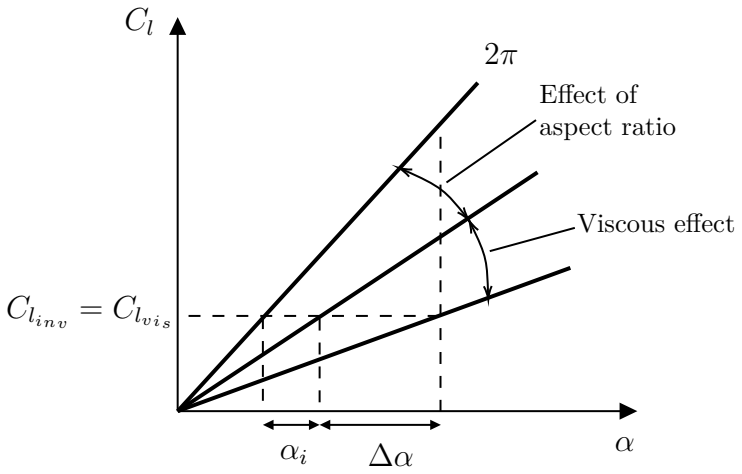

Figure 6.2 Representation of the correction angle of attack.

6.1.1 Coupling with infinite swept wing data

The coupling algorithm defined previously is intended for pure 2D sectional data that does not include cross-flow effects. Although several authors[76, 81] have discussed the treatment of 2.5D and the interpretation of the downwash within lifting-line methods, there are still small yet important differences in their treatment. Here, the problem is revisited using analytical swept wing theory that shed novel lights.

For swept wings, the cross-flow component plays an important role in regards of flow separation and compressibility. Indeed, the flow physics over the wing cannot be accurately modeled without accounting for these effects. To demonstrate the compressibility effect with the sweep angle, the lift-curve slope is computed for a NACA 0012 in inviscid conditions for a range of Mach numbers from 0.2 to 0.85. Figure 6.3 presents the lift-curve slope as a function of Mach number for three sweep angles: 0° (2D), 15° and 30°. These results are computed in inviscid conditions. The effect of cross-flow becomes significant as the sweep angle increases and as the Mach number increases as well. At a Mach number of 0.85, the 2D lift-curve slope is roughly two times higher than the lift-curve slope with a sweep of 30°.

Consequently, when treating swept wings in a compressible flow, the cross-flow must be included in order for the physics to be modeled accurately. The effect of sweep also affects the boundary layer. The surface flow solution over a 2D and 2.5D NACA 0012 is presented in Figure 6.4 with the skin friction lines. It clearly shows that the flow physics is highly impacted by the sweep angle. Indeed, the transonic shock position is much more upstream for the solution with a sweep angle. Furthermore, the solution with zero sweeps has a shock induced separation, while the skin friction lines for the solution with sweep shows a fully

attached flow.

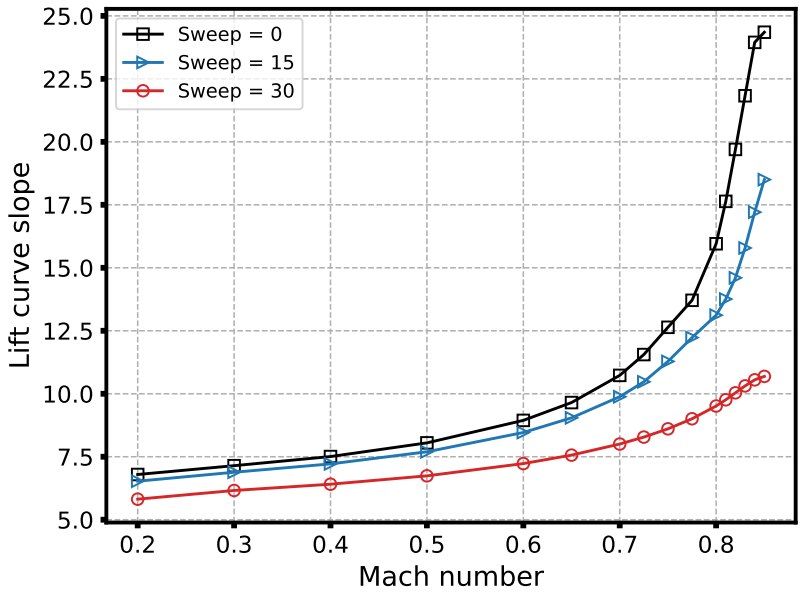

Figure 6.3 Effect of sweep over the lift-curve slope of a NACA0012 in inviscid conditions.

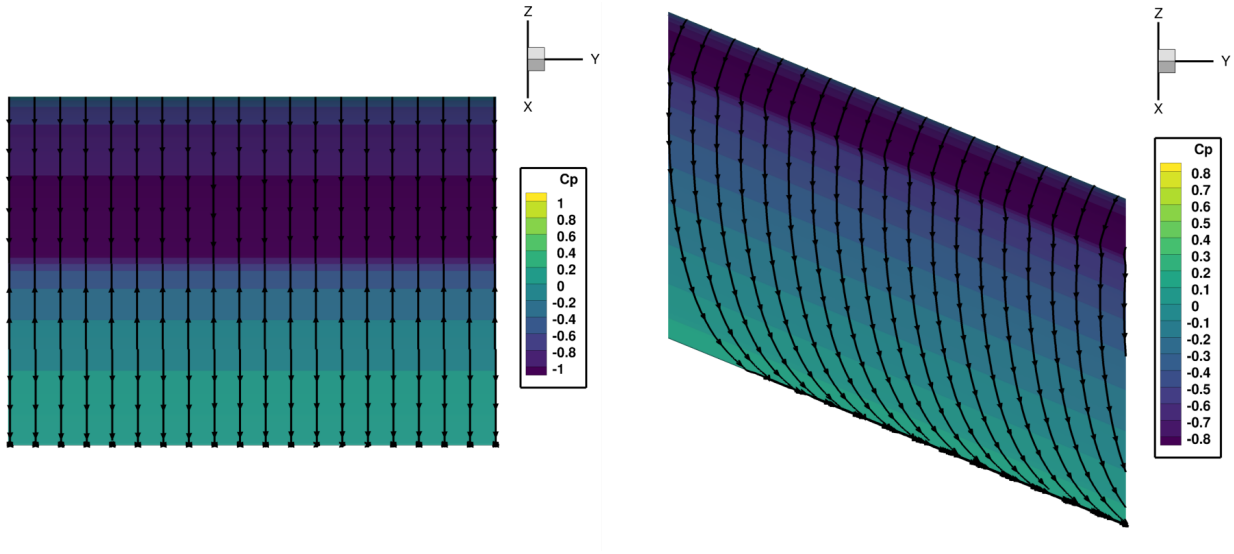

(a) Sweep = 0°

(b) Sweep = 30°

Figure 6.4 Effect of sweep over the surface flow solution for a NACA0012 at Mach = 0.8, Reynolds = 1M and AoA = 1.5°. Skin friction lines are shown in black.

The infinite swept wing condition is related to the geometry and velocity as depicted in Figure 6.5. Using the sweep angle ϕ, the freestream vector is decomposed into a cross-flow

component $V_{\parallel}$ and a normal flow component $V_{\perp}$.

$$V_{\perp} = V_{\infty} \cos \phi \tag{6.8}$$

$$V_{\parallel} = V_{\infty} \sin \phi \tag{6.9}$$

For an infinitely swept wing, the parallel flow component does not see any changes in geometry. Thus, any derivative in the y' direction is equal to zero.

$$\frac{\partial()}{\partial y'} = 0 \tag{6.10}$$

This condition can be used to solve the 2.5D solution using a two-dimensional flow solver[82], where the flow is solved in the transformed frame of reference x'-y'. Therefore, only the normal flow component $V_{\perp}$ sees an airfoil, which explains why the sweep angle can reduced significantly any compressibility effect, since the effective Mach number seen by the wing is reduced by $\cos \phi$.

$$Mach_{\perp} = Mach_{\infty} \cos \phi \tag{6.11}$$

The flow solution depends only on the projected normal airfoil geometry, which has higher thickness and higher camber than the streamwise geometry. The projected normal chord is therefore also related to the streamwise chord by the sweep angle

$$c_{\perp} = c \cos \phi \tag{6.12}$$

These differences translate in different lift, drag and moment values between the 2D and 2.5D solution. The final VLM solution will therefore be affected by whether a 2D of 2.5D solution is used for the sectional corrections.

However, the coupling algorithm presented previously is incompatible with infinite swept wing data. To demonstrate this incompatibility, the lifting-line theory derived[119, 120, 121] for infinite swept wings is used. The lift-curve slope at any given section is represented by

$$C_{l_{\alpha}} = 2\pi \frac{\cos \phi}{\sin \pi n_0} \frac{2n}{1 - \pi n(\cot \pi n - \cot \pi n_0)} \tag{6.13}$$

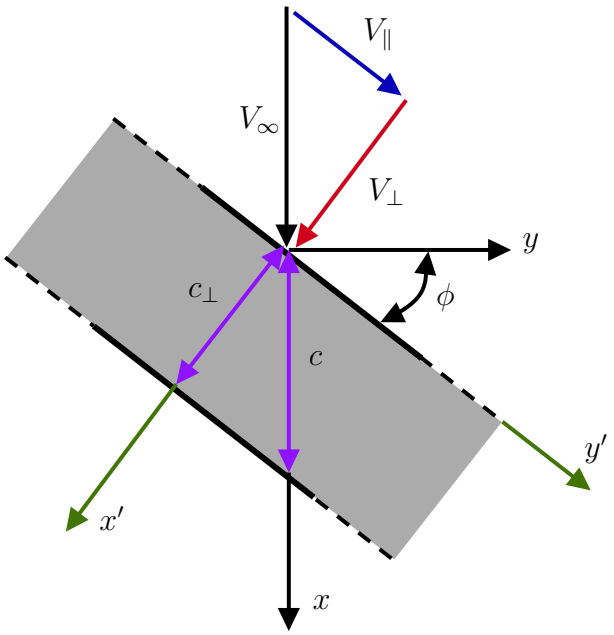

Figure 6.5 Geometry and velocity relation for an infinite swept wing.

For an infinitely swept wing, $n = n_0 = \frac{1}{2}$ and the lift-curve slope becomes

$$C_{l_\alpha} = 2\pi \cos\phi \tag{6.14}$$

The change in sectional lift-curve slope can be seen as a change in the effective angle of attack[119, 120]. If the effective AoA of a section is related to the sectional lift as

$$\alpha_e = \frac{C_l}{2\pi} \tag{6.15}$$

then the effective AoA in the section normal to the sweep is

$$\alpha_{e_\perp} = \frac{C_l}{C_{l_{\alpha\perp}}} = \frac{C_l}{2\pi \cos\phi} \tag{6.16}$$

and

$$\frac{\alpha_e}{\alpha_{e_\perp}} = \frac{2\pi \cos\phi}{2\pi} \rightarrow \alpha_e = \alpha_{e_\perp} \cos\phi \tag{6.17}$$

In other words, the computed database using the infinite swept wing condition will include the effect of sweep in the effective angle of attack. However, the effect of sweep over α_e is

also included by the VLM model. Consequently, if 2.5D sectional data is used directly with the coupling algorithm presented previously, the effect of sweep will be accounted for twice. To demonstrate this, a constant chord 30° swept wing is used with a semi-span of 5.0 and an aspect ratio of 10.0. The database used for sectional corrections is generated using the thin airfoil theory (lift-curve slope of 2π). Since the VLM collocation point position are derived to provide a slope of 2π in 2D, the solution using sectional corrections provides the exact same solution as the standard VLM, see Figure 6.6. However, if an infinite swept wing database is used instead ($2\pi\cos(\phi)$), the solution is not equal to the standard VLM as shown in Figure 6.6, where the computed spanload is well underestimated. This difference is explained by the effective AoA used in the coupling algorithm to interpolate the lift coefficient from the database. It requires modification to exclude the effect of sweep, since the infinite swept wing aerodynamic database already includes the effect of sweep. Therefore, the induced angle of attack from the sweep must be defined and subtracted from Equation 6.7.

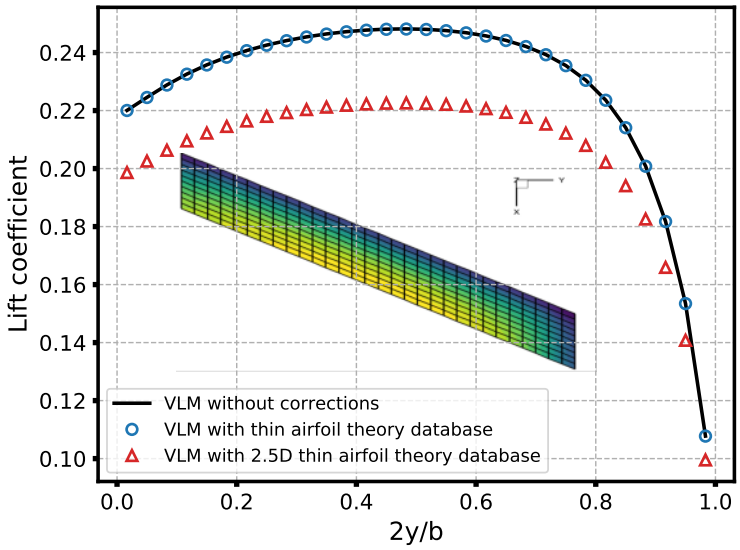

Figure 6.6 Spanload for a 30° swept wing computed with the VLM and using theoretical database as corrections with original coupling algorithm.

Using thin airfoil theory, the induced AoA from sweep is defined as

$$\alpha_{i_{sweep}} = \frac{C_l - C_{l_{2.5D}}}{2\pi} \tag{6.18}$$

and with $C_{l_{2.5D}} = 2\pi\cos\phi$, it becomes

$$\alpha_{i_{sweep}} = \alpha_e(1 - \cos\phi) \tag{6.19}$$

With the definition of $\alpha_{i_{sweep}}$, Equation 6.5 is redefined as

$$C_{l_{inv}} = C_{l_{visc}} = 2\pi(\alpha_e - \alpha_{i_{sweep}} + \Delta\alpha) \tag{6.20}$$

which becomes

$$\alpha_e = \left[\frac{C_{l_{inv}}}{2\pi} - \Delta\alpha\right] \cdot \frac{1}{cos\phi} \tag{6.21}$$

The modified α_e, Equation 6.21, is then simply replaced in the coupling algorithm. Note that if $\phi = 0$, the original formulation is retrieved. Therefore, with Equation 6.21, the coupling algorithm is general for any sectional data, with or without sweep. If the spanload for the 30° swept wing is computed using the modified coupling algorithm, the solution is now exact with the standard VLM as expected, see Figure 6.7.

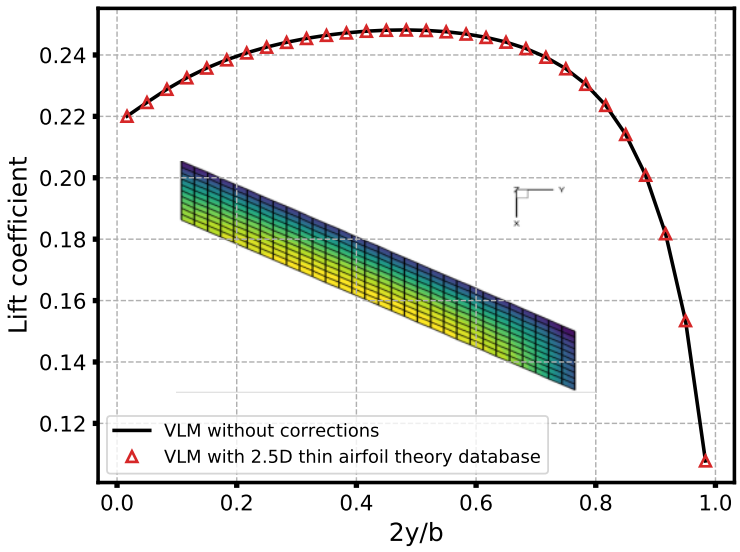

Figure 6.7 Spanload for a 30° swept wing computed with the VLM and using 2.5D theoretical database as corrections with modified coupling algorithm.

6.2 Steady compressibility correction

Even though some compressibility is incorporated through the computed database, the VLM must also incorporate compressibility corrections in its formulation to yield to correct distribution of effective angle of attack when the Mach number increases. This is accomplished with the Prandtl-Glauert compressibility correction. The Prandtl-Glauert equation is ob-

tained from the small-disturbance transonic equation, by removing nonlinear terms, which yields

$$(1 - M_\infty^2)\phi_{xx} + \phi_{yy} + \phi_{zz} = 0 \tag{6.22}$$

The Laplace equation is retrieved by applying the Prandlt-Glauert (PG) transformation to Equation 6.22, which is defined as

$$\begin{Bmatrix} \bar{x} \\ \bar{y} \\ \bar{z} \end{Bmatrix} = \begin{Bmatrix} x \\ \beta y \\ \beta z \end{Bmatrix} \tag{6.23}$$

where

$$\beta = \sqrt{1 - M_\infty^2} \tag{6.24}$$

The PG transformation converts the compressible problem into an incompressible one (Laplace's equation),

$$\phi_{\bar{x}\bar{x}} + \phi_{\bar{y}\bar{y}} + \phi_{\bar{z}\bar{z}} = 0 \tag{6.25}$$

which can be solved by the standard VLM. The transformed geometry is shrunken in the y and z direction, thus reducing geometric angles and the aspect ratio. Finally, when the transformed problem has been solved, the final compressible circulation Γ is retrieved by converting back from the transformed problem as follows

$$\Gamma = \frac{\bar{\Gamma}}{\beta^2} \tag{6.26}$$

The PG transformation is suited only for subsonic speeds, below the critical Mach number. However, the use of high-fidelity sectional data coupled with the PG transformation enables the VLM to compute transonic solution, but the coupling algorithm presented previously requires a minor modification due to the PG transformation.

The effective angle of attack formulation in the coupling algorithm, Equation 6.21, is based on incompressible thin airfoil theory, thus a slope of 2π is used, which is the actual slope for a vortex ring with the *1/4-3/4* rule. However, this is no longer true with the PG transformation. Fortunately, the PG compressibility correction in 2D simplifies to

$$C_{l_{\alpha,comp}} = \frac{C_{l_{\alpha,incomp}}}{\beta} \tag{6.27}$$

and the evaluation of α_e becomes

$$\alpha_e = \left[\frac{C_{l_{inv}}}{2\pi/\beta} - \Delta\alpha\right] \cdot \frac{1}{cos\phi} \tag{6.28}$$

With Equation 6.28, the coupling algorithm is now compatible with the compressible solution computed by the VLM using the PG transformation. The nonlinear process is therefore summarized as follows

1. Compute a steady 2.5D RANS database (α, C_l, C_d, C_m) for a given airfoil geometry, sweep angle ϕ, Mach number and Reynolds number.
2. Apply the Prandtl-Glauert Transformation for a given M_∞ (Equation 6.25)
3. Solve the transformed linear system to obtain $\bar{\Gamma}$
4. Apply the reverse transformation to obtain the compressible circulation (Equation 6.26)
5. For every spanwise section, compute $C_{l_{inviscid}}$ and the effective angle of attack

$$\alpha_e = \left[\frac{C_{l_{inv}}}{2\pi/\beta} - \Delta\alpha\right] \cdot \frac{1}{cos\phi} \tag{6.29}$$

6. Interpolate the corresponding C_l in the associated database with α_e
7. Update the local angle of attack

$$\alpha_{local} = \alpha_{local} + \frac{C_l - C_{l_{inviscid}}}{2\pi/\beta} \tag{6.30}$$

8. Update the local AoA in the RHS and repeat until the lift coefficient is converged for a given tolerance value (ϵ)

$$||C_{l_{inviscid}} - C_l||_2 < \epsilon \tag{6.31}$$

To demonstrate the VLM's fidelity with the coupling process using 2.5D sectional data, a simple constant chord NACA0012 wing is used with an aspect ratio of 10 and a sweep angle of 30°. The lift-curve slope is computed for different Mach numbers and compared against RANS solutions from CHAMPS in Figure 6.8. The VLM compares well against CHAMPS,

the compressibility effect is well captured. Furthermore, the predicted maximum angle of attack is also in good agreement with CHAMPS. The overall lift coefficient is well predicted by the VLM and the load distribution along the span is also well predicted, as depicted in Figure 6.9. For the spanload result, a slightly more realistic wing is used with a taper ration of 0.5 and with a twist distribution of 4° at the root and −4° at the tip. Again, the VLM compares well against 3D RANS and a stalled section of the wing is even captured at an angle of attack of 9°, albeit at a more inboard position.

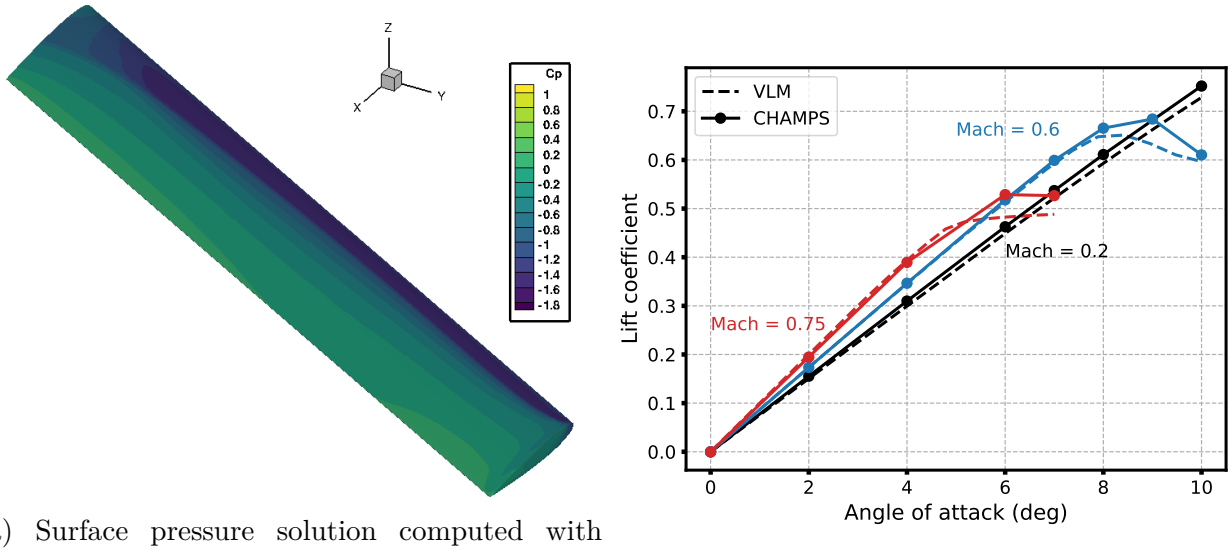

(a) Surface pressure solution computed with CHAMPS at AoA = 6.0°

(b) Lift coefficient as a function of angle of attack

Figure 6.8 NACA0012 wing, Reynolds = 1M.

6.3 Pitching moment correction

The coupling algorithm applies corrections to the lift, but not for the pitching moment. Since thin lifting surface methods cannot provide accurate predictions of the pitching moment and that the aerodynamic moment has a strong influence over the aeroelastic response, a second correction is required. This is a topic addressed by Mukherjee et al. [79] and Mukherjee and Gopalarathnam [80] via a decambering approach, but in this work the chordwise distribution of circulation is scaled to match the pitching moment from the computed database. This is an under-determined problem since they are two equations, one for the lift and one for the pitching moment, but there are many values of circulation along the chord depending on the chordwise discretization. In this framework, the scaling factors for the circulation values are solved using a least square approach and the under-determined system is defined for every

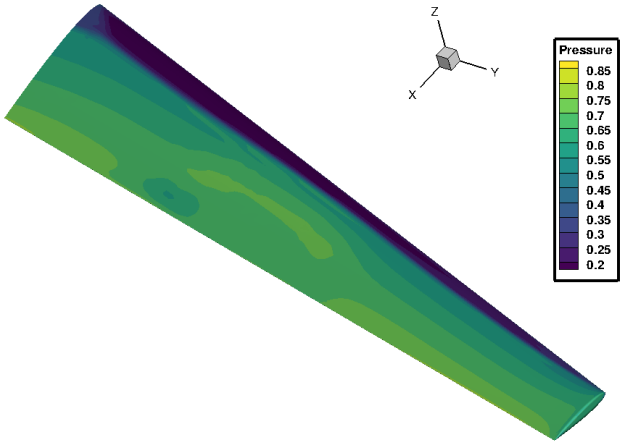

(a) Surface pressure solution computed with CHAMPS at AoA = 9.0°

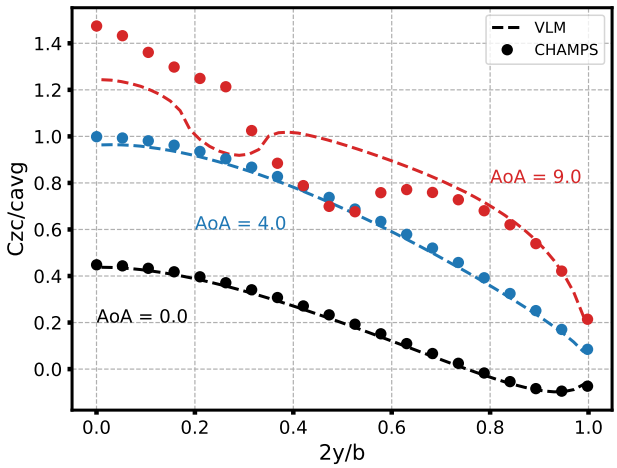

(b) Spanload

Figure 6.9 NACA0012 wing at Mach = 0.60 and Reynolds = 1M.

spanwise section as

$$\begin{pmatrix} \rho\Gamma_1(\boldsymbol{U}_1 \times \boldsymbol{dl}_1) & \rho\Gamma_2(\boldsymbol{U}_2 \times \boldsymbol{dl}_2) & \dots & \rho\Gamma_j(\boldsymbol{U}_j \times \boldsymbol{dl}_j) \\ \rho\Gamma_1(\boldsymbol{U}_1 \times \boldsymbol{dl}_1) \times \boldsymbol{r} & \rho\Gamma_2(\boldsymbol{U}_2 \times \boldsymbol{dl}_2) \times \boldsymbol{r} & \dots & \rho\Gamma_j(\boldsymbol{U}_j \times \boldsymbol{dl}_j) \times \boldsymbol{r} \end{pmatrix} \begin{pmatrix} 1+\epsilon_1 \\ 1+\epsilon_2 \\ \vdots \\ 1+\epsilon_j \end{pmatrix} = \begin{pmatrix} L \\ M_{1/4c} \end{pmatrix} \tag{6.32}$$

where j is the number of chordwise panel and $\boldsymbol{r}$ is the distance between the midpoint of the vortex segment and the section quarter-chord point. Equation 6.32 is solved for $(1+\epsilon_j)$, which are the scaling values to match the lift and moment from the computed database represented by L and $M_{1/4c}$ respectively. The scaling term is defined as $(1+\epsilon_j)$ to minimize changes to the VLM solution[68]. Note that the pitching moment correction is applied after the initial coupling algorithm on the lift is converged. The correction creates a camber effect and if it is performed within the iterative coupling scheme, it would induce a numerical error in the evaluation of the effective angle of attack, since the zero-lift AoA is assumed to be zero.

The chordwise distribution of the VLM coupled with sectional data from a NACA 0012 is presented in Figure 6.10 with and without the pitching moment correction. The solutions presented in Figure 6.10 show that the pitching moment correction applies minimal and smooth changes to the local circulation as expected. Additionally, the pitching moment as

a function of angle of attack for the 30° swept NACA 0012 wing is compared against the RANS solution of CHAMPS in Figure 6.11. The VLM solution with the pitching moment correction provides an accurate evaluation of the pitching moment.

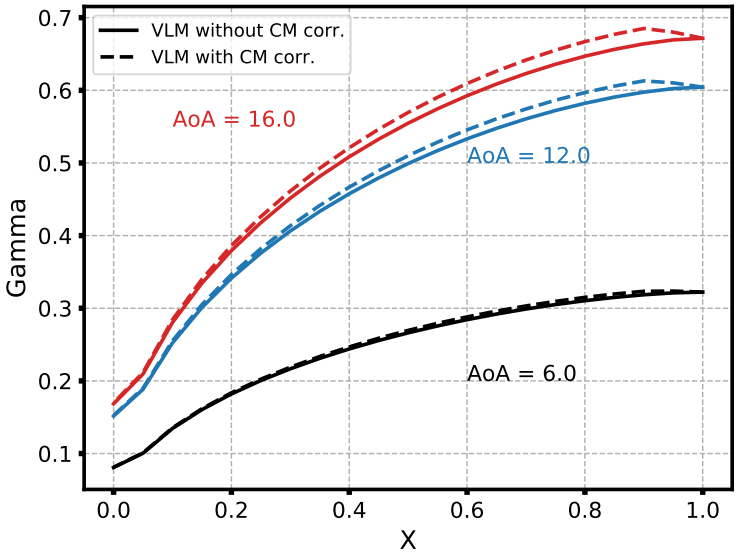

Figure 6.10 Impact of pitching moment correction over the circulation Γ chordwise distribution for a 2D NACA0012 at Mach = 0.2 and Reynolds = 1M.

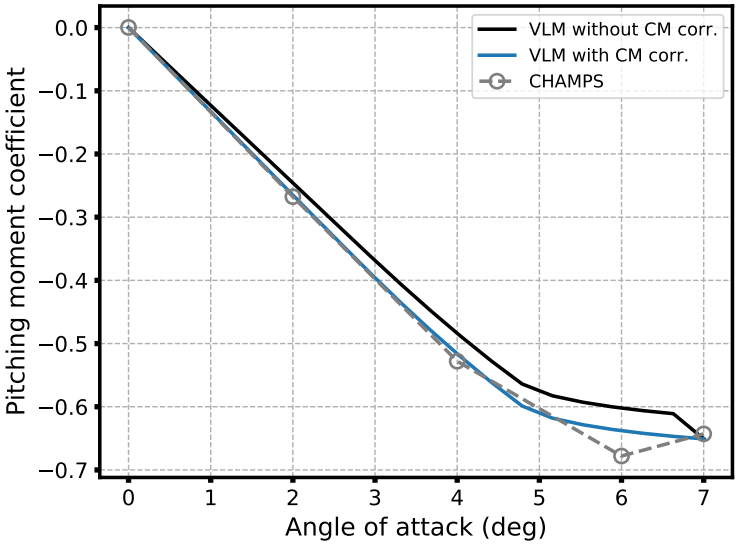

Figure 6.11 Pitching moment correction for a 30° swept NACA0012 wing at Mach = 0.75 and Reynolds = 1M.

6.3.1 Unsteady extension

The steady coupling algorithm previously defined can be extended to an unsteady simulation without any modifications. The Kutta-Joukowski formulation of lift is quasi-steady by nature, thus when computing the sectional lift coefficient, unsteady effects due to the wing motion and the wake are included. Since the high-fidelity database remains steady, the coupling algorithm holds under the quasi-steady assumption, thus for reduced frequency under approximately 0.1. However, it will be shown in Section 6.5 that accurate results are still achieved for higher reduced frequencies. Note that the evaluation of the sectional lift coefficient for the coupling algorithm must exclude the time derivative term $d\Gamma/dt$. Since the high-fidelity data is steady, it is computed once and can be used for any motion and any reduced frequencies thereby providing flexibility and efficiency. A fully unsteady coupling algorithm using unsteady data has been developed[122], providing higher non-linear modeling capabilities such as dynamic stall. However, a new database is required for different motions and different reduced frequencies requiring many expensive high-fidelity 2D unsteady solutions. In this work, a flexible and fast turnaround tool is sought; thus the quasi-steady formulation is used. These quasi-steady corrections provide some form of compressibility, but the unsteady compressibility effect is missing from the potential kernel, which has a significant impact over the aerodynamic response. In Section 6.4, the unsteady compressibility effect is introduced in the HB VLM kernel by means of an approximation of the retarded time.

Furthermore, the pitching moment correction cannot be performed within the unsteady simulation. The scaling values are precomputed in steady conditions, because the high-fidelity data is steady. If the correction is computed in unsteady conditions, it would yield incorrect values for the moment since the effect of induced velocities from structural motion would be neglected. This limitation is imposed by the steady nature of the high-fidelity data used for sectional corrections. Consequently, the unsteady pitching moment will be less accurate since the VLM does not yield accurate solutions for moments, due to the absence of thickness. Even though a steady correction for the moment is included, the unsteady part remains uncorrected. This limitation, however, enables greater flexibility by keeping the high-fidelity database steady.

6.4 Unsteady compressibility

For the VLM, steady compressible effects are modeled with the Prandtl-Glauert transformation and it is accurate for subsonic speed below the critical Mach number. For unsteady

compressible flow, the PG transformation is not sufficient and an additional correction is required in the form of a time lag.

The linearized subsonic potential equation is derived from the Transonic Small Disturbance (TSD) equation[123] by omitting the nonlinear terms resulting in the following equation

$$(1 - M_\infty^2)\boldsymbol{\phi}_{xx} + \boldsymbol{\phi}_{yy} + \boldsymbol{\phi}_{zz} = \frac{2M_\infty^2}{U_\infty}\boldsymbol{\phi}_{xt} + \frac{M_\infty^2}{U_\infty^2}\boldsymbol{\phi}_{tt} \tag{6.33}$$

The left-hand side of Equation 6.33 corresponds to the steady Prandtl-Glauert equation. For unsteady compressible flows, the PG transformation remains a good approximation of Equation 6.33 for moderate Mach numbers and moderate reduced frequencies[124]. However, for higher fidelity, the time lag effect must be accounted for. If small disturbance is assumed, the linear compressible wave equation is expressed in terms of small potential as

$$\nabla^2\boldsymbol{\phi} = \frac{1}{a_\infty^2}\frac{\partial^2\boldsymbol{\phi}}{\partial t^2} \tag{6.34}$$

A fundamental solution to Equation 6.34 is given by the disturbance due to a stationary point source as follows[125]

$$\boldsymbol{\phi}(x, y, z, t) = -\frac{1}{4\pi r} f\Big(t - \frac{r}{a_\infty}\Big) \tag{6.35}$$

where f represents the fluctuation of strength with time at a distance r from the source. Equation 6.35 indicates that a perturbation is felt only after a certain time delay, $\frac{r}{a_\infty}$, also known as the retarded time[56]. Consequently, time and space are coupled together as the Mach number increases and the Lorentz transformation[67, 125] is involved in the derivation process. If a moving source is considered along with a Galilean transformation of the flow field coordinates moving with the freestream, the potential becomes

$$\boldsymbol{\phi}_s(r, t) = -\frac{1}{4\pi R} f(t - \tau) \tag{6.36}$$

where

$$R = \sqrt{(x - \xi)^2 + \beta^2(y - \eta)^2 + \beta^2(z - \zeta)^2} \tag{6.37}$$

and the retarded time τ is expressed as

$$\tau = \frac{-M^2(x - \xi) + MR}{V_\infty \beta^2} \tag{6.38}$$

where M represents the Mach number. The acceleration doublet potential of the DLM

is derived from Equation 6.34 and includes directly the expression of the retarded time. Unfortunately, the VLM cannot integrate into its kernel the retarded time, thus rendering vortex methods inadequate for compressible unsteady flows. However, it will be shown that it is possible to include an approximation of the retarded time that improves significantly the solution for unsteady compressible flows. Note that this formulation assumes that the freestream is aligned with the x axis.

Since a periodic flow is considered, the expression of retarded time can be incorporated in the HB formulation of the UVLM directly as a lag term

$$\boldsymbol{A} \sum_{n=-N}^{N} \hat{\boldsymbol{\Gamma}} \cdot e^{j\omega n(t-\tau)} + \boldsymbol{B} \sum_{n=-N}^{N} \hat{\boldsymbol{\Gamma}} \cdot e^{j\omega n(t-(i+1)\Delta t-\tau)} + \sum_{n=-N}^{N} \hat{\boldsymbol{V}} \cdot e^{j\omega nt} = 0 \tag{6.39}$$

However, the lag term includes a distance between the point at which the influence is to be computed and the position of the perturbation. For a vortex ring, this influence is a sum of the 4 vortex segments. Therefore, when computing the influence of a vortex ring, a different value of τ must be computed for each vortex segment and included in the various terms of the Fourier series, where the vortex segment midpoint is used as an approximation for the position in space (ξ, η, ζ) of the perturbation, see Figure 6.12. For example, the influence of panel j on panel i is expressed as

$$I = \sum_{s=1}^{4} A_{ij}^{s} \Big[a_0^{(j)} + \sum_{n=1}^{N} (a_n^{(j)} cos(\omega n(t-\tau_s) + b_n^{(j)} sin(\omega n(t-\tau_s)) \Big] \tag{6.40}$$

where s defines a segment of the vortex ring and A_{ij} is the standard influence computed with Biot-Savart.

To summarize the framework, the steady Prandtl-Glauert transformation is applied to the UVLM along with the retarded time to include compressibility effects. Moreover, sectional data computed with higher-fidelity is iteratively coupled with the various sections of the wing. It will be shown in the following sections that these corrections altogether provide superior modeling capabilities to include the effects of compressibility, airfoil thickness, viscosity and flow separation for both swept and unswept wings.

6.5 Numerical verification against URANS

The numerical verification is performed in 2D and 3D. For the 2D verification, a pitching NACA 0012 is used for different reduced frequencies and different Mach numbers. For the 3D verification, a constant chord NACA 0012 wing with a 30° sweep is used. The wing has

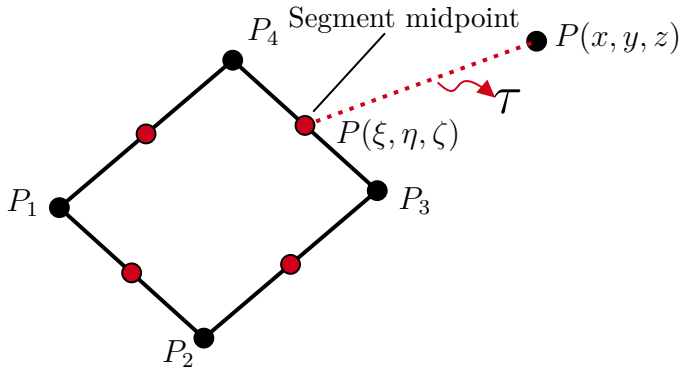

Figure 6.12 Illustration of the computation of the retarded time.

an aspect ratio of 10 and the solution for a pitching motion is compared at three different reduced frequencies (0.1, 0.2 and 0.3) and four different Mach numbers (0.2, 0.5, 0.6 and 0.7). CHAMPS[93] is used to generate the high-fidelity unsteady solutions and the steady 2D/2.5D data used for the sectional corrections of the HB VLM. The Spalart-Allmaras turbulence model[126] is used for the simulation in viscous conditions and a dual time stepping approach[127] with a second order backward difference scheme is used for the time domain Euler/RANS solutions. One thousand steps per period is also used for the time domain solution with at least four periods simulated to ensure a converged periodic solution. Details on the computational grids are given in Appendix C.

6.5.1 2D pitching wing

In this section, the harmonic balance VLM with sectional corrections and with the retarded time formulation is verified against Euler and RANS time domain solutions computed with CHAMPS for a 2° amplitude pitching airfoil around the quarter-chord point. For the HB VLM, the 2D cases are performed by using a wing of very high aspect ratio (> 1000) and with a discretization of 5 panels along the span. The HB VLM mesh has 15 panels chordwise and the wake is discretized accordingly.

First, the lift coefficient as a function of angle of attack is compared for a reduced frequency of 0.1 at a Mach number of 0.6 in inviscid conditions. The results are presented in Figure 6.13. The first solution of the HB-VLM in blue is incompressible, while the other two have the PG transformation and the retarded time respectively. All three solutions from the HB VLM are without sectional corrections and they are compared against the time domain Euler solution of CHAMPS. The steady PG correction gives a better evaluation of the slope, but the hysteresis is not captured, while the addition of the retarded time gives a solution

comparable to CHAMPS. However, the overall slope is slightly underestimated along with the hysteresis. The effect of thickness is not included, thus by adding sectional corrections using a steady database for the same NACA 0012 at the same conditions, the computed lift coefficient is improved when compared to CHAMPS, see Figure 6.14. Indeed, the hysteresis is well captured, but the slope is slightly overestimated. Nonetheless, an accurate result is achieved with the addition of these three corrections.

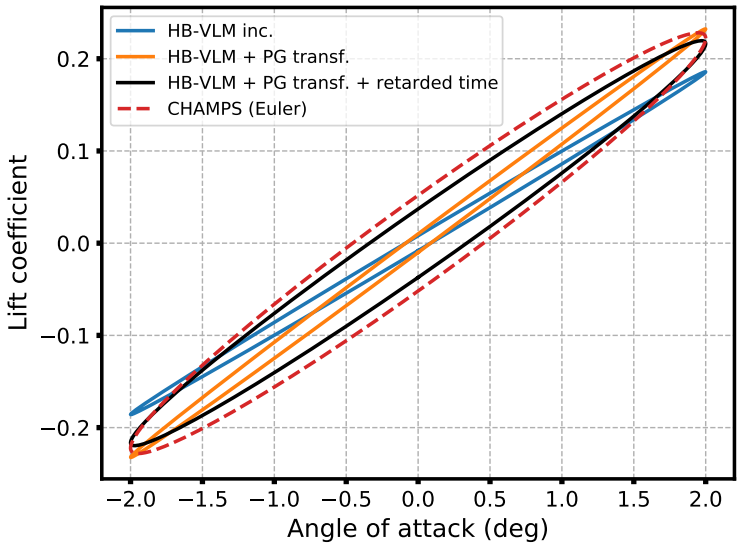

Figure 6.13 Effect of compressibility for a 2° amplitude pitching NACA 0012 airfoil.

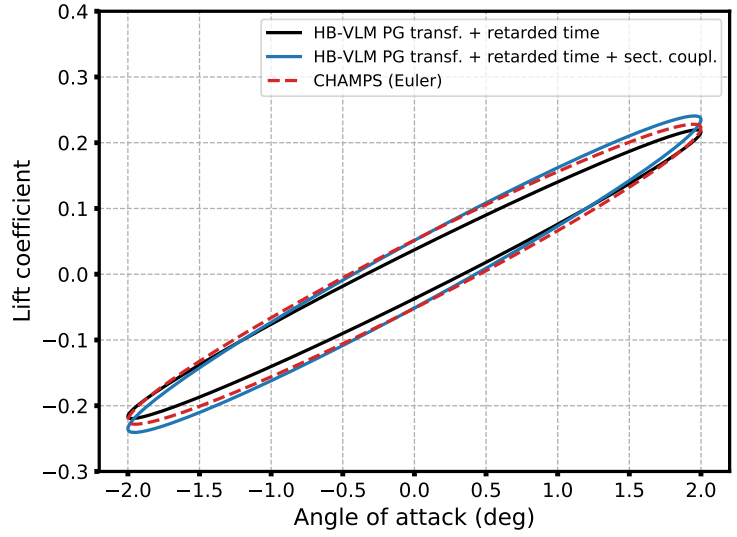

Figure 6.14 2° amplitude pitching NACA 0012 airfoil with sectional corrections.

For unsteady solutions, the slope and hysteresis are two important features that characterize

the aerodynamic response of pitching airfoils and these two characteristics are easier to analyze using complex numbers. Indeed, if the unsteady lift coefficient is represented in terms of a complex amplitude for the first harmonic, the real part represents the slope and the imaginary part represents the hysteresis.

Figure 6.15 compares both the real and imaginary parts of the lift for the first harmonic between the HB VLM with all three corrections and the Euler solution computed with CHAMPS for various reduced frequencies and various Mach numbers. Note that for the reminder of the paper, the harmonic balance VLM with all three corrections will be referred to as NonLinear HB VLM (NL-HB VLM). For the low Mach numbers of 0.2 and 0.4, the NL-HB VLM solution compares well with the Euler solution for all reduced frequencies, thus showing that the quasi-steady sectional corrections provide accurate results even at a high reduced frequency of 0.3. However, as the Mach number increases, the real part of the lift is overestimated by the NL-HB VLM. Nonetheless, the overall trend in terms of reduced frequencies is still well captured at a Mach number of 0.75.

For the imaginary part, the negative peak value appearing at a reduced frequency of around 0.07 is slightly underestimated as the Mach number increases. Moreover, at a Mach number of 0.75, the imaginary response from the NL-HB VLM deviates significantly from the Euler solution at a reduced frequency 0.2 and higher. Since the sectional corrections are quasi-steady and that the retarded time is approximated, the NL-HB VLM is expected to lose accuracy as the flow conditions approach the critical Mach number. Figure 6.17 shows the Euler solution at a Mach number of 0.75 and a reduced frequency of 0.3 where a transonic shock appears in the solution. Nonetheless, these results show that the NL-HB VLM is capable of capturing the global unsteady aerodynamic response of a NACA 0012 for moderate reduced frequencies and Mach numbers. The sensitivity due to the number of panels along the chord is presented in Figure 6.16 showing that 15 panels are sufficient to represent the real and imaginary solution of the lift.

To demonstrate the impact of the retarded time over the unsteady solution, the real and imaginary part of the lift are compared for the same conditions as in Figure 6.15, but with and without the addition of the retarded time. These results are presented in Figure 6.18 and clearly shows that even for a low Mach number of 0.4, the retarded time plays a critical role in the unsteady aerodynamic response for both the real and imaginary parts. At a Mach number of 0.75, the difference is significant when the retarded time is not included. Consequently, even though the retarded time is approximated using the vortex segment midpoint, its influence improves significantly the compressible solution.

Before viscous effects are introduced, the pitching moment is investigated. The same analysis

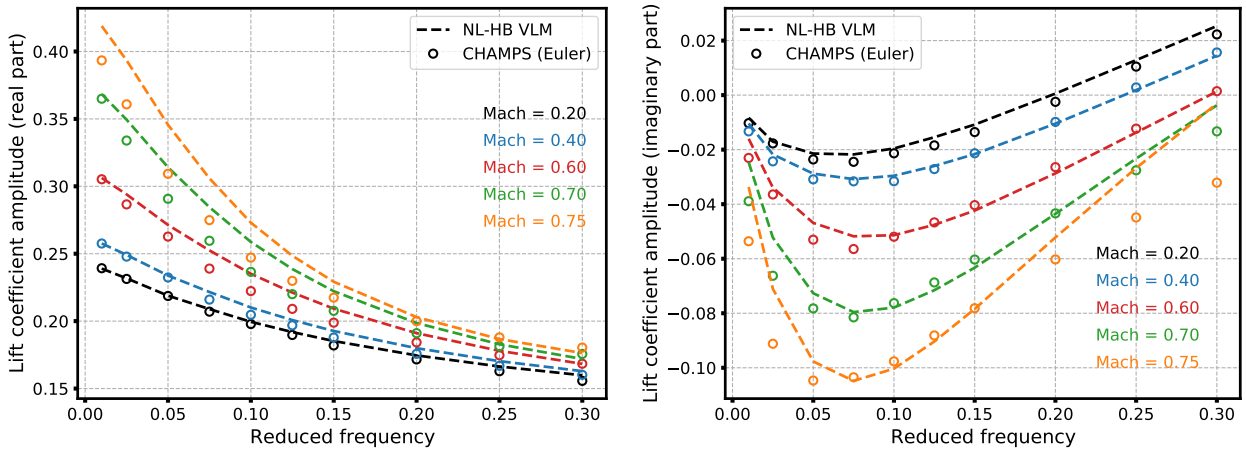

(a) Real part (b) Imaginary part

Figure 6.15 Complex amplitude for the first harmonic of lift in inviscid conditions for a 2° amplitude pitching NACA 0012.

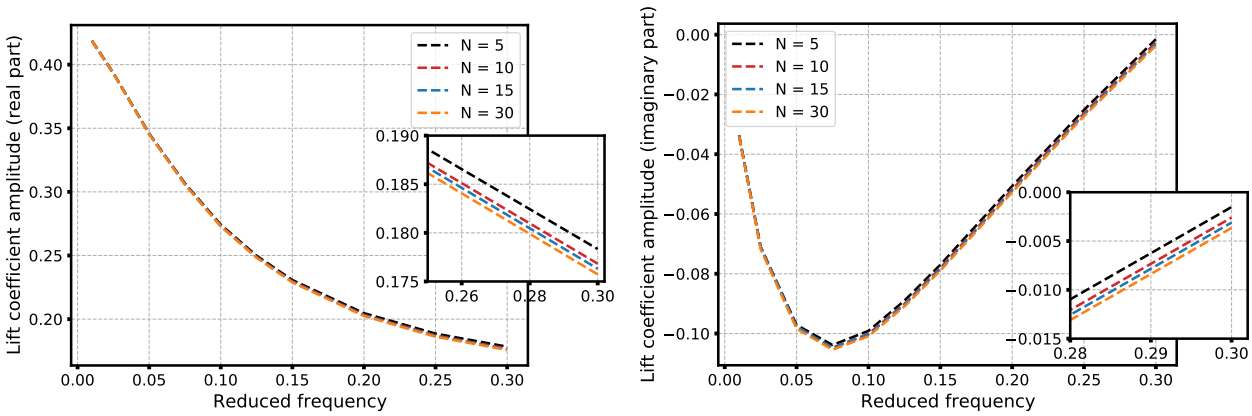

(a) Real part (b) Imaginary part

Figure 6.16 Chordwise panel convergence at Mach = 0.750.

is performed for the real and imaginary of the pitching moment in inviscid conditions, see Figure 6.19. As mentioned in Section 6.3.1, the unsteady pitching motion is expected to be less accurate due to the limitation of the quasi-steady correction and the absence of thickness in the VLM model. Indeed, the results show that the NL-HB VLM cannot compute accurately the unsteady pitching moment for Mach numbers higher than 0.7. At a Mach number of 0.75, they are important discrepancies that are most likely due to the presence of a transonic shock as shown in Figure 6.17, which is not captured by the NL-HB VLM. Nonetheless, the

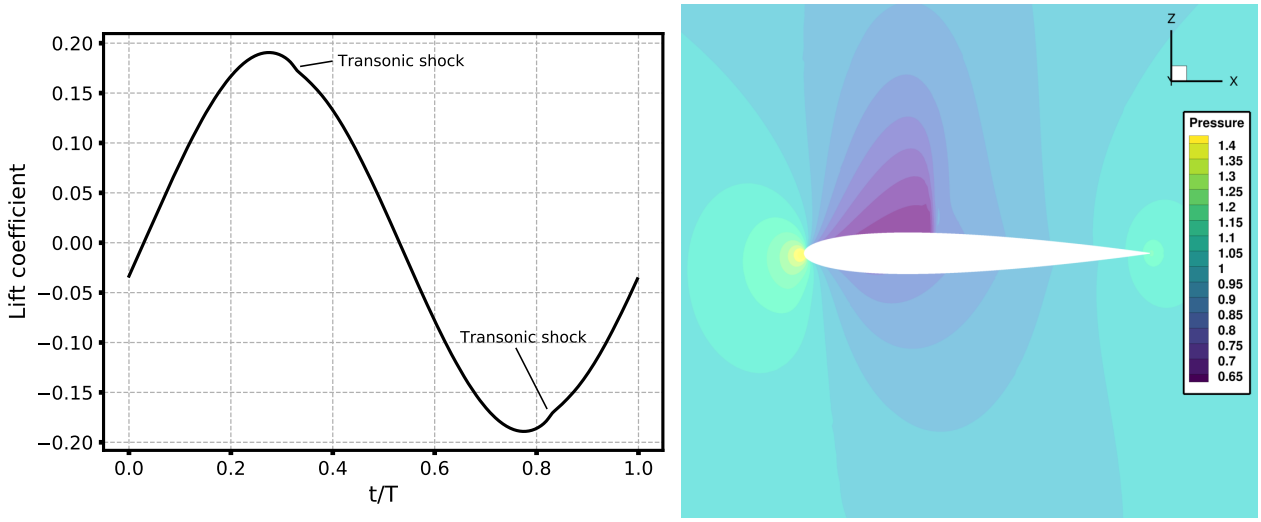

(a) Lift coefficient (b) Flow solution at t/T = 0.33

Figure 6.17 Euler solution at Mach = 0.75 and k = 0.3.

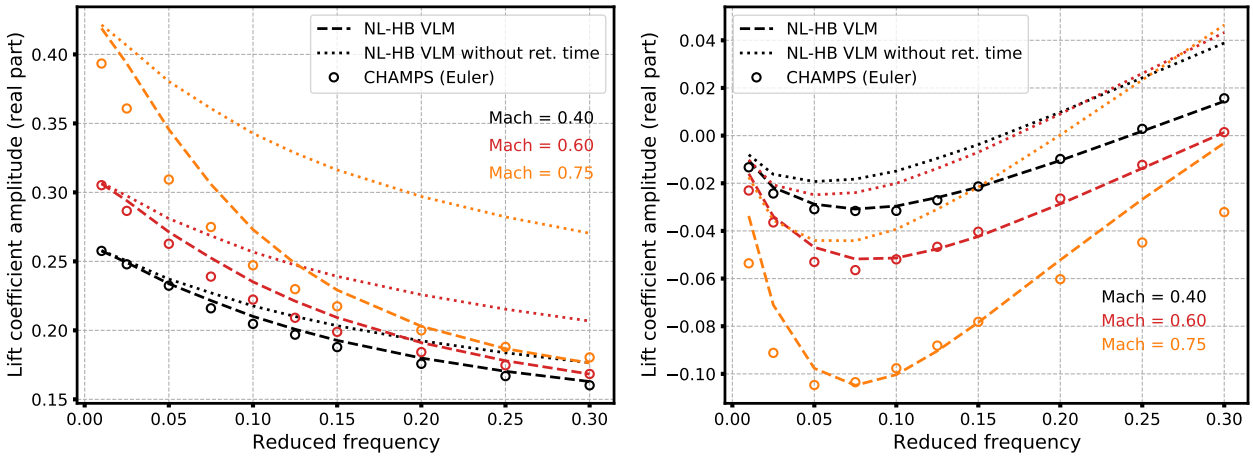

(a) Real part (b) Imaginary part

Figure 6.18 Effect of the retarded time on the unsteady solution for a 2° amplitude pitching NACA 0012 in inviscid conditions.

overall pitching moment as a function of reduced frequency is still well captured for the lower Mach and it will be shown in Chapter 7 that this is sufficient to capture non-linear flutter boundaries.

Previous results were performed in inviscid conditions, but viscous effects are now considered through the sectional data in a fully turbulent condition using the Spalart-Allmaras turbulence model with a Reynolds number set to one million. For the NL-HB VLM, only the

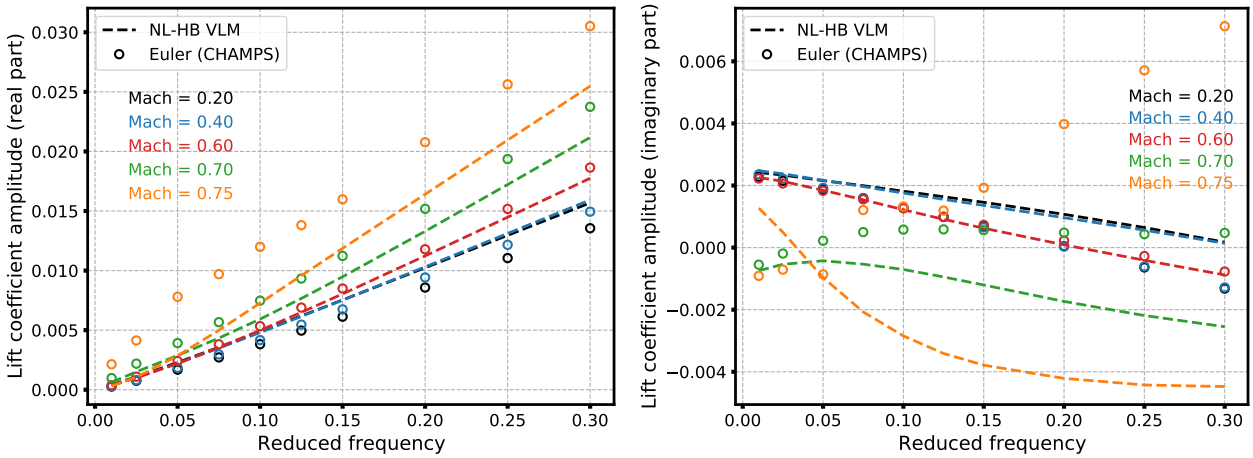

(a) Real part

(b) Imaginary part

Figure 6.19 Amplitude of first harmonic for the pitching moment in inviscid conditions for a pitching motion.

database used for sectional corrections is changed with data computed in viscous conditions. The real and imaginary part of the lift are presented in Figure 6.20. The same trend is observed, where the real part of the lift compares well against the unsteady RANS solution. However, an offset is observed for the imaginary part of the lift, but the effect of reduced frequency and compressibility are well captured. The same solutions are presented again in Figure 6.21, but in terms of difference in lift using the solution at a Mach number of 0.2 as reference. For the imaginary part, the difference in lift due to Mach number is well captured by the NL-HB VLM when compared to CHAMPS, thus confirming that the sensitivity to compressibility is accurate within the NL-HB VLM. However, the error is important at a Mach number of 0.75 and a reduced frequency of 0.3, thus showing the limits of the proposed approach.

The NL-HB VLM's sensitivity to the airfoil's geometry is also verified by performing the same pitching motion on a NACA 4412, thus the same thickness but with a nonzero camber. The solution is again compared with high-fidelity at a Mach number of 0.6 and a reduced frequency of 0.1, see Figure 6.22. The solution for the NACA 4412 is similar than the NACA 0012 in terms of amplitude and hysteresis and compares well with CHAMPS. However, the difference in the mean lift coefficient due to camber estimated by the NL-HB VLM is underestimated by 3% when compared to the high-fidelity solution. The mean lift coefficient for the NACA 4412 is estimated at 0.521 for the NL-HB VLM and at 0.537 for CHAMPS.

The error between the NL-HB VLM and the time domain high-fidelity solutions is examined

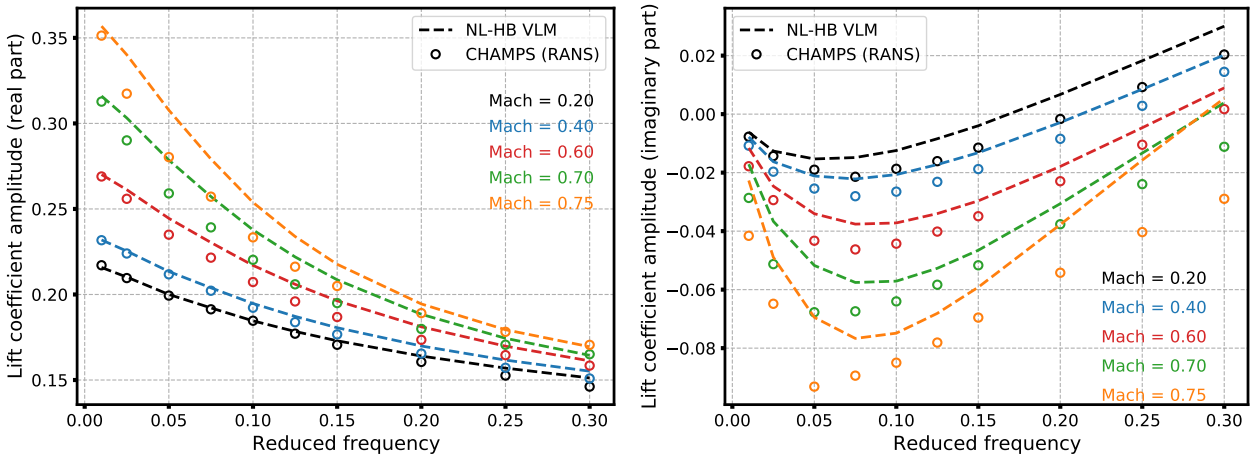

(a) Real part

(b) Imaginary part

Figure 6.20 Complex amplitude for the first harmonic of lift in viscous conditions at a Reynolds number of 1M for a 2° amplitude pitching motion.

for the real and imaginary part of the lift and for every Mach number. For example, the error on the real part of the lift is computed as follows

$$\{RMS(Error)\}_{\mathrm{Re}} = \left\{ \sqrt{\sum_{k=1}^{N} \frac{(C_{l,k}^{\mathrm{VLM}} - C_{l,k}^{\mathrm{CHAMPS}})^2}{N}} \right\}_{\mathrm{Re}} \tag{6.41}$$

where the maximum value of the high-fidelity solution is taken as reference and N is the number of reduced frequencies. The errors for inviscid and viscous conditions as a function of Mach number are shown in Figure 6.23. The error behaves similarly as a function of Mach number for the real and imaginary part. For a Mach number below 0.6, the error is smaller than 0.01 for both inviscid and viscous conditions. Using the average real lift coefficient of CHAMPS at a Mach number of 0.6 as reference, it translates to an error of about 4.8%. Even though the error becomes more important at higher Mach numbers, it remains acceptable in view of the fact that the sectional corrections are performed with steady data only.

The last 2D case is again a pitching NACA 0012, but at a high mean angle of attack near the stall point. These conditions are chosen to demonstrate the capabilities of the NL-HB VLM to capture nonlinear aerodynamics and its spectral convergence as well. The mean angle of attack is 15° and the amplitude is 1°. The database used for sectional corrections is shown in Figure 6.24 along with the unsteady solution computed with the NL-HB VLM. At 15°, in steady conditions, the NACA 0012 is near the maximum angle of attack, which induces an unsteady nonlinear aerodynamic response through the coupling algorithm. As shown in

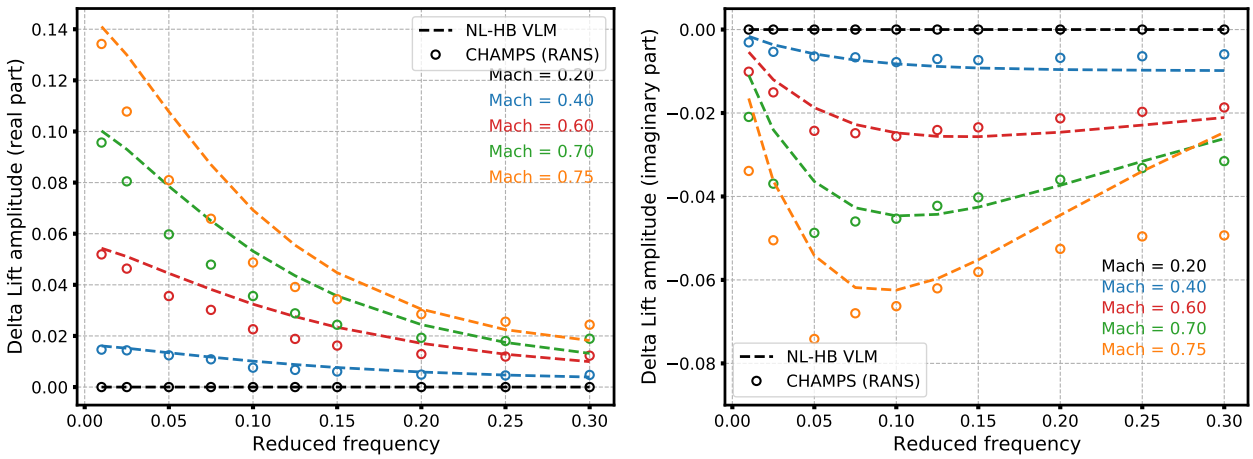

(a) Real part (b) Imaginary part

Figure 6.21 Difference of lift in viscous conditions at a Reynolds number of 1M for a 2° amplitude pitching motion. The solution at a Mach number of 0.2 is taken as reference.

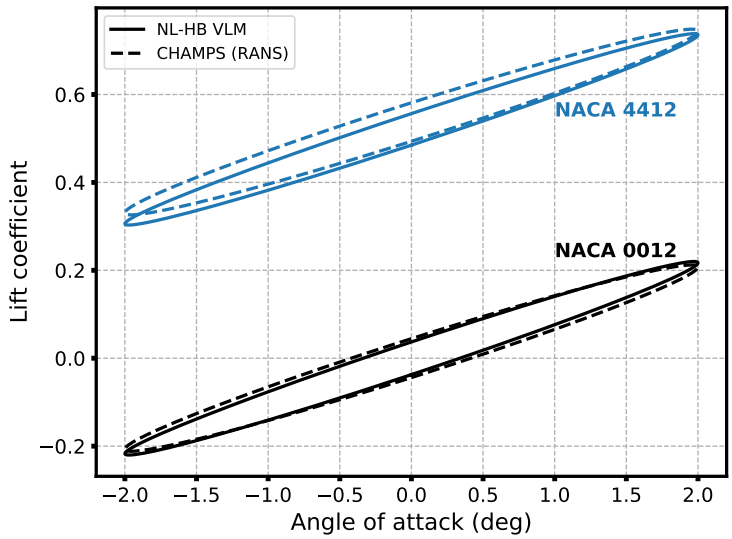

Figure 6.22 Pitching NACA 4412 in viscous conditions at a Reynolds number of 1M for a 2° amplitude pitching motion at a Mach number of 0.6 and at a reduced frequency of 0.1.

Figure 6.24, more than 6 harmonics are necessary to obtain a converge solution, thereby showing that the NL-HB VLM is capable of capturing nonlinear effects from flow separation.

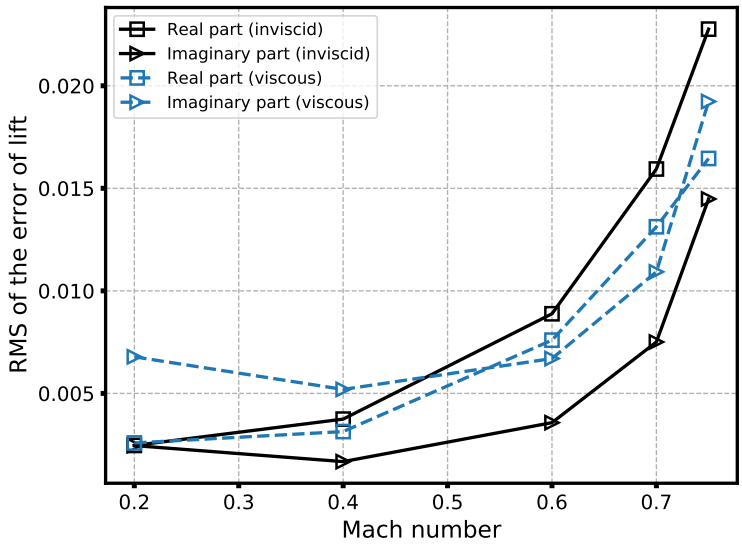

Figure 6.23 RMS error of the real and imaginary part of the lift in inviscid and viscous conditions using the high-fidelity solutions as reference for the NACA 0012 with a 2° amplitude pitching motion.

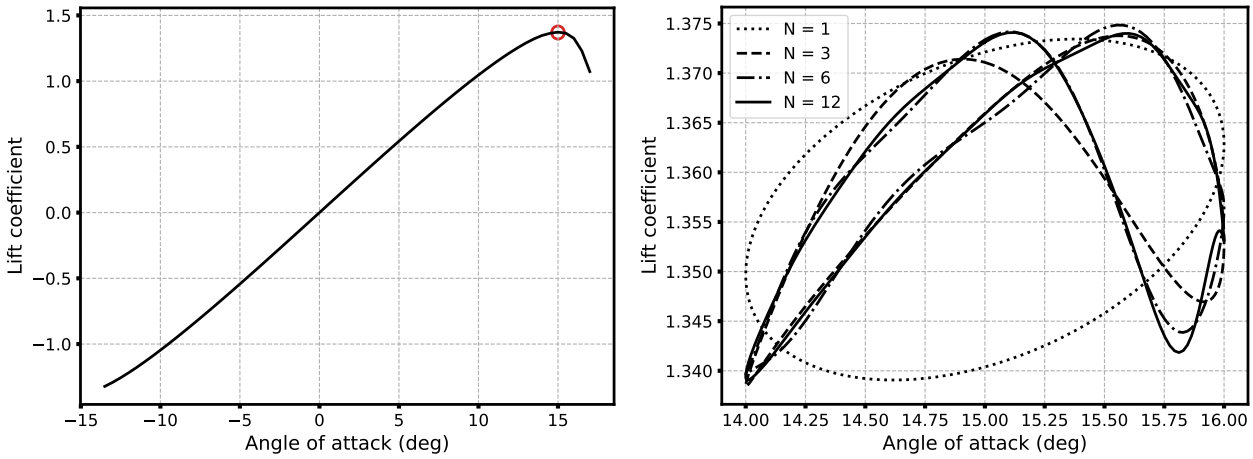

(a) Steady lift coefficient used as corrections

(b) Spectral convergence of the HB VLM

Figure 6.24 Pitching NACA 0012 at a mean angle of attack of 15° at a Mach number of 0.2 and a Reynolds number of 1M.

6.5.2 Infinite swept wing conditions

The NL-HB VLM has been verified in 2D against Euler and RANS unsteady solutions. The next verification is performed on an infinite swept wing (2.5D) to verify that the approximated retarded time is also accurate in these conditions, where compressibility is particularly

affected when the geometry is swept. The verification is performed again for various reduced frequencies and various Mach numbers on the NACA 0012, but for a heaving motion of $0.2\frac{h}{c}$ amplitude and an infinite wing with a sweep angle of 30°. The steady database used for corrections is also generated in 2.5D for a sweep angle of 30°. The real and imaginary part of the first harmonic for the lift coefficient are compared in Figure 6.25. The results show that the Mach number used to compute the compressibility correction and the retarded time should take into account the sweep angle. Indeed, the Mach number normal to the sweep line, $\text{Mach}_\perp$ should be used. The impact of the chosen Mach number is clearly seen on the real part of the lift, where results using $\text{Mach}_\perp$ provide a more accurate solution when compared to high-fidelity models. For the imaginary part, the effect of using $\text{Mach}_\perp$ becomes significant at a Mach number of 0.7 and for reduced frequencies higher than 0.1.

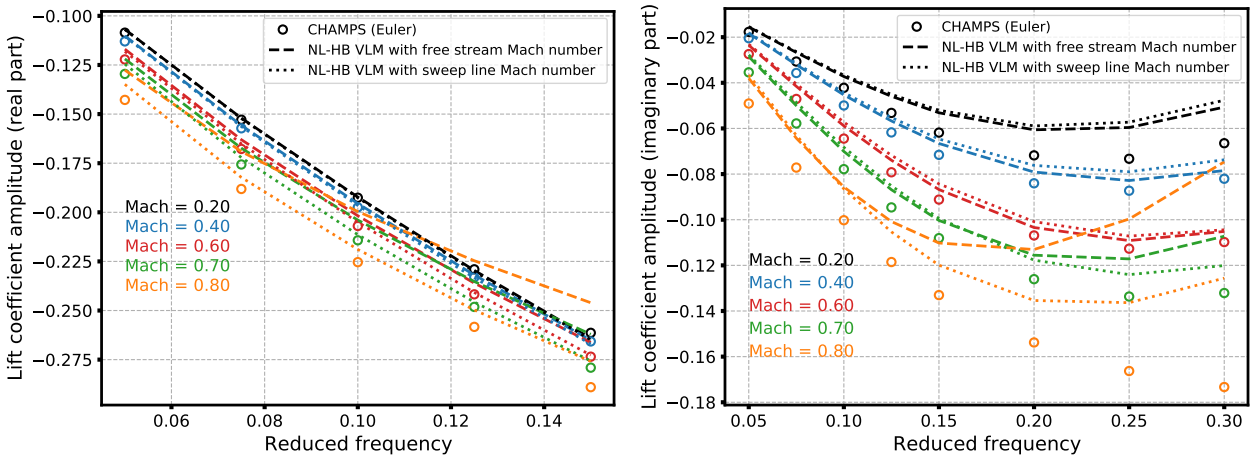

(a) Real part

(b) Imaginary part

Figure 6.25 Complex amplitude for the first harmonic of lift in inviscid conditions for infinite swept wing conditions with a 30° sweep and a heaving motion.

6.5.3 3D pitching wing

The 3D case is a constant chord NACA 0012 wing with a 30° sweep and an aspect ratio of 10, see Figure 6.26. The wing is pitching at a mean angle of attack of 0° with a 2° amplitude. The wing is pitching around the y axis at the quarter chord point of the root. The NL-HB VLM is compared against CHAMPS in viscous conditions at a Reynolds number of 1M at three different reduced frequencies (0.1, 0.2 and 0.3) and at four different Mach numbers (0.2, 0.4, 0.6 and 0.7). The standard Sparlart-Allmaras turbulence model is used and the results for the lift and pitching moment are presented in Figure 6.27 and 6.28 respectively.

Details on the computational grid are given in Appendix C. For the NL-HB VLM, the wing is discretized with 15 panels along the chord and 50 panels along the span. The wake is discretized using the wing's TE spacing with 100 chord length.

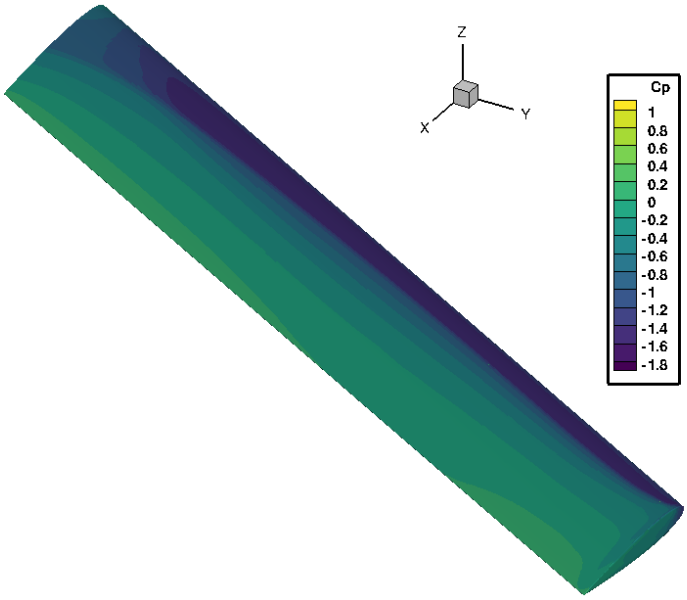

Figure 6.26 Surface solution for the NACA 0012 wing at a Mach number of 0.6 computed with CHAMPS.

The 3D results are consistent with the 2D results, where the NL-HB VLM compares well with the high-fidelity solutions, especially at lower Mach numbers and lower reduced frequencies. As the Mach number increases with the reduced frequency, the amplitude of the lift response is underestimated. However, the effect of reduced frequency over the hysteresis is well captured, even for the higher Mach number of 0.7. Moreover, the root mean square of the error on the lift coefficient is shown in Figure 6.29. The RMS is computed using 200 points equally spaced along the periodic solution of the lift. Even at a Mach number of 0.7 and at a reduced frequency of 0.3, the error remains under 0.009. To further highlight the importance of retarded time for unsteady compressible flows, the solution without retarded time is shown in Figure 6.30 for a Mach number of 0.6. The retarded time has a strong impact over the hysteresis, which corresponds to the imaginary part of the complex amplitude of lift. The amplitude is, however, well captured at the lower reduced frequencies without the retarded time. These results indicate that the steady PG transformation along with the quasi-steady corrections remains accurate for moderate Mach numbers and reduced frequencies, which is consistent with the findings of [124]. However, it confirms that the retarded time is critical for an improved compressible solution.

As long as the nonlinear effects due to transonic conditions are not too strong, the NL-HB

VLM is capable of providing accurate results comparable to high-fidelity and more than two orders of magnitude faster as well. Table 6.1 presents a comparison of the overall compute time and the required computing resources for the NL-HB VLM and time domain URANS solution. In this comparison, the generation of the steady database for the NL-HB VLM is not included since it is computed once per Mach number and it can be used for any motion and any reduced frequency. The URANS simulations are performed in the time domain; thus four periods must be computed in order to obtain a fully converged periodic solution, which explains the much higher compute time. A frequency domain solver would reduce significantly the compute time, but the NL-HB VLM would still be more than two orders of magnitude faster. Additionally, the NL-HB VLM requires only a single desktop while a 3D URANS simulation demands larger computing resources to achieve acceptable compute times. The CPU cost of the 3D URANS solution is 4 orders more expensive on a per-core basis, even assuming near 100% scaling capabilities for the URANS solver as demonstrated in [93].

Table 6.1 Comparison of overall compute time for the NACA 0012 wing pitching motion.

	NL-HB VLM	3D URANS
Mesh generation	< 1 sec.	~ 30 min.
Solving process	~ 15 sec.	~ 5 hr.
CPU	Intel i9-9900K (8 cores)	Intel Xeon Skylake (56 cores)
# of CPU	1	2

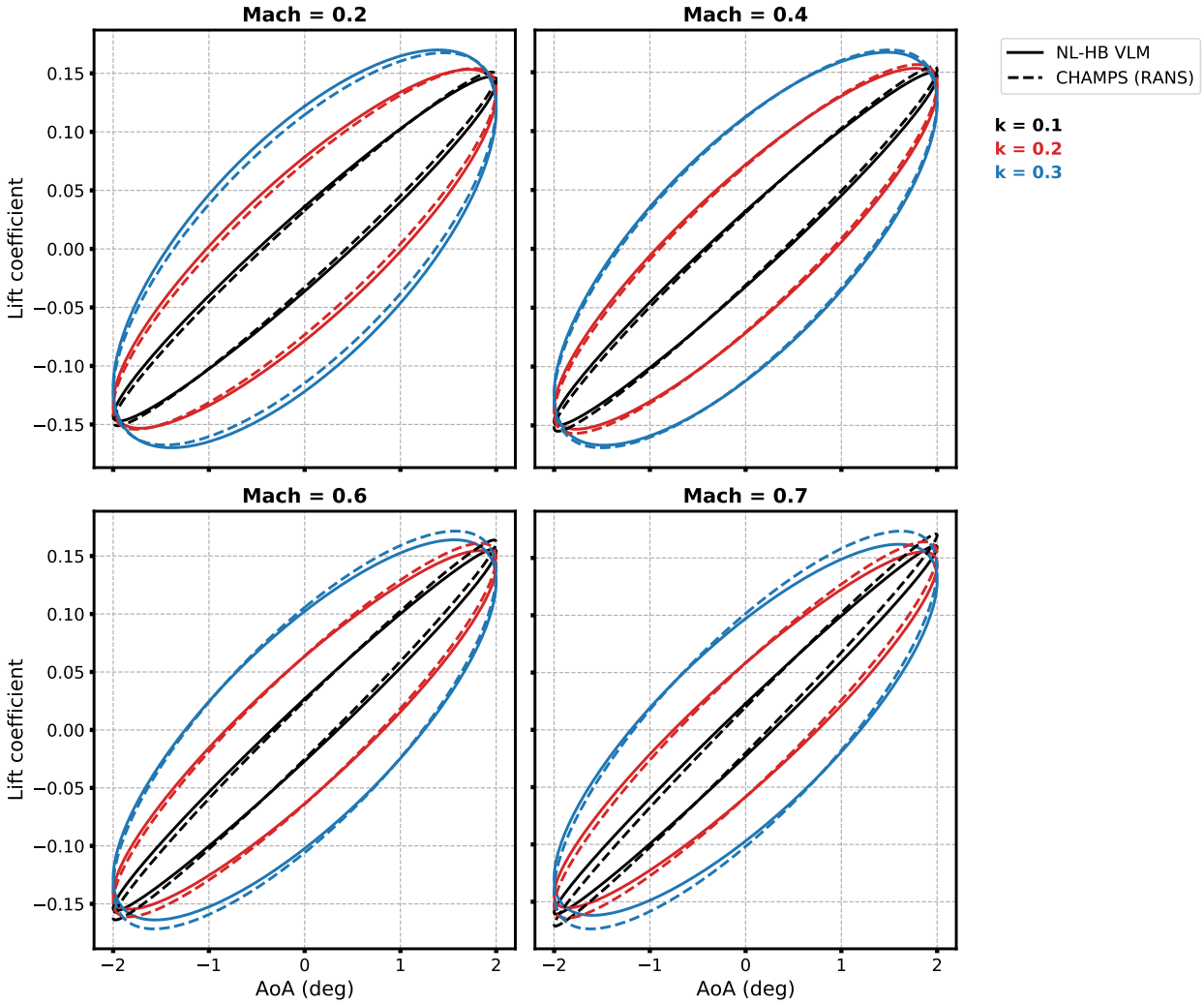

Figure 6.27 Lift coefficient for a pitching NACA 0012 30° swept wing at a Reynolds number of 1M.

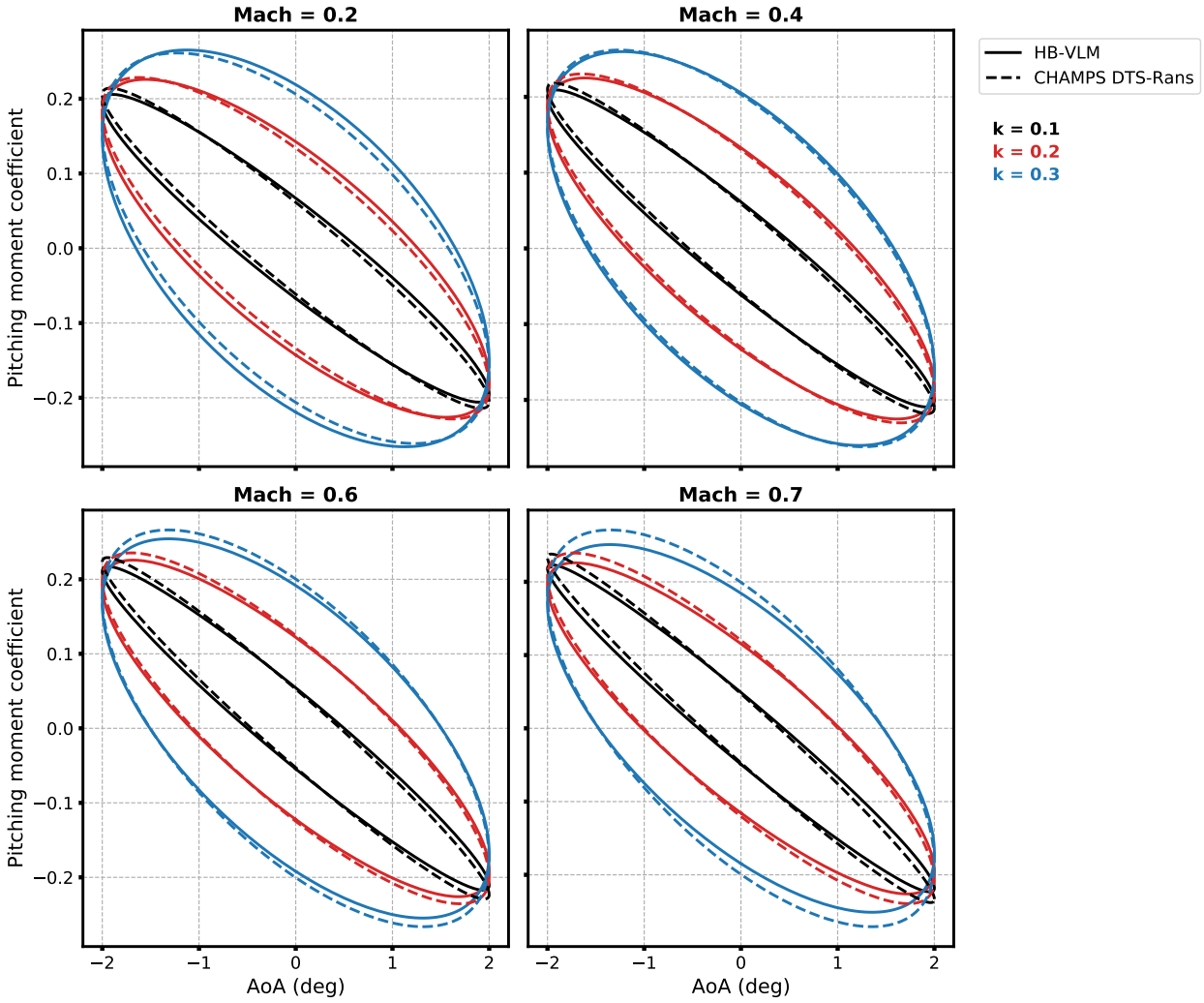

Figure 6.28 Pitching moment coefficient for a harmonically pitching NACA0012 30° swept wing at Reynolds = 1.0.

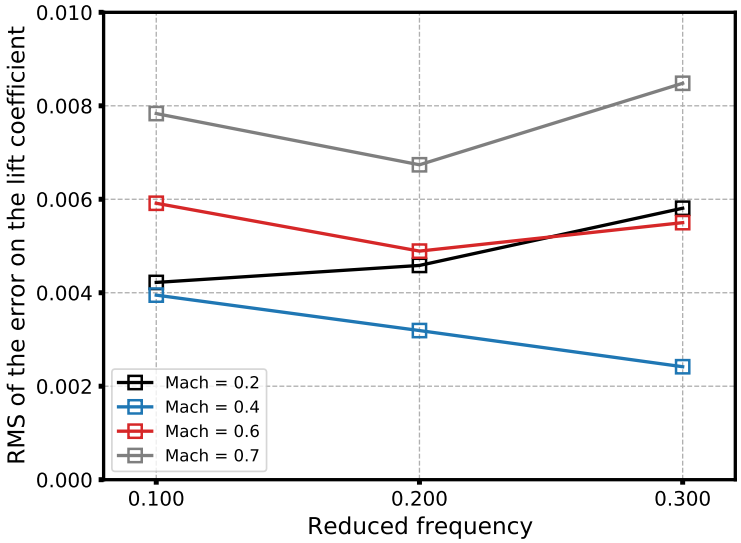

Figure 6.29 RMS of the error on the lift coefficient for a pitching NACA 0012 30° swept wing at a Reynolds number of 1M.

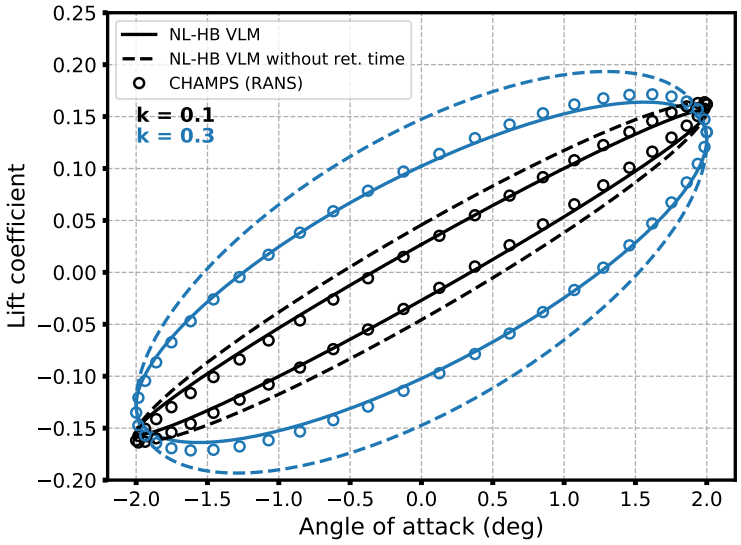

Figure 6.30 Lift coefficient for a pitching NACA 0012 30° swept wing at a Reynolds number of 1M and Mach number of 0.6.

6.6 Summary

The goal of this chapter is to introduce viscous and compressibility effects into the unsteady vortex lattice method through its harmonic balance formulation. Viscous and transonic effects are added through the standard sectional coupling algorithm based on local angle of attack correction using steady 2D solutions computed with a RANS flow solver. The effect due to cross flow for swept wings are introduced through a careful treatment of the coupling algorithm based on the analytical lifting-line formulation for swept wings.

The effect of compressibility is divided into a steady and unsteady contribution. The steady contribution is added through the well-known Prandtl-Glauert transformation. The unsteady contribution, related to the time lag, is introduced with an approximation of the retarded time formulated from the linear compressible wave equation using the vortex segment midpoint as an approximation of the perturbation position in space.

The NL-HB VLM is compared against high-fidelity Euler and RANS time domain solution for a harmonically pitching NACA 0012 airfoil and a NACA 0012 wing. The results show that the NL-HB VLM is capturing the effect of unsteady compressibility with the effect of reduced frequency for a wide range of Mach numbers. However, when strong nonlinear effects are present due to transonic conditions especially for higher reduced frequencies, the solution computed with the NL-HB VLM deviates from the Euler or RANS solution, thus limiting its range of application. Indeed, as the Mach number increases, it is expected that the NL-HB VLM will provide accurate results for the real part of lift, while the imaginary part will exhibit larger errors as transonic conditions are reached. However, when examined under delta form, the predictions are accurate as high as Mach 0.7, k=0.3 or Mach 0.75, k=0.2 for a 12% thick unswept airfoil. Thus, for a typical transport aircraft with swept wings, this level of accuracy combined with four orders runtime speedup per available cores compared to 3D unsteady URANS makes the method ideally suited for preliminary and conceptual multidisciplinary analysis and design optimization.

CHAPTER 7 DYNAMIC AEROELASTIC ANALYSES

In this chapter, the nonlinear harmonic balance VLM, which was derived in the previous chapter, is applied to dynamic aeroelastic problems. The HB/LCO approach[29, 128, 129] is used to compute flutter boundaries and limit cycles oscillations. The first section focuses on 2D cases using a typical two DOF aeorelastic section. Thereafter, the NL-HB VLM is applied to 3D problems: the BSCW supercritical wing from the AeroElastic Prediction Workshop 2 (AePW2) and the well-known Agard wing. Both flutter and LCO are investigated in 2D and 3D.

7.1 Two degree-of-freedom

If the two DOF aeroelastic system of Figure 7.1 is considered, the equation of motions is described by

$$m\ddot{h} + S_\alpha \ddot{\alpha} + K_h h = -L \tag{7.1}$$

$$S_\alpha \ddot{h} + I_\alpha \ddot{\alpha} + K_\alpha \alpha = M_{\text{e.a.}} \tag{7.2}$$

where h and α are the plunge and pitch degree of freedom respectively, m is the airfoil sectional mass, K_h and K_α are the plunge and pitch stiffness respectively, S_α the first moment of inertia about the elastic axis and I_α is the second moment of inertia. The right-hand side of Equation 7.1 and 7.2 correspond to aerodynamic loading, the lift (L) and the moment about the elastic axis ($M_{\text{e.a.}}$).

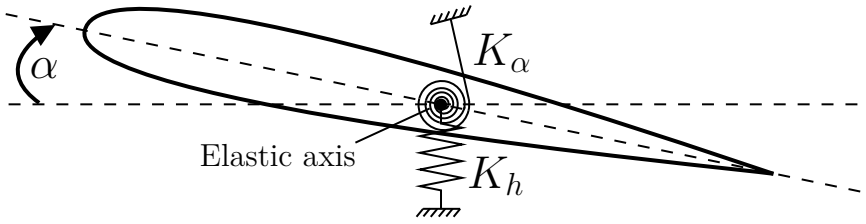

Figure 7.1 Typical two DOF aeroelastic system.

In the frequency domain and in nondimensional form, the equations of motion are rewritten[14] as

$$\left[-\bar{\omega}^2 \begin{pmatrix} 1 & x_\alpha \\ x_\alpha & r_\alpha^2 \end{pmatrix} + \frac{4}{\bar{V}^2} \begin{pmatrix} \frac{\omega_h^2}{\omega_\alpha^2} & 0 \\ 0 & r_\alpha^2 \end{pmatrix} \right] \begin{bmatrix} \bar{h} \\ \bar{\alpha} \end{bmatrix} = \frac{4}{\pi\mu} \begin{bmatrix} -\bar{C}_l(\bar{h}, \bar{\alpha}, \bar{\omega}) \\ 2\bar{C}_m(\bar{h}, \bar{\alpha}, \bar{\omega}) \end{bmatrix} \tag{7.3}$$

where $\bar{\omega}$ is the reduced frequency defined as

$$\bar{\omega} = \frac{\omega c}{V} \tag{7.4}$$

and c the chord length of the airfoil and r_α the radius of gyration about the elastic axis. The plunge and pitch motions are now expressed in terms of complex amplitude for a single harmonic motion and the aerodynamic response is expressed similarly with the complex amplitude of lift ($\bar{C}_l$) and moment ($\bar{C}_m$). Furthermore, the ratio of natural uncoupled frequency of pitch and plunge ($\frac{\omega_h^2}{\omega_\alpha^2}$) is now an input to the aeroelastic system.

For flutter analyses, the aerodynamic response can be assumed linear for small harmonic motion and the generalized aerodynamic matrix can be computed for small deflections of plunge and pitch. Thereafter, the flutter point can be computed using the determinant approach[130]. For LCO solutions, the HB/LCO method can be used, where the pitch motion is defined as the independent variable with a prescribed real valued amplitude. By prescribing the pitch amplitude instead of the reduced velocity, the complete unstable LCO branch can be captured. A nonlinear system of equations is then formed with the following unknowns

$$\boldsymbol{L} = \begin{Bmatrix} \bar{\omega} \\ \bar{V} \\ (\frac{\bar{h}}{\bar{\alpha}})_{Re} \\ (\frac{\bar{h}}{\bar{\alpha}})_{Im} \end{Bmatrix} \tag{7.5}$$

where $\bar{V}$ is the reduced velocity defined as

$$\bar{V} = \frac{V}{\omega_\alpha b} \tag{7.6}$$

The real and imaginary part of Equation 7.3 are then redefined in an augmented system[14] with real values as

$$\boldsymbol{R} = \begin{bmatrix} -\bar{\omega}(\frac{\bar{h}}{\bar{\alpha}})_{Re} & +\frac{4}{\bar{V}^2}\frac{\omega_h^2}{\omega_\alpha^2}(\frac{\bar{h}}{\bar{\alpha}})_{Re} & -\bar{\omega}^2 x_\alpha & +\frac{4}{\pi\mu\bar{\alpha}}(\bar{C}_l)_{Re} \\ -\bar{\omega}(\frac{\bar{h}}{\bar{\alpha}})_{Im} & +\frac{4}{\bar{V}^2}\frac{\omega_h^2}{\omega_\alpha^2}(\frac{\bar{h}}{\bar{\alpha}})_{Im} & & +\frac{4}{\pi\mu\bar{\alpha}}(\bar{C}_l)_{Im} \\ -\bar{\omega}x_\alpha(\frac{\bar{h}}{\bar{\alpha}})_{Re} & -\bar{\omega}^2 r_\alpha^2 & +\frac{4}{\bar{V}^2}r_\alpha^2 & -\frac{8}{\pi\mu\bar{\alpha}}(\bar{C}_m)_{Re} \\ -\bar{\omega}x_\alpha(\frac{\bar{h}}{\bar{\alpha}})_{Im} & & & -\frac{8}{\pi\mu\bar{\alpha}}(\bar{C}_m)_{Im} \end{bmatrix} = 0 \tag{7.7}$$

Thereafter, a Newton-Raphson method is applied[29] to solve Equation 7.7

$$\boldsymbol{L}^{n+1} = \boldsymbol{L}^n - \left[\frac{\partial \boldsymbol{R}(\boldsymbol{L}^n)}{\partial \boldsymbol{L}}\right]^{-1} \boldsymbol{R}(\boldsymbol{L}^n) \tag{7.8}$$

and the Jacobian matrix $\frac{\partial \boldsymbol{R}(\boldsymbol{L^n})}{\partial \boldsymbol{L}}$ is approximated using a forward finite difference. Consequently, every iteration of the Newton-Raphson requires four evaluations of the aerodynamic response using the NL-HB VLM. One evaluation is required to compute $\boldsymbol{R}(\boldsymbol{L^n})$ and three more evaluations are necessary to compute the Jacobian matrix with forward differences for sensitivities in regards of $\bar{\omega}$, $(\frac{\bar{h}}{\bar{\alpha}})_{Re}$ and $(\frac{\bar{h}}{\bar{\alpha}})_{Im}$. Since the NL-HB VLM is nondimensional, its sensitivity in terms of the reduced velocity $\bar{V}$ is zero. The solving process is illustrated in Figure 7.2.

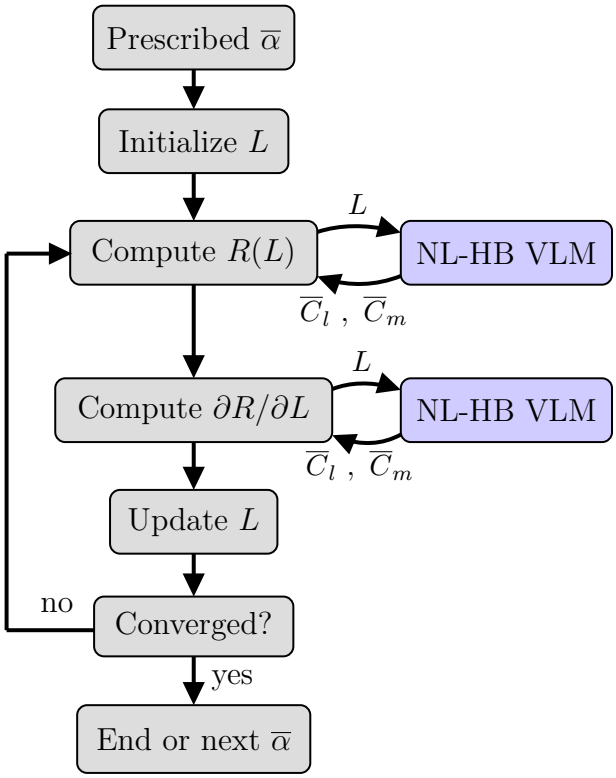

Figure 7.2 Illustration of the HB/LCO approach with the NL-HB VLM.

Flutter solutions are solved by prescribing a very small amplitude value of pitch (i.e. 0.001). Thereafter, the solution process is continued with increasing values of pitch amplitude to solve the LCO branch. Since a Newton-Raphson method is used, every point on the LCO branch is solved in just a few (3-5) iterations using the previous point as the initial solution. Furthermore, every NL-HB VLM calls inside the iterative process is performed in just a few seconds, hence a full LCO branch can be computed in under five minutes depending on the number of harmonics used for the aerodynamic model. This HB/LCO approach is used for every result presented next. The 2D configuration is modeled with a very large aspect ratio wing (> 1000) for the NL-HB VLM with 15 panels along the chord and 5 panels along the span.

7.1.1 Isogai Configuration

The Isogai configuration[131, 132] is meant to reproduce a typical section for a transonic swept wing where the pitching axis is forward of the section leading edge point. The airfoil for the section is a NACA 64A010A. The structural parameters are presented in Table ref 7.1 where a represents the location of the elastic axis measured positive aft of the airfoil mid-chord. The NL-HB VLM is compared against two other results from the literature: Timme

Table 7.1 Isogai structural parameters

a	ω_h/ω_α	μ	r_α^2	x_α
-1.0	1.0	60.0	3.48	1.8

and Badcock [133] and Li and Ekici [134]. All results for this configuration are in inviscid conditions and a steady lift-curve slope computed with CHAMPS in inviscid condition as well is used for the sectional corrections for the NL-HB VLM. Li *et al.* are using the one-shot harmonic balance with a Euler flow solver to obtain the flutter point, while Timme *et al.* are solving directly the stability problem (eigenvalues) problem where the Jacobian matrix is computed with a Euler flow solver. The computed flutter boundary is presented in Figure 7.3, where the flutter speed index is defined as

$$V_{si} = \frac{\bar{V}}{\sqrt{\mu}} \tag{7.9}$$

where the mass ratio μ is defined as

$$\mu = \frac{m}{\pi \rho b^2} \tag{7.10}$$

The NL-HB VLM solution, which includes all compressibility corrections and sectional corrections is represented by the black line in Figure 7.3. The two gray lines are solution from the NL-HB VLM, but without the retarded time effect for the square markers and without sectional corrections for the triangle markers. This comparison confirms again the critical impact of these two corrections. Without sectional corrections from a 2D steady high-fidelity solution, the effect of thickness is not captured and the pitching moment cannot be modeled accurately. Consequently, the flutter boundary has a significant offset and the upper branch of the flutter boundary is not captured. On the other hand, if sectional corrections are applied but without the retarded time, the strong nonlinearity at high Mach numbers is captured, but there is approximately a 30% difference in the predicted flutter speed index at a Mach number of 0.6 when compared to Timme *et al.*. The complete NL-HB VLM compares well with Timme *et al.* up to a Mach number of 0.8. The nonlinear jump between

the two branches in the flutter boundary is captured sooner at around 0.87, while the results of Timme *et al.* show a jump at around 0.89. Nonetheless, the NL-HB VLM is capable of capturing the two branches, which are found by simply choosing different initial point in the Newtown-Raphson procedure. Thereafter, the solver converges to the closest point on the nearest branch.

These aeroelastic results are consistent with the results presented in Chapter 6, where the NL-HB VLM shows impressive accuracy for lower subsonic speed. As the Mach number increases, the NL-HB VLM is less accurate and cannot capture the full nonlinearity from compressibility and transonic conditions. Thus, the flutter dip present at a Mach number of 0.85 is underestimated. However, the global flutter boundary, including the upper and lower branches, is still well captured. The figure highlights the smoothness of the present approach compared to the high-fidelity results. This is a desirable property during design phases. Furthermore, the entire boundary is computed under 10 minutes elapsed time with a standard computer (Intel i9-9900k), another sought-after property during preliminary design. The two DOF aeroelastic system with the NL-HB VLM is further analyzed in the next sections with LCO consideration as well.

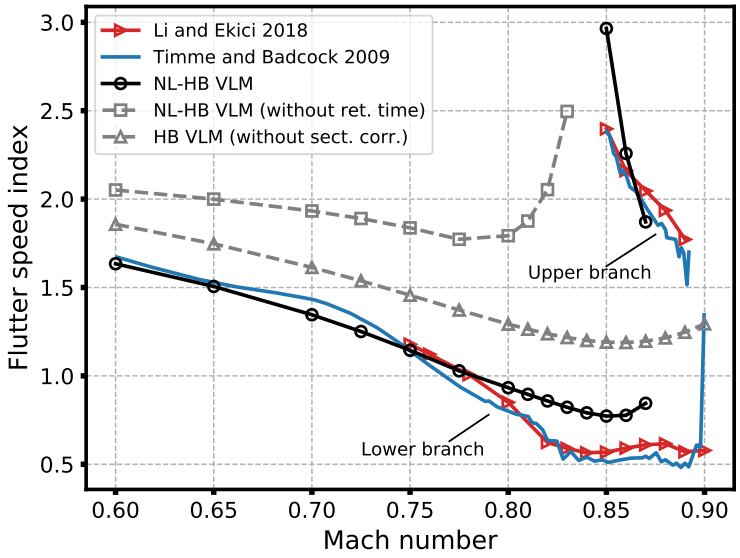

Figure 7.3 Flutter speed index as a function of the Mach number for the Isogai configuration.

7.1.2 NACA 64A010A

In this section, the two DOF system is further analyzed with the same airfoil, the NACA 64A010A, but with different structural parameters[14]. Two values of natural frequency ratio

$\frac{\omega_h}{\omega_\alpha}$ are considered: 0.5 and 0.8. A frequency ratio of 0.5 is characterized by a plunge-dominant motion, while a more complex plunge-pitch motion is dominant for a frequency ratio of 0.8. The frequency ratio of 0.8 is analyzed first followed by the results for the frequency ratio of 0.5. The structural parameters are defined in Table 7.2.

Table 7.2 NACA 64A010A structural parameters

a	μ	r_α^2	x_α
-0.3	100.0	0.75	0.25

The flutter reduced velocity and reduced frequency for $\omega_h/\omega_\alpha = 0.8$ are presented in Figure 7.4. The NL-HB VLM is compared against two Euler solutions: Kholodar et al. [14] and CHAMPS. The solution of CHAMPS has been computed by evaluating the generalized aerodynamic force matrix using very small motion amplitude of pitch and plunge in inviscid conditions, from which the first harmonic is extracted for the lift and moment. Thereafter, the flutter point is found using the determinant approach[130]. For Kholodar et al. [14], the HB/LCO approach is also used and the aerodynamic forces are evaluated using a harmonic balance Euler flow solver.

For a Mach number below 0.725, the predicted reduced velocity from the NL-HB VLM is in good agreement with the solution of CHAMPS. The same trend is observed for the reduced frequency also. Unfortunately, the dip in the flutter boundary is underestimated, which is consistent with previous results where the NL-HB VLM has reached its limitation. However, the trend at high Mach numbers (> 0.8) where the flutter reduced velocity suddenly increases is well captured by the NL-HB VLM. This behavior in the flutter boundary is strongly influenced by the pitching moment. Indeed, Figure 7.4 shows that if the moment correction is removed from the iterative process within the NL-HB VLM, the sudden increase in flutter reduced velocity seen after a Mach number of 0.8 is not captured. The pitching moment is in fact greatly affected by the airfoil's geometry and by compressibility effect as well. It must therefore be considered within the coupling algorithm of the NL-HB VLM to achieve better modeling capabilities.

The next configuration is similar to the previous one with the only exception that the natural frequency ratio is set to 0.5. This leads to a more plunge-dominant motion with a higher flutter reduced velocity and lower reduced frequency. The complete flutter boundary is presented in Figure 7.5. For this configuration, the dip in the flutter boundary is smaller than for the previous configuration, thus leading to a better prediction for the NL-HB VLM. Furthermore, the sudden increase in reduced velocity after a Mach number of 0.8 is captured and corresponds well to the solution of Kholodar et al. [14] for both the reduced velocity and

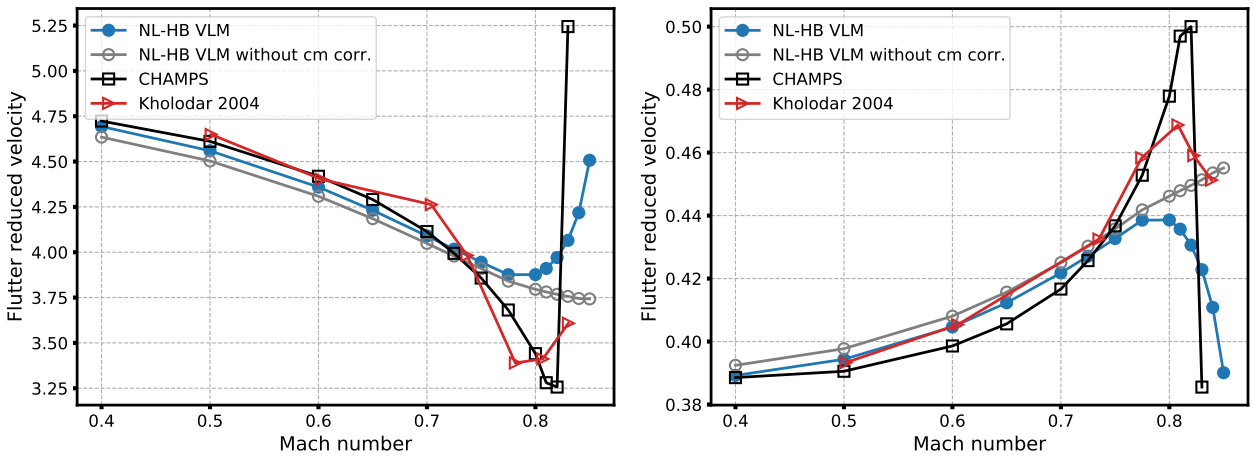

(a) Flutter reduced velocity (b) Flutter reduced frequency

Figure 7.4 Flutter boundary for the NACA 64A010A for $\omega_h/\omega_\alpha = 0.8$ in inviscid conditions.

the reduced frequency.

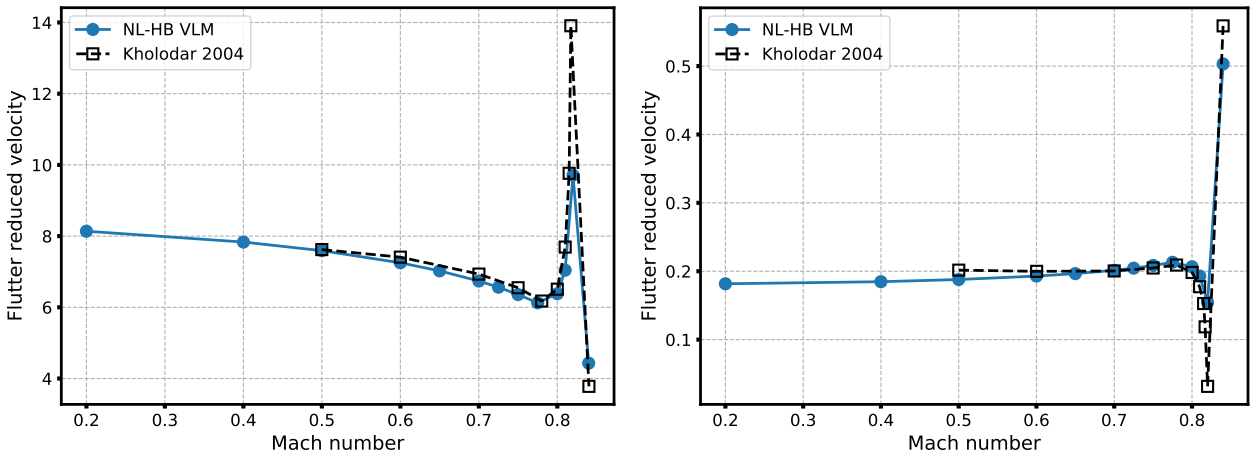

(a) Flutter reduced velocity (b) Flutter reduced frequency

Figure 7.5 Flutter boundary for the NACA 64A010A for $\omega_h/\omega_\alpha = 0.5$ in inviscid conditions.

The next analysis concerns the limit cycle oscillations for the case with $\omega_h/\omega_\alpha = 0.5$. The LCO branches are computed as a function of the pitch amplitude, since it is the chosen independent variable. Figure 7.6 compares the computed LCO branches of the NL-HB VLM with the results from Kholodar et al. [14] using an HB Euler flow solver. When compared to these, all the LCO trends are captured by the NL-HB VLM. Indeed, the weak unstable branches at Mach numbers of 0.6, 0.7 and 0.75 are all captured up to a pitch amplitude of

seven degrees and the strong stable branches at a Mach number of 0.8 and 0.81 are also fully captured. Thereafter, a weak and almost linear LCO branch is recovered at a Mach number of 0.84, which is also captured by the NL-HB VLM. This result shows that enough flow physics is transferred through the quasi-steady coupling algorithm, thus providing sufficient accuracy to capture LCO trend at high Mach numbers.

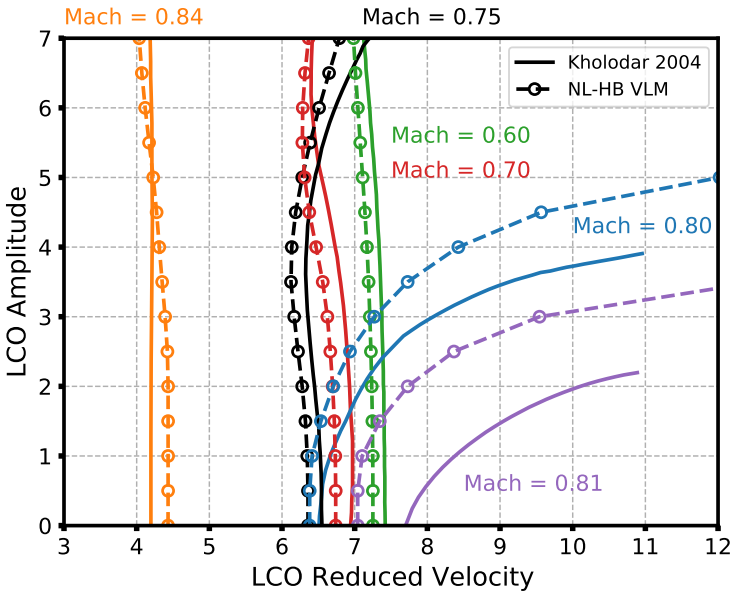

Figure 7.6 LCO branches for the NACA 64A010A in inviscid conditions for $\omega_h/\omega_\alpha = 0.5$.

The convergence of the residual for each amplitude of the LCO branch at a Mach number of 0.7 is shown in Figure 7.7. The tolerance of the solver is set to 10^{-12} and the first amplitude converges within 8 iterations. Under ideal conditions, the Newton-Raphson method should provide quadratic convergence rate. Therefore, using the previous solution as a starting point, the subsequent amplitudes are solved in about four iterations approximately since the initial point is near the final solution. Each iteration of the HB/LCO approach requires 4 aerodynamic evaluations for a total of 284 NL-HB VLM run. Since each run requires just a few seconds, the entire process is very efficient.

All results presented in Figure 7.6 were computed with only one harmonic for the aerodynamic model, which is sufficient for most conditions. At a Mach number of 0.80, where the LCO nonlinearity is strong, Figure 7.8 shows that more than one harmonic is only necessary for larger amplitudes. The spectral convergence is achieved with approximately three harmonics. Therefore, one harmonic is satisfactory for the weak LCOs.

Finally, viscous effects are considered for the LCO branches as well. The Reynolds number is chosen arbitrarily to one million and the steady database used for sectional corrections

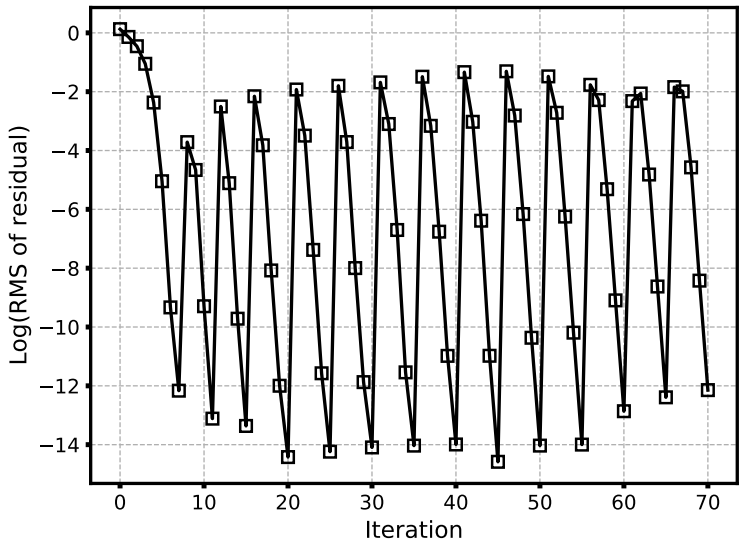

Figure 7.7 Convergence of the HB/LCO solver at a Mach number of 0.7.

is computed in fully turbulent conditions with the Spalart-Allmaras turbulence model. The viscous results are compared against the inviscid solutions in Figure 7.9. The main differences are seen for the higher Mach numbers only. In inviscid conditions, the branches at Mach numbers of 0.8 and 0.81 exhibit a strong nonlinearity that is most likely damped by viscous effects. At a Mach number of 0.84, the LCO trend remains similar in viscous conditions but the flutter reduced velocity is higher. Note that computing the LCO branch in viscous conditions does not incur more computational cost for the NL-HB VLM, since only the sectional data is changed.

For the typical two DOF aeroelastic section, the NL-HB VLM shows impressive modeling capabilities, especially at high Mach numbers where it was shown in Chapter 6 that the approach is less accurate near and beyond the critical Mach number. Indeed, for the Isogai configuration, the two branches of the flutter boundary were captured and in good agreement with high-fidelity Euler solutions. Moreover, it was shown that the NL-HB VLM is also capable of capturing strong stable LCO branches and weak unstable branches as well with comparable fidelity to Euler solutions. Furthermore, viscous conditions are easily computed by simply changing the steady database for a viscous one. In the next section, 3D aeroelastic problems are considered.

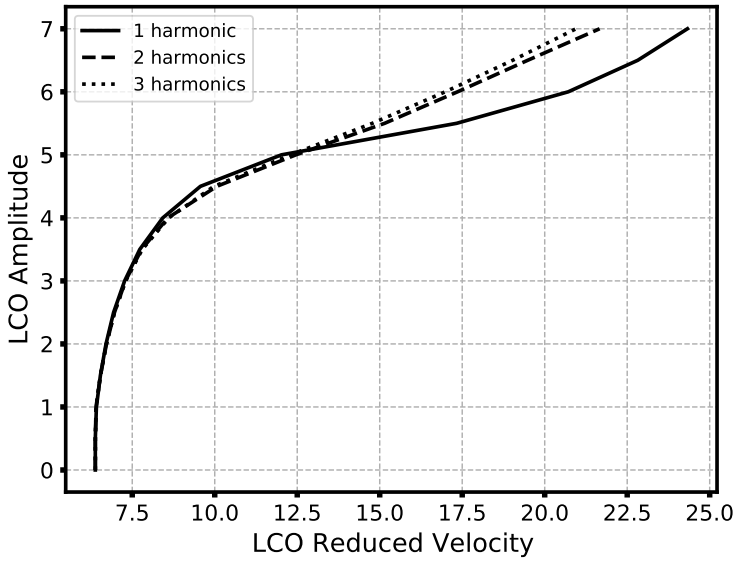

Figure 7.8 LCO spectral convergence for the NACA 64A010A at Mach = 0.8.

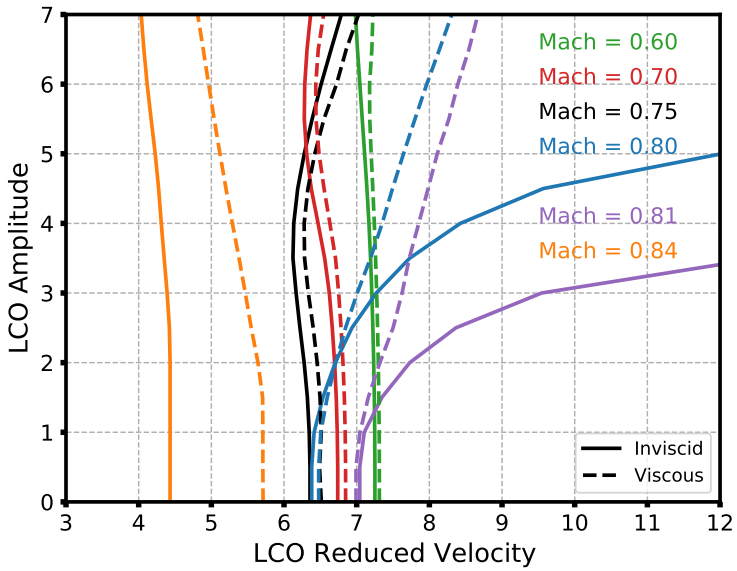

Figure 7.9 LCO branches for the NACA 64A010A - inviscid vs viscous for $\omega_h/\omega_\alpha = 0.5$.

7.2 3D aeroelastic configurations

For the following 3D aeroelastic problems, the nondimensional aeroelastic system of equations defined in Chapter 3 (Equation 3.18) is used.

$$\frac{1}{\tilde{V}^2 \mu \omega_\alpha} \cdot \tilde{\boldsymbol{M}}[\bar{\boldsymbol{W}} - \boldsymbol{I} \cdot k^2]\tilde{\boldsymbol{q}} = \tilde{\boldsymbol{F}} \cdot \frac{c^3}{8\mu\nu}$$

Furthermore, the same HB/LCO method applied for the two-DOF aeroelastic system is used, where a real value is prescribed for the amplitude of the first mode. Therefore, the nonlinear system of equation is defined as

$$\boldsymbol{R} = \left[\frac{1}{\tilde{V}^2\mu\omega_\alpha}\cdot\tilde{\boldsymbol{M}}[\bar{\boldsymbol{W}} - \boldsymbol{I}\cdot k^2]\frac{\tilde{\boldsymbol{q}}}{\tilde{q}_1} - \tilde{\boldsymbol{F}}\cdot\frac{c^3}{8\mu\nu}\right] = 0 \tag{7.11}$$

and the vector of unknowns $\boldsymbol{L}$ is

$$\boldsymbol{L} = \begin{Bmatrix} k \\ \tilde{V} \\ \left(\frac{\tilde{q}_2}{\tilde{q}_1}\right)_{Re} \\ \left(\frac{\tilde{q}_2}{\tilde{q}_1}\right)_{Im} \\ \vdots \\ \left(\frac{\tilde{q}_n}{\tilde{q}_1}\right)_{Re} \\ \left(\frac{\tilde{q}_n}{\tilde{q}_1}\right)_{Im} \end{Bmatrix} \tag{7.12}$$

where n is the number of modes retained for the structural model. The flutter point is found by prescribing a small value for the amplitude of the first mode and the system is solved with a Newton-Raphson approach. For the two DOF, the number of structural modes is fixed to two, but for general 3D aeroelastic problems the number of retained structural modes varies with the problem at hand. Therefore, the computation of the Jacobian matrix can increase significantly with the number of structural modes. Consequently, improvements like the one-shot harmonic balance[134] or the fixed point iteration[21] have been developed to remove the dependency of the aerodynamic model in regards of the structural modes. In this work, however, since the aerodynamic model does not incur a serious computational cost, the standard HB/LCO approach is used for the general 3D aeroelastic system.

Two problems are considered: the supercritical BSCW wing from the Aeroelastic Workshop 2 (AePW2) and the well-known Agard wing. The flutter point for both configurations is compared with results from the literature using high-fidelity aerodynamic models and the LCO behavior in viscous conditions is also investigated for the Agard wing.

7.2.1 Aeroelastic Prediction Workshop 2

The aeroelastic prediction workshop series is intended to provide an open forum in regards of aeroelastic simulation best practices and promote analysis guidelines and lessons learned as well. For the AePW2[135], two cases of flutter were proposed on the supercritical BSCW wing at high Mach numbers. The airfoil is a supercritical SC(2)-0414 with 14% thickness and the wing is rigid with a pitch/plunge motion only. The wing's geometry and structural model

are presented in Figure 7.10. As shown in Figure 7.10b, the springs are attached at the root mid-chord point, thus the wing is pitching about the mid-chord. The FEM model is generated with NASTRAN and consists of rigid flat plates. The interpolation of forces between the structural model and the aerodynamic model is performed as described in Chapter 3 using radial basis functions. The conditions for the two flutter cases of the AePW2 are presented in Table 7.3. Flutter experimental data is available for case 2 only.

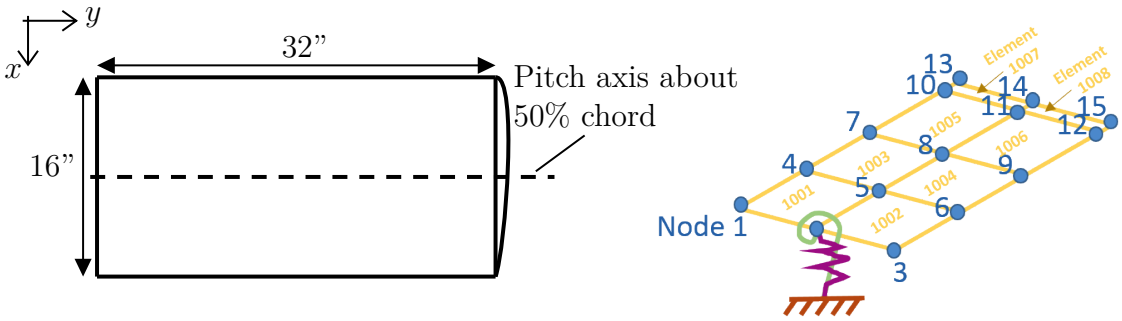

(a) Wing description (b) FEM model description[135]

Figure 7.10 BSCW supercritical wing configuration.

Table 7.3 AePW2 flutter cases

	Case 2	**Case 3C**
Mach	0.74	0.85
AoA	0.0	5.0
Reynolds number	4.450×10^6	4.491×10^6
Mass ratio	685.6	883.1
Exp. flutter dyn. press.	168.8 psf	–
Exp. flutter frequency	4.3 Hz	–

For both cases, steady solutions using CHAMPS were computed for the sectional corrections for the NL-HB VLM using the flow conditions of Table 7.3. For case 3C, there is a shock induced separation as shown in Figure 7.11, thus two databases were computed for this case with different turbulence model (Spalart-Allmaras[126] and Menter κ-ω SST[136]) to investigate their impact over the predicted flutter solution and if this sensitivity is captured through the coupling algorithm with the NL-HB VLM. The wing is discretized with 20 panels along the chord and 30 panels along the span.

The steady lift coefficient and pitching moment as a function of the angle of attack are first compared against results from the AePW2 in Figure 7.12. The results from the AePW2 are computed with FUN3D. The steady aerodynamic coefficients are compared for three Mach

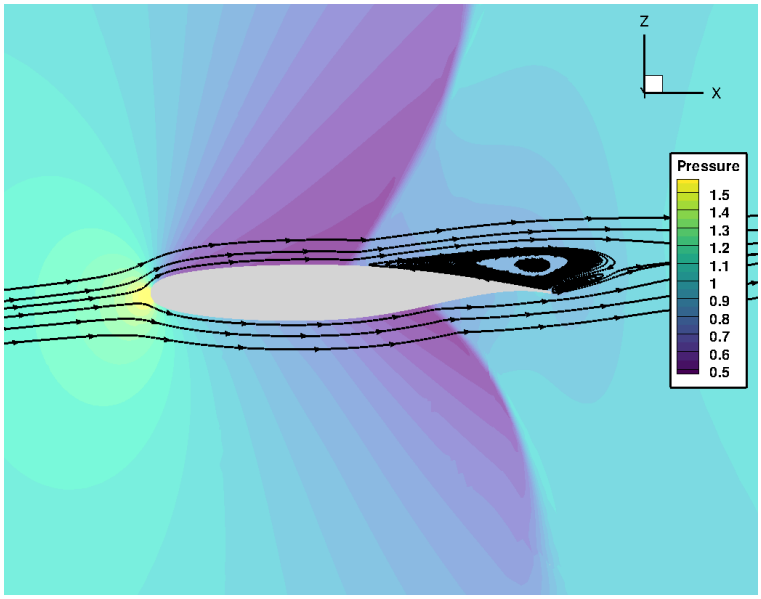

Figure 7.11 Steady flow solution at Mach = 0.85 and AoA = 5.0° computed with CHAMPS.

numbers: 0.70, 0.74 and 0.85. At 0.70 and 0.74, the NL VLM compares well with FUN3D for both the lift coefficient and the pitching moment. The NL VLM predicts a lower $C_{L_{max}}$ than FUN3D, but the effect of Mach number is well captured. For the solution at a Mach number of 0.85, strong flow separation is present, thus creating the differences seen in Figure 7.12. However, the inflection in the lift and in the pitching moment curves for the results computed with FUN3D are also captured with the NL VLM at about the same angle of attack, showing that nonlinear effects due to high Mach numbers and flow separation are well modeled by the NL VLM. Furthermore, the effect of the turbulence model creates small differences in the lift and moment solutions, but it is not significant. Therefore, only small differences are expected for the predicted flutter speed and flutter frequency in regards of the turbulence model.

The predicted flutter dynamic pressure and flutter frequency from the workshop participant for Case 2 and Case 3C are presented in Figure 7.13 and 7.14 respectively, along with the solution computed with the NL-HB VLM. For case 2, the predicted dynamic pressure is 168.74 psf, while the experimental value is 168.8 psf. For the frequency, the NL-HB VLM predicts a value of 4.1 Hz, while the experimental value is 4.3 Hz. Overall, the proposed approach provides accurate results for Case 2 when compared to the experimental data. Furthermore, there is a large variation among the participants ranging from 150 to 210 psf for the dynamic pressure for Case 2 and this variation is even more important for Case 3C. Indeed, for the case at a Mach number of 0.85 and 5° AoA, the mean dynamic pressure for

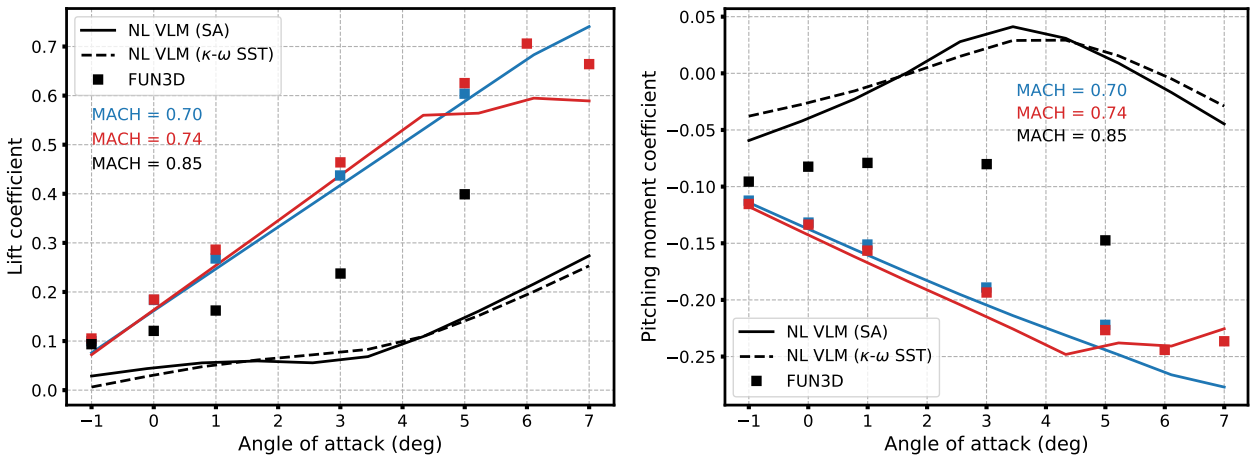

(a) Lift coefficient

(b) Pitching moment about wing leading edge

Figure 7.12 Steady lift and pitching moment coefficient as a function of AoA.

the workshop results is 410.94 psf with a standard deviation of 161.71 psf, or 39% of the mean value. For the NL-HB VLM, the computed flutter dynamic pressure is 227.66 psf when using the Spalart-Allmaras model and 253.89 psf when using the Menter κ-ω SST model, which represents a difference of 11% due to the turbulence model. This is a relatively small difference considering the participant spread. The NL-HB VLM predicts a dynamic pressure significantly lower than the workshop average, but the flutter frequency of 4.88 Hz is in good agreement with the workshop average of 5.05 Hz.

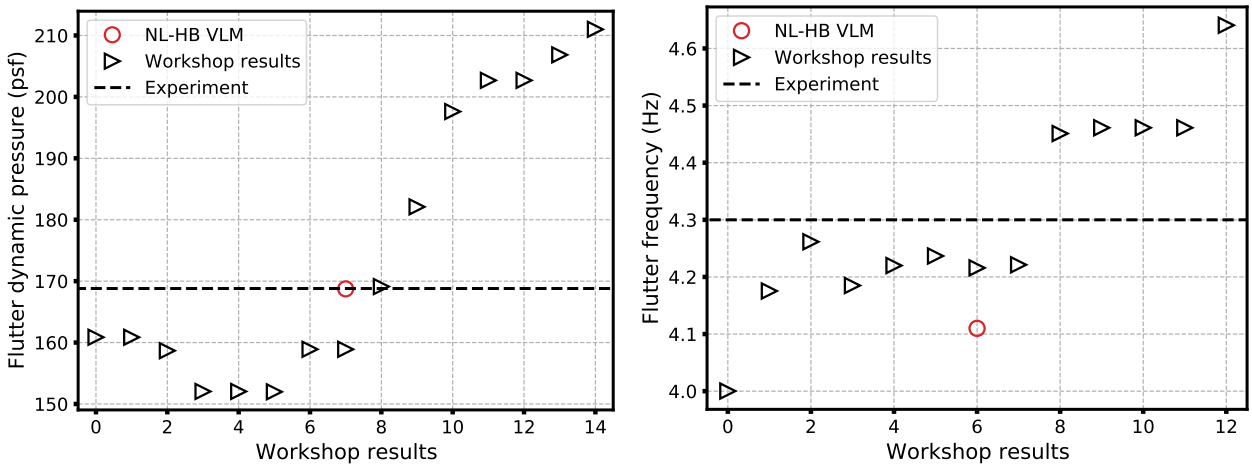

(a) Flutter dynamic pressure

(b) Flutter frequency

Figure 7.13 Flutter boundary for case 2 at a Mach number of 0.74 and angle-of-attack of 0°.

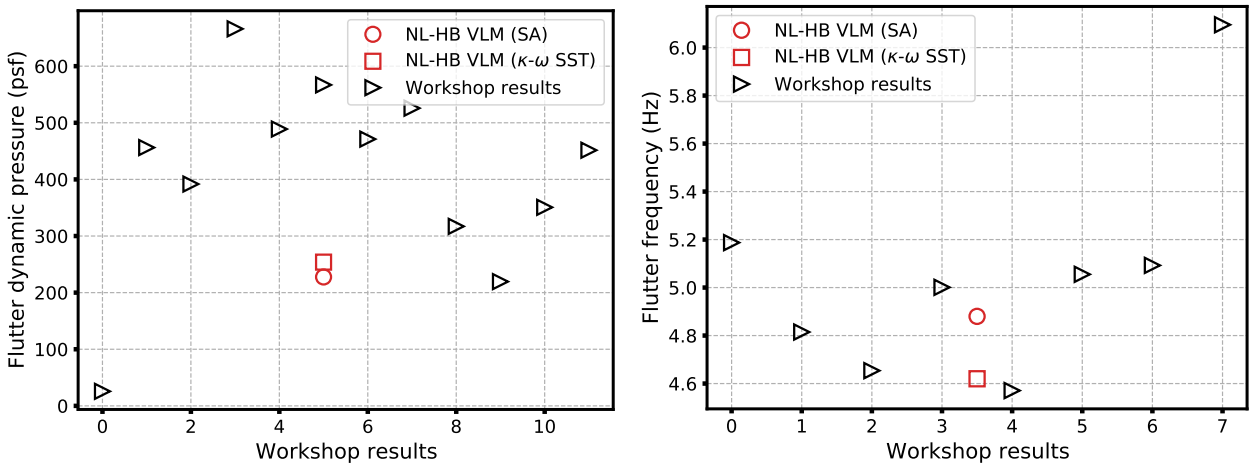

(a) Flutter dynamic pressure

(b) Flutter frequency

Figure 7.14 Flutter boundary for case 3C at a Mach number of 0.85 and angle-of-attack of 5°.

7.2.2 Agard wing

The last 3D aeroelastic case is the famous Agard wing 445.6. The wing has an aspect ratio of 1.65, a taper ratio 0.66 and a quarter-chord sweep of 45°, see Figure 7.15. The low aspect ratio and 45° sweep angle are stretching the limits of the VLM model as well as the 2.5D hypothesis especially near the symmetry plane. The wing's airfoil is a NACA 65A004 with 4% thickness. The FEM model is generated with NASTRAN using quadrilateral plate element and the material properties are listed in Table 7.4. The structural grid consists of 20 panels chordwise and 50 panels spanwise. The computed natural frequencies are presented in Table 7.5 and the interpolated mode shapes on the aerodynamic grid are shown in Figure 7.16, where the aerodynamic grid is also discretized with 20 panels chordwise and 50 panels spanwise. The computed natural frequencies are in good agreement with the experimental values, but the measured natural frequencies for the first four modes are used in the aeroelastic system as suggested by Yates [36]. The sectional data for the NL-HB VLM are computed with a 45° sweep angle and the Spalart-Allmaras turbulence model is used for the viscous simulations. A database is computed for every Mach number considered in inviscid and viscous conditions and with the corresponding Reynolds number from the experiment.

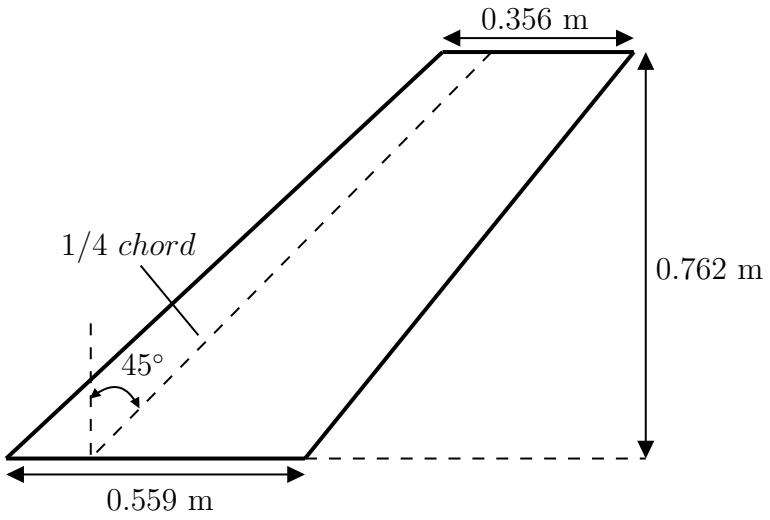

Figure 7.15 Agard wing geometry.

Table 7.4 Agard 445.6 material properties.

Density	381.98 kg/m^3
Young's modulus	3151.1 MPa
Orhtogonal young's modulus	416.2 MPa
Rigidity modulus	439.2 MPa
Poisson's ratio	0.31

Table 7.5 Agard 445.6 natural frequencies for weakened model 3.

Mode	**Computed**	**Measured**
First bending	9.54	9.60
First torsion	40.25	38.10
Second bending	50.25	50.70
Second torsion	97.19	98.50

Flutter results

For the aeroelastic computation, the first six modes are retained, which is sufficient to achieve a converged flutter solution[20]. The conditions at which the flutter point is computed are listed in Table 7.6 and the resulting flutter reduced velocity and flutter frequency ratio (ω/ω_α) are presented in Figure 7.17 with comparison against the experimental results and solutions from the literature using high-fidelity aerodynamic flow solvers.

The Agard wing is a relatively thin wing, thus the aerodynamic remains mostly linear, even at high Mach numbers. The dip in the flutter boundary is not caused by transonic effects[137],

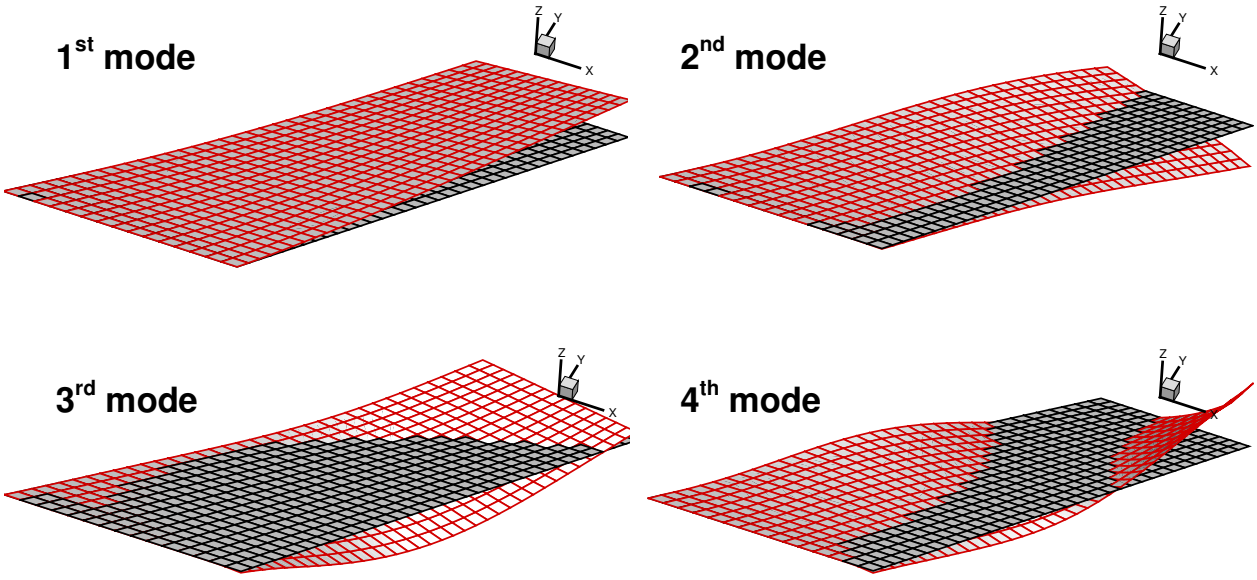

Figure 7.16 Agard wing first and second modes of bending and torsion.

since transonic conditions are achieved at a Mach number of about 0.98[137]. Consequently, the dip is caused by compressibility only. Unfortunately, the NL-HB VLM solution does not capture the dip. However, the flutter speed is well captured for the Mach numbers of 0.338, 0.499 and 0.678. The flutter frequency is also well captured, where the trend as a function of Mach number corresponds to the experiment. For the supersonic conditions, the NL-HB VLM cannot be used since the model requires additional modification.

Table 7.6 Agard 445.6 conditions.

Mach number	**Mass ratio**	ω_α (rad/s)
0.338	12.568	238.0
0.499	33.465	239.3
0.678	68.753	239.3
0.901	143.92	239.3
0.960	225.82	239.3

LCO results

The LCO behavior of the Agard wing is investigated in viscous conditions for the same flutter conditions presented previously. The Spalart-Allmaras turbulence model was used to

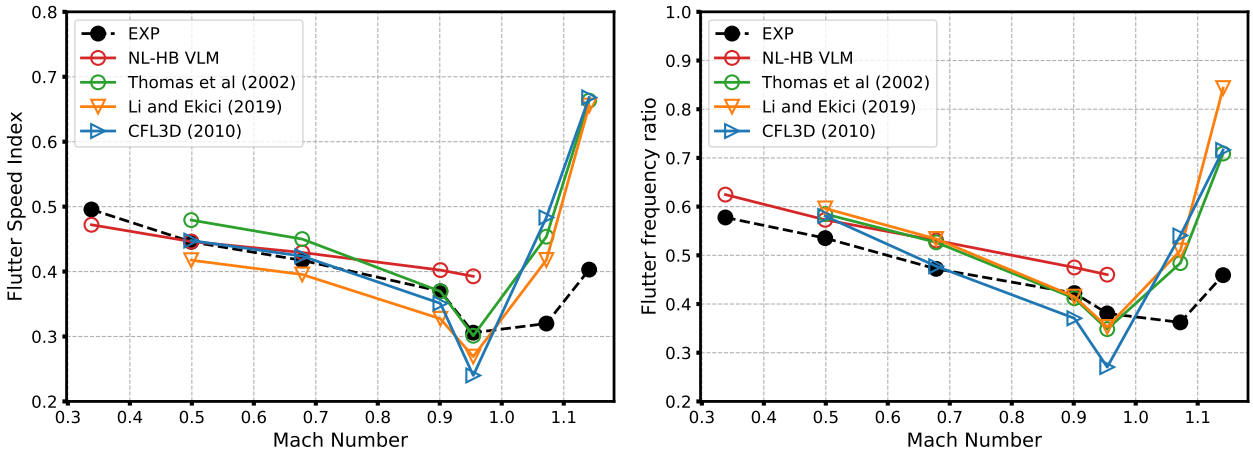

(a) Flutter speed index

(b) Flutter frequency ratio

Figure 7.17 Flutter boundary for the Agard wing in inviscid conditions.

generate the steady viscous database and the LCO branches are shown in Figure 7.18. As expected, all LCO branches are almost linear due to the aerodynamics that remains mostly linear due to the wing's very low thickness. However, it can be seen that for the lower Mach numbers ($\leq$ 0.678), the LCO is stable, while for the higher Mach numbers weak unstable LCOs are observed. This behavior could be explained by compressibility effect, but also by the dominant motion of the LCO. Indeed, if the real and imaginary part of the amplitude for the first torsion mode is compared for the different Mach numbers, see Figure 7.19, a torsion dominated motion is observed for a Mach number of 0.338. Thereafter, the motion becomes bending dominant as the Mach number increases. These results are consistent with findings from the literature[137].

7.3 Summary

The goal of this chapter is to apply the nonlinear harmonic balance VLM to dynamic aeroelastic problems in 2D and 3D. Flutter and LCO solutions are successfully computed using the HB/LCO approach with a Newton-Raphson solver. In 2D over a typical two-DOF aeroelastic system, the flutter boundary is computed efficiently and with comparable accuracy than high-fidelity Euler solutions. Indeed for the Isogai configuration, the two branches of the flutter boundary are captured. However, the dip at a Mach number of 0.85 is underestimated. Furthermore, the HB/LCO method is applied to limit cycle oscillations on the NACA 64A010A. The NL-HB VLM is capable of capturing accurate LCO trends up to a Mach number of 0.84.

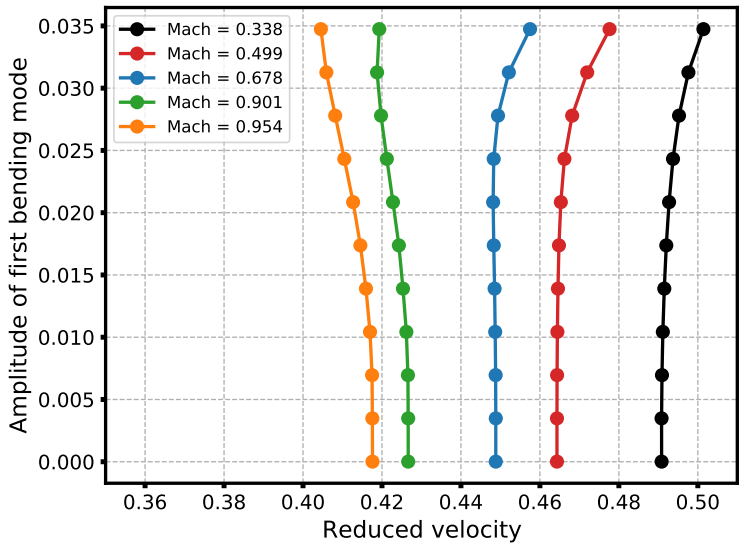

Figure 7.18 LCO amplitudes for the Agard wing in viscous conditions.

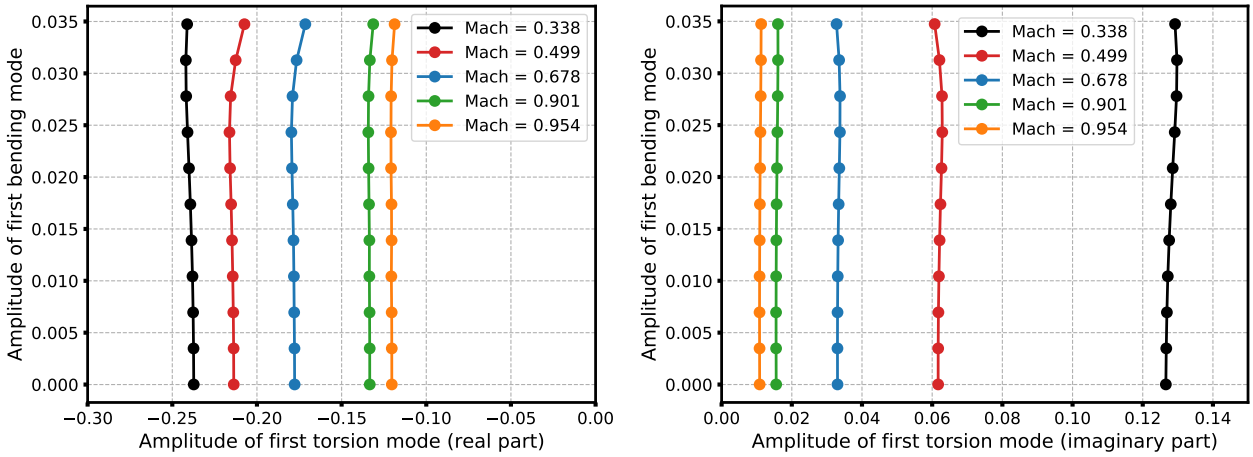

(a) Real part

(b) Imaginary part

Figure 7.19 LCO real and imaginary part for the amplitude of the first torsion mode.

In 3D, the HB/LCO method is applied to the supercritical BSCW wing and the Agard wing. For the BSCW wing, the computed flutter point for case 2 is almost exactly equal to the experiment, while for case 3C the flutter dynamic pressure is underestimated when compared to the average value from the workshop participants. Finally, the NL-HB VLM is applied to the Agard wing and the computed flutter boundary for both the speed index and frequency correspond well to the experiment up to a Mach number of 0.678. Unfortunately, the dip in the boundary at a Mach number of 0.954 is not captured. These conditions are beyond

the range of applicability for the NL-HB VLM. Moreover, the Agard wing has a very low aspect ratio and a large sweep angle, thus creating complicated physics to model for the VLM. Nonetheless, the LCO trend in viscous conditions are analyzed for the Agard wing, showing that a torsion dominant motion is present at lower Mach numbers, while a bending dominant motion is found at higher Mach numbers.

The results presented in this Chapter show that the NL-HB VLM is capable of capturing nonlinear flutter/LCO solutions for a wide range of Mach numbers and with more than 4 orders of magnitude faster than high-fidelity solutions. The proposed approach is flexible, robust and it requires only two-dimensional high-fidelity solutions. However, the model is inadequate to fully characterize the flutter dip due to nonlinear compressibility or transonic conditions. These limitations are in part induced by the unsteady compressibility, which is approximated and derived from linear unsteady compressible theory. Furthermore, the sectional corrections are quasi-steady only and nonlinear compressible unsteady effects are therefore not included. Nonetheless, the proposed model satisfies the overarching goal to develop more accurate models towards preliminary transonic aircraft design.

CHAPTER 8 CONCLUSION

This chapter concludes the thesis. A summary of the work is presented in Section 8.1 followed by the main contributions of this research. Thereafter, the limitations of the proposed framework are listed and discussed along with potential solutions to overcome these limitations.

8.1 Summary of Works

The Unsteady Vortex Lattice Method has become a widely used approach for nonlinear dynamic problems. It's formulation is simple and allows complex motions to be modeled with wake interaction, providing interesting modeling capabilities. It is also a boundary element method, therefore only a surface mesh is necessary, making the approach efficient. Consequently, the UVLM provides an interesting alternative to the DLM for aeroelastic problems.

However, the UVLM is a time-domain approach, which is not fully compatible with the industry standard for stability analysis in the context of flutter analyses. Moreover, the method models incompressible, inviscid and irrotation flow conditions only. Consequently, the work presented in this thesis addresses these problems by first extending the UVLM to the frequency domain to provide a formulation similar to the DLM for flutter analyses, but without the limiting assumptions of the DLM. As a result, the linear frequency domain VLM is directly compatible with industry-standard analysis tools for flutter and the approach can model general in-plane and out-of-plane kinematics without external corrections. This was demonstrated with a T-tail flutter configuration where the effect of mean angle of attack can be captured.

A linear frequency domain formulation is limited to linear aeroelastic problems, such as flutter. For limit cycle oscillation, nonlinear dynamics must be modeled. Therefore, a nonlinear frequency domain extension of the UVLM is also proposed, using the harmonic balance approach. The harmonic balance VLM provides the same nonlinear dynamic modeling capabilities than the UVLM, but more efficiently. Indeed, the periodic solution is solved directly using several time instances equally spaced along the period, which are then coupled together through a discrete Fourier transform. The spectral convergence of the HB VLM on nonlinear dynamic problems has been shown, even on a wake-interaction problem. However, the approach is still limited to incompressible and inviscid flows.

Corrections are therefore proposed to circumvent these limitations. Viscous effects are added

through an iterative process where a local angle of attack correction is computed with sectional data obtained from two-dimensional high-fidelity flow solvers. These two-dimensional flow solutions include cross-flow effect through the infinite swept wing condition to better model the flow physics over swept wings. Therefore, the coupling algorithm is revisited for infinite swept wing conditions using thin-airfoil theory to ensure an exact coupling scheme for swept wings. Afterward, the compressibility correction is investigated for steady and unsteady conditions. The steady compressible problem can be converted to Laplace's equation using the Prandtl-Glauert transformation, but the unsteady compressible problem cannot be solved by the standard Biot-Savart kernel for Vortex Lattice Methods. A fundamental concept arising in unsteady compressible flows is that a perturbation is felt only after a certain time delay, depending on the position in space relative to the perturbation. The time delay depends on the Mach number and is derived from the linear compressible wave equation. This time delay, also known as retarded time, is present in the DLM kernel and an approximation is proposed for the frequency domain VLM. The added retarded time improves significantly the HB VLM solution in unsteady compressible flow and it is verified against multiple (U)RANS solutions for pitching and heaving motions.

Finally, the HB VLM approach with viscous and compressible effects is applied to aeroelastic problems in 2D and 3D. The proposed approach captures the nonlinear flutter boundary along with unstable and strong stable LCO branches. Furthermore, the flutter dynamic pressure for case 2 of the AePW2 is accurately captured when compared to the experimental data. The HB VLM is also used to investigate the LCO behavior of the Agard wing in viscous conditions, showing consistent results with the literature. Overall, the HB VLM provides accurate aeroelastic results, but with more than four orders of magnitude faster than high-fidelity Euler and RANS flow solvers.

8.2 Contributions

The key contributions of this work are

1. Extension of the time domain UVLM to the linear and nonlinear frequency domain using the harmonic balance approach;

2. Extension of a steady AoA coupling algorithm to unsteady solutions, along with a modification of the UVLM kernel to include the retarded time effect for unsteady compressible flows;

3. Application of the frequency domain VLM for linear and nonlinear aeroelastic problems with the HB/LCO approach.

8.2.1 Frequency domain VLM

An important contribution from this work is the extension of the time domain UVLM toward the frequency domain. A linearized frequency domain formulation of the UVLM has been explored in the past[48, 49], but in this thesis a general formulation including general kinematics has been derived. The novelty in this general formulation is that the generalized aerodynamic force matrix is derived with in-plane kinematics along with static loading, which are two important elements in the context of T-tail flutter that the DLM cannot model. It was shown that the frequency domain VLM can be applied to T-tail flutter problems directly without external corrections. Moreover, the effect of static loading over the H-tail is fully captured by the general formulation.

One of the most important contribution of this work is the extension of the UVLM to the nonlinear frequency domain using the harmonic balance. To the best of the author's knowledge, this has never been done before, making this contribution the main novelty of this thesis. The harmonic balance formulation enables the UVLM to model nonlinear dynamics much more efficiently, by solving directly the periodic solution with a prescribed number of harmonics using a discrete Fourier transform. As a result, complex motions are solved with the same level of fidelity, but with around one order of magnitude faster depending on the number of chosen harmonics. In the context of nonlinear aeroelastic problems, the HB VLM formulation can provide additional design capabilities.

8.2.2 Viscous and compressible corrections for unsteady flows

The second most important contribution in this work concerns the viscous and compressible corrections for unsteady flows. The addition of these corrections enable the proposed approach to extend the range of application to unswept and swept wings in conditions near the transonic regime. In the development of the sectional coupling algorithm, corrections using infinite swept wing data was revisited to shed novel lights on the evaluation of the effective angle of attack to yield an exact formulation with theoretical thin airfoil theory.

However, the main novelty is the interpretation of unsteady compressible effects and its appromixation for the VLM kernel. A fundamental concept of unsteady linear compressible flow is the retarded time and it is essential that this effect is included in the aerodynamic model to provide accurate solutions for unsteady compressible flows. Indeed, it was shown that the effect of the retarded time is significant even in low subsonic conditions. To the best of the author's knowledge, it is the first time that a formulation of the retarded time is applied to the Vortex Lattice Method. Consequently, it is the first VLM formulation capable

of modeling compressible unsteady flows and it is therefore a main contribution to the field of Vortex Lattice Methods.

8.2.3 Application to linear and nonlinear aeroelastic problems

The last key contribution is the application of the Harmonic Balance VLM with viscous and compressible corrections to linear and nonlinear aeroelastic problems. The NL-HB VLM has been applied with the HB/LCO approach to enable efficient flutter and LCO analysis. It was shown that the approach is capable of capturing nonlinear flutter boundaries with non-unique solutions, along with LCO behaviors up to a Mach number of 0.84. The LCO/HB VLM methodology could have a significant contribution for aircraft design, since it provides impressive modeling capabilities with fidelity comparable to high-fidelity solvers in subsonic conditions, but with more than four orders of magnitude faster. Furthermore, the framework provides smooth functional, essential when performing design iterations. Consequently, the LCO/HB VLM could enable more aeroelastic analyses during the early the design process of the aircraft, which could have potentially a significant impact over the aircraft's performances.

8.3 Limitations

The limitations of the proposed approach are mainly related to the prescribed wake, the quasi-steady nature of the sectional coupling algorithm and the unsteady compressibility effect. These limitations are further discussed in the next sections.

8.3.1 Prescribed wake

For Vortex Lattice Methods, the wake is responsible for the aerodynamic lag and for the frequency domain formulation presented in this thesis, a shape must be assumed and prescribed in order to yield an exact solution. For typical aircraft configurations, where the wake convects with the freestream, a prescribed shape can be applied easily. However, in the case of rotor-wake interaction, a shape for the wake cannot be assumed or prescribed, since wake-rollup plays a significant role in the final shape of the wake. Therefore, the frequency domain formulations presented in this work are limited to applications where the wake rollup does not affect significantly the aerodynamics over the wing and the overall shape of the wing.

8.3.2 Quasi-steady coupling algorithm

It was important for this work that the high-fidelity sectional data used for corrections remains steady. This requirement is necessary to ensure that the overall process is efficient and flexible. The sectional high-fidelity data can be used for any reduced frequency and any motions, while if unsteady solutions were used, a specific database would be required for every reduced frequency and every motion. Consequently, it provides efficiency and flexibility, but the coupling algorithm is limited to the quasi-steady regime for low reduced frequencies. Even though it was shown that accurate results are achieved for high-reduced frequencies, nonlinear flow physics near the transonic regime is not well captured and it affects the fidelity of the approach for the evaluation of the flutter dip boundary at higher Mach numbers. Furthermore, nonlinear unsteady flow conditions, such as dynamic stall, cannot be fully captured either. Unfortunately, this limitation is necessary for efficiency and flexibility.

There is also a second limitation due to the quasi-steady nature of the coupling algorithm and it concerns the pitching moment. Lifting bodies are modeled with thin surfaces, thus the computed pitching moment is intrinsically false. In steady conditions, accurate pitching moment is obtained with the sectional coupling, since the database provide the correct pitching moment of the section. However, in unsteady conditions, the sectional database does not have the influence of the induced velocity from rigid displacement or from structural deformation. Consequently, the pitching moment computed with the VLM cannot be simply replaced with the value from the database. The proposed solution to this problem was to combine both values. Aeroelastic predictions were improved with this correction, but the accuracy of the pitching moment is still limited.

8.3.3 Unsteady compressibility

Vortex Lattice Methods are incapable of modeling unsteady compressible flows, but a solution was proposed to include the effect of time lag due to compressibility. This was achieved through the introduction of the retarded time in the frequency domain formulation of the VLM. The retarded time is derived from linear compressible flow theory and its value was approximated using the vortex segment midpoint as the position in space of the perturbation. Since the retarded time is not fully integrated into the Biot-Savart kernel, errors are induced from the approximation, which in turn limits the modeling capabilities. Additionally, the unsteady compressible effect is derived from the linear compressible wave equation, therefore the method is inadequate for nonlinear compressible flow conditions.

8.4 Future research

The main limitations of the proposed framework concerns unsteady compressibility. As a result, a recommendation is made to further develop the retarded time formulation and to explore the use of TSD as a replacement of the VLM to better model compressibility. Finally, a suggestion is made to improve the structural model and the HB/LCO approach.

8.4.1 Retarded time

As mentioned in Section 8.3.3, the retarded time is only approximated and it is not fully integrated within the Biot-Savart kernel. In this work, a simple approximation for the position in space of the perturbation is used, thus it would be worthwhile to study alternate approximation to yield potentially more accurate evaluation of the retarded time.

8.4.2 3D arbitrary bodies

The current framework is based on the VLM, which models thin lifting surfaces only. Consequently, it would be of interest to explore the use of doublet/source singularities, like the panel method, to model thick bodies. As a result, the fuselage effect over the wing spanload could be modeled accurately, thereby increasing the fidelity for aircraft configurations.

8.4.3 Transonic Small Disturbance approach with sectional corrections

The proposed model uses corrections to introduce compressibility. Therefore, a recommendation is made to study the use of TSD methods instead of the VLM, since the TSD equation is derived directly from the linearized subsonic potential equation. In other words, the TSD equation models directly compressibility without additional corrections. Therefore, it provides a better estimation of unsteady compressibility, but viscous and thickness effects are also omitted like the VLM. If the quasi-steady coupling algorithm is transposed to the TSD model, it could yield an efficient aeroelastic tool with better modeling capabilities at higher Mach numbers.

8.4.4 Nonlinear structural model

In this work, the structural model was considered linear and represented by superposition of mode shapes. Future research could consider the use of a nonlinear structural model using the harmonic balance approach as well. As a result, large nonlinear deflections could be considered.

8.4.5 Improvement of HB/LCO approach

The last recommendation concerns the HB/LCO approach, since the method does not scale well with the number of structural degrees of freedom. Indeed, the evaluation of the Jacobian matrix requires several aerodynamic sensitivity evaluation in regards of each degree of freedom. In order to circumvent this problem, the harmonic balance one-shot approach from Li and Ekici [23] could be implemented. In their work, the aerodynamic evaluations are independent of the number of structural degrees of freedom, which could yield an even more efficient aeroelastic framework. Otherwise, an adjoint-based approach, inspired by the work of Kontogiannis and Laurendeau [138] could be used.

REFERENCES

[1] Working Towards Ambitious Targets, . URL https://www.iata.org/en/programs/environment/climate-change/.

[2] Neal A. Harrison, Gregory M. Gatlin, Sally A. Viken, Michael Beyar, Eric D. Dickey, Krishna Hoffman, and Eric Y. Reichenbach. Development of an Efficient M=0.80 Transonic Truss-Braced Wing Aircraft. In *AIAA Scitech 2020 Forum*, AIAA SciTech Forum. American Institute of Aeronautics and Astronautics, January 2020. doi: 10.2514/6.2020-0011. URL https://arc.aiaa.org/doi/10.2514/6.2020-0011.

[3] Max M. J. Opgenoord, Mark Drela, and Karen E. Willcox. Influence of Transonic Flutter on the Conceptual Design of Next-Generation Transport Aircraft. *AIAA Journal*, 57(5):1973–1987, 2019. ISSN 0001-1452. doi: 10.2514/1.J057302. URL https://doi.org/10.2514/1.J057302. Publisher: American Institute of Aeronautics and Astronautics _eprint: https://doi.org/10.2514/1.J057302.

[4] How the albatross is inspiring next generation of aircraft wings, . URL https://www.airbus.com/newsroom/press-releases/en/2019/06/how-the-albatross-is-inspiring-next-generation-of-aircraft-wings.html.

[5] Boeing: Spreading our wings: Boeing unveils new Transonic Truss-Braced Wing, . URL https://www.boeing.com/features/2019/01/spreading-our-wings-01-19.page.

[6] A. R. Collar. The First Fifty Years of Aeroelasticity. December 1978.

[7] Max M. Opgenoord, Mark Drela, and Karen E. Willcox. Towards a Low-Order Model for Transonic Flutter Prediction. In *8th AIAA Theoretical Fluid Mechanics Conference*. American Institute of Aeronautics and Astronautics, June 2017. URL https://arc.aiaa.org/doi/10.2514/6.2017-4340.

[8] P. Piperni, A. DeBlois, and R. Henderson. Development of a Multilevel Multidisciplinary-Optimization Capability for an Industrial Environment. *AIAA Journal*, 51(10):2335–2352, 2013. ISSN 0001-1452. doi: 10.2514/1.J052180. URL https://doi.org/10.2514/1.J052180.

[9] Arthur Rizzi. Modeling and simulating aircraft stability and control—The SimSAC project. *Progress in Aerospace Sciences*, 47(8):573–588, November 2011. ISSN 0376-

0421. doi: 10.1016/j.paerosci.2011.08.004. URL http://www.sciencedirect.com/science/article/pii/S0376042111000704.

[10] Jiří Čečrdle. 1 - Introduction to aircraft aeroelasticity and whirl flutter. In Jiří Čečrdle, editor, *Whirl Flutter of Turboprop Aircraft Structures*, pages 1–12. Woodhead Publishing, Oxford, January 2015. ISBN 978-1-78242-185-6. doi: 10.1533/9781782421863.1. URL http://www.sciencedirect.com/science/article/pii/B9781782421856500015.

[11] Earl Dowell. *A Modern Course in Aeroelasticity: Fifth Revised and Enlarged Edition*. Solid Mechanics and Its Applications. Springer International Publishing, 5 edition, 2015. ISBN 978-3-319-09452-6. doi: 10.1007/978-3-319-09453-3. URL https://www.springer.com/gp/book/9783319094526.

[12] Grigorios Dimitriadis. *Introduction to Nonlinear Aeroelasticity*. Aerospace Series. Wiley, 2017. ISBN 978-1-118-61347-4. URL http://gen.lib.rus.ec/book/index.php?md5=8a7e4237880ac42244c72d58aab6b9eb.

[13] Jan R. Wright and Jonathan Edward Cooper. *Introduction to Aircraft Aeroelasticity and Loads*. Wiley, Chichester, West Sussex, United Kingdom, 2 édition edition, 2015. ISBN 978-1-118-48801-0.

[14] Denis B. Kholodar, Earl H. Dowell, Jeffrey P. Thomas, and Kenneth C. Hall. Limit Cycle Oscillation of a Typical Airfoil in Transonic Flow. *Journal of Aircraft*, 41(5):1067–1072, 2004. doi: 10.2514/1.618. URL https://doi.org/10.2514/1.618. Publisher: American Institute of Aeronautics and Astronautics _eprint: https://doi.org/10.2514/1.618.

[15] Charbel Farhat. CFD-Based Nonlinear Computational Aeroelasticity. In *Encyclopedia of Computational Mechanics Second Edition*, pages 1–21. American Cancer Society, 2017. ISBN 978-1-119-17681-7. doi: 10.1002/9781119176817.ecm2063. URL https://onlinelibrary.wiley.com/doi/abs/10.1002/9781119176817.ecm2063. _eprint: https://onlinelibrary.wiley.com/doi/pdf/10.1002/9781119176817.ecm2063.

[16] Charbel Farhat, Michel Lesoinne, and Nathan Maman. Mixed explicit/implicit time integration of coupled aeroelastic problems: Three-field formulation, geometric conservation and distributed solution. *International Journal for Numerical Methods in Fluids*, 21(10):807–835, 1995. ISSN 1097-0363. doi: https://doi.org/10.1002/fld.1650211004. URL https://onlinelibrary.wiley.com/doi/abs/10.1002/fld.1650211004. _eprint: https://onlinelibrary.wiley.com/doi/pdf/10.1002/fld.1650211004.

[17] Charbel Farhat, Philippe Geuzaine, and Gregory Brown. Application of a three-field nonlinear fluid–structure formulation to the prediction of the aeroelastic parameters of an F-16 fighter. *Computers & Fluids*, 32(1):3–29, January 2003. ISSN 0045-7930. doi: 10.1016/S0045-7930(01)00104-9. URL http://www.sciencedirect.com/science/article/pii/S0045793001001049.

[18] H. J. Hassig. An approximate true damping solution of the flutter equation by determinant iteration. *Journal of Aircraft*, 8(11):885–889, November 1971. ISSN 0021-8669. doi: 10.2514/3.44311. URL https://arc.aiaa.org/doi/10.2514/3.44311.

[19] Pierre-Olivier Tardif and Siva Nadarajah. Three-Dimensional Aeroelastic Solutions via the Nonlinear Frequency-Domain Method. *AIAA Journal*, 55(10):3553–3569, 2017. ISSN 0001-1452. doi: 10.2514/1.J054849. URL https://doi.org/10.2514/1.J054849.

[20] Hang Li and Kivanc Ekici. Aeroelastic Modeling of the AGARD 445.6 Wing Using the Harmonic-Balance-Based One-Shot Method. *AIAA Journal*, 57(11):4885–4902, 2019. ISSN 0001-1452. doi: 10.2514/1.J058363. URL https://doi.org/10.2514/1.J058363.

[21] Jeffrey Thomas and Earl Dowell. A Fixed Point Iteration Approach for Harmonic Balance Based Aeroelastic Computations. In *2018 AIAA/ASCE/AHS/ASC Structures, Structural Dynamics, and Materials Conference*. American Institute of Aeronautics and Astronautics. doi: 10.2514/6.2018-1446. URL https://arc.aiaa.org/doi/abs/10.2514/6.2018-1446. _eprint: https://arc.aiaa.org/doi/pdf/10.2514/6.2018-1446.

[22] Jeffrey P. Thomas, Earl H. Dowell, and Kenneth C. Hall. Nonlinear Inviscid Aerodynamic Effects on Transonic Divergence, Flutter, and Limit-Cycle Oscillations. *AIAA Journal*, 40(4):638–646, 2002. ISSN 0001-1452. doi: 10.2514/2.1720. URL https://doi.org/10.2514/2.1720. Publisher: American Institute of Aeronautics and Astronautics _eprint: https://doi.org/10.2514/2.1720.

[23] Hang Li and Kivanc Ekici. Improved One-Shot Approach for Modeling Viscous Transonic Limit Cycle Oscillations. *AIAA Journal*, 56(8):3138–3152, May 2018. ISSN 0001-1452. doi: 10.2514/1.J056969. URL https://arc.aiaa.org/doi/10.2514/1.J056969.

[24] Freddie D. Witherden and Antony Jameson. Aerodynamics. In *Encyclopedia of Computational Mechanics Second Edition*, pages 1–107. American Cancer Society, 2017. ISBN 978-1-119-17681-7. doi: 10.1002/9781119176817.ecm2062. URL https:

//onlinelibrary.wiley.com/doi/abs/10.1002/9781119176817.ecm2062. _eprint: https://onlinelibrary.wiley.com/doi/pdf/10.1002/9781119176817.ecm2062.

[25] Jiri Blazek. *Computational Fluid Dynamics: Principles and Applications*. Butterworth-Heinemann, 3 edition, 2015. ISBN 978-0-08-099995-1. URL http://gen.lib.rus.ec/book/index.php?md5=18183d5057954a766d5fab46b9edb179.

[26] Frédéric Plante, Julien Dandois, Samir Beneddine, Éric Laurendeau, and Denis Sipp. Link between subsonic stall and transonic buffet on swept and unswept wings: from global stability analysis to nonlinear dynamics. *Journal of Fluid Mechanics*, 908, February 2021. ISSN 0022-1120, 1469-7645. doi: 10.1017/jfm.2020.848. Publisher: Cambridge University Press.

[27] Michael Iovnovich, Daniella E. Raveh, Dan Michaels, and Motti Adar. Computational Study of Transonic Limit Cycle Oscillation Phenomenon on F-16 Fighter Aircraft. *Journal of Aircraft*, 54(2):783–793, 2017. ISSN 0021-8669. doi: 10.2514/1.C033918. URL https://doi.org/10.2514/1.C033918.

[28] Denis B. Kholodar, Jeffrey P. Thomas, Earl H. Dowell, and Kenneth C. Hall. Parametric Study of Flutter for an Airfoil in Inviscid Transonic Flow. *Journal of Aircraft*, 40(2):303–313, 2003. doi: 10.2514/2.3094. URL https://doi.org/10.2514/2.3094. Publisher: American Institute of Aeronautics and Astronautics _eprint: https://doi.org/10.2514/2.3094.

[29] Jeffrey P. Thomas, Earl H. Dowell, and Kenneth C. Hall. Nonlinear Inviscid Aerodynamic Effects on Transonic Divergence, Flutter, and Limit-Cycle Oscillations. *AIAA Journal*, 40(4):638–646, 2002. ISSN 0001-1452. doi: 10.2514/2.1720. URL https://doi.org/10.2514/2.1720.

[30] Joseph Katz and Allen Plotkin. *Low-Speed Aerodynamics*. Cambridge University Press, Cambridge, 2 edition edition, February 2001. ISBN 978-0-521-66552-0.

[31] A. V. Balakrishnan. Transonic Small Disturbance Potential Equation. *AIAA Journal*, 42(6):1081–1088, 2004. ISSN 0001-1452. doi: 10.2514/1.5101. URL https://doi.org/10.2514/1.5101. Publisher: American Institute of Aeronautics and Astronautics _eprint: https://doi.org/10.2514/1.5101.

[32] Tuncer Cebeci and Jean Cousteix. *Modeling and Computation of Boundary-Layer Flows: Laminar, Turbulent and Transitional Boundary Layers in Incompressible and*

Compressible Flows. Springer-Verlag, Berlin Heidelberg, 2 edition, 2005. ISBN 978-3-540-27624-1. URL //www.springer.com/la/book/9783540276241.

[33] John T. Batina. Efficient algorithm for solution of the unsteady transonic small-disturbance equation. *Journal of Aircraft*, 25(7):598–605, July 1988. doi: 10.2514/3.45629. URL https://arc.aiaa.org/doi/10.2514/3.45629. Publisher: American Institute of Aeronautics and Astronautics.

[34] T. M. van Opstal, S. J. Hulshoff, and C. V. Verhoosel. A Robust Solution Procedure for the Transonic Small-Disturbance Equation in Fluid-Structure Interactions. *The Open Aerospace Engineering Journal*, 4(1), March 2011. URL https://benthamopen.com/ABSTRACT/TOAEJ-4-1.

[35] Robert M. Bennett, John T. Batina, and Herbert J. Cunningham. Wing-flutter calculations with the CAP-TSD unsteady transonic small-disturbance program. *Journal of Aircraft*, 26(9):876–882, 1989. doi: 10.2514/3.45854. URL https://doi.org/10.2514/3.45854. Publisher: American Institute of Aeronautics and Astronautics _eprint: https://doi.org/10.2514/3.45854.

[36] E. Carson Yates. AGARD standard aeroelastic configurations for dynamic response. Candidate configuration I.-wing 445.6. Technical report, August 1987. URL https://ntrs.nasa.gov/search.jsp?R=19880001820.

[37] John Anderson. *Fundamentals of Aerodynamics*. McGraw-Hill Education, New York, 5 edition edition, February 2010. ISBN 978-0-07-339810-5.

[38] Brian Maskew. Program VSAERO theory document: A computer program for calculating nonlinear aerodynamic characteristics of arbitrary configurations. Technical Report NASA-CR-4023, NASA, September 1987. URL https://ntrs.nasa.gov/search.jsp?R=19900004884.

[39] J. L. Hess and A. M. O. Smith. Calculation of potential flow about arbitrary bodies. *Progress in Aerospace Sciences*, 8:1–138, January 1967. ISSN 0376-0421. doi: 10.1016/0376-0421(67)90003-6. URL http://www.sciencedirect.com/science/article/pii/0376042167900036.

[40] Kenneth C. Hall, Jeffrey P. Thomas, and W. S. Clark. Computation of Unsteady Nonlinear Flows in Cascades Using a Harmonic Balance Technique. *AIAA Journal*, 40 (5):879–886, 2002. ISSN 0001-1452. doi: 10.2514/2.1754. URL https://doi.org/10.2514/2.1754.

[41] Arathi Gopinath and Antony Jameson. Time Spectral Method for Periodic Unsteady Computations over Two- and Three- Dimensional Bodies. In *43rd AIAA Aerospace Sciences Meeting and Exhibit*, Reno, Nevada, January 2005. American Institute of Aeronautics and Astronautics. doi: 10.2514/6.2005-1220. URL https://arc.aiaa.org/doi/abs/10.2514/6.2005-1220.

[42] Matthew McMullen, Antony Jameson, and Juan Alonso. Acceleration of convergence to a periodic steady state in turbomachinery flows. In *39th Aerospace Sciences Meeting and Exhibit*, Reno, Nevada, January 2001. American Institute of Aeronautics and Astronautics. doi: 10.2514/6.2001-152. URL https://arc.aiaa.org/doi/abs/10.2514/6.2001-152.

[43] Kenneth C. Hall, Kivanc Ekici, Jeffrey P. Thomas, and Earl H. Dowell. Harmonic balance methods applied to computational fluid dynamics problems. *International Journal of Computational Fluid Dynamics*, 27(2):52–67, February 2013. ISSN 1061-8562. doi: 10.1080/10618562.2012.742512. URL https://doi.org/10.1080/10618562.2012.742512.

[44] T. M. Cameron and J. H. Griffin. An Alternating Frequency/Time Domain Method for Calculating the Steady-State Response of Nonlinear Dynamic Systems. *Journal of Applied Mechanics*, 56(1):149–154, March 1989. ISSN 0021-8936. doi: 10.1115/1.3176036. URL http://dx.doi.org/10.1115/1.3176036.

[45] Weigang Yao and Simão Marques. Application of a high-order CFD harmonic balance method to nonlinear aeroelasticity. *Journal of Fluids and Structures*, 74(Supplement C):427–444, October 2017. ISSN 0889-9746. doi: 10.1016/j.jfluidstructs.2017.06.014. URL http://www.sciencedirect.com/science/article/pii/S0889974616300615.

[46] Sergio González Horcas, François Debrabandere, Benoît Tartinville, Charles Hirsch, and Grégory Coussement. Extension of the Non-Linear Harmonic method for the study of the dynamic aeroelasticity of horizontal axis wind turbines. *Journal of Fluids and Structures*, 73:100–124, August 2017. ISSN 0889-9746. doi: 10.1016/j.jfluidstructs.2017.06.008. URL http://www.sciencedirect.com/science/article/pii/S0889974616306302.

[47] A. C. L. M. van Rooij, J. Nitzsche, and R. P. Dwight. Prediction of Aeroelastic Limit-Cycle Oscillations Based on Harmonic Forced-Motion Oscillations. *AIAA Journal*, 55 (10):3517–3529, June 2017. ISSN 0001-1452. doi: 10.2514/1.J055852. URL https://doi.org/10.2514/1.J055852.

[48] Tobias Mauermann. *Flexible Aircraft Modelling for Flight Loads Analysis of Wake Vortex Encounters*. PhD thesis, Institute of Aeroelasticity Gottingen, June 2010.

[49] G. Dimitriadis, N. F. Giannelis, and G. A. Vio. A modal frequency-domain generalised force matrix for the unsteady Vortex Lattice method. *Journal of Fluids and Structures*, 76(Supplement C):216–228, January 2018. ISSN 0889-9746. doi: 10.1016/j.jfluidstructs.2017.10.010. URL http://www.sciencedirect.com/science/article/pii/S088997461730186X.

[50] Eduardo Manuel Pizarro Gomes Pepe. *Numerical Implementation of a Frequency-Domain Panel Method for Flutter Prediction of a 3D Wing*. PhD thesis, Instituto Superior Técnico, Lisboa, Portugal, April 2015.

[51] M. K. Laha. A vortex lattice method for thin wings oscillating in ideal flow. *The Aeronautical Journal*, 97(969):314–320, November 1993. ISSN 0001-9240, 2059-6464. doi: 10.1017/S0001924000026567. URL https://www.cambridge.org/core/journals/aeronautical-journal/article/vortex-lattice-method-for-thin-wings-oscillating-in-ideal-flow/12B8B7A5C83582CE7A2EC4BB89541F6D.

[52] Matthieu Parenteau, Gérald Carrier, and Éric Laurendeau. Multidisciplinary Design Optimization of Wing Planform Using a Coupled VLM/RANS Solver. Toronto, May 2017. Canadian Aeronautics and Space Institute.

[53] E. Albano and W. P. Rodden. A doublet-lattice method for calculating lift distributions on oscillating surfaces in subsonic flows. *AIAA Journal*, 7(2):279–285, 1969. ISSN 0001-1452. doi: 10.2514/3.5086. URL https://arc.aiaa.org/doi/abs/10.2514/3.5086.

[54] W. P. Rodden, J. P. Giesing, and T. P. Kalman. Refinement of the nonplanar aspects of the subsonic doublet-lattice lifting surface method. *Journal of Aircraft*, 9(1):69–73, 1972. ISSN 0021-8669. doi: 10.2514/3.44322. URL https://doi.org/10.2514/3.44322.

[55] T. P. Kalman, W. P. Rodden, and J. P. Giesing. Application of the Doublet-Lattice Method to Nonplanar Configurations in Subsonic Flow. *Journal of Aircraft*, 8(6):406–413, 1971. doi: 10.2514/3.59117. URL https://doi.org/10.2514/3.59117.

[56] Max Blair. A Compilation of the Mathematics Leading to the Doublet Lattice Method. Technical report, Wright Laborator, December 1991. URL http://www.dtic.mil/dtic/tr/fulltext/u2/a256304.pdf.

[57] William P. Rodden, Paul F. Taylor, and Samuel C. McIntosh. Further Refinement of the Subsonic Doublet-Lattice Method. *Journal of Aircraft*, 35(5):720–727, 1998. ISSN 0021-8669. doi: 10.2514/2.2382. URL https://doi.org/10.2514/2.2382.

[58] C. Rehbach. Numerical calculation of three-dimensional unsteady flows with vortex sheets. *La Recherche Aerospatiale, Sept.-Oct. 1977, p. 289-298. In French.*, pages 289–298, October 1977. ISSN 0379-380X. URL http://adsabs.harvard.edu/abs/1977ReAer.....289R.

[59] S M Belotserkovskii. Study of the Unsteady Aerodynamics of Lifting Surfaces Using the Computer. *Annual Review of Fluid Mechanics*, 9(1):469–494, 1977. doi: 10.1146/annurev.fl.09.010177.002345. URL https://doi.org/10.1146/annurev.fl.09.010177.002345. _eprint: https://doi.org/10.1146/annurev.fl.09.010177.002345.

[60] Joseba Murua. *Flexible Aircraft Dynamics with a Geometrically-Nonlinear Description of the Unsteady Aerodynamics*. PhD thesis, Imperial College London, May 2012.

[61] Minu Jeon, Seunghoon Lee, and Soogab Lee. Unsteady vortex lattice method coupled with a linear aeroelastic model for horizontal axis wind turbine. *Journal of Renewable and Sustainable Energy*, 6(4):042006, July 2014. doi: 10.1063/1.4890830. URL https://aip.scitation.org/doi/abs/10.1063/1.4890830.

[62] Thomas Lambert, Norizham Abdul Razak, and Grigorios Dimitriadis. Vortex Lattice Simulations of Attached and Separated Flows around Flapping Wings. *Aerospace*, 4(2):22, April 2017. doi: 10.3390/aerospace4020022. URL http://www.mdpi.com/2226-4310/4/2/22.

[63] A. Röttgermann, R. Behr, Ch. Schöttl, and S. Wagner. Calculation of Blade-Vortex Interaction of Rotary Wings in Incompressible Flow by an Unsteady Vortex-Lattice Method Including Free Wake Analysis. In Wolfgang Hackbusch, editor, *Numerical Techniques for Boundary Element Methods*, Notes on Numerical Fluid Mechanics (NNFM), pages 153–166. Vieweg+Teubner Verlag, Wiesbaden, 1992. ISBN 978-3-663-14005-4.

[64] Joseba Murua, Rafael Palacios, and J. Michael R. Graham. Applications of the unsteady vortex-lattice method in aircraft aeroelasticity and flight dynamics. *Progress in Aerospace Sciences*, 55:46–72, November 2012. ISSN 0376-0421. doi: 10.1016/j.paerosci.2012.06.001. URL http://www.sciencedirect.com/science/article/pii/S0376042112000620.

[65] Joseba Murua, Pablo Martínez, Héctor Climent, Louw van Zyl, and Rafael Palacios. T-tail flutter: Potential-flow modelling, experimental validation and flight tests. *Progress in Aerospace Sciences*, 71:54–84, November 2014. ISSN 0376-0421. doi: 10.1016/j.paerosci.2014.07.002. URL http://www.sciencedirect.com/science/article/pii/S0376042114000669.

[66] Louw H. van Zyl and Edward H. Mathews. Aeroelastic Analysis of T-Tails Using an Enhanced Doublet Lattice Method. *Journal of Aircraft*, 48(3):823–831, May 2011. doi: 10.2514/1.C001000. URL https://arc.aiaa.org/doi/10.2514/1.C001000.

[67] H. G. Küssner. General Airfoil Theory. Technical Report 979, NACA, June 1941. URL https://ntrs.nasa.gov/citations/19930094437.

[68] Carmine Valente, Christopher Wales, Dorian Jones, Ann Gaitonde, Jonathan E. Cooper, and Yves Lemmens. A Doublet-Lattice Method Correction Approach for High Fidelity Gust Loads Analysis. In *58th AIAA/ASCE/AHS/ASC Structures, Structural Dynamics, and Materials Conference*. American Institute of Aeronautics and Astronautics. doi: 10.2514/6.2017-0632. URL https://arc.aiaa.org/doi/abs/10.2514/6.2017-0632.

[69] Rafael Palacios, H. Climent, A. Karlsson, and B. Winzell. Assessment of Strategies for Correcting Linear Unsteady Aerodynamics using CFD or Test Results. In *International Forum on Aeroelasticity and Structural Dynamics*, pages 195–210, Madrid, Spain, 2001. URL https://spiral.imperial.ac.uk/bitstream/10044/1/1359/1/IFASD2001-074.pdf.

[70] J. Brink-Spalink and J. Bruns. Correction of unsteady aerodynamic influence coefficients using experimental or CFD data. In *41st Structures, Structural Dynamics, and Materials Conference and Exhibit*. American Institute of Aeronautics and Astronautics. doi: 10.2514/6.2000-1489. URL https://arc.aiaa.org/doi/abs/10.2514/6.2000-1489. _eprint: https://arc.aiaa.org/doi/pdf/10.2514/6.2000-1489.

[71] J. P. Kalman Giesing. Correction factory techniques for improving aerodynamic prediction methods. Technical report, May 1976. URL https://ntrs.nasa.gov/search.jsp?R=19760016071.

[72] Jean-Jacques Chattot. Analysis and Design of Wings and Wing/Winglet Combinations at Low Speeds. In *42nd AIAA Aerospace Sciences Meeting and Exhibit*, Reno, Nevada, 2004. American Institute of Aeronautics and Astronautics. doi: DOI: 10.2514/6.2004-220. URL https://arc.aiaa.org/doi/abs/10.2514/6.2004-220.

[73] S. Gallay and E. Laurendeau. Nonlinear Generalized Lifting-Line Coupling Algorithms for Pre/Poststall Flows. *AIAA Journal*, 53(7):1784–1792, 2015. ISSN 0001-1452. doi: 10.2514/1.J053530. URL https://doi.org/10.2514/1.J053530.

[74] Sylvain Gallay, Shahin Ghasemi, and Eric Laurendeau. Sweep effects on non-linear Lifting Line Theory near Stall. In *52nd Aerospace Sciences Meeting*. American Institute of Aeronautics and Astronautics, July 2017. URL https://arc.aiaa.org/doi/abs/10.2514/6.2014-1105.

[75] C. P. van Dam. The aerodynamic design of multi-element high-lift systems for transport airplanes. *Progress in Aerospace Sciences*, 38(2):101–144, February 2002. ISSN 0376-0421. doi: 10.1016/S0376-0421(02)00002-7. URL http://www.sciencedirect.com/science/article/pii/S0376042102000027.

[76] Sylvain Gallay. *Algorithmes de couplage RANS et ecoulement potentiel*. phd, Ecole Polytechnique de Montreal, February 2016. URL https://publications.polymtl.ca/2061/.

[77] W. R. Sears. Some Recent Developments in Airfoil Theory. *Journal of the Aeronautical Sciences*, 23(5):490–499, 1956. doi: 10.2514/8.3588. URL https://doi.org/10.2514/8.3588.

[78] J. B. Lan Tseng. Calculation of aerodynamic characteristics of airplane configurations at high angles of attack. Technical report, NASA, October 1988. URL https://ntrs.nasa.gov/search.jsp?R=19880019507.

[79] Rinku Mukherjee, Ashok Gopalarathnam, and Sung Wa Kim. An Iterative Decambering Approach for Post-Stall Prediction of Wing Characteristics using known Section Data. In *41nd AIAA Aerospace Sciences Meeting and Exhibit*, Reno, Nevada, 2003. American Institute of Aeronautics and Astronautics. URL http://archive.org/details/nasa_techdoc_20040085758.

[80] Rinku Mukherjee and Ashok Gopalarathnam. Post-Stall Prediction of Multiple-Lifting-Surface Configurations Using a Decambering Approach. In *42nd AIAA Aerospace Sciences Meeting and Exhibit*. American Institute of Aeronautics and Astronautics, July 2017. URL https://arc.aiaa.org/doi/abs/10.2514/6.2004-219.

[81] Matthieu Parenteau, Kurt Sermeus, and Eric Laurendeau. VLM Coupled with 2.5D RANS Sectional Data for High-Lift Design. In *2018 AIAA Aerospace Sciences Meeting*, Orlando, January 2018. American Institute of Aeronautics and Astronautics.

[82] Simon Bourgault-Côté, Shahin Ghasemi, Ali Mosahebi, and Éric Laurendeau. Extension of a Two-Dimensional Navier–Stokes Solver for Infinite Swept Flow. *AIAA Journal*, 55(2):662–667, 2017. ISSN 0001-1452. doi: 10.2514/1.J055139. URL https://doi.org/10.2514/1.J055139.

[83] Alexandros Kontogiannis, Matthieu Parenteau, and Eric Laurendeau. Viscous-Inviscid Analysis of Transonic Swept Wings using 2.5D RANS and Parametric Shapes. In *AIAA Scitech 2019 Forum*. American Institute of Aeronautics and Astronautics. doi: 10.2514/6.2019-2116. URL https://arc.aiaa.org/doi/abs/10.2514/6.2019-2116.

[84] Matthieu Parenteau, Gérald Carrier, and Eric Laurendeau. Combined High-speed and High-lift Wing Aerodynamic Optimization Using a Coupled VLM-2.5D RANS Approach. *Progress in Aerospace Sciences*.

[85] Matthieu Parenteau and Éric Laurendeau. Nonlinear Frequency-Domain Solver for Vortex Lattice Method. *AIAA Journal*, 56(6):2242–2251, 2018. ISSN 0001-1452. doi: 10.2514/1.J056704. URL https://doi.org/10.2514/1.J056704. Publisher: American Institute of Aeronautics and Astronautics _eprint: https://doi.org/10.2514/1.J056704.

[86] S. Gallay and E. Laurendeau. Preliminary-Design Aerodynamic Model for Complex Configurations Using Lifting-Line Coupling Algorithm. *Journal of Aircraft*, 53(4):1145–1159, 2016. ISSN 0021-8669. doi: 10.2514/1.C033460. URL https://doi.org/10.2514/1.C033460.

[87] Atanas Grozdanov and Eric Laurendeau. TRANSONIC AEROELASTICITY USING THE 2.5D NON-LINEARVORTEX-LATTICE METHOD. In *International Forum on Aeroelasticity and Structural Dynamics*, Como, Italy, June 2017. URL https://www.asdjournal.org/public/Proceedings/IFASD_2017/IFASD-2017-079.pdf.

[88] Robert D. Cook David S. Malkus Michael E. Plesha Robert J. Witt. *Concepts and Applications of Finite Element Analysis, 4th Edition*. Wiley, New York, NY, 2001. ISBN 978-0-471-35605-9.

[89] A. Dharmasaroja, C. G. Armstrong, A. Murphy, T. T. Robinson, S. H. M. McGuinness, N. L. Iorga, and J. R. Barron. Load Case Characterization for the Aircraft Structural Design Process. *AIAA Journal*, 55(8):2783–2792, May 2017. ISSN 0001-1452. doi: 10.2514/1.J055544. URL https://arc.aiaa.org/doi/10.2514/1.J055544. Publisher: American Institute of Aeronautics and Astronautics.

[90] E. Garrigues. A Review of Industrial Aeroelasticity Practices at Dassault Aviation for Military Aircraft and Business Jets. pages 1–34, 2018. doi: 0.12762/2018.AL14-09.

[91] Paul Vazhayil Thomas, Mostafa S. A. ElSayed, and Denis Walch. Development of high fidelity reduced order hybrid stick model for aircraft dynamic aeroelasticity analysis. *Aerospace Science and Technology*, February 2019. ISSN 1270-9638. doi: 10.1016/j.ast.2019.02.030. URL http://www.sciencedirect.com/science/article/pii/S1270963818316675.

[92] Mostafa S. A. Elsayed, Ramin Sedaghati, and Mohammed Abdo. Accurate Stick Model Development for Static Analysis of Complex Aircraft Wing-Box Structures. *AIAA Journal*, 47(9):2063–2075, September 2009. ISSN 0001-1452. doi: 10.2514/1.38447. URL https://arc.aiaa.org/doi/10.2514/1.38447.

[93] Matthieu Parenteau, Simon Bourgault-Cote, Frédéric Plante, Engin Kayraklioglu, and Eric Laurendeau. Development of Parallel CFD Applications with the Chapel Programming Language. In *AIAA Scitech 2021 Forum*, AIAA SciTech Forum. American Institute of Aeronautics and Astronautics, January 2021. doi: 10.2514/6.2021-0749. URL https://arc.aiaa.org/doi/10.2514/6.2021-0749.

[94] Chapel: Productive Parallel Programming, . URL https://chapel-lang.org/.

[95] E Pistolesi. Considerations on the Mutual Interference of Aerofoil Systems. Technical report, L.G.L., 1937.

[96] H. van der Vorst. Bi-CGSTAB: A Fast and Smoothly Converging Variant of Bi-CG for the Solution of Nonsymmetric Linear Systems. *SIAM Journal on Scientific and Statistical Computing*, 13(2):631–644, March 1992. ISSN 0196-5204. doi: 10.1137/0913035. URL http://epubs.siam.org/doi/abs/10.1137/0913035.

[97] Seong Yong Wie, Seongkyu Lee, and Duck Joo Lee. Potential Panel and Time-Marching Free-Wake-Coupling Analysis for Helicopter Rotor. *Journal of Aircraft*, 46(3):1030–1041, May 2009. doi: 10.2514/1.40001. URL https://arc.aiaa.org/doi/10.2514/1.40001. Publisher: American Institute of Aeronautics and Astronautics.

[98] G. H. Vatistas, V. Kozel, and W. C. Mih. A simpler model for concentrated vortices. *Experiments in Fluids*, 11(1):73–76, April 1991. ISSN 1432-1114. doi: 10.1007/BF00198434. URL https://doi.org/10.1007/BF00198434.

[99] M. (Michael) Scully. *Computation of helicopter rotor wake geometry and its influence on rotor harmonic airloads*. Thesis, Massachusetts Institute of Technology, 1975. URL

https://dspace.mit.edu/handle/1721.1/64826. Accepted: 2011-07-18T13:51:05Z ISSN: 0193-4929.

[100] Abu Kebbie-Anthony, Nail A. Gumerov, Sergio Preidikman, Balakumar Balachandran, and Shapour Azarm. Fast Multipole Accelerated Unsteady Vortex Lattice Method Based Computations. *Journal of Aerospace Information Systems*, 16(6):237–248, April 2019. doi: 10.2514/1.I010690. URL https://arc.aiaa.org/doi/10.2514/1.I010690. Publisher: American Institute of Aeronautics and Astronautics.

[101] Robert J. S. Simpson, Rafael Palacios, and Joseba Murua. Induced-Drag Calculations in the Unsteady Vortex Lattice Method. *AIAA Journal*, 51(7):1775–1779, 2013. ISSN 0001-1452. doi: 10.2514/1.J052136. URL https://doi.org/10.2514/1.J052136.

[102] Theodore Theodorsen. General Theory of Aerodynamic Instability and the Mechanism of Flutter. Technical Report 496, NACA, January 1949. URL https://ntrs.nasa.gov/search.jsp?R=19930090935.

[103] Herbert Wagner. Über die Entstehung des dynamischen Auftriebes von Tragflügeln. *ZAMM - Journal of Applied Mathematics and Mechanics / Zeitschrift für Angewandte Mathematik und Mechanik*, 5(1):17–35, January 1925. ISSN 1521-4001. doi: 10.1002/zamm.19250050103. URL http://onlinelibrary.wiley.com/doi/10.1002/zamm.19250050103/abstract.

[104] C. Farhat, M. Lesoinne, and P. Le Tallec. Load and motion transfer algorithms for fluid/structure interaction problems with non-matching discrete interfaces: Momentum and energy conservation, optimal discretization and application to aeroelasticity. *Computer Methods in Applied Mechanics and Engineering*, 157(1):95–114, April 1998. ISSN 0045-7825. doi: 10.1016/S0045-7825(97)00216-8. URL http://www.sciencedirect.com/science/article/pii/S0045782597002168.

[105] Holger Wendland. *Scattered Data Approximation*. Cambridge Monographs on Applied and Computational Mathematics. Cambridge University Press, Cambridge, 2004. ISBN 978-0-521-84335-5. doi: 10.1017/CBO9780511617539. URL https://www.cambridge.org/core/books/scattered-data-approximation/980EEC9DBC4CAA711D089187818135E3.

[106] Thomas Rendall and Christian Allen. Efficient Mesh Motion Using Radial Basis Functions with Data Reduction Algorithms. In *46th AIAA Aerospace Sciences Meeting and*

Exhibit, Aerospace Sciences Meetings. American Institute of Aeronautics and Astronautics, January 2008. doi: 10.2514/6.2008-305. URL https://arc.aiaa.org/doi/10.2514/6.2008-305.

[107] Andreas K. Michler. Aircraft control surface deflection using RBF-based mesh deformation. *International Journal for Numerical Methods in Engineering*, 88(10):986–1007, 2011. ISSN 1097-0207. doi: 10.1002/nme.3208. URL https://onlinelibrary.wiley.com/doi/abs/10.1002/nme.3208. _eprint: https://onlinelibrary.wiley.com/doi/pdf/10.1002/nme.3208.

[108] L. Kedward, C. B. Allen, and T. C. S. Rendall. Efficient and exact mesh deformation using multiscale RBF interpolation. *Journal of Computational Physics*, 345:732–751, September 2017. ISSN 0021-9991. doi: 10.1016/j.jcp.2017.05.042. URL https://www.sciencedirect.com/science/article/pii/S0021999117304254.

[109] Chunhua Sheng and Christian B. Allen. Efficient Mesh Deformation Using Radial Basis Functions on Unstructured Meshes. *AIAA Journal*, 51(3):707–720, 2013. ISSN 0001-1452. doi: 10.2514/1.J052126. URL https://doi.org/10.2514/1.J052126. Publisher: American Institute of Aeronautics and Astronautics _eprint: https://doi.org/10.2514/1.J052126.

[110] T. C. S. Rendall and C. B. Allen. Efficient mesh motion using radial basis functions with data reduction algorithms. *Journal of Computational Physics*, 228(17):6231–6249, September 2009. ISSN 0021-9991. doi: 10.1016/j.jcp.2009.05.013. URL http://www.sciencedirect.com/science/article/pii/S0021999109002721.

[111] A. de Boer, M. S. van der Schoot, and H. Bijl. Mesh deformation based on radial basis function interpolation. *Computers & Structures*, 85(11):784–795, June 2007. ISSN 0045-7949. doi: 10.1016/j.compstruc.2007.01.013. URL http://www.sciencedirect.com/science/article/pii/S0045794907000223.

[112] Christian Allen and Thomas Rendall. Unified Approach to CFD-CSD Interpolation and Mesh Motion Using Radial Basis Functions. In *25th AIAA Applied Aerodynamics Conference*. American Institute of Aeronautics and Astronautics. doi: 10.2514/6.2007-3804. URL https://arc.aiaa.org/doi/abs/10.2514/6.2007-3804.

[113] R. K. Beatson, J. Levesley, and C. T. Mouat. Better bases for radial basis function interpolation problems. *Journal of Computational and Applied Mathematics*, 236(4):434–446, September 2011. ISSN 0377-0427. doi: 10.1016/j.cam.2011.06.030. URL http://www.sciencedirect.com/science/article/pii/S0377042711003669.

[114] Marilyn Smith, Carlos Cesnik, Dewey Hodges, and Kenneth Moran. An evaluation of computational algorithms to interface between CFD and CSD methodologies. In *37th Structure, Structural Dynamics and Materials Conference*. American Institute of Aeronautics and Astronautics. doi: 10.2514/6.1996-1400. URL https://arc.aiaa.org/doi/abs/10.2514/6.1996-1400.

[115] T. C. S. Rendall and C. B. Allen. Unified fluid–structure interpolation and mesh motion using radial basis functions. *International Journal for Numerical Methods in Engineering*, 74(10):1519–1559, 2008. ISSN 1097-0207. doi: 10.1002/nme.2219. URL https://onlinelibrary.wiley.com/doi/abs/10.1002/nme.2219. _eprint: https://onlinelibrary.wiley.com/doi/pdf/10.1002/nme.2219.

[116] Holger Wendland. Piecewise polynomial, positive definite and compactly supported radial functions of minimal degree. *Advances in Computational Mathematics*, 4(1): 389–396, December 1995. ISSN 1572-9044. doi: 10.1007/BF02123482. URL https://doi.org/10.1007/BF02123482.

[117] Robert J. Simpson and Rafael Palacios. Numerical aspects of nonlinear flexible aircraft flight dynamics modeling. In *54th AIAA/ASME/ASCE/AHS/ASC Structures, Structural Dynamics, and Materials Conference*. American Institute of Aeronautics and Astronautics, 2013. URL https://arc.aiaa.org/doi/abs/10.2514/6.2013-1634.

[118] Nathan L. Mundis and Dimitri J. Mavriplis. GMRES applied to the Time Spectral and Quasi-periodic Time Spectral Methods. In *21st AIAA Computational Fluid Dynamics Conference*, AIAA 2013-3084, San Diego, CA, June 2013. American Institute of Aeronautics and Astronautics. doi: 10.2514/6.2013-3084. URL https://arc.aiaa.org/doi/abs/10.2514/6.2013-3084.

[119] D. Kuchemann. A Simple Method for Calculating the Span and Chordwise Loading on Straight and Swept Wings of any Given Aspect Ratio at Subsonic Speeds. Technical Report ARC-R/M-2935, AERONAUTICAL RESEARCH COUNCIL LONDON (ENGLAND), AERONAUTICAL RESEARCH COUNCIL LONDON (ENGLAND), August 1952. URL http://www.dtic.mil/docs/citations/ADA951920.

[120] A. Rosen and O. Rand. The aerodynamic behavior of infinite swept wings - Another point of view. *Journal of Aircraft*, 22(1):83–85, 1985. doi: 10.2514/3.45084. URL https://doi.org/10.2514/3.45084. Publisher: American Institute of Aeronautics and Astronautics _eprint: https://doi.org/10.2514/3.45084.

[121] Jackson Reid. *A General Approach to Lifting-Line Theory, Applied to Wings with Sweep*. PhD thesis, August 2020. URL https://digitalcommons.usu.edu/etd/7842.

[122] Matthieu Parenteau, Frederic Plante, Eric Laurendeau, and Michel Costes. Unsteady Coupling Algorithm for Lifting-Line Methods. In *55th AIAA Aerospace Sciences Meeting*, Dallas, January 2017. American Institute of Aeronautics and Astronautics. doi: 10.2514/6.2017-0951. URL https://arc.aiaa.org/doi/abs/10.2514/6.2017-0951.

[123] Tuncer Cebeci, Jian P. Shao, Fassi Kafyeke, and Eric Laurendeau. *Computational Fluid Dynamics for Engineers: From Panel to Navier-Stokes Methods with Computer Programs*. Springer-Verlag, Berlin Heidelberg, 2005. ISBN 978-3-540-27717-0. doi: 10.1007/3-540-27717-X. URL https://www.springer.com/gp/book/9783540277170.

[124] Noud P. M. Werter, Roeland De Breuker, and Mostafa M. Abdalla. Continuous-Time State-Space Unsteady Aerodynamic Modeling for Efficient Loads Analysis. *AIAA Journal*, 56(3):905–916, 2018. ISSN 0001-1452. doi: 10.2514/1.J056068. URL https://doi.org/10.2514/1.J056068. Publisher: American Institute of Aeronautics and Astronautics _eprint: https://doi.org/10.2514/1.J056068.

[125] Ashish Tewari. *Aeroservoelasticity: Modeling and Control*. Control Engineering. Springer-Verlag, New York, 2015. ISBN 978-1-4939-2367-0. doi: 10.1007/978-1-4939-2368-7. URL https://www.springer.com/gp/book/9781493923670.

[126] P. Spalart and S. Allmaras. A one-equation turbulence model for aerodynamic flows. In *30th Aerospace Sciences Meeting and Exhibit*, Aerospace Sciences Meetings. American Institute of Aeronautics and Astronautics, January 1992. doi: 10.2514/6.1992-439. URL https://arc.aiaa.org/doi/10.2514/6.1992-439.

[127] Antony Jameson. Time dependent calculations using multigrid, with applications to unsteady flows past airfoils and wings. In *10th Computational Fluid Dynamics Conference*, Fluid Dynamics and Co-located Conferences. American Institute of Aeronautics and Astronautics, June 1991. doi: 10.2514/6.1991-1596. URL https://arc.aiaa.org/doi/10.2514/6.1991-1596.

[128] Jeffrey P. Thomas, Earl H. Dowell, and Kenneth C. Hall. A Harmonic Balance Approach for Modeling Three-Dimensional Nonlinear Unsteady Aerodynamics and Aeroelasticity. pages 1323–1334. American Society of Mechanical Engineers Digital Collection, June 2008. doi: 10.1115/IMECE2002-32532. URL https://asmedigitalcollection.asme.org/IMECE/proceedings/IMECE2002/36592/1323/297092.

[129] Jeffrey P. Thomas, Earl H. Dowell, and Kenneth C. Hall. Modeling Viscous Transonic Limit Cycle Oscillation Behavior Using a Harmonic Balance Approach. *Journal of Aircraft*, 41(6):1266–1274, 2004. doi: 10.2514/1.9839. URL https://doi.org/10.2514/1.9839. Publisher: American Institute of Aeronautics and Astronautics _eprint: https://doi.org/10.2514/1.9839.

[130] Jordan B. Schwarz, Earl H. Dowell, Jeffrey P. Thomas, Kenneth C. Hall, Russ D. Rausch, and Robert E. Bartels. Improved Flutter Boundary Prediction for an Isolated Two-Degree-of-Freedom Airfoil. *Journal of Aircraft*, 46(6):2069–2076, 2009. doi: 10.2514/1.30703. URL https://doi.org/10.2514/1.30703. Publisher: American Institute of Aeronautics and Astronautics _eprint: https://doi.org/10.2514/1.30703.

[131] Koji Isogai. Transonic dip mechanism of flutter of a sweptback wing. II. *AIAA Journal*, 19(9):1240–1242, 1981. ISSN 0001-1452. doi: 10.2514/3.7853. URL https://doi.org/10.2514/3.7853. Publisher: American Institute of Aeronautics and Astronautics _eprint: https://doi.org/10.2514/3.7853.

[132] Koji Isogai. On the Transonic-Dip Mechanism of Flutter of a Sweptback Wing. *AIAA Journal*, 17(7):793–795, 1979. ISSN 0001-1452. doi: 10.2514/3.61226. URL https://doi.org/10.2514/3.61226. Publisher: American Institute of Aeronautics and Astronautics _eprint: https://doi.org/10.2514/3.61226.

[133] S. Timme and K. J. Badcock. Oscillatory Behavior of Transonic Aeroelastic Instability Boundaries. *AIAA Journal*, 47(6):1590–1592, June 2009. ISSN 0001-1452. doi: 10.2514/1.40497. URL https://arc.aiaa.org/doi/10.2514/1.40497. Publisher: American Institute of Aeronautics and Astronautics.

[134] Hang Li and Kivanc Ekici. A novel approach for flutter prediction of pitch–plunge airfoils using an efficient one-shot method. *Journal of Fluids and Structures*, 82:651–671, October 2018. ISSN 0889-9746. doi: 10.1016/j.jfluidstructs.2018.08.012. URL http://www.sciencedirect.com/science/article/pii/S0889974618301932.

[135] Jennifer Heeg, Pawel Chwalowski, Daniella E. Raveh, Adam Jirasek, and Mats Dalenbring. Overview and Data Comparisons from the 2nd Aeroelastic Prediction Workshop. In *34th AIAA Applied Aerodynamics Conference*, AIAA AVIATION Forum. American Institute of Aeronautics and Astronautics, June 2016. doi: 10.2514/6.2016-3121. URL https://arc.aiaa.org/doi/10.2514/6.2016-3121.

[136] F. R. Menter. Two-equation eddy-viscosity turbulence models for engineering applications. *AIAA Journal*, 32(8):1598–1605, 1994. ISSN 0001-1452. doi: 10.2514/3.12149.

URL https://doi.org/10.2514/3.12149. Publisher: American Institute of Aeronautics and Astronautics _eprint: https://doi.org/10.2514/3.12149.

[137] Walter A. Silva, Pawel Chwalowski, and Boyd N. Perry. Evaluation of Linear, Inviscid, Viscous, and Reduced-Order Modeling Aeroelastic Solutions of the AGARD 445.6 Wing Using Root Locus Analysis. In *55th AIAA/ASME/ASCE/AHS/ASC Structures, Structural Dynamics, and Materials Conference*. American Institute of Aeronautics and Astronautics, January 2014. doi: 10.2514/6.2014-0496. URL https://arc.aiaa.org/doi/abs/10.2514/6.2014-0496. _eprint: https://arc.aiaa.org/doi/pdf/10.2514/6.2014-0496.

[138] Alexandros Kontogiannis and Eric Laurendeau. Adjoint State of Nonlinear Vortex-Lattice Method for Aerodynamic Design and Control. *AIAA Journal*, 59(4):1184–1195, February 2021. ISSN 0001-1452. doi: 10.2514/1.J059796. URL https://arc.aiaa.org/doi/10.2514/1.J059796. Publisher: American Institute of Aeronautics and Astronautics.

[139] Robert T. Jones. Operational treatment of the nonuniform-lift theory in airplane dynamics. October 1938. URL http://ntrs.nasa.gov/search.jsp?R=19930081472.

[140] Denis Kholodar. *Aeroelastic response of an airfoil with structural and aerodynamic nonlinearities*. PhD thesis, 2002. OCLC: 51858026.

APPENDIX A VALIDATION OF THE TIME DOMAIN UVLM

The lift calculation from Theodorsen[102] is divided in two components, a circulatory contribution and an apparent mass constribution.

$$L_{Theodorsen} = \rho b^2\Big(U_\infty \pi\dot{\alpha} + \pi\ddot{h} - \pi b a\ddot{\alpha}\Big) + 2\pi\rho U_\infty bC(k)\Big(U_\infty\alpha + \dot{h} + b(\frac{1}{2} - a)\dot{\alpha}\Big) \tag{A.1}$$

Where C(k) is the complex Theodorsen Function in the form of Hankel functions H

$$C(k) = F(k) + iG(k) \tag{A.2}$$

$$= \frac{H_1^{(2)}(k)}{H_1^{(2)}(k) + iH_0^{(2)}(k)} \tag{A.3}$$

Because of the Theodorsen Function $C(k)$, this lift formulation is restricted to simple harmonic oscillations. It is possible to extend the lift formulation from Theodorsen to arbritrary motion by changing the part of the lift associated with $C(k)$, which is the circulatory part of the lift L_c.

$$L_c(t) = 2\pi\rho U_\infty bC(k)w(t) \tag{A.4}$$

$$w(t) = \Big(U_\infty\alpha + \dot{h} + b(\frac{1}{2} - a)\dot{\alpha}\Big) \tag{A.5}$$

With the Duhamel integral, L_c can be defined in terms of the Wagner function[103] $\phi(s)$:

$$L_c(s) = 2\pi\rho U_\infty b\Big[w(0)\phi(s) + \int_0^s \frac{dw(\sigma)}{d\sigma}\phi(s-\sigma)d\sigma\Big] \tag{A.6}$$

$$\phi(s) = \frac{1}{2\pi i}\int_\infty^\infty \frac{C(k)}{k}e^{iks}dk \tag{A.7}$$

With Jone's approximation[139] of Wagner's function:

$$\phi(s) \cong b_0 + b_1 e^{-\beta_1 s} + b_2 e^{-\beta_2 s} \tag{A.8}$$

where $b_0 = 1,\ b_1 = -0.165,\ b_2 = -0.335,\ \beta_1 = 0.0455,\ \beta_2 = 0.3$

As Developped by Kholodar[140], instead of integrating $L_c(s)$ from zero to the current time at each time step, $L_c(s)$ can be represented as a sum of augmented state that will be recalculated each time step as a solution of simple ODE. After integrating $L_c(s)$ by parts twice:

$$\frac{L_c(s)}{-2\pi\rho Ub} = [b_0 + b_1 + b_2]w(s) + b_1\beta_1 \int_0^s w(\sigma)e^{-\beta_1(s-\sigma)}d\sigma + b_2\beta_2 \int_0^s w(\sigma)e^{-\beta_2(s-\sigma)}d\sigma \quad \text{(A.9)}$$

Let's denote the last two terms as augmented states $x_{aug1}(s)$ and $x_{aug2}(s)$

$$x_{aug1}(s) = b_1\beta_1 \int_0^s w(\sigma)e^{-\beta_1(s-\sigma)}d\sigma \quad \text{(A.10)}$$

Which has the Laplace transform:

$$X_{aug1}(p) = b_1\beta_1 W(p)\frac{1}{p+\beta_1} \quad \text{(A.11)}$$

After taking the inverse, one obtains that x_{aug1} satisfies(the same holds for x_{aug2}):

$$\frac{dx_{aug1}(s)}{ds} + \beta_1 x_{aug1}(s) = b_1\beta_1 w(s) \quad \text{(A.12)}$$

The augmented states $x_{aug1}(s)$ and $x_{aug2}(s)$ are then evaluated at each time step with a simple Runge Kutta 4 scheme. This formulation apply fto arbritary motion and can be easily integrated into the coupling scheme. The UVLM is compared against Jone's approximation of Wagner's function in Figure A.1 for a sudden acceleration of a flat plate.

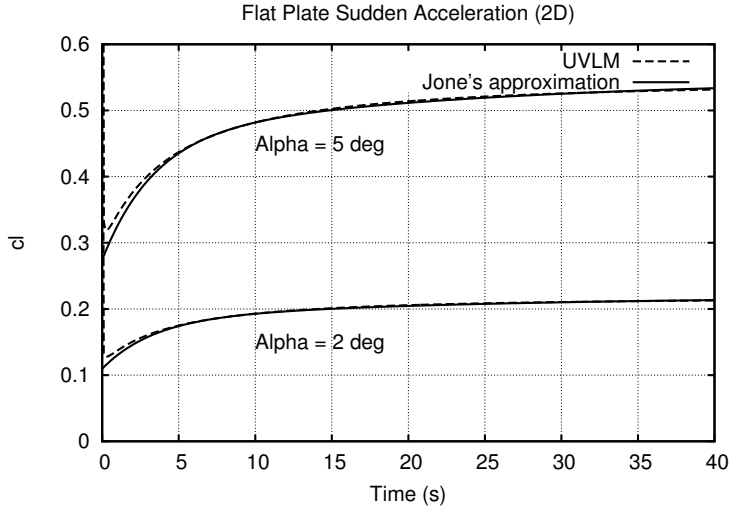

Figure A.1 Validation of the UVLM against Jone's approximation of Wagner's funtions for a sudden acceleration of a flat plate.

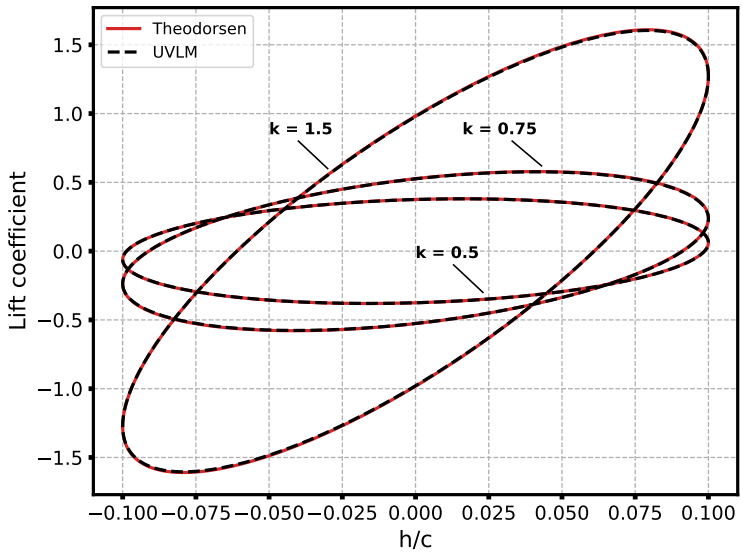

Figure A.2 2D lift coefficient for a harmonic heave motion

APPENDIX B VERIFICATION OF THE HB VLM

The HB VLM is verified with the well known Theodorsen formulation of unsteady lift. Since the HB VLM and the Theodorsen formulation are both in the frequency domain and derived from thin airfoil theory, they should provide the same results for simple heave and pitch harmonic motions. Single harmonic motions are computed, thus only one harmonic is necessary for the Fourier series to accurately represent in time the solution. In order to obtain 2D results with the HB VLM, an aspect ratio of 1000 is used with 5 panels spanwise. The solution of the lift coefficient is verified in Figure B.1 for three different reduced frequencies.

Furthermore, once converged, the iterative approach produces the same results as the direct approach as presented in Table B.1, where the heave motion is performed at a reduced frequency of 0.75 with $0.1/c$ amplitude and the pitch motion is performed at a reduced frequency of 0.2 with two degrees amplitude. The iterative approach provides equal accuracy than the direct approach and the difference in the solution between the two methods are down to machine accuracy.

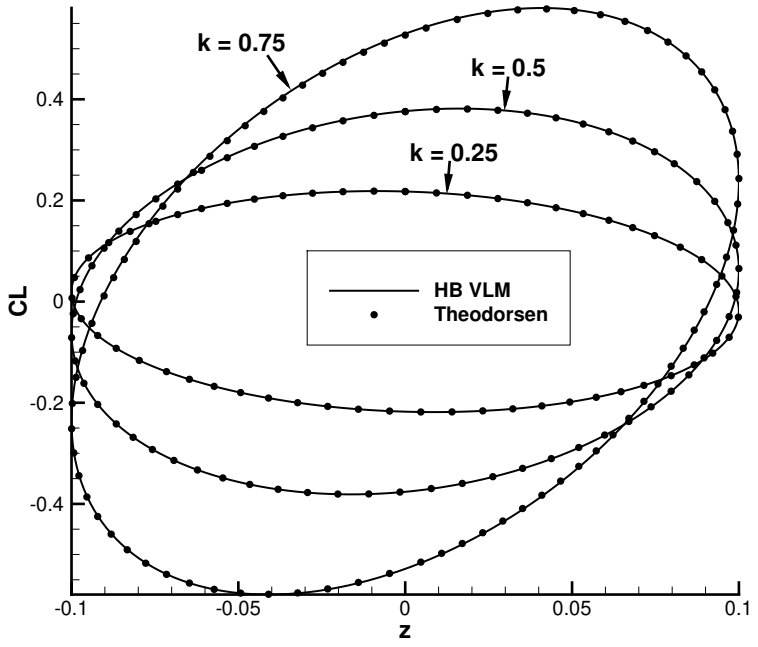

Figure B.1 Lift coefficient for a harmonic heave motion at three different reduced frequencies with 10 chordwise panels; $h = 0.1\sin(\omega t)$

Table B.1 Absolute differences of Fourier coefficients solution between the iterative and the direct approaches

	Fourier Coefficients		
	$\mathbf{a_0}$	$\mathbf{a_1}$	$\mathbf{b_1}$
Heave motion	1.1×10^{-15}	3.1×10^{-15}	1.6×10^{-15}
Pitch motion	0.6×10^{-15}	0.6×10^{-15}	1.0×10^{-15}

APPENDIX C COMPUTATIONAL GRIDS

All grids are generated with Pointwise. The 2D grids are generated with the hyperbolic mesh extrusion method, while the 3D grid is generated using the T-REX method. The first layer spacing is computed to ensure a y^+ of around 0.5 for a Reynolds number of one million. Snapshots of the grids are presented in Figures C.1 to C.5.

The 2D grids have 300 points along the airfoil and about 155 points from the airfoil to the farfield. The first layer spacing is 8×10^{-6} and the growth rate is 1.1.

The 3D grid is composed of mixed elements: hexahedral, prism, pyramid and tetrahedral. The surface mesh has 14,845 elements for a total of 1,462,827 elements for the entire grid. The first layer spacing is 8×10^{-6} and the growth rate is 1.15.

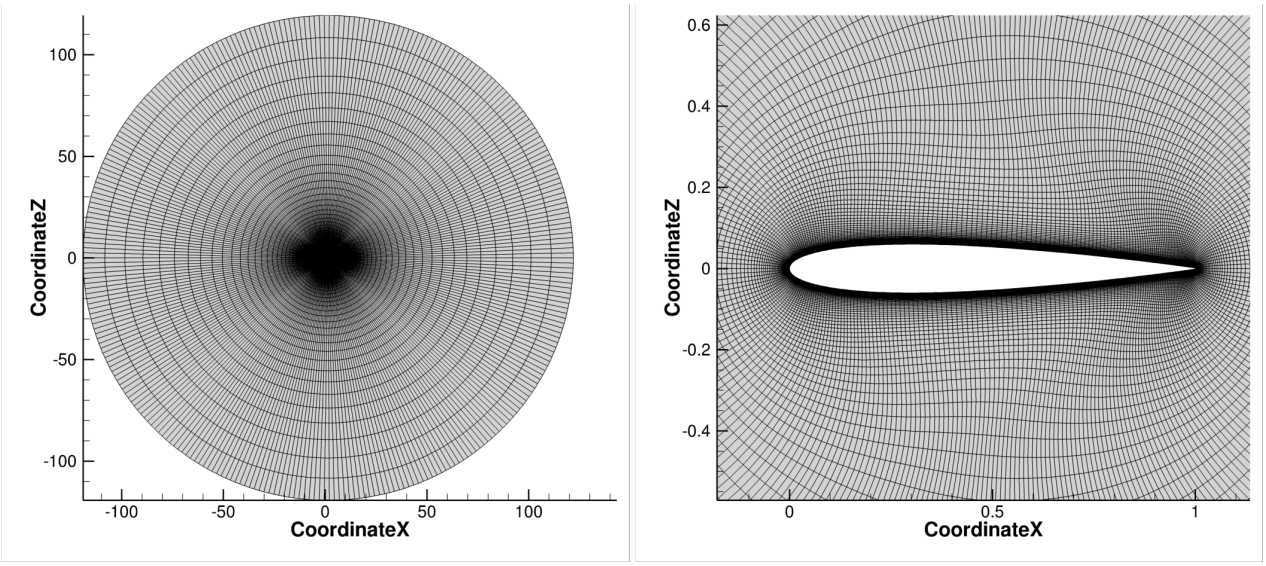

Figure C.1 Grid for the NACA 0012 for RANS simulations.

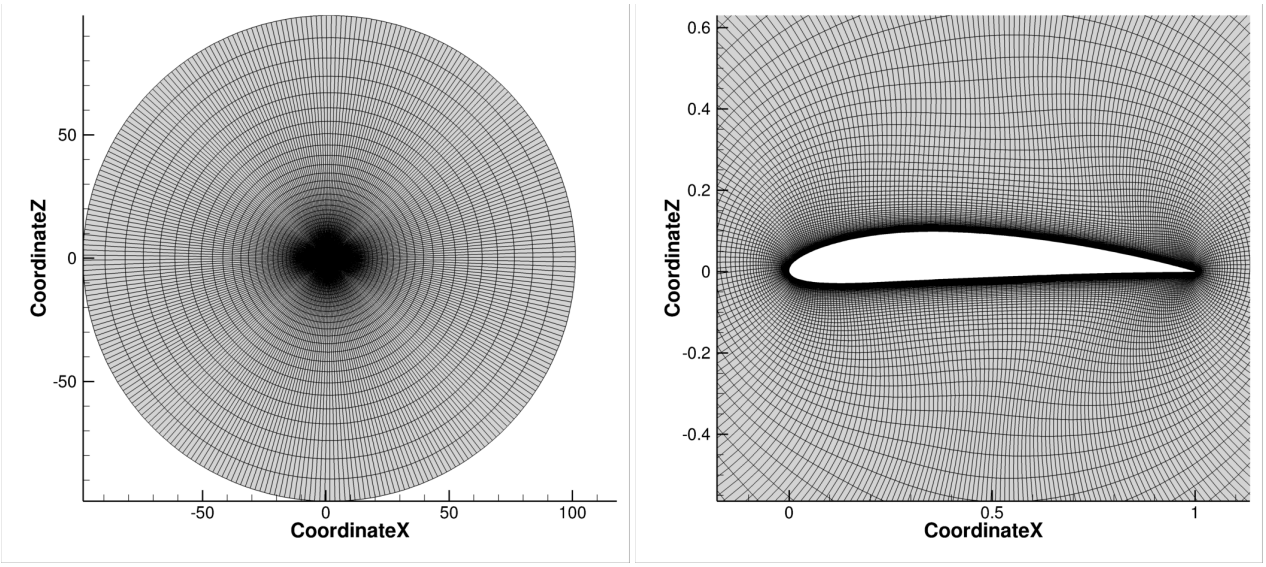

Figure C.2 Grid for the NACA 4412 for RANS simulations.

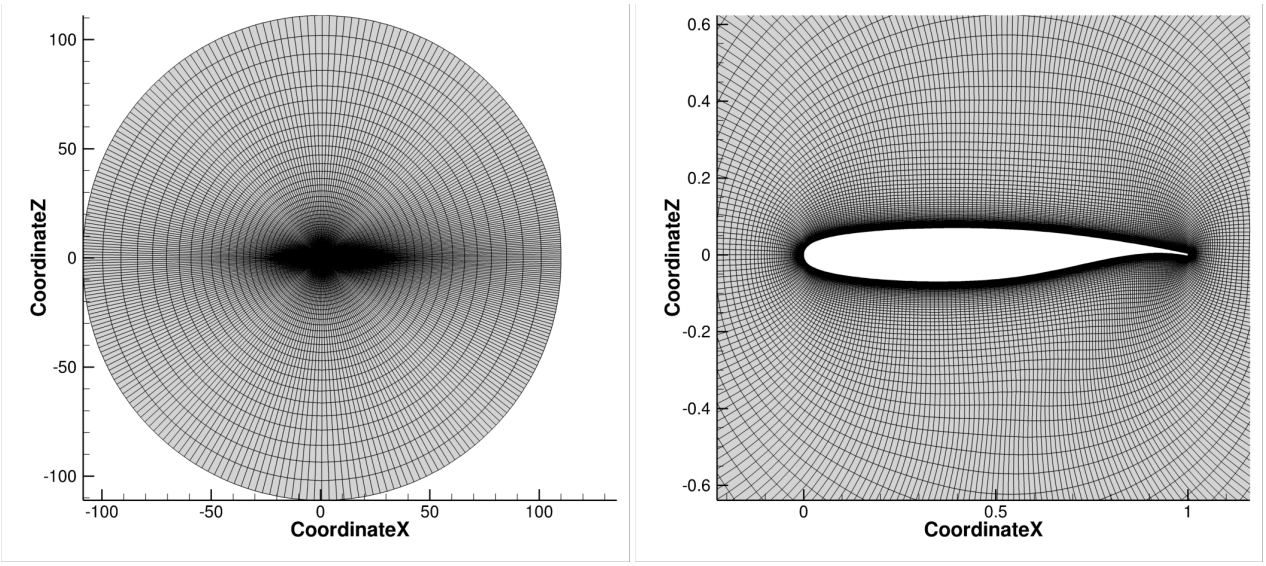

Figure C.3 Grid for the BSCW critical wing for RANS simulations.

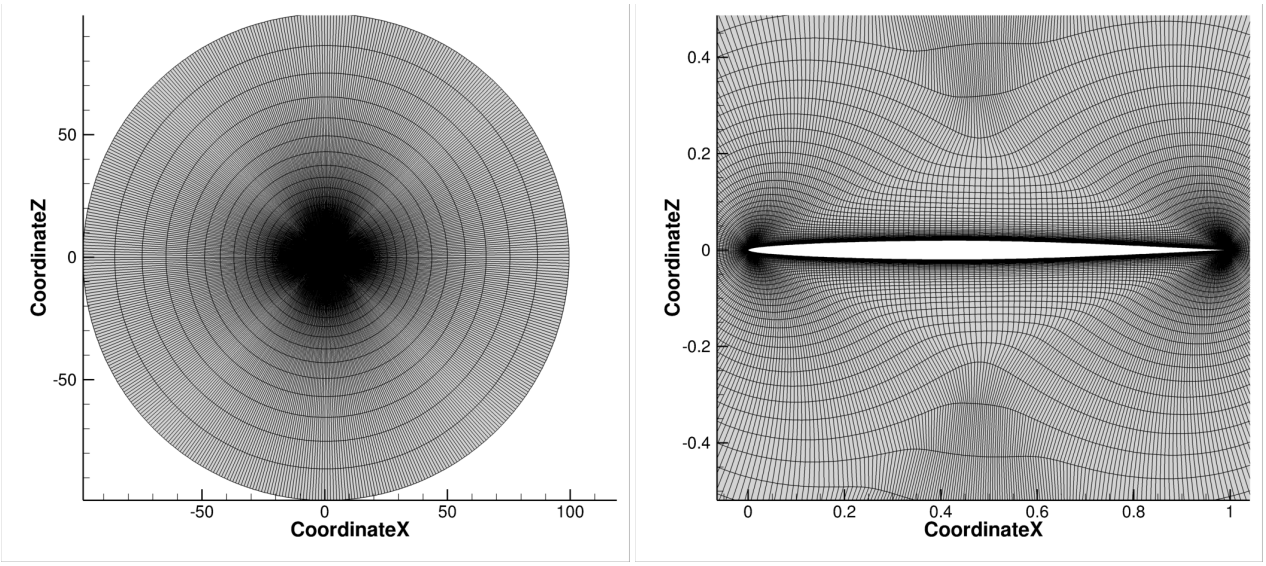

Figure C.4 Grid for the Agard wing for RANS simulations.

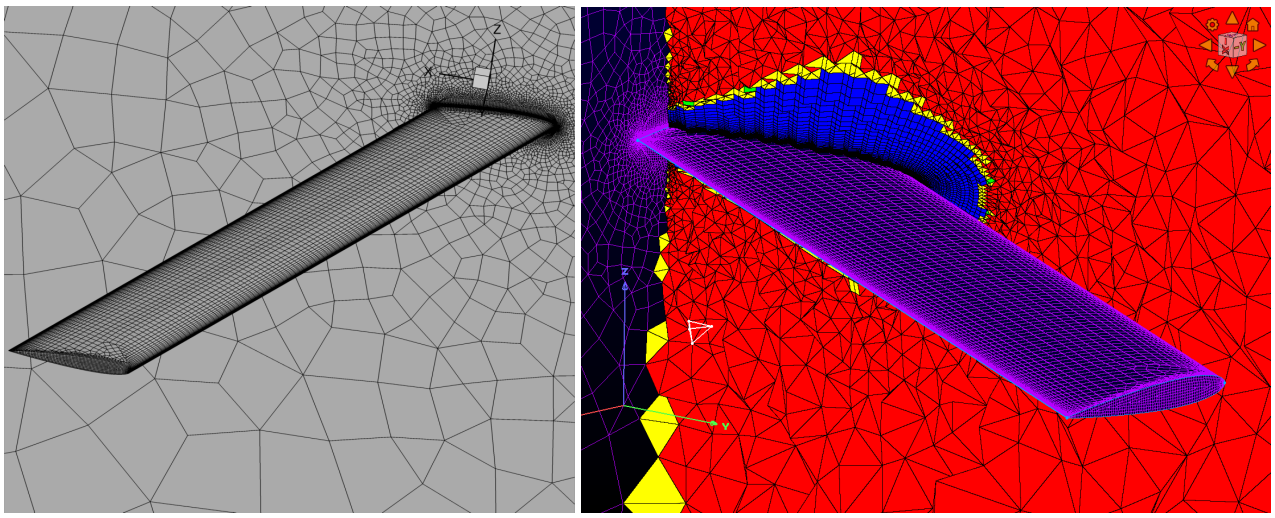

Figure C.5 Grid for the NACA 0012 30° swept wing for RANS simulations.